Author:
Mattioni, Filippo

Title:
Thermally induced multi-stable composites for morphing aircraft applications

Thermally induced multi-stable composites for morphing aircraft applications

Filippo Mattioni

17th August 2009

A dissertation submitted to the University of Bristol in accordance with the requirements of the degree of Doctor of Philosophy in the Faculty of Engineering

Abstract

This research focuses on the realisation of 'shape-adaptable' systems through unsymmetric laminates. The residual stress field which is built-into this type of laminates, is used to obtain panels with two or more equilibrium states. Such systems provide a possible solution for the realisation of morphing structures because they allow to simultaneously fulfil the contradictory requirements of flexibility and stiffness.

An analytical model to describe the equilibrium configurations of bi-stable composites is developed. A new formulation of the displacement field allows to extend the previous analytical models that could only take into account free boundary conditions.

Three concepts for the realisation of morphing structures are presented and analysed. The Variables Sweep Wingbox aims at the realisation of a novel wing-swing mechanism, based on composite spars which allow a continuous deformation of the wing shape. The Bi-stable Blended Winglet proposes a lift augmentation device which both for take-off and cruise operations when in a configuration similar to that of a traditional winglet. Finally, the Variable Camber Trailing Edge shows two different methods to modify the camber of an airfoil by using unsymmetric patches of laminate to drive the shape change of the wing.

Throughout the analysis, experimental testing has been used to validate the analytical and numerical findings as well as to prove the feasibility of the proposed application concepts.

To my parents, for their education
To my ex-girlfriend, now my wife,
for her patience and encouragement

Acknowledgements

I would like to thank Professor Michael Friswell for giving me the opportunity to join the Morphing Aircraft Group and for his support to finalise my efforts for this work.
I am grateful to Dr Paul Weaver for his enthusiasm, encouragement and guidance that allowed this thesis to be written.
I am also grateful to Dr Alvin Gatto and Dr Kevin Potter, without whom most of the experimental work of this thesis would have never been possible.
Finally, I would like to thank my colleagues Nima, David, Cezar, Patrick, Enrique, Maurizio and Alberto for their time. It is through our endless discussions that most of the problems of this thesis have been resolved.
The financial support of the European Community through the Marie Curie Research Training Network, is also gratefully acknowledged.

Declaration

I declare that the work in this dissertation was carried out in accordance with the Regulations of the University of Bristol. The work is original except where indicated by special reference in the text. No part of the dissertation has been submitted for any other academic award. All views expressed in the dissertation are those of the Author.

Signature: 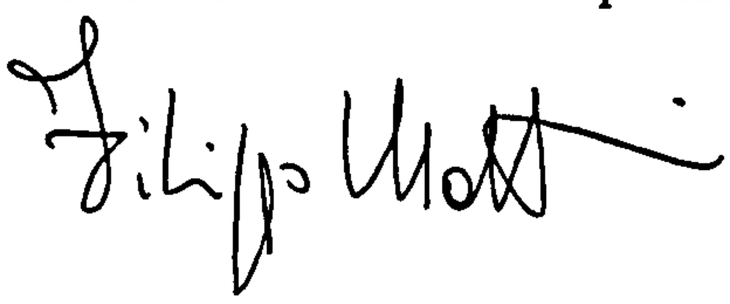

Word count: 31000

Contents

List of Figures

List of Tables

Nomenclature

Q_{ij} ij element of the reduced stiffness matrix

$\underline{\underline{Q}}$ reduced stiffness matrix

N_l number of layers in the laminate

A_{ij} ij element of the membrane stiffness matrix

$\underline{\underline{A}}$ membrane stiffness matrix

B_{ij} ij element of the extension-bending stiffness matrix

$\underline{\underline{B}}$ extension-bending stiffness matrix

D_{ij} ij element of the bending stiffness matrix

$\underline{\underline{D}}$ bending stiffness matrix

N_i i^{th} element of the in-plane forces vector per unit length acting on a laminate

$\underline{N}$ in-plane forces vector per unit length acting on a laminate

M_i i^{th} element of the moment vector per unit length acting on a laminate

$\underline{M}$ moment vector per unit length acting on a laminate

E_{11} Longitudinal stiffness of a unidirectional orthotropic lamina

E_{22} Transverse stiffness of a unidirectional orthotropic lamina

G_{12} Shear modulus of a unidirectional orthotropic lamina

ν_{12} Poisson's ratio of a unidirectional orthotropic lamina

α_1 longitudinal coefficient of thermal expansion of a unidirectional orthotropic lamina

α_2 transverse coefficient of thermal expansion of a unidirectional orthotropic lamina

w displacement of the laminate in the z direction

R undeformed transverse curvature radius of a shell structure

r deformed longitudinal curvature radius of a shell structure

k_i i^{th} component of the curvature vector

$\underline{k}$ curvature vector

α_i i^{th} component of the coefficient of thermal expansion vector

ϵ_i i^{th}component of the in-plane strain vector

$\underline{\epsilon}$ in-plane strain vector

ΔT temperature difference between the highest curing temperature and room temperature

t thickness of the composite part

L edge length

FEA Finite Element Analysis

FEM Finite Element Model

IFH Integral Folding Hinge

UAV Unmanned aerial vehicle

l rolling moment

m pitch moment

n yaw moment

Y side force

α angle of attack

Λ sweep angle

γ cant angle

C_L coefficient of lift

as after snap

bs before snap

RMS root mean square

CFRP carbon fibre reinforced plastic

Throughout the paper matrices will be indicated by double underline, vectors by single underline and scalars by no underline

Chapter 1

Introduction

"Aprono le ali
scendono in picchiata
atterrano meglio di aeroplani
cambiano le prospettive al mondo
voli imprevedibili ed ascese velocissime
traiettorie impercettibili
codici di geometria esistenziale"
Franco Battiato, "*Gli uccelli*" [1]

In the common language, the word "morphing", can have a rather large and misleading number of meanings. In particular, when referred to the natural environment, there are many examples of morphing: chamaeleon and fishes can change the colour of their skins to hide or hunt, while birds can seamlessly adapt their body shape to suit a particular task. These two examples, can indeed be considered the state of the art of two different categories of "morphing": a first type which refers more to the appearance of an object and a second which refers primarily to the external shape of the object. For the purpose of this thesis, the second meaning of the word morphing is adopted and dealing in particular with aeronautical structures, birds will be taken as the primary source of inspiration. For these reasons in the following pages, the shape

[1] "They open the wings, dash down, land better than aircraft, change perspectives to the world, unpredictable flights and fastest soaring, unperceivable trajectories, codes of existential geometry"...the birds.

change of which birds' wings are capable, during different flight conditions, should be kept in mind as the "reference" wing morphing.

1.1 The morphing aircraft project

Like birds, aircraft follow specific mission profiles. While for birds these profiles might be "take off", "mission" (i.e. hunt or migration) and "landing", for aircraft there is not much difference and a mission generally consists of take-off, climb, the mission itself, descent and landing. To specify the design envelope for the vehicle, design points are chosen within each part of the mission and then, to fulfill the requirements, the best compromise among the possible configurations is selected. It is therefore evident that the result is an aircraft which is not optimal for any of the given design point [Stanewsky, 2000]. Off-design flight conditions have significant aerodynamic and structural drawback such as increased drag penalty and off-design structural deformation [Papila et al., 2004]. These conditions are true for both long distance transport aircraft, where the large quantities of fuel burnt in-flight lead to a considerable change in the aircraft mass and aerodynamic requirements, and also for fighter aircraft, where the manoeuvrability requirements constraint most of the flight envelope. It is evident that the ability to adapt the wing shape to different flight conditions would limit these problems and also it would give a single aircraft the capability to achieve multi-objective mission roles thus reducing the operational costs of having several aircraft, each suited to a different type of mission. However, from current trends in this research area [Bae et al., 2005, Frank et al., 2008, Thill et al., 2008, Jha and Kudva, 2004], it is clearly evident that the practical realisation of a morphing structure is a particularly demanding goal with substantial effort still required. This is primarily due to the need of any proposed morphing airframe to simultaneously fulfill the contradictory requirements of flexibility and stiffness. On one hand for low speed aircraft, it is always possible to rely on the elasticity of the material to achieve small deformations by mean of simple actuators, on the other hand this solution is not applicable to high speed aircraft because of the imposed stiffness and strength requirements. These would require a huge power consumption which would simply lead to an unacceptable weight penalty. Currently, to overcome this, the most efficient solution is to rigidly actuate small parts of the main structure. The moveable parts are, generally, rigid bodies linked to the main structure via hinges. This technique, though reliable, introduces discontinuities in the aerodynamic flow field and in the structure, and place limitations on manoeuvrability and efficiency, producing non-optimal designs for many flight conditions. It is for these reasons that recently many projects have focused on

realising the so called "morphing technologies". To describe this "scenario", a few of the proposed solutions will be summarised in the following paragraphs.

Overview of previous morphing research

The German Aerospace Centre (DLR) investigated the possibility of flexible ribs through the "flexible rib" [Monner, 2001] and the "belt rib" [Campanile and Sachau, 2000, Campanile and Anders, 2008] concepts. They both aim to realise variable camber profiles by acting on the trailing edge part of wings of civil transport aircraft. This is used to achieve both chord-wise and span-wise camber variation to optimise L/D and reduce the root bending moment. The finger concept mimics the human finger by relying on a kinematic chain to obtain a gradual deflection of the trailing edge. The ribs are realised by combining rigid plate elements together through prismatic and revolute joints. Each rib is actuated at one single point and the rotation of the driving element is gradually transferred to the other elements thus achieving a smooth contour variation. A scheme with the component elements and their assembly is shown in Fig.1.1. Each plate element is actually made of three separate panel bonded together with two cut-outs for the prismatic and the revolute joints. The flexible ribs are connected to the upper and the lower skin of the airfoil by linear slide bearings, positioned along the skin according to the local loading conditions.

The concept behind the "belt rib" (ref. Fig.1.2) is the "structronic" approach where solid-state actuators (such as piezoceramics and shape-memory alloy) are integrated in a flexible structure. The result is a lighter structural system with the absence of hinges or bearings, together with the multi-functionality of solid-state actuators. Additional advantages are the surface's smoothness, the absence of wear and play and the possibility of having multiple degrees of freedom. The belt-rib is also a novel approach for the realisation of the rib structure. The aircraft industry generally uses shear web rib design [Niu, 1999b], which usually produces in-plane rigid members; conversely the "belt rib" allows in-plane deformation, though virtually restricted to one degree of freedom. The structural frame of the belt-rib consists in a closed shell *(belt)* reinforced by in-plane stiffeners *(spokes)*. The spokes are connected to the belt by mean of solid-state hinges while their placement is obtained through an optimisation process. The purpose of this choice is that the belt rib structure approximates a one degree of freedom mechanism, as far as only the kinematics is considered. The prototype shown in Fig.1.2 was designed to act as a variable-camber landing flap. The distribution of the spokes allows large camber changes in the aft part of the flap. The deformation is transmitted to the profile

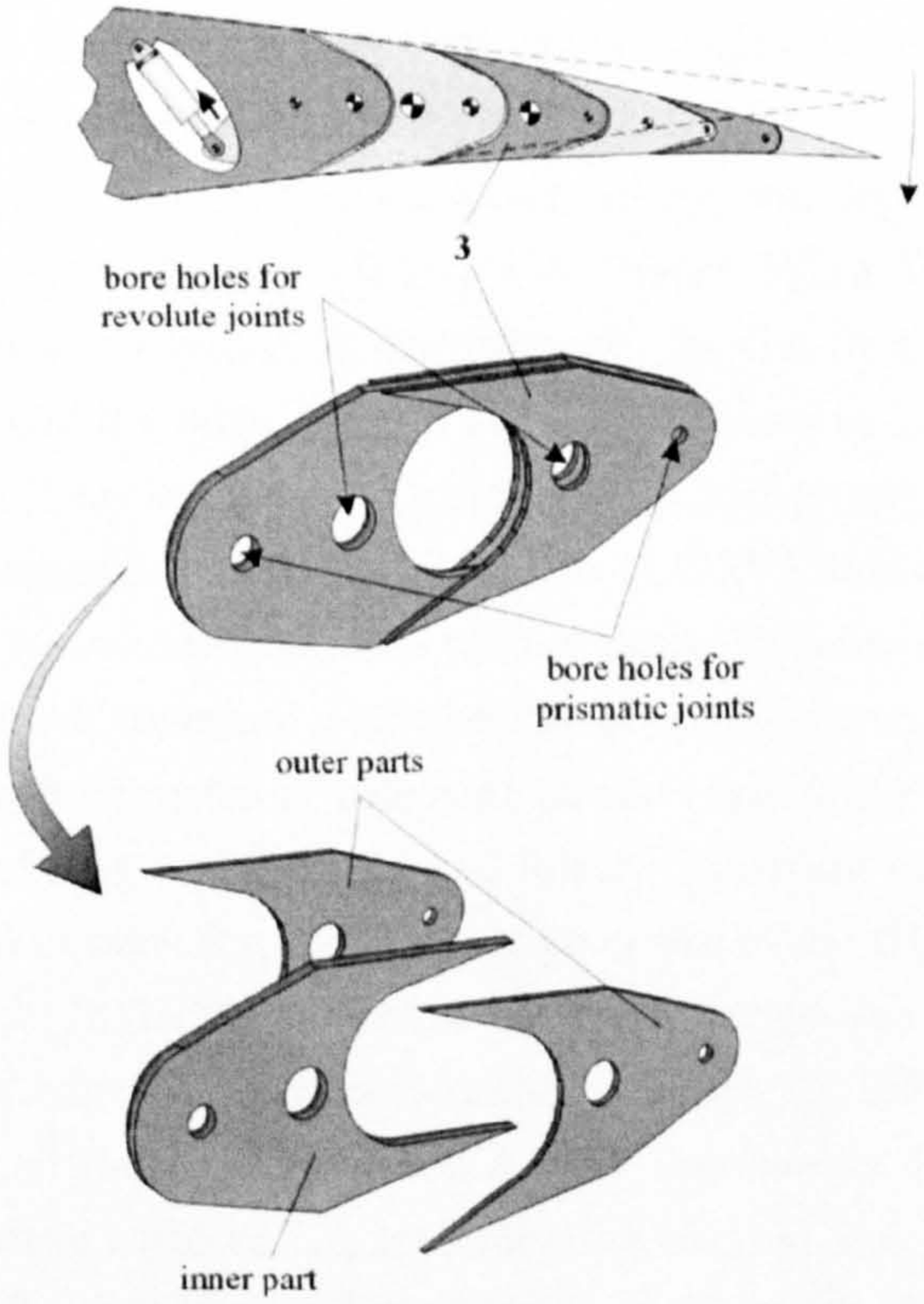

Figure 1.1: DLR flexible rib concept [Monner, 2001]

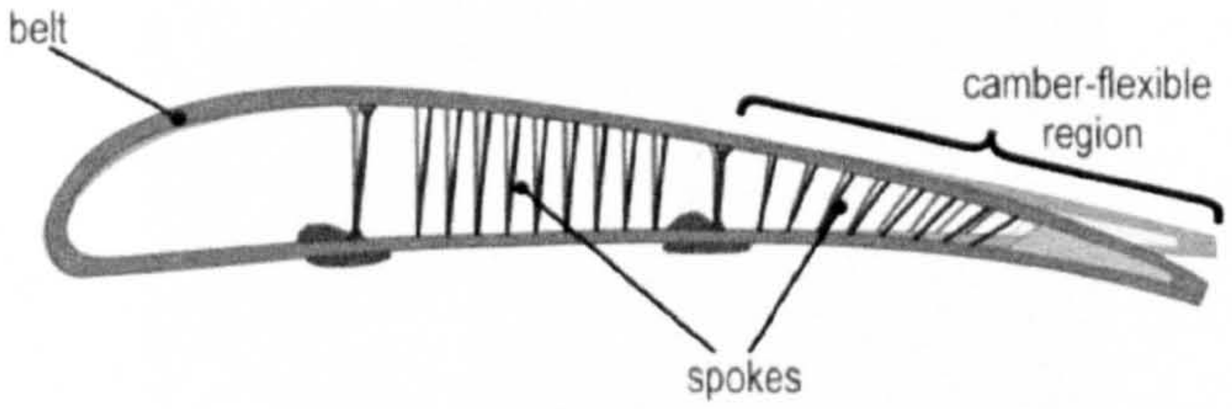

Figure 1.2: DLR belt rib concept [Campanile and Sachau, 2000]

of the rib (hence to the airfoil) by mean of the belt which runs continuously around the profile. The spokes are linked to the belt and by changing their angle with respect to the belt, the airfoil profile changes gradually.

One of the biggest effort in adaptive wing technology, was represented by the Defence Advanced Research Project Agency (DARPA)'s Smart Wing Program which started in 1995. The program was divided in two phases. In the first phase Shape Memory Alloy-based hinge-less trailing edge, control surfaces and active variable wing twist were investigated through 16% scale models. During the second phase, which started in 1998, a bigger 30% scale unmanned combat air vehicle (UCAV) was designed and tested in the wind tunnel. The tests confirmed the aerodynamic benefits shown during Phase 1. DARPA was also involved, together with the Air Force Research Laboratories (AFRL), in the Morphing Aircraft Structures program in the realisation of demonstration tests for an UCAV capable of long range cruise and loiter, transition into high speed dash and kill, and finally transition back for the long range cruise home [Bye and McClure, 2007].

FlexSys [Kota et al., 2003] developed a "smooth, hinge-free wing whose compliant trailing and/or leading edges morph on demand to adapt to different flight conditions". Using wind-tunnel experiments they noted a 25% increase in lift coefficient and 51% increase in the lift to drag ratio as the leading edge camber was changed from 0^0 to 6^0. In addition to this, deflecting the trailing edge from 0^0 to 6^0, they showed a low airfoil drag of 0.006 for the lift coefficient ranging from 0 to 1.5. The project was developed with the help of Lockheed Martin and is undergoing extensive testing. Little is know about the internal structure, materials and weight penalty. An example of the deformation achievable is shown in Fig.1.3.

Nextgen [Bowman et al., 2007] focused on the realisation of large geometry changes. To achieve this, 20 different configuration concepts have been generated. From these concepts a final design, termed "batwing", was chosen. The design is capable of a large variation of aspect ratio (200%), wing span (40%) and wing area (70%). Particular attention was devoted to the design of the wing skins which need to possess low in-plane

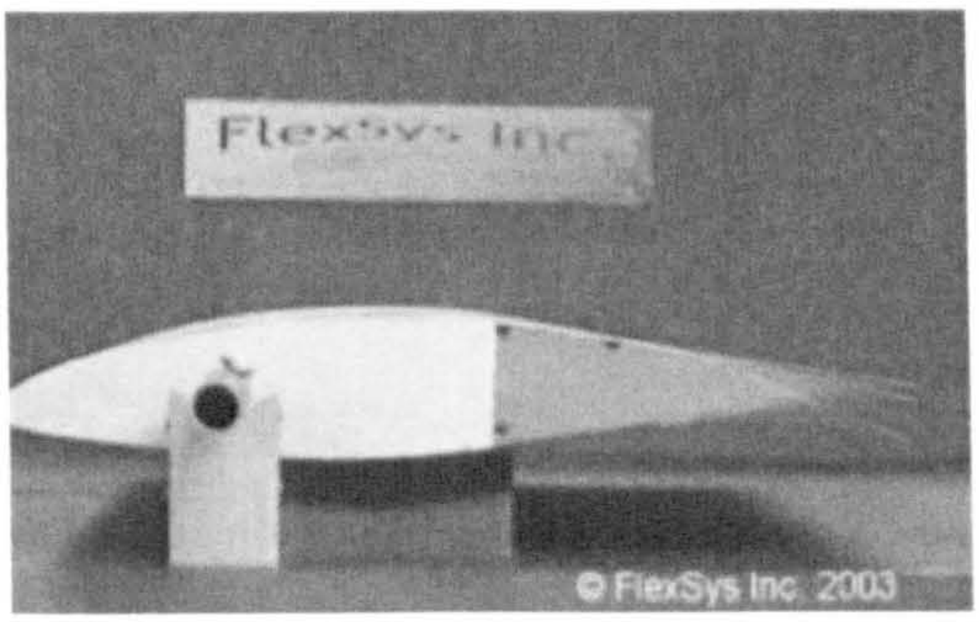

Figure 1.3: Flexsys variable camber wing [Kota et al., 2003]

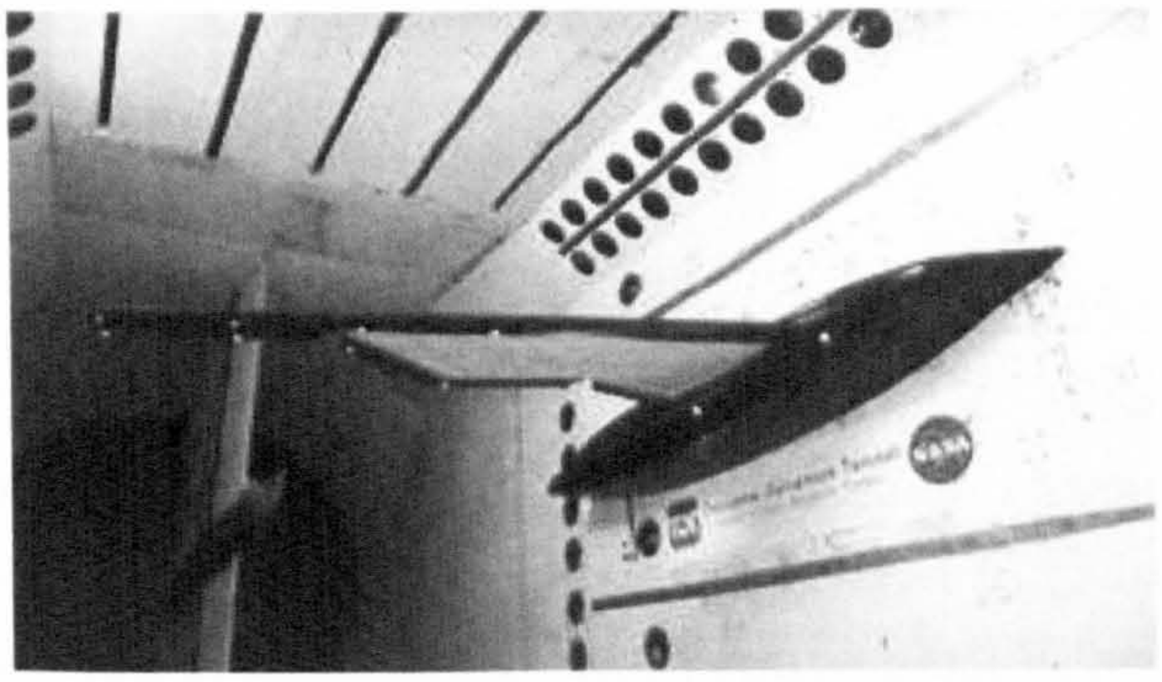

Figure 1.4: Batwing model in the NASA Langley transonic tunnel [Bowman et al., 2007]

stiffness to allow for in-plane morphing but high out-of-plane stiffness to withstand the aerodynamic loads. Figure 1.4 shows the wing tunnel model.

The Active Aeroelastic Aircraft Structures (3AS) was a european project aimed at developing novel design concepts to improve the efficiency of aircraft through continuous shape adjustments. One of the main concept was the development of active aeroelastic structures to allow aeroelastic deflections to be used in a beneficial manner. The range of application varied from large transport jet airplanes to UAVs and Remote Piloted Vehicle (RPV). Exploiting the aerodynamic flow to induce induce deformations could lead to reduce energy requirements for the actuating systems [Kuzmina et al., 2002]. By changing the position, orientation and stiffness of the spars, the shear centre of the wing is shifted and it is possible to controll the aeroelastic behaviour. As a result, the bending moment and the twist distribution will change along the wing [Amprikidis and Cooper, 2003, 2004a]. In case of long range transport aircraft, the 3AS progeamme, investigated through wind tunnel models several concepts such as control surfaces at the wing tip, modification of the inboard aileron to provide a continuous deformed surface and replacement of conventional tail plane with smaller all-moving version with variable

rotational stiffness. This latter concept was aimed at reducing the overall weight of the aircraft due to the use of oversized vertical fin, which are generally needed to compensate for the reduce control efficiency at high speed [Amprikidis and Cooper, 2004b].
These are just a few of the research groups which are investigating the feasibility of morphing aircraft solutions. Each group approaches the problem from different angles but it is clear that a trade-off between structural/aerodynamic efficiency and aircraft adaptability must be made. Also, the number of proposals in this respect is quite large and it is hard to quantify whether any of these concepts is clearly better than another one. For these reasons, the realisation of shape-adaptable structures remains a challenging field, still open to new design concepts.

Compliant mechanism

Compliant mechanisms generally consist of monolithic structures which rely on their elastic deformation to achieve a desired geometry variation. They present several advantages such as reduced complexity and wear. The main characteristic is the ability to distribute the localised actuation force to a wider area in order to produce a shape change with very low stress concentration [Kota et al., 2003]. The distributed flexibility eliminates discontinuities into the structure, which are responsible for stress concentrations typical of rigid bodies assemblies. A hole to connect a hinged part, for example, can increase the local stresses by a factor of 4 or 5 [Young, 2001], requiring a considerable local reinforcement and weight penalty. Opposite to this, a compliant hinge, distributes the stresses more evenly and therefore the additional reinforcement is reduced to a minimum. In addition, compliant mechanisms have several functional advantages such as lighter weight and the ability to generate backlash, friction and noise free motion. One of the main drawbacks of this type of system is that they rely heavily on complex optimisation procedures to achieve a good efficiency and also their ability to replace structural members is limited by the low stiffness of the component members [Saggere and Kota, 1999]. On a morphing structure for aeronautical applications compliant mechanisms would naturally find a place within wing covers, ribs and aerodynamic fairings.

1.2 Outline of the thesis

Having outlined the current research area, the thesis will now investigate the feasibility of morphing structures realised by making use of unsymmetrically laminated composites. As has been shown, the area of interest is vast and a comprehensive investigation of all the

aspects is hard to conceive and therefore, attention will be focused on two main aspects: modelling and application. The next chapter will present a few basic principles required for the analysis of laminated composites and a review of the literature on unsymmetric laminates. The last part of the chapter will present a few introductory examples that show the potential for unsymmetric laminates. Chapter 3 is devoted to the analytical and numerical modelling of unsymmetric laminates. Finally, Chapter 4 will focus on the applicative side presenting a few concepts for morphing structures realised by mean of thermally induced multi-stable composites.

Chapter 2

Composite materials and unsymmetric laminates

The key point for the realisation of a morphing structure, is to be able to find the right balance between structural compliance and stiffness. For this purpose composite materials seem to offer a promising solution. There are several properties which make composite interesting for this area of research. Their high strength and low weight remain an important combination, but most important is the ability to tailor their properties for a specific purpose which makes them particularly suitable for these types of applications. In particular composite materials offer a low coefficient of thermal expansion (CTE), a characteristic which is very important for the applications presented in this study. Composites have excellent fatigue characteristics and provide design/fabrication flexibility that can significantly decrease the number of parts needed for specific applications which translates into a finished product that requires less raw material, fewer joints and shorter assembly time. Composites differ from traditional materials in that composite parts comprise two distinctly different components, fibres and matrix. These, though remaining discrete, interact with each other to make a new material whose properties combine the advantages of both components. Thin glass fibres, for example, exhibit relatively high tensile strength, but are susceptible to damage. By contrast, most polymer resins are weak in tensile strength but are extremely tough. When combined, however, the fibre and resin each counteract the other's weakness, producing a material far more useful than either of its individual components. Of course this comes with a price and in fact, for many applications, the advantages are still offset by the added complexity associated with designing and manufacturing composite based structures. Composite materials require, generally, a more difficult manufacturing process and the fabrication

still relies heavily on hand labour and it is difficult to automate. In addition, from a design point of view the additional degrees of freedom require, in turn, greater capabilities to determine the optimal combination of all the parameters for an efficient design. When trying to optimise a structure made out of composites, it is not uncommon to deal with a number of parameters which is by far greater than that of equivalent metal structures and therefore for these reasons designing a structure which truly benefits from composites, requires considerable effort during the design stage. One other major inconvenience, at least for aerospace grade components, is the expensive manufacturing process they require to achieve the aforementioned properties. To obtain the best properties, the most widespread and reliable process is that of autoclave curing of pre-preg fabrics. These are generally hand laid, even though a certain degree of automation is now possible, on a tool which can be made of composite or metal. The tool itself requires quite a great deal of attention since it has to match the thermal properties of the composite, be able to withstand high curing temperatures, pressures and be dimensionally stable [Pinto et al., 2008]. Durability of the tool is also a cost sensitive factor. For example, when dealing with small volumes of production the cost of tooling can account for up to 90% of the final cost of the part [Pinto et al., 2008] because it is not possible to offset the costs over a large number of parts. Composite manufacturing also requires a considerable amount of ancillary material which is wasted at the end of each production cycle and whose cost can be significant. All this, coupled with the lack of know-how and automation, makes composites extremely expensive to manufacture and, despite their superior properties, are often discarded as an alternative. However this is rapidly changing and recent advances in manufacturing are making composite structures more and more competitive.

2.1 Basic analysis of composite materials

To design a composite structure, different approaches are possible depending on what is to be investigated. For example, if the material properties need to be tailored for a particular set of constraints, an in-depth analysis of the way the constituent materials interact with each other will be required and therefore the "micro-mechanical" approach is more suited. If the attention is more focused on the overall mechanical behaviour, a more general approach is appropriate and therefore the "macro-mechanical" analysis will be considered. From a theoretical point of view, the two approaches are intertwined with each other, since the macro-mechanics of composites is based on the assumption made for the micro-mechanics. The main difference, in fact, resides more on the results which may be obtained using one or the other method. The micro-mechanical analysis is

aimed at describing the relations which link the constituent materials, while the macro-mechanical analysis provides a set of equations which allow to design and analyse the basic components of structural systems, without paying too much attention to what is the composite made of. In the next paragraphs the basic principle of composite material analysis will be presented.

2.1.1 Micro-mechanics

Micro-mechanical analysis is used to design the mechanical properties of composites having, as a starting point, the mechanical characteristics of the basic components, namely the fibres and the matrix. One of the most commonly used method is the "rule of mixtures", a mathematical model based on simplifying assumptions on the physical behaviour of the constituent materials (fibres uniform, parallel and continuous and perfect bonding between fibre and matrix). According to these simplifications and considering a unidirectional lamina with principal material direction 1 (i.e. longitudinal) and 2 (i.e. transverse) , the following equations are obtained

$$E_{11} = E_f V_f + E_m(1 - V_f) \tag{2.1}$$

$$E_{22} = \frac{E_f E_m}{E_m V_f + E_f(1 - V_f)} \tag{2.2}$$

$$\nu_{12} = \nu_f V_f + \nu_m(1 - V_f) \tag{2.3}$$

$$\frac{1}{G_{12}} = \frac{V_f}{G_f} + \frac{1 - V_f}{G_m} \tag{2.4}$$

$$\alpha_1 = \frac{1}{E_1}[\alpha_f E_f V_f + \alpha_m E_m(1 - V_f)] \tag{2.5}$$

$$\alpha_2 = \alpha_f V_f(1 + \nu_f) + \alpha_m(1 - V_f)(1 + \nu_m) - \alpha_1 \nu_{12}] \tag{2.6}$$

where the index "f" and "m" refer to the matrix and the fibre respectively and V_f is the fibre volume fraction. The fibre volume fraction is a particularly important parameter as it mainly determines the performance of the composite. If the volume fraction is too low, the reinforcement fibres will be ineffective. Conversely if it is too high, the lamina will be too dry and the load will not be transferred between the fibres. A typical value for

V_f for pre-impregnated composites is approximately 0.63. Equation (2.1) is obtained by assuming that the fibre and matrix reach the same strain level, while Eq. (2.2) assumes that the stress level is the same. The above mentioned assumptions work quite well for the longitudinal modulus and usually Eq. (2.1) is well supported by experimental tests. The prediction for the transverse stiffnesses and shear modulus in unidirectional composites are difficult because of their sensitivity to voids and the fact that Poisson's contractions at the transverse fibre-matrix interface are neglected.

The mathematical models are based on assumptions and in addition they do not account for defects and operator errors and therefore mechanical tests are usually required to certify that the assumed properties are in fact achieved. To compensate for the inevitable variability of the results, statistical analysis is used to obtain the mean values than can be used for engineering analysis.

2.1.2 Classic lamination theory

The set of equations which relate the stresses and strains in a composite structure, is know as Classical Lamination Theory (often referred to as "CLT") [Jones, 1999]. The basic assumptions (with reference to Fig.2.1) are:

- each material ply is considered homogeneous and the fibre/matrix interface is ignored
- linear elastic behaviour is considered
- only thin plates or shells are considered and therefore the material is assumed to be in a state of plane stress
- Kirchhoff-Love assumptions: straight lines perpendicular to the mid-plane before deformation remain straight, in-extensible and perpendicular to the mid-plane after deformation.
- the tangential displacements, u and v, are linear functions of the through-thickness (z) coordinate.
- thickness variations of the laminate are neglected and are small compared with the length of the edges of the plate
- the theory ignores the effects of neighbouring edges, stiffness and other discontinuities

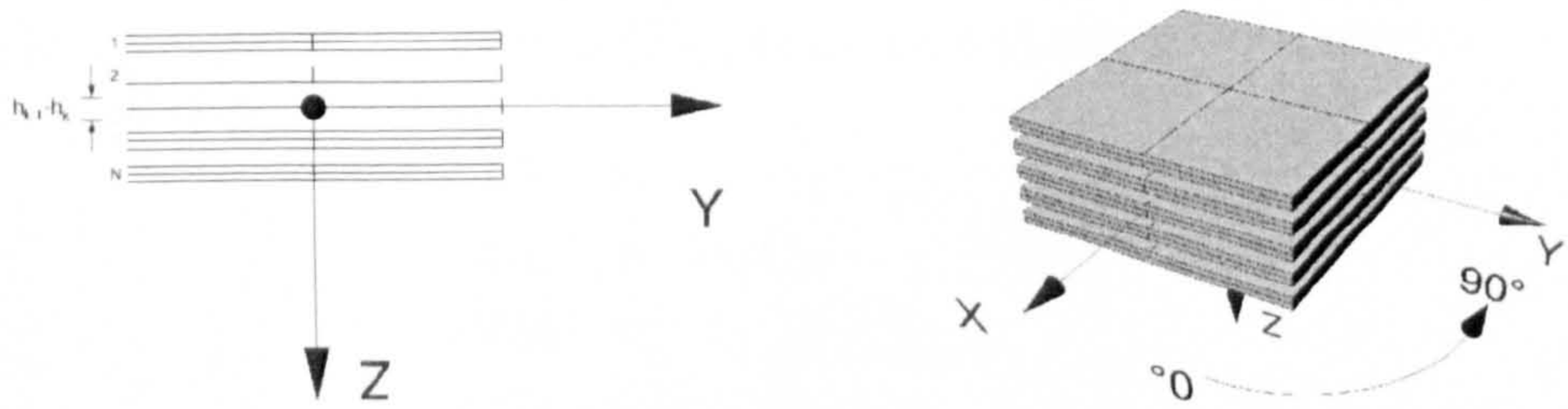

Figure 2.1: Reference system used for the laminate material properties

- the in-plane strains, ϵ_x, ϵ_y and γ_{xy}, are assumed to be small compared with unity.

According to these assumptions the displacements u, v and w are of the form:

$$\begin{aligned} u(x,y,z) &= u^0(x,y) - z\frac{\partial w^0}{\partial x}(x,y) \\ v(x,y,z) &= v^0(x,y) - z\frac{\partial w^0}{\partial y}(x,y) \\ w(x,y,z) &= w^0(x,y) \end{aligned} \tag{2.7}$$

where the index "0" refers to the mid-plane. Using the strain-displacement relationship, the strain expressions are

$$\begin{aligned} \epsilon_x &= \epsilon_x^0 + zk_x^0 \\ \epsilon_y &= \epsilon_y^0 + zk_y^0 \\ \gamma_{xy} &= \gamma_{xy}^0 + zk_{xy}^0 \end{aligned} \tag{2.8}$$

where

$$\epsilon_x^0 = \frac{\partial u^0}{\partial x}\epsilon_y^0 = \frac{\partial v^0}{\partial y}\gamma_{xy}^0 = \frac{\partial u^0}{\partial y} + \frac{\partial v^0}{\partial x} \tag{2.9}$$

$$k_x^0 = -\frac{\partial^2 w^0}{\partial x^2}k_y^0 = -\frac{\partial^2 w^0}{\partial y^2}k_{xy}^0 = -2\frac{\partial^2 w^0}{\partial x \partial y} \tag{2.10}$$

k_x^0 and k_y^0 are the bending curvatures experienced by the mid-surface in the xz and yz planes respectively; k_{xy}^0 is the twisting curvature caused by out-of-plane twisting of the mid-surface.

With the previous assumptions, the stress-strain relation with respect to the local material axes (1,2), can be written as:

$$\begin{bmatrix} \sigma_{11} \\ \sigma_{22} \\ \tau_{12} \end{bmatrix} = \begin{bmatrix} C_{11} & C_{12} & 0 \\ C_{12} & C_{22} & 0 \\ 0 & 0 & C_{66} \end{bmatrix} \cdot \begin{bmatrix} \epsilon_{11} \\ \epsilon_{22} \\ \gamma_{12} \end{bmatrix} \tag{2.11}$$

where only 4 independent constants $(E_{11}, E_{22}, G_{12}, \nu_{12})$ are present, since

$$\begin{aligned} C_{11} &= \frac{E_{11}}{(1-\nu_{12}\nu_{21})} \\ C_{12} &= \nu_{12}C_{21} = \frac{\nu_{12}E_{22}}{1-\nu_{12}\nu 21} \\ C_{22} &= \frac{E_{22}}{(1-\nu_{12}\nu_{21})} \\ C_{66} &= G_{12} \end{aligned} \tag{2.12}$$

By applying the transformation matrix T (given in Eq. 2.13) to Eq. (2.11) it is possible to obtain the stress-strain relations for global laminate axes at an arbitrary angle θ with respect to the material axes (x,y) (ref. Eq.(2.14))

$$T = \begin{bmatrix} \cos^2\theta & \sin^2\theta & -2\sin\theta\cos\theta \\ \sin^2\theta & \cos^2\theta & 2\sin\theta\cos\theta \\ \sin\theta\cos\theta & -\sin\theta\cos\theta & \cos^2\theta - \sin^2\theta \end{bmatrix} \tag{2.13}$$

$$\begin{bmatrix} \sigma_x \\ \sigma_y \\ \tau_{xy} \end{bmatrix} = \begin{bmatrix} Q_{11} & Q_{12} & Q_{12} \\ Q_{12} & Q_{22} & Q_{26} \\ Q_{16} & Q_{26} & Q_{66} \end{bmatrix} \cdot \begin{bmatrix} \epsilon_x \\ \epsilon_y \\ \gamma_{xy} \end{bmatrix} \tag{2.14}$$

By substituting Eq.2.8 into Eq.2.14, the expression at any distance z from the mid-plane is obtained

$$\begin{bmatrix} \sigma_x \\ \sigma_y \\ \tau_{xy} \end{bmatrix}^{(k)} = \begin{bmatrix} Q_{11} & Q_{12} & Q_{12} \\ Q_{12} & Q_{22} & Q_{26} \\ Q_{16} & Q_{26} & Q_{66} \end{bmatrix}^{(k)} \cdot \begin{bmatrix} \epsilon_x^0 + zk_x^0 \\ \epsilon_y^0 + zk_y^0 \\ \gamma_{xy}^0 + zk_{xy}^0 \end{bmatrix} \tag{2.15}$$

Equation (2.15) allows the stress level at each ply to be calculated for any given fibre orientation, and therefore it is particularly useful for design purposes. By integrating Eq.(2.15) with respect to z, the stress resultants are also obtained. If the thickness and the mechanical properties of each lamina can be considered constant throughout the lamina thickness, which is acceptable for most engineering analysis, the integration over z is reduced to a summation over the number of plies (i.e.N_l) and becomes

$$N_i = \int_{-t/2}^{t/2} \sigma_i dz = \sum_{k=1}^{N_l} \sum_{j=1}^{N} Q_{ij}^{(k)} \epsilon_j^{(k)} (h_k - h_{k-1}) \tag{2.16}$$

$$M_i = \int_{-t/2}^{t/2} \sigma_i \cdot z dz = \frac{1}{2} \sum_{k=1}^{N_l} \sum_{j=1}^{N} Q_{ij}^{(k)} \epsilon_j^{(k)} \left(h_k^2 - h_{k-1}^2\right) \tag{2.17}$$

where t is the thickness of the laminate and $\sigma_i = \sum_{j=1}^{N} Q_{ij}^{(k)} \epsilon_j^{(k)}$ is the *i-th* stress component in the *k-th* lamina. For convenience, the expression of the stress resultants, both forces and moments per unit length, are re-arranged into the following form

$$\begin{bmatrix} N \\ -- \\ M \end{bmatrix} = \begin{bmatrix} A & | & B \\ -- & & -- \\ B & | & D \end{bmatrix} \cdot \begin{bmatrix} \epsilon^0 \\ -- \\ k^0 \end{bmatrix} \tag{2.18}$$

where

$$\begin{aligned} A_{ij} &= \sum_{k=1}^{N_l} Q_{ij}^{(k)} (h_k - h_{k-1}) \\ B_{ij} &= \tfrac{1}{2} \sum_{k=1}^{N_l} Q_{ij}^{(k)} (h_k^2 - h_{k-1}^2) \\ D_{ij} &= \tfrac{1}{3} \sum_{k=1}^{N_l} Q_{ij}^{(k)} (h_k^3 - h_{k-1}^3) \end{aligned} \tag{2.19}$$

For general laminates with arbitrary orientations for each ply, it is not possible to simplify for the stiffness matrices. However if conditions of symmetry with respect to the mid-plane or orientations are built into the laminate, it is possible to identify special classes of laminates which have useful properties for design purposes. The most common laminates used in manufacturing are those that are symmetric with respect to the mid-plane. In this case the B matrix terms are zero and, as shown by Eq. 2.20, the extension and the bending problems are de-coupled and therefore can be dealt with separately.

$$\begin{bmatrix} N \\ -- \\ M \end{bmatrix} = \begin{bmatrix} A & | & 0 \\ -- & & -- \\ 0 & | & D \end{bmatrix} \cdot \begin{bmatrix} \epsilon^0 \\ -- \\ k^0 \end{bmatrix} = \begin{bmatrix} A \cdot \epsilon^0 \\ -- \\ D \cdot k^0 \end{bmatrix} \tag{2.20}$$

Looking at the expanded form of the stiffness matrix for a general symmetric laminate (ref. Eq.2.21), it can be noticed that a bending-twist coupling can be still present (terms D_{16} and D_{26}). By limiting the angles orientations of the plies to 0° and 90° (i.e. cross-ply), this can be eliminated.

$$\begin{bmatrix} N_x \\ N_y \\ N_{xy} \\ M_x \\ M_y \\ M_{xy} \end{bmatrix} = \begin{bmatrix} A_{11} & A_{12} & 0 & 0 & 0 & 0 \\ A_{11} & A_{22} & 0 & 0 & 0 & 0 \\ 0 & 0 & A_{66} & 0 & 0 & 0 \\ 0 & 0 & 0 & D_{11} & D_{12} & D_{16} \\ 0 & 0 & 0 & D_{12} & D_{22} & D_{26} \\ 0 & 0 & 0 & D_{16} & D_{26} & D_{66} \end{bmatrix} \cdot \begin{bmatrix} \epsilon_x \\ \epsilon_y \\ \epsilon_{xy} \\ k_x \\ k_y \\ k_{xy} \end{bmatrix} \tag{2.21}$$

A class of laminates, generally avoided in manufacturing, but of particular interest for this study, is that of unsymmetric cross-ply laminates. In this case the terms B_{11} and

B_{22} are present and therefore an in-plane force will cause an out of plane displacement (extension-bending coupling). Unsymmetric laminates will be analysed in depth in the following paragraphs.

2.1.3 Environmental effects

Most of the special properties of the structures presented in this study, are obtained thanks to the high curing temperature to which aerospace grade composites are subjected during their manufacturing process. For this reason, it is of paramount importance to be able to quantify the environmental effects such as those of temperature, and Eq. (2.14) can be modified by including the free thermal strain as

$$\begin{bmatrix} \sigma_x \\ \sigma_y \\ \tau_{xy} \end{bmatrix} = \begin{bmatrix} Q_{11} & Q_{12} & Q_{12} \\ Q_{12} & Q_{22} & Q_{26} \\ Q_{16} & Q_{26} & Q_{66} \end{bmatrix} \cdot \begin{bmatrix} \epsilon_x - \alpha_x \Delta T \\ \epsilon_y - \alpha_y \Delta T \\ \gamma_{xy} - \alpha_{xy} \Delta T \end{bmatrix} \tag{2.22}$$

where the coefficients of thermal expansion, for the global laminate axis, can be computed starting from those for the local material axes as

$$\begin{aligned} \alpha_x &= \alpha_1 \cos^2\theta + \alpha_2 \sin^2\theta \\ \alpha_y &= \alpha_1 \sin^2\theta + \alpha_2 \cos^2\theta \\ \alpha_{xy} &= 2(\alpha_1 - \alpha_2)\cos\theta \sin\theta \end{aligned} \tag{2.23}$$

The classical lamination theory can then be modified to include the free thermal stress resultants to give

$$\begin{bmatrix} N \\ -- \\ M \end{bmatrix} = \begin{bmatrix} A & | & B \\ -- & & -- \\ B & | & D \end{bmatrix} \cdot \begin{bmatrix} \epsilon^0 \\ -- \\ k^0 \end{bmatrix} - \begin{bmatrix} N^{th} \\ -- \\ M^{th} \end{bmatrix} \tag{2.24}$$

where

$$\begin{aligned} N_i^{th} &= \sum_{k=1}^{N_l} \sum_{j=1}^{N} Q_{ij}^{(k)} \alpha_j^{(k)} (h_k - h_{k-1}) \Delta T \\ M_i^{th} &= \tfrac{1}{2} \sum_{k=1}^{N_l} \sum_{j=1}^{N} Q_{ij}^{(k)} \alpha_j^{(k)} (h_k^2 - h_{k-1}^2) \Delta T \end{aligned} \tag{2.25}$$

are known are thermal stresses and resultants.

Moisture content has similar effects to those of thermal stresses and it can be modelled is a very similar way. For the study presented however, only dry laminates have been considered since taking into account of both moisture and thermal effects would require an extremely large number of experimental tests, which is beyond the scope of the work.

2.2 Unsymmetric laminates

Unsymmetric laminates are not new to the composite research field but are mainly used for non structural applications such as material properties testing. The main characteristic is the non-symmetrical stacking sequence that often generates warpage during cool-down from high curing temperature. A part manufactured in this way, will therefore have a poor geometric tolerance and will inevitably be discarded. It is for this reason that unsymmetric laminates are avoided in the design guidelines for composite structures. However, there are circumstances for which the room-temperature shape is not randomly distorted but has a more regular pattern in the deformation. This is the case of unsymmetric cross-ply laminates whose post-cure shape is cylindrical [Hyer, 1981a]. This suggested that what has historically been regarded as an unwanted feature, could actually be an advantage for special design requirements. In addition, being able to reduce the manufacturing costs is a considerable advantage as mentioned in the previous chapter. Cost-reduction and special design features therefore provide a valid justification to further investigate their behaviour.

2.2.1 Previous work on unsymmetric laminates

Since 1980 several papers have investigated the room-temperature shapes of plates with unsymmetric stacking sequences. Hyer [1981b, 1985] observed the room temperature shape of several unsymmetric plates and developed a Rayleigh-Ritz technique to model the energetic content of the structure and to predict the room-temperature equilibrium shape for square cross-ply laminates. Hyer and Bhavani [1984] showed that the Classic Lamination Theory fails to predict the displacements of unsymmetric laminates because the magnitude of the displacements does not fall within the linear assumptions. By adding von Karman non-linear terms in the strain formulation and using a Rayleigh-Ritz technique with polynomial approximation of the displacement field, he developed a model able to describe the post curing shape of the laminates. Dang and Tang [1986] presented a modified formulation to include laminates with arbitrary lay-up and angles, however they obtained a system of equations which proved difficult to solve and were unable to determine physical solutions. The original model from Hyer assumed the shear strains to be zero, an assumption which was proved partially acceptable by Jun and Hong [1990], who increased the number of terms in the polynomial functions. They showed that shear strain is significant in the range of medium width-to-thickness ratio and therefore additional degrees of freedom should be considered in the spatial variation of strains and displacements. Later Jun and Hong [1992] developed a formulation of the model

which included all the spatial variations of strain. Schlecht et al. [1995] confirmed the results obtained by Hyer using Finite Element Analysis and later Schlecht and Schulte [1999] applied the same analysis to different laminate sizes, shapes and arbitrary lay-up angles. The work done by Schlecht and Schulte also showed that with Finite Element Analysis it is possible to obtain a deeper insight of the phenomenon by computing the curvatures and stresses in all the areas of the domain. They also simulated the elastic response of the panel when subjected to an external force. As experimentally observed, the cylindrical configuration that unsymmetric laminates exhibits at room temperature, can be snapped to another cylindrical configuration by a simple snap-through action. The two configurations have their generators parallel to the x and y-axes respectively while the curvatures are equal and opposite. This behaviour, which is referred to as "bi-stable", is of great importance for the study herein presented, as will be explained later.

In the 1990's numerous papers focusing on the analysis and modelling of the snap-through phenomenon have been published. Dano and Hyer [1996] modelled the snap-through from one cylindrical configuration to another one using a Rayleigh-Ritz approach to model the strain energy of the system and the work performed by external forces to induce the snap. For their study, the snap-through was initiated by shape memory wires attached to the panels in such a way that the shrinkage of the wires exerted the necessary snap-through forces. Dano and Hyer [1998] improved their original model by adding more terms in the strain expressions and also by deriving the expression of the in-plane displacements through the integration of the in-plane strains. The addition of several terms, in the strain expressions, made it possible to predict the configurations of general unsymmetric laminates with arbitrary ply orientations. Later Dano and Hyer [2003] proved that the number of terms actually required could be reduced and the same model was then extended to include the snap-through analysis using shape memory wires. Recently, numerous analytical and numerical studies [Schultz and Hyer, 2003, Portela et al., 2008, Hufenbach et al., 2006], investigated piezoelectric patches as actuation systems.

More recently, the possibility of using unsymmetric laminates for the realisation of adaptive structures has been investigated. Hufenbach and Gude [2002] developed a genetic algorithm to scan the multidimensional search space of different laminate lay-ups to realise a desired curvature and confirmed that optimisation procedures enable the efficient design of composites for the adjustment of the curvature to technical demands. Finally, Schultz [2008] and Diaconu et al. [2008] proposed several applications of unsymmetric laminates for aerodynamic applications.

Using unsymmetric laminates is one of possible way to obtain bi-stable structures.

In fact they can also be realised by taking advantage of particular geometrical properties of the structures or by prestressing the material [Kebadze et al., 2004]. Schioler and Pellegrino [2004] proposed beam-like or surface-like structures that included a large number of bi-stable elements. The bi-stable elements were realised through low-cost snap-through struts, whose two different lengths provided the required bi-stable feature. The assembly thus obtained, was made by 30 bi-stable members which made it possible to obtain over 1 billion different configurations. Potter and Weaver [2004] adopted a slightly different approach to generate bi-stable plates. The idea consisted in using local patches of unsymmetric laminates within a symmetrically laminated panel. This was obtained by interleaving the basic laminate with thin unidirectional strips transversely oriented with respect to the adjacent plies. The transverse strips induce a residual stress field in a localised area by constraining the shrinkage of the neighbouring ply during the cool-down. This in turn, causes the strips to buckle, giving rise to distortions of the whole laminate. This technique can, in principle, be used to obtain multiple stable configurations for the panel.

2.3 Thermally induced bi-stable composites

Manipulating the thermal strain field represents a convenient way of generating out-of-plane deformations, in addition the energy required for doing so is already required to the cure of the composite part. Furthermore, the amount of data available in the literature makes a good starting point for the development of a more "application oriented" study, such as the one herein presented. This section will provide a more physical insight into the generation of the out-of-plane deformations generated within unsymmetric laminates.

Gigliotti et al. [2003] provided a useful insight to understand the mechanisms that contribute to causing stresses in unsymmetric laminates. The main causes given are:

- mismatch of thermal properties of the laminate plies
- chemical shrinkage of the matrix resin system
- tool-part interaction
- non-uniformity of the cure degree, temperature or fibre volume through the laminate thickness

A detailed consideration of each element would require a large number of experiments and modelling which is outside the scope of this study. In addition, for the laminates

considered here, which are thin, orthotropic and epoxy based, it can be assumed that the main cause for residual stresses is due to the mismatch of the thermal properties and therefore the remaining items will not be included in the analytical and numerical modelling presented later. To understand the mechanical process better, it is worth considering a simple composite square plate made of two plies, one at 0° and the other one at 90° (refer to Fig.2.1). The autoclave-cure procedure is as follows:

- Application of full vacuum (1 bar) and 7 bar autoclave pressure.
- Heating at $1-3\,^{\circ}C$/min to $110\,^{\circ}C$ then pause for 60 minutes.
- Heating at $1-3\,^{\circ}C$/min to $180\,^{\circ}C$ and hold for 120 minutes.
- Cool at $2-5\,^{\circ}C$ per minute
- Vent autoclave pressure when the component reaches $60\,^{0}C$ or below.

A scheme is shown in Fig. 2.2.

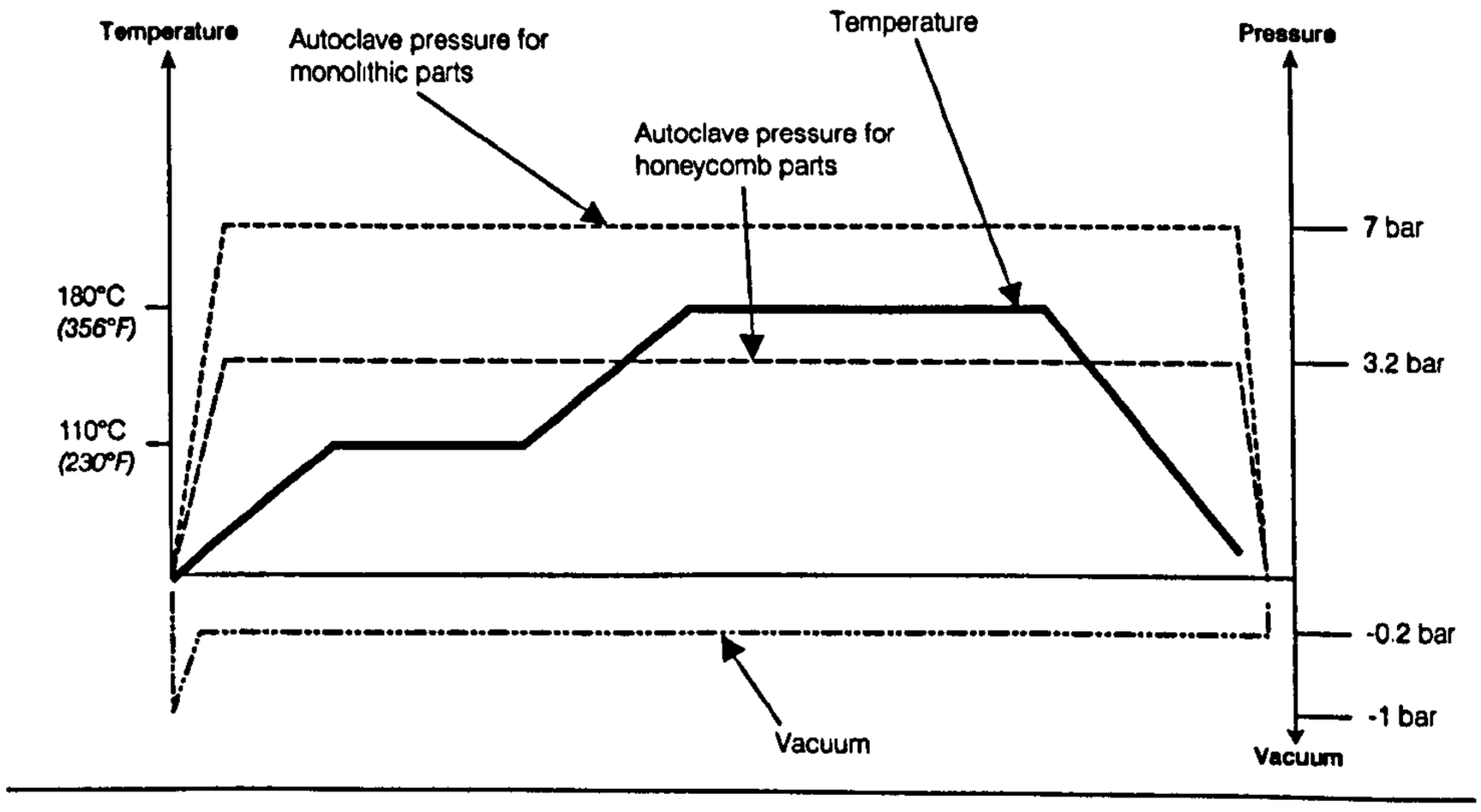

Figure 2.2: Cure cycle for monolithic and honeycomb components

At the maximum curing temperature, the resin matrix which holds the fibres together, is in its liquid state and there is no stress at the interface between the plies. Once the curing process is completed and the specimen is cooled down, the matrix starts shrinking and the interaction between adjacent plies starts. As a first approximation we can consider that the thermal properties of the laminated plate are essentially determined by the fibres and the matrix: along the 0°-direction the thermal expansion is dominated by the low coefficient of thermal expansion (CTE) of the fibres, whereas

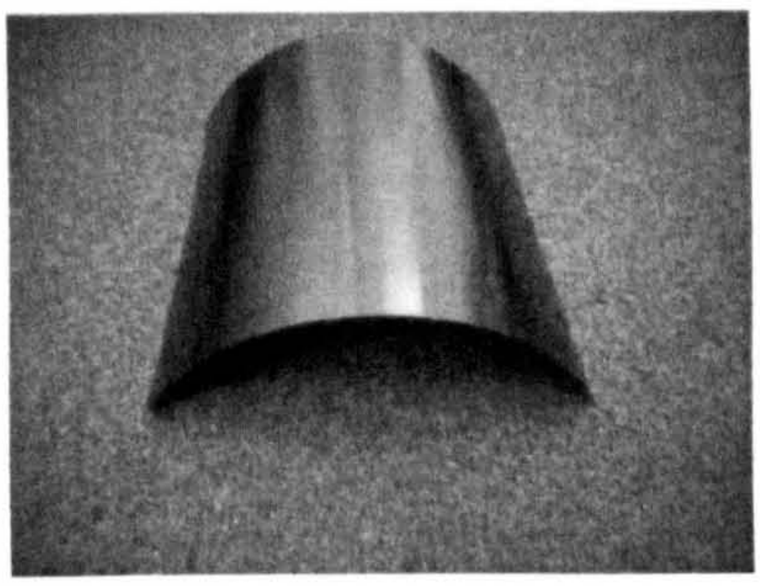

(a) 1^{st} Configuration

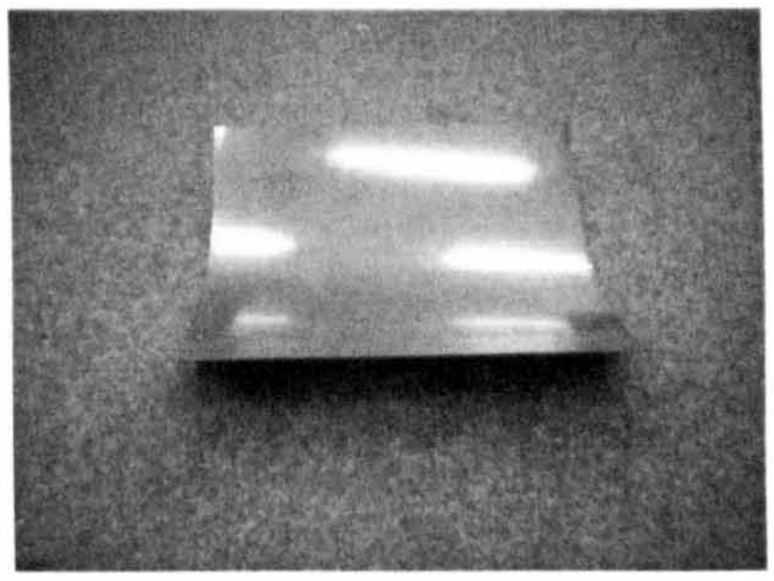

(b) 2^{nd} Configuration

Figure 2.3: Room-temperature shapes for the 2 layered $[0^0/90^0]_T$ square panel

along the 90°-direction the CTE is close to that of the matrix, which is usually two orders of magnitude greater than that of the carbon fibres. Typical properties for a pre-preg carbon-epoxy laminate are shown in table 2.1. The overall effect is that each lamina will try to shrink in the direction perpendicular to the material fibres (90°) and will remain almost unchanged in the direction parallel to the fibres (0°). If the laminae were on its own, transverse shrinkage of the panel would take place. In fact, the lamina underneath, rotated by 90°, will constrain the deformation and a considerable stress is built at the interface between the two layers. The unsymmetric stacking sequence will then produce bending moments within the laminate which, for small deflections and linear approximation, would find equilibrium in a saddle shaped plate. As mentioned before, the magnitude of the displacements will create geometrically non-linear effects resulting in two cylindrical configurations each with generators oriented at 0° and 90° respectively (ref. to Fig. 2.3).

From a design point of view, these two states of equilibrium represent the capability for the panel to be flexible and stiff at the same time, which is one of the most important requirements for shape-adaptable systems. The amount of curvature obtainable with a single panel is a non-linear function of the thickness and the aspect ratio. To date no analytical expression which quantifies the phenomenon is available and therefore a trial and error process is employed to investigate the possible configurations. Several papers which try to correlate the geometric dimensions with the curvature and the bi-stability of the panel have been published. Hufenbach et al. [2002] performed an in-depth parametric analysis on the stability of glass and carbon fibre unsymmetric cross-ply and angle-ply laminates. In the study, thermal stresses as well as moisture and chemical shrinkage are considered in the formulation of the internal strain energy and then an optimisation technique is used to determine the stable stationary points of the strain energy of the

laminate, which correspond to the equilibrium configuration. Applying this analysis to panels with different aspect ratios and layer thickness ratios allowed the two diagrams shown in Fig. 2.4 and in Fig. 2.5 to be obtained. Figure 2.4 correlates the edge length with the curvature and shows that for a given laminate and material, the bi-stability (i.e. cylindrical configurations) of the panel is possible if the edge length is above a certain value (point B in the diagram), below this, only a saddle shape configuration exists. This highlights the importance of the thickness-edge length ratio for the bi-stability of the panel. Figure 2.5 shows a similar result, however this time it is the ratio between thicknesses of the layers with different orientations (here 0° and 90°) that determines the bi-stable region. In particular, it is shown that it is possible to obtain two cylindrical configurations only for layer-thickness ratios between 0.27 and 0.73 approximately.

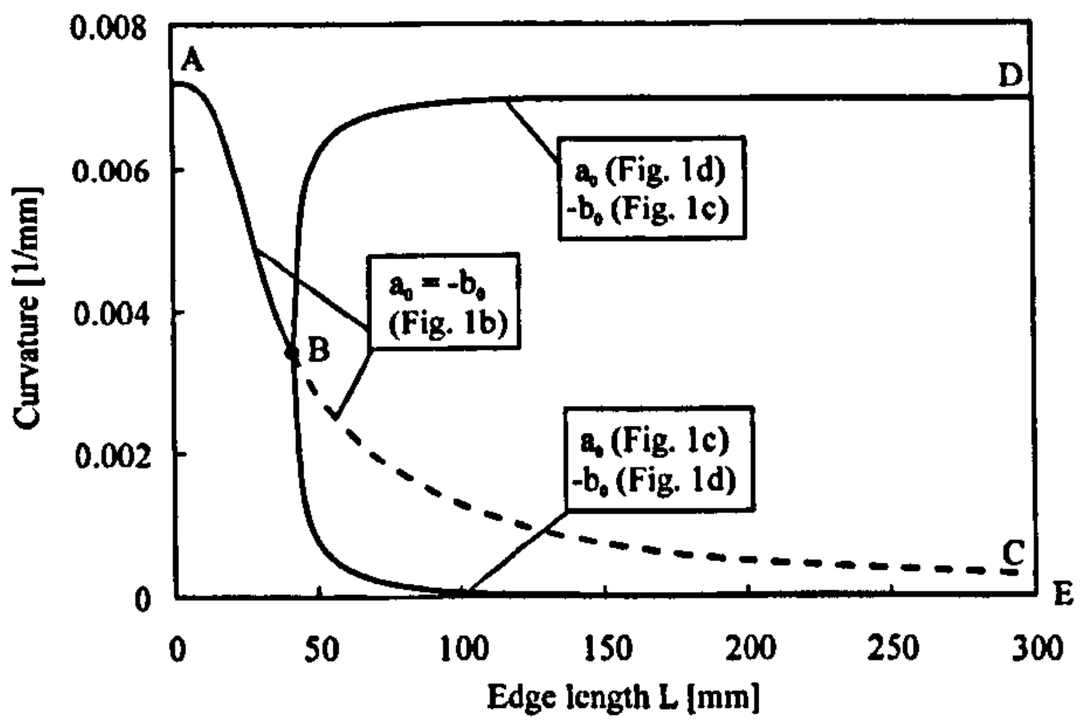

Figure 2.4: $[0_2/90_2]$ CFRP-laminate curvatures vs. laminate edge length L [Hufenbach et al., 2002]

Gigliotti et al. [2004] performed a similar study but expressed the most important parameters with non-dimensional quantities such as the non-dimensional curvature $a^* = \frac{aL^2}{t}$ and the non-dimensional length $L^* = \frac{L^2}{t^2}\alpha \cdot \Delta T$. In addition, they found that, for cross-ply square plates, it is possible to establish the following relationship

$$(L^*_{A'}) \cdot (t_0/t_{90})^3 = \text{const} \tag{2.26}$$

where $L^*_{A'}$ is the minimum length for which a square panel with a given thickness ratio t_0/t_{90} is bi-stable. This relation allows the range of existence of multiple solutions to be found for a given thickness ratio by knowing the corresponding values for a reference case. The importance of the aspect ratio was also investigated by analysing rectangular plates with an aspect ratio of 10. The plates were effectively narrow strips and their room-temperature was predominantly cylindrical with a lateral bow caused by the anticlastic

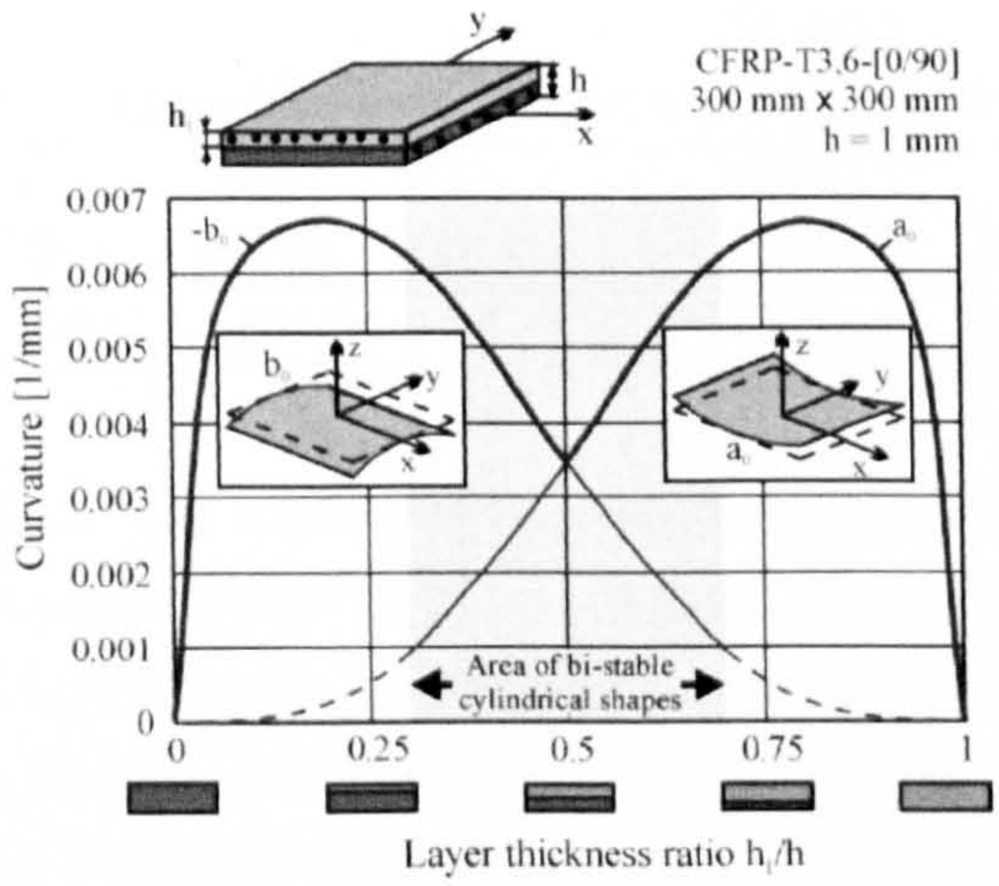

Figure 2.5: Curvatures of a CFRP laminate with variable layer ratio [Hufenbach et al., 2002]

effect. This configuration is in agreement with that predicted by the classic lamination theory and shows that for high aspect ratios there is a loss of bi-stability and the non-linear effects are almost negligible.

2.4 Preliminary remarks on past research

To summarise, it is worth mentioning a few remarks on the previous work done in the area of unsymmetric laminates. The room-temperature shapes of unsymmetric laminates is a well understood phenomenon. All the previous research agrees on some preliminary conclusions for the equilibrium configurations and the dependency on geometric parameters:

- the amount of curvature is inversely proportional to the thickness
- the presence of the anticlastic curvature, which is a measure of the non-linearity, is recovered for high aspect ratios.
- there are critical values for the thickness ratio and side length below which there is a loss of bi-stability

The main areas of investigation are modelling, actuation and applications. The first, which is the most developed, is mainly based on Rayleigh-Ritz or numerical approaches to capture the stable configurations. The actuation study, which also models the elastic response, is focused on the use of piezoelectric patches and shape memory wires. The

Table 2.1: Typical material properties for a pre-preg carbon fibre lamina

Material	E_{11} [GPa]	E_{22} [GPa]	G_{12} [GPa]	v	α_1 [1/°C]	α_2 [1/°C]	t [mm]
T300/914	130	10	4.4	0.3	-1.8e-8	30e-6	0.125

latter part, the applications, can doubtless be considered "work in progress": only a few concepts for applications are presented and few of them are beyond the conceptual stage.

On the modelling side, it is worth mentioning that most of the mathematical models, if not all, are applied to simple square and rectangular panels. Each case assumes free-free boundary conditions meaning that the panel is left free to deform and only the rigid body motions are constrained. In the author's opinion, to take real advantage of the characteristics of bi/multi-stable unsymmetric laminates, it is necessary to adopt an approach similar to that of Potter and Weaver [2004], in which the unsymmetric laminate is part of a pre-existing structure thus making it possible to combine the benefits of composite structures with the shape-adaptability of unsymmetric laminates. For this to be accomplished, it is important to understand the relationship between unsymmetric laminates and the potential neighbouring structure. This could, for example, lead to the loss of bi-stability or conversely the non-linear behaviour could be detrimental to the performance of the original structure. In addition to this, it is necessary to have a deeper understanding of the snap-through phenomenon (if and how it is possible to control it) and of geometric quantities such as thickness, edge length and shape, which influence greatly the geometry and the stability (i.e. robustness) of the configurations. As far as the actuation is concerned, it must be mentioned that the solutions proposed highlight how it is possible to obtain elegant solutions for self-contained devices (i.e. laminated piezoelectric patches), however, no mention is made of the practical feasibility of some systems. If on one hand piezoelectric patches seem to be the best solution for their ease of application, the energy required for the snap-through could be prohibitive if the thickness of the plate increases [Portela et al., 2008]. On the other hand, an actuation method based on concentrated forces, seems to be an efficient way of initiating the snap-through but it is more difficult to realise. These aspects must be considered at an early design stage to prevent trivial constraints from hindering the practical application of unsymmetric laminates.

2.5 The potential of unsymmetric laminates and bi-stable structures

This section will present a few preliminary examples of what is possible to realise through unsymmetric laminates. The examples are mostly simulated with FEA (Finite Elements Analysis) and will point out some of the difficulties inherent in the numerical modelling when multiple equilibrium paths are possible.

Variable curvature shell This example is focused on showing the benefits of realising complex geometries by making use of simple flat tools. The traditional manufacturing of autoclave cured composite parts, requires the fabric layers to be laid up on a $3D$ female or male mould, previously machined or assembled from smaller components. The tool must satisfy a number of requirements such as compatibility with the thermal properties of the composite, resistance to the high pressure and temperature during the curing cycle and eventually guarantee a life span compatible with the production volumes for which it has been designed [Niu, 2000]. In addition to this, composite manufacturing requires a large quantity of ancillary material (vacuum-bag, breather sheet, debonding layer, sealant etc.) which is wasted at the end of each production cycle. For the most simple shapes, such as flat panels, it is possible to make use of re-usable vacuum-bags which greatly reduces production time and wastage. For complex geometries, conversely, this is not possible and the costs are considerably higher. To show what is possible by simply tailoring cross-ply unsymmetric laminates, a few examples will be shown in the following paragraphs. The first example is a panel with dimensions 180×360 mm which has been manufactured using unidirectional pre-pregs carbon fibre laminae. The material properties are shown in table 2.1 while the curing cycle is that typical of carbon-epoxy composites (ref. Fig. 2.2), with a maximum curing temperature of approximately $180\,^{\circ}C$. The laminate is made of 8 layers with orientations at 0^0 and 90^0 and it is divided in two areas with different ratios between the layers at 0^0 and 90^0. The stacking sequence is shown in Fig. 2.6. The difference in the layer orientation ratio will, as shown by the various analytical models mentioned in Section 2.2, produce a variation in the transverse curvature and the neat result will be a shell with two different radii of curvature, one for each stacking sequence. This can be predicted quite easily with FEA simulation and Fig. 2.7 shows the shape obtained for the experimental specimen next to that predicted numerically. The concept can be extended to any number of lamination areas (and potentially orientation), an example with four different curvatures is shown in Fig. 2.8

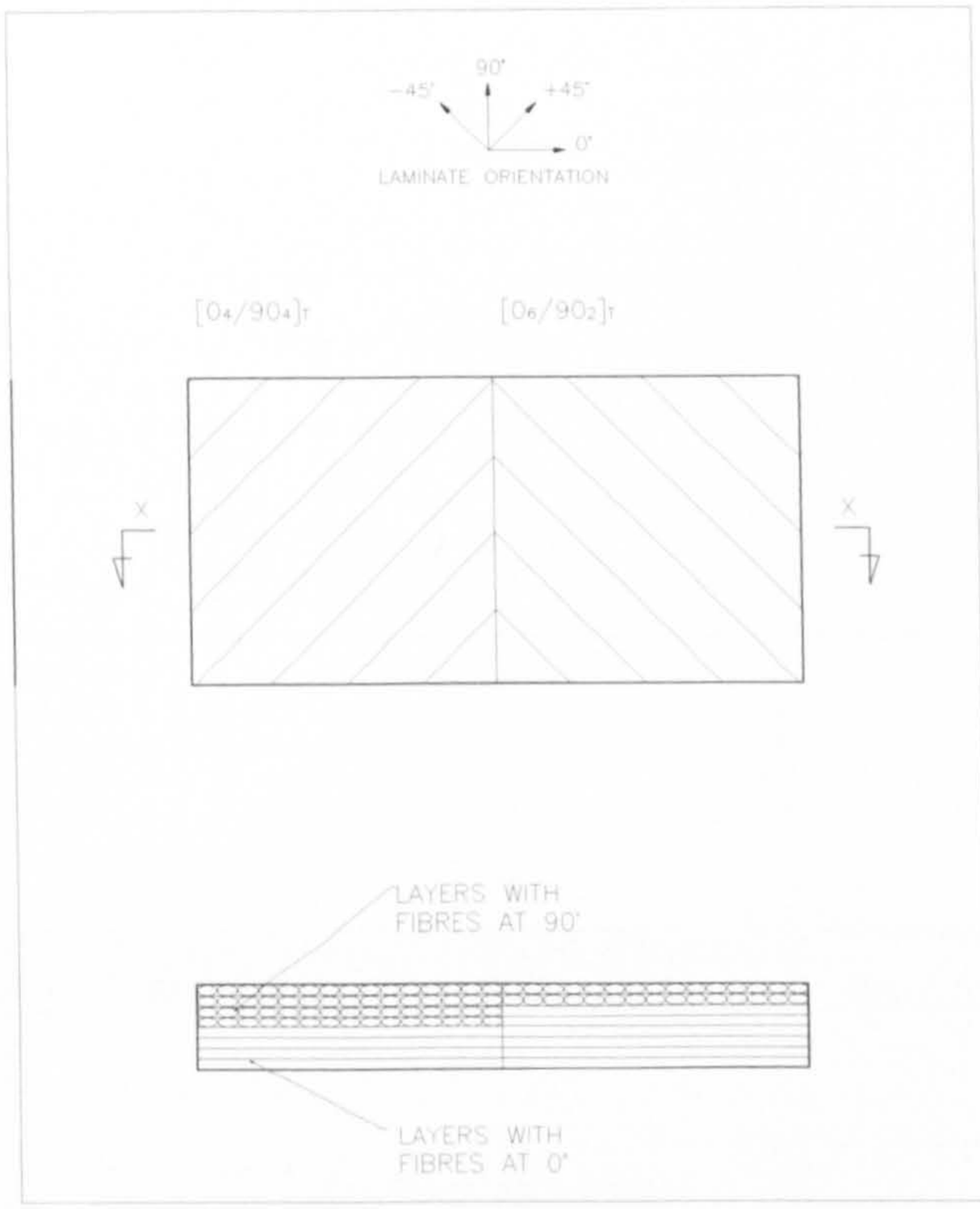

Figure 2.6: Stacking sequence for the variable curvature shell

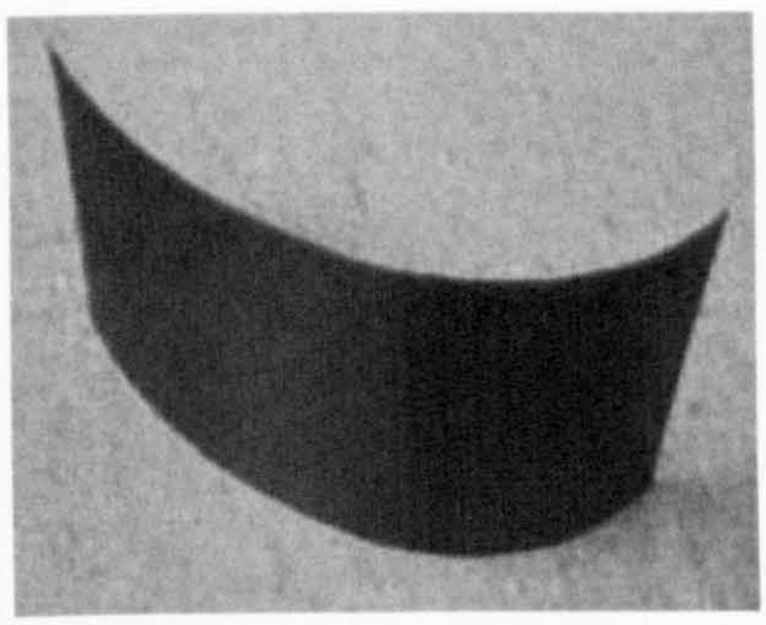

(a) Experimental specimen

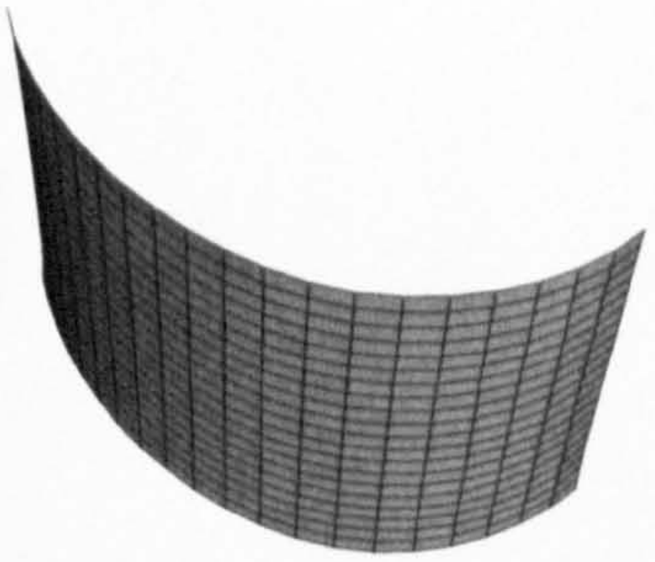

(b) Numerical model

Figure 2.7: Variable curvature shell obtained from unsymmetric laminates

The previous examples have in common the fact that the residual stress in the longitudinal direction is much greater than that in the transverse direction and therefore only one curvature is visible. If the two residual stress fields have a similar magnitude,

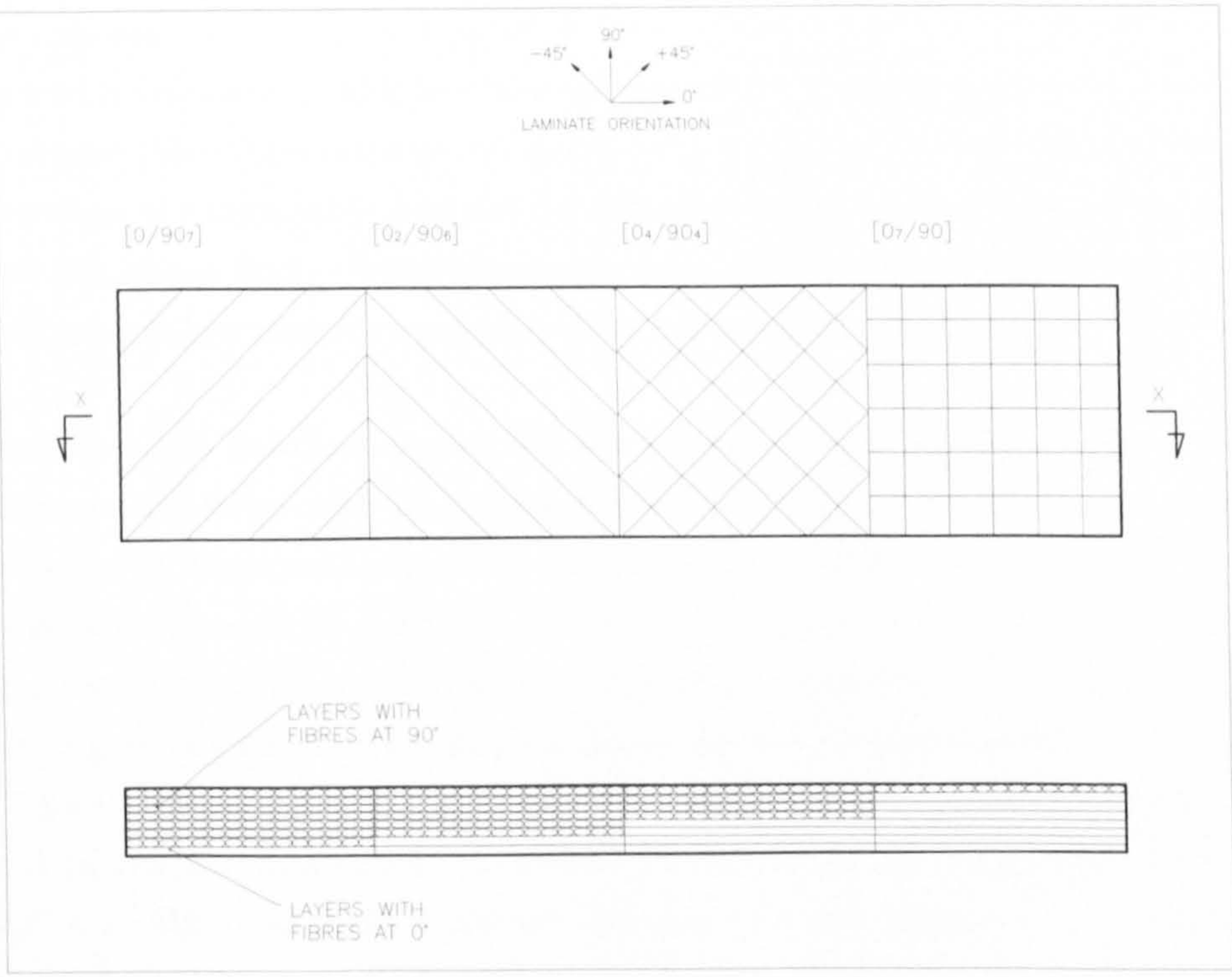

(a) Stacking sequence

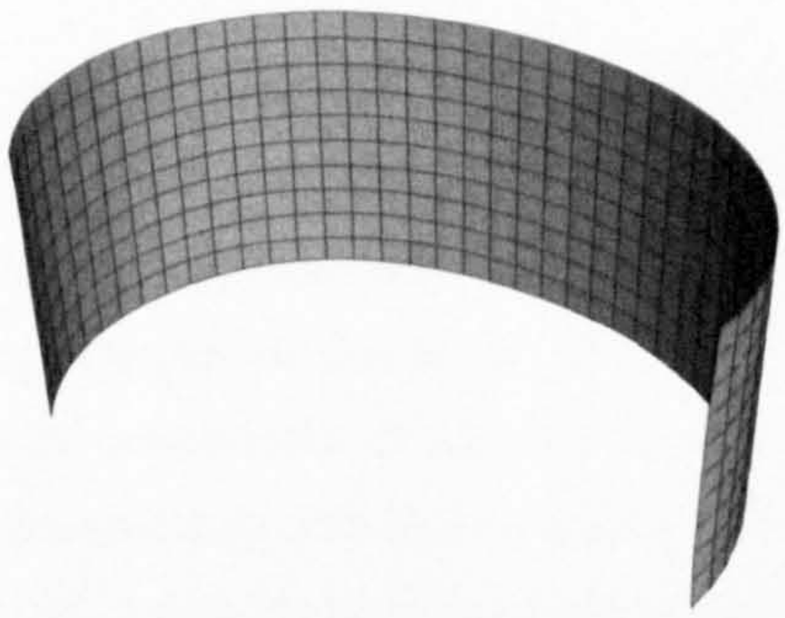

(b) Numerical model

Figure 2.8: FEA of a shell with four different longitudinal curvatures

the scenario changes completely. This is shown in Fig. 2.9, the left hand side of the shell has a predominant number of layers with fibres at 90° and therefore only the curvature along the 0° direction is visible. Moving towards the right end of the shell, the number of layers in the 0° direction increases and so does the transverse curvature. The right end

shows the opposite behaviour compared to that of the left end and only the transverse curvature can be observed. The key part of this shell is represented by the two central laminate zones. Here the number of layers is more balanced and this results in two residual stresses of comparable magnitude. The final result is that the stresses along the 0° and 90° directions find equilibrium either in the first configuration or in the second configuration meaning that it is possible to have bi-stable behaviour (ref. Fig. 2.9).

Square plate with reinforcement strips This example shows the effect of adding local reinforcement strips with transverse orientation with respect to layers underneath. A square panel is laminated according to according to Fig. 2.10. The panel is made of two plies with fibre at 0^0 with two additional strips at the sides with fibres at 90^0. During the cool-down, the transverse shrinkage of the layers at 0^0 will compress the two strips creating an asymmetric loading condition that will cause the two strips at 90^0 to buckle. The low bending stiffness in the 90^0-direction produce a cylindrical shape as a resultant of the thermal action. Likewise for the previous example, a second stable configuration is obtained, this is almost flat and the two lateral strips exhibit a very small curvature in the opposite direction (ref. to Fig. 2.11).

These two examples highlight a very important aspect of the residual stresses: if stress resultant in one direction is similar in magnitude to that in the other direction, then multiple equilibrium shapes are obtained and it is possible to snap from one shape to the other by the simple application of a concentrated load.

IFH The INTEGRAL FOLDING HINGE or TAPE SPRING HINGE has been extensively studied [Soykasap, 2007, Seffen et al., 2000] and found application in deployable components for aerospace applications. It consists of a straight strip section of a cylindrical shell whose most common application probably is the "*tape-measure*". The main characteristics is its moment-rotation behaviour as shown in Fig. 2.12. For small rotations it is linear elastic whereas the moment is almost constant for large rotations. This means that for applied loads below M^*, the structural behaviour will be that of a beam, and for loads greater than M^* it will behave like an elastic hinge making it possible to obtain large deformation with minimal energy input. This unique characteristic is mostly due to the transverse curvature radius and therefore can be realised with any material. It is rather difficult to use metals for structural applications since the increase in thickness, to achieve acceptable bending stiffness, would require an unacceptably high value for M^*. By making use of composite materials, the properties can be tailored to a large extent and therefore using tape springs as main structural components is possible.

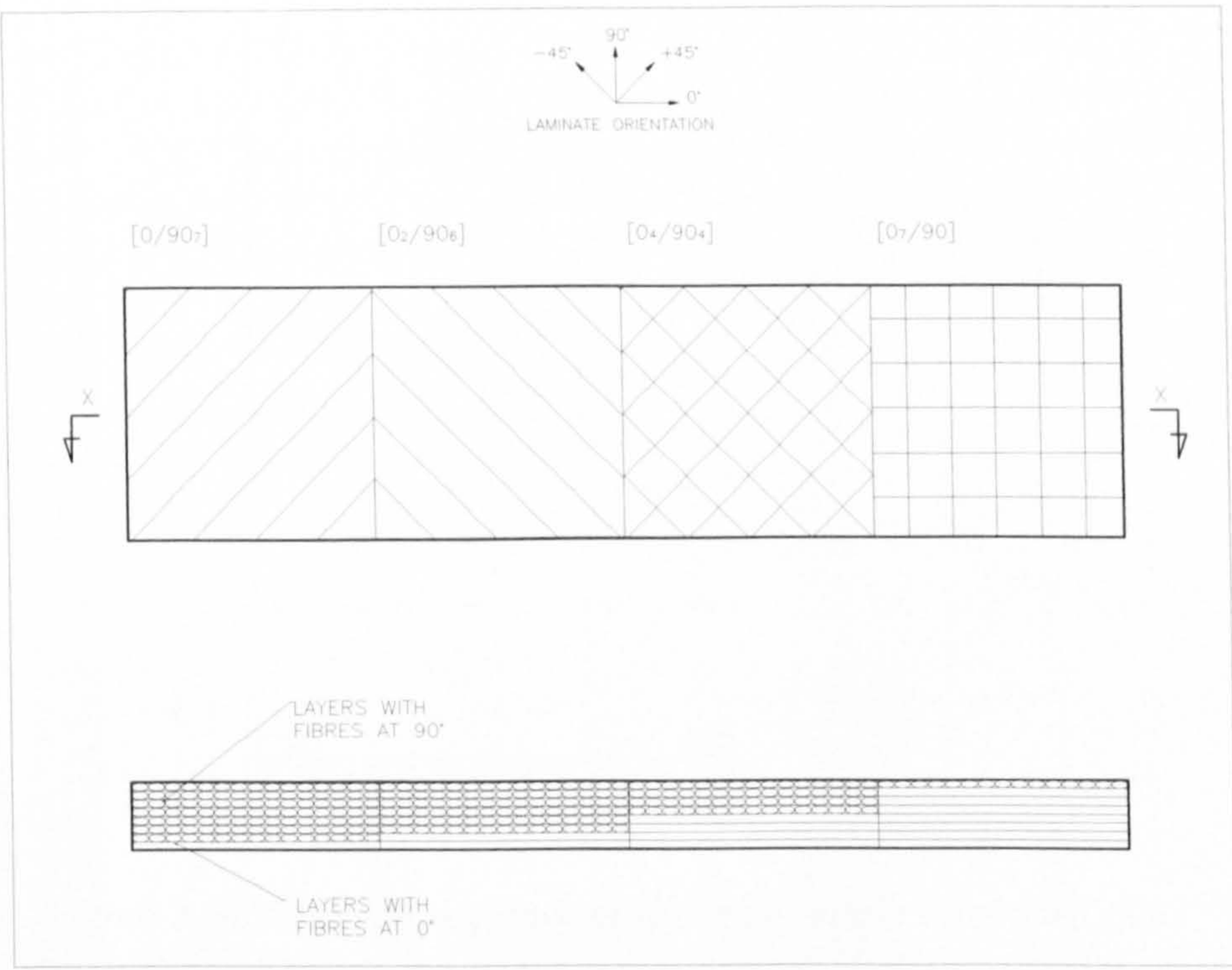

(a) Stacking sequence

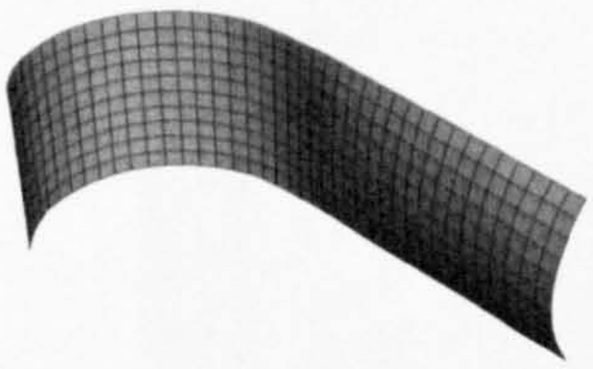

(b) First configuration

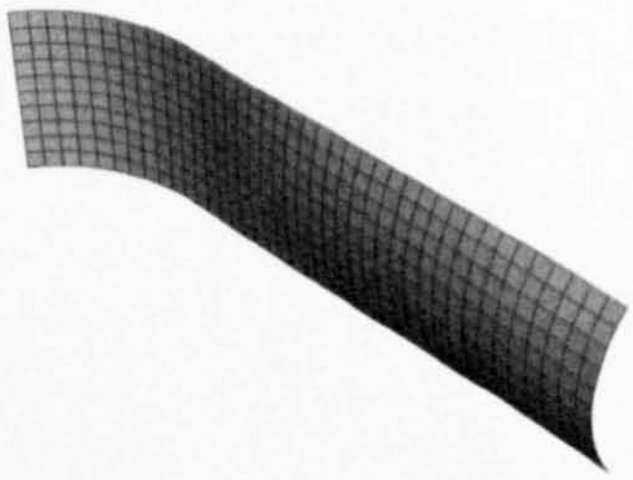

(c) Second configuration

Figure 2.9: Multiaxial curvature shell

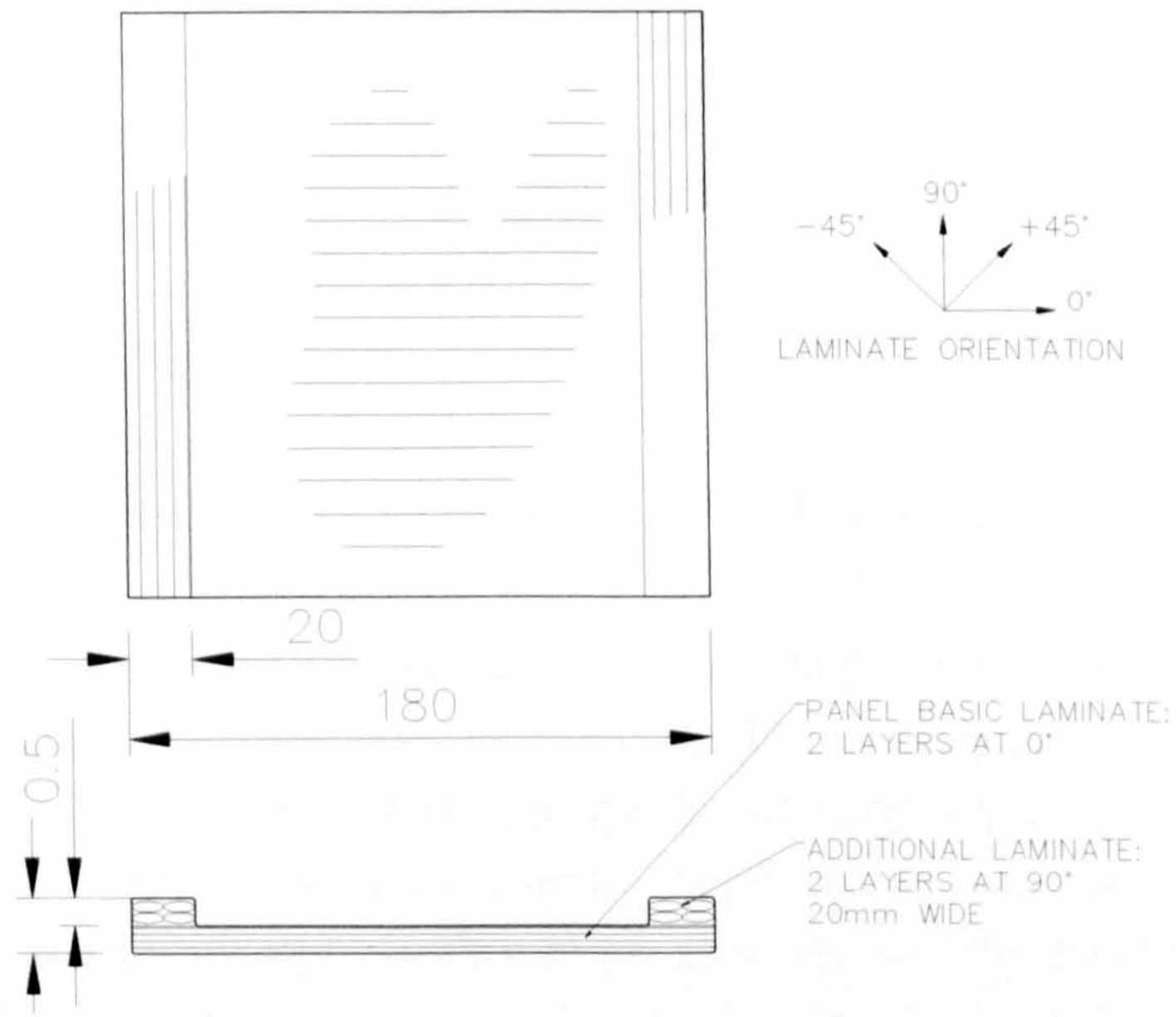

Figure 2.10: Stacking sequence of the transversely reinforced plate

(a) Curved shape

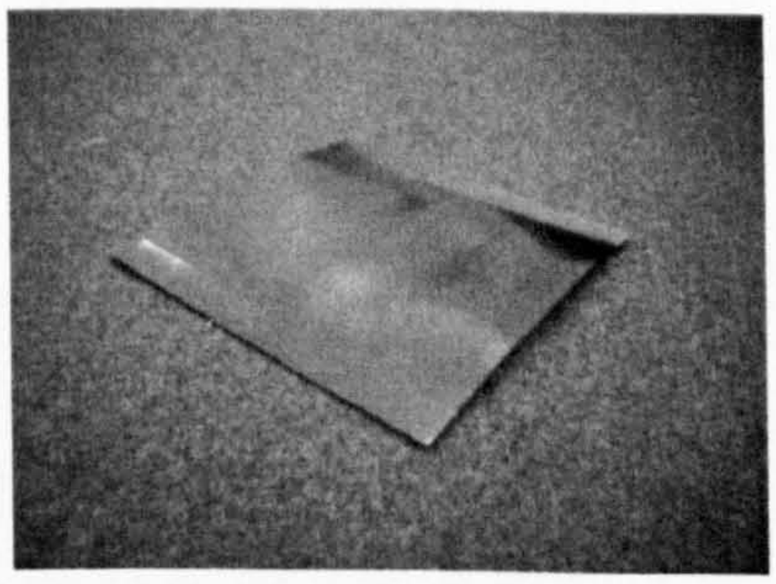

(b) Flat" shape

Figure 2.11: Stable shapes for the laterally reinforced panel

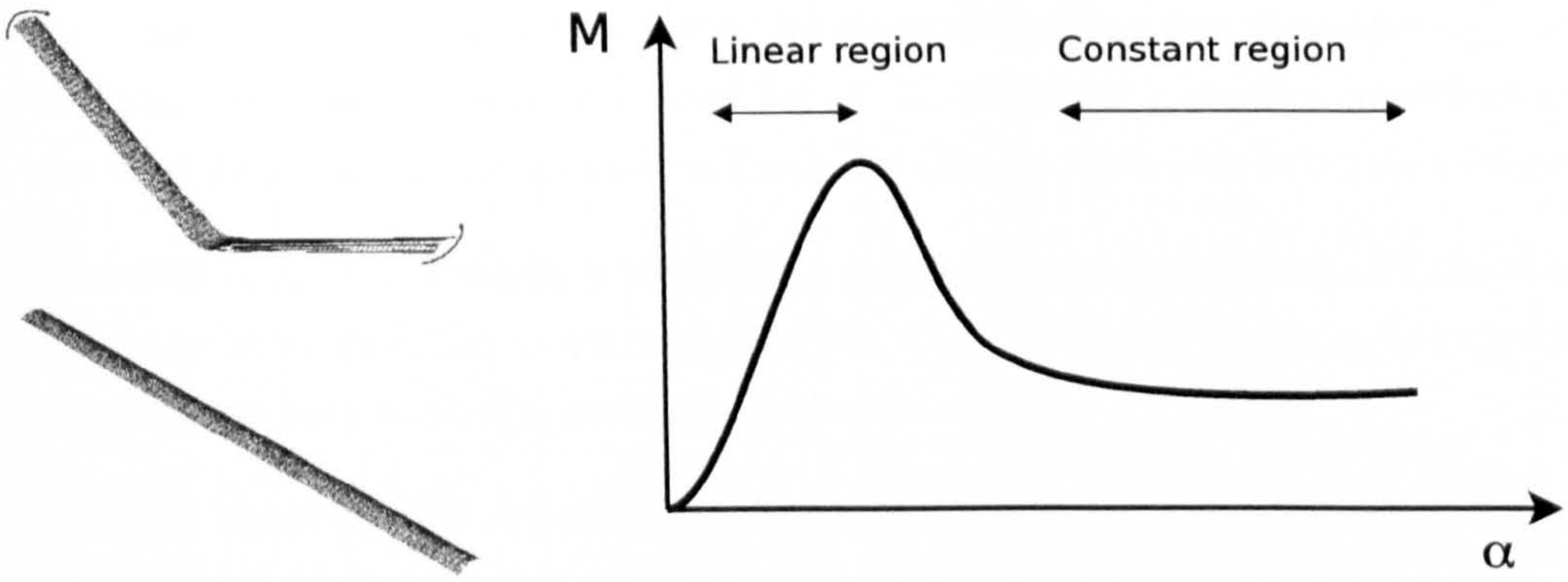

Figure 2.12: Qualitative moment-rotation behaviour of tape springs

Remarks on the examples These examples have highlighted some of the potential of unsymmetric laminates and bi-stable structures. They clearly show that, with simple ply orientations and by making use of appropriate stacking sequences, it is possible to obtain a significant modification of the original shape. In the examples shown, the fibre orientation is limited to cross-ply laminates for good reason. By making use of angle-plies, it is in fact possible to obtain a much greater range of shapes, however the design envelope is so vast that considering all of the possibilities at once would be confusing and therefore only 0° and 90° angles have been considered throughout this study. The attention is focused on understanding the behaviour and the physical limits of this class of laminates and once this step is completed, it will be simple enough to consider additional degrees of freedom. The possibility of having more than one geometric configuration for the same panel, means that it is possible to snap from one configuration to another by means of an actuation system. More importantly, the actuator is only required to provide energy during the snap-through process and not to maintain the shape. It is important to note that these devices do not add mechanical complexity to the host system, because they are intrinsically simple and do not rely on external components to achieve their properties. Furthermore, no special manufacturing method is required and therefore the additional cost for their use should be very limited.

From the analysis of these example, a few important issues arose:

- using the guidelines obtained from the previous works, the prediction of the equilibrium shapes does not present particular difficulties if only one configuration is possible, at room-temperature. If more than one exists, the analysis is not trivial and several ways to obtain a solution are available but not all of them guarantee satisfactory results.

- the analysis of the bifurcation loads, when investigating the snap-through, is difficult and requires considerable user input. In addition, a careful consideration of the boundary conditions applied to the FEM (Finite Elements Model) is necessary.

- The wide variety of boundary conditions, geometric configurations and the difficulties associated with the numerical analysis, show the need for extended analytical solutions to help with the preliminary design stage.

The following chapters will describe attempts to investigate these issues and provide potential solution where possible.

Chapter 3

Modelling

Modelling the mechanical and physical characteristics of unsymmetric laminates is, indeed, the first step required to investigate their potential. This chapter presents an analytical model and a numerical procedure developed for this purpose. It is worth mentioning that the development of the analytical model required, at times, the use of numerical analyses to verify which of the simplifying assumptions were acceptable. This lead to an almost simultaneous development of the analytical model and the numerical procedure, which explains why the numerical analysis is also used to validate the analytical model.

3.1 Analytical modelling

This section will present an analytical formulation to model the displacements and the equilibrium shapes of unsymmetric laminates. The starting point is represented by the model developed originally by Hyer [1985] and later modified by Dano and Hyer [2002]. First, the original model is presented, then the shape functions that model the out-of-plane displacements are modified to include variations of the curvatures within the domain. The new analytical formulation is compared with results from the literature and finite element analysis for a square plate and it is then tested for laminates with piecewise variation of lay-up in the planform. The results are validated against finite element analysis and experimental tests and a good correlation is obtained. Finally, a parametric study is made on the effect of changing the orientation of the fibres and the laminate thickness.

3.1.1 Dano-Hyer's model for the square plate

The model originally proposed expresses the strain energy of an unsymmetric panel subjected to thermal loads. Using a Rayleigh-Ritz technique, the total potential energy (Π) of the composite structure in plane-stress and subjected to a difference in temperature, is expressed as a function of the mid-plane strains (ϵ^0), the curvatures (k^0) and the laminate stiffness

$$\Pi = \int_{-\frac{L_x}{2}}^{\frac{L_x}{2}} \int_{-\frac{L_y}{2}}^{\frac{L_y}{2}} \left(\frac{1}{2} \begin{bmatrix} \underline{\varepsilon}^0 \\ \underline{k}^0 \end{bmatrix}^T \begin{bmatrix} \underline{\underline{A}} & \underline{\underline{B}} \\ \underline{\underline{B}} & \underline{\underline{D}} \end{bmatrix} \begin{bmatrix} \underline{\varepsilon}^0 \\ \underline{k}^0 \end{bmatrix} - \begin{bmatrix} \underline{\varepsilon}^0 \\ \underline{k}^0 \end{bmatrix}^T \begin{bmatrix} \underline{N}^{th} \\ \underline{M}^{th} \end{bmatrix} \right) dxdy \quad (3.1)$$

In order to be able to predict the stable configurations after cool-down, the mid-plane strain component ϵ^0 and k^0 are expressed as polynomial functions with unknown coefficients that have to be determined by minimising the total potential energy. It is noteworthy that the function chosen for the approximation must satisfy at least the essential boundary conditions. As mentioned in the previous chapters, the possible functions chosen to model the out-of-plane displacement and strains are several but to the best of the author's knowledge, those introduced by Dano and Hyer [2002] performed best. The approximation function chosen to model the out-of-plane displacement is

$$w(x,y) = -\frac{1}{2}(w_{20}\,x^2 + w_{02}\,y^2 + w_{11}\,x\,y) \quad (3.2)$$

where w_{20}, w_{02} and w_{11} are unknown coefficients which represent, respectively, the negative of the curvatures in the x and y directions and the negative of the twist curvature, as

$$k_x^0 = -\frac{\partial^2 w^0}{\partial x^2} = w_{20} \quad k_y^0 = -\frac{\partial^2 w^0}{\partial y^2} = w_{02} \quad k_{xy}^0 = -2\frac{\partial^2 w^0}{\partial x \partial y} = w_{11} \quad (3.3)$$

It is very important to note that this choice of displacement function assumes the curvature to be constant throughout the domain. To obtain the shear deformation, γ_{xy}^0, compatibility relations are applied. The total strain vector $\epsilon = \epsilon^0 + zk^0$ includes von Karman non-linear terms for the mid-plane strains. This requirement is a mandatory feature as Hyer and Bhavani [1984] showed that the classical lamination theory fails to capture the room-temperature shape of cross ply laminates. The mid-plane strain vector

formulation then becomes

$$\underline{\varepsilon}^0 = \left\{ \begin{array}{c} \varepsilon_x^0 \\ \varepsilon_x^0 \\ \gamma_{xy}^0 \end{array} \right\} = \left\{ \begin{array}{c} \frac{\partial u^0}{\partial x} + \frac{1}{2}\left(\frac{\partial w^0}{\partial x}\right)^2 \\ \frac{\partial v^0}{\partial y} + \frac{1}{2}\left(\frac{\partial w^0}{\partial y}\right)^2 \\ \frac{\partial u^0}{\partial y} + \frac{\partial v^0}{\partial x} + \frac{\partial w^0}{\partial x}\frac{\partial w^0}{\partial y} \end{array} \right\} \tag{3.4}$$

while the curvature vector is

$$\underline{k}^0 = - \left\{ \begin{array}{c} w_{20} \\ w_{02} \\ w_{11} \end{array} \right\} \tag{3.5}$$

The expression assumed that the strain is given by

$$\begin{aligned} \epsilon_x^0 &= \epsilon_{x00} + \epsilon_{x20}x^2 + \epsilon_{x11}xy + \epsilon_{x02}y^2 \\ \epsilon_y^0 &= \epsilon_{y00} + \epsilon_{y20}x^2 + \epsilon_{y11}xy + \epsilon_{y02}y^2 \end{aligned} \tag{3.6}$$

The in-plane displacement functions are then

$$\begin{aligned} u^0(x,y) &= \int \left[\varepsilon_x^0 - \tfrac{1}{2}\left(\tfrac{\partial w}{\partial x}\right)^2\right] dx + h(y) \\ v^0(x,y) &= \int \left[\varepsilon_y^0 - \tfrac{1}{2}\left(\tfrac{\partial w}{\partial y}\right)^2\right] dy + g(x) \end{aligned} \tag{3.7}$$

The unknown functions $h(y) = u_{01}\,y + u_{03}\,y^3$ and $g(x) = v_{10}\,x + v_{30}\,x^3$ are chosen to obtain the required degrees of freedom for the displacements. Rigid body rotations are eliminated by equating the coefficients of the first order terms of the variables x and y. The shear strain is simply

$$\gamma_{xy}^0 = \frac{\partial u^0}{\partial y} + \frac{\partial v^0}{\partial x} + \frac{\partial w^0}{\partial x}\frac{\partial w^0}{\partial y} \tag{3.8}$$

3.1.2 Extension of the existing models

As shown in the previous section, the procedure to express the total potential energy Π as a function of the displacement coefficients, material properties and temperature change, is well-established and so far it has been successfully applied to panels with uniform stacking sequences. The study presented herein modifies the existing models to consider piecewise variation of the lay-up in the planform, thus accounting for boundary conditions embedded into the structure. The purpose is to provide an engineering tool

that can help at the preliminary design stage of unsymmetrical laminated structures. With such a model it is possible to analyse the equilibrium configurations of structures for more practical applications, such as those described by Diaconu et al. [2008]. It has been observed that, to model boundary conditions that are not simply free edges, the hypothesis of constant curvatures has to be removed since it is too restrictive. This is clearly understood by examining the bending behaviour of a plate in the region close to the edge where a constraining moment is applied. From the kinematics it is known that the bending moment in a plate is proportional to the curvature and therefore whenever a moment is applied to an edge, a variation in the local curvature is expected. For this reason the curvature must be allowed to vary across the domain and therefore a fourth order displacement function is chosen as a basis to extend the model. The out-of-plane displacement function can be regarded as the result of the product of two parabolas along the principal directions (i.e. parabolic variation of the curvatures)

$$w(x,y) = P(x) \cdot G(y) \tag{3.9}$$

where

$$\begin{aligned} P(x) &= p_0 + p_1 x + p_2 x^2 \\ G(y) &= g_0 + g_1 y + g_2 y^2 \end{aligned} \tag{3.10}$$

To simplify the computation of derivatives and integrals by symbolic manipulation software, the previous expression is re-arranged as

$$w(x,y) = w_{00} + w_{01}y + w_{02}y^2 + w_{10}x + w_{11}xy + w_{12}xy^2 + w_{20}x^2 + w_{21}x^2y + w_{22}x^2y^2 \tag{3.11}$$

Within this notation, the first subscript refers to the order of the x-variable while the second one refers to the order of the y-variable. The polynomial functions chosen by Dano and Hyer to model the strain displacements provide an adequate number of degrees of freedom and therefore their expression is unchanged. For completeness they are presented, with the different notation adopted here, as

$$\begin{aligned} \varepsilon_x^0 &= \epsilon_{x00} + \epsilon_{x20}x^2 + \epsilon_{x11}xy + \epsilon_{x02}y^2 \\ \varepsilon_y^0 &= \epsilon_{y00} + \epsilon_{y20}x^2 + \epsilon_{y11}xy + \epsilon_{y02}y^2 \end{aligned} \tag{3.12}$$

The shear deformation is determined using the procedure outlined before. The drilling degree of freedom is eliminated by imposing $u_{01} = v_{10}$. This model has 20

unknown coefficients.

3.1.3 Application to a square plate

To validate the effectiveness of the modified model and before applying it to more complex types of structures, a square plate with all edges free is considered. The results obtained are then compared with Hyer's model and FEA. The total potential energy is assembled and minimised with the help of the symbolic manipulation software Maple 9.5. The equilibrium configurations are obtained by using a non-linear optimisation subroutine "`NLPSolve`" that finds the local minima of a non-linear function. This greatly simplifies the solution of the system of non-linear equations that are obtained when minimising the total energy. Furthermore, the boundary conditions and the other constraints imposed on the model can be directly implemented as constraints in the optimisation process. In this way, it is easier to automate the process for parametric studies and it is possible to avoid the difficulties encountered when finding the solution through a Newton-Raphson scheme (typically the sensitivity with respect to the initial guess). The comparison is carried out for a square plate with side length L of 180 mm and stacking sequence $[0_4^0/90_4^0]_T$. Table 3.1 shows the values of the total potential energy and of the principal curvatures (k_x and k_y) for the two equilibrium configurations. Figure 3.1 shows a superposition of the three equilibrium shapes obtained respectively with Hyer's model, the extended model and FEA. Figure 3.2 shows three sections of the plate obtained at the centre and at 80% of the semi-span of the panel respectively. To highlight the differences between the three models the vertical displacement has been amplified by a factor of 5. As can be seen, the differences between the three models are very small all over the panel and the greater difference is found within the regions close to the edges. Here the configuration computed with the higher order model has a slight parabolic variation of the edge shape whereas the panel obtained with Hyer's model shows an almost perfectly straight edge. The FEA predicts an edge that is almost flat in the central part and slightly curved towards the corners. In this area the displacements are particularly difficult to match with those obtained with the FEA because of the steep variation of the curvatures. Both the model developed by Hyer and its extension are not able to describe accurately the local displacement in this region since they have been developed to obtain a good approximation of the overall deformation and not of the local effects close to the boundary. A detailed analysis of the boundary layer area requires a different type of approximation functions and it is beyond the scope of this study. Figure 3.3 shows a comparison of the values of the curvatures for the two analytical models at a section

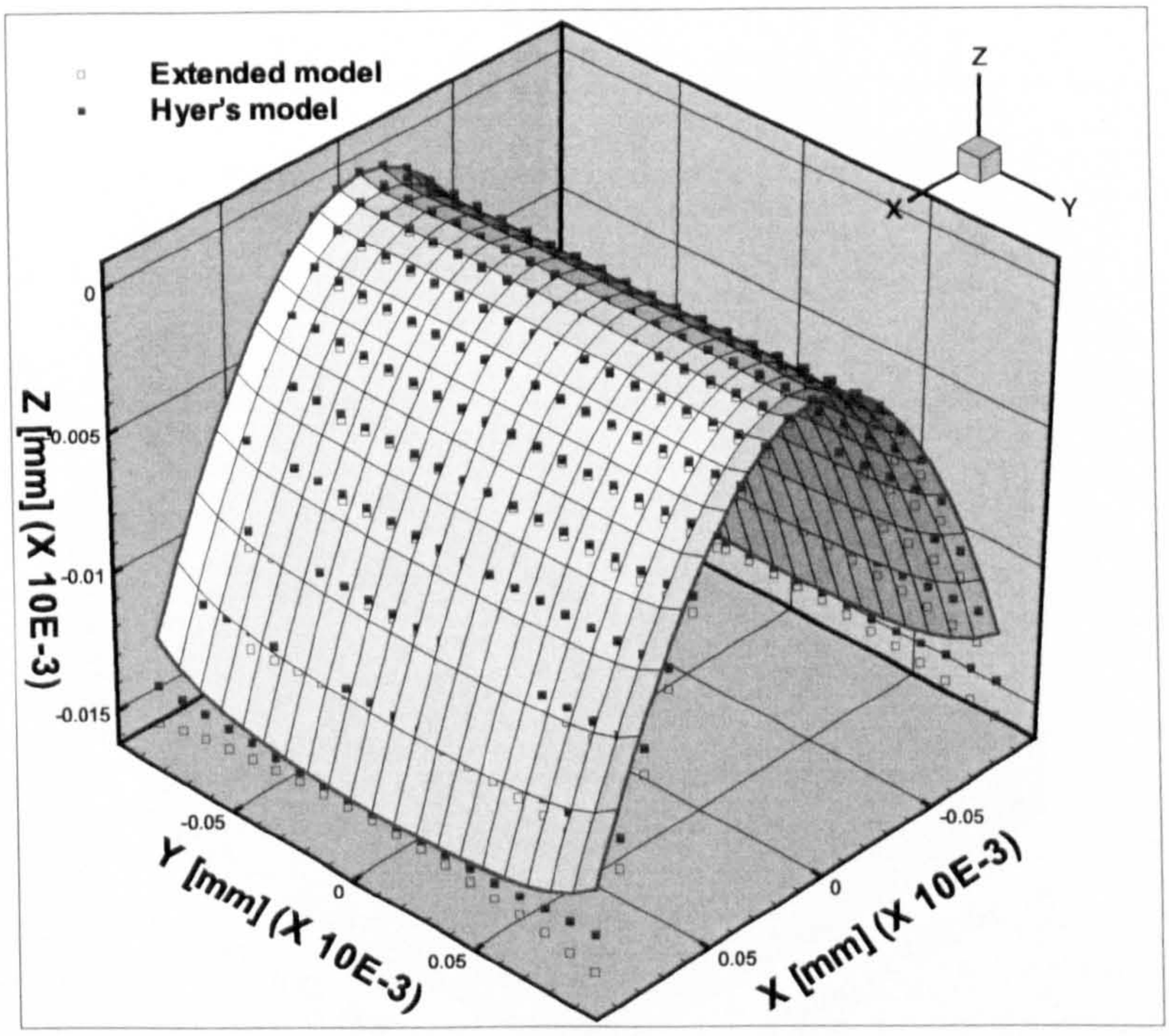

Figure 3.1: Hyer's model and Extended model overlaid onto the FE model

taken at the centre of the plate. It is clear that the higher order model predicts quadratic curvature while the previous model has a constant value throughout the domain.

3.1.4 Application to a compound plate

The results obtained for the square plate show a satisfactory agreement between the two analytical models and therefore the higher order model is applied to the analysis of panels with piecewise variation of the laminate in the planform. A test structure for this purpose is obtained by joining together two square plates with different stacking sequences. The panel measures 360mm×180mm and the coordinate systems used throughout this section are shown in Fig. 3.4. The material properties are those of typical pre-preg carbon-epoxy laminates and are listed in Table 2.1. The left hand side of the plate has a symmetric stacking sequence $[0_2^0/90_2^0]_{SYM}$ while the right hand side has an unsymmetric lay-up $[0_4^0/90_4^0]_{TOT}$. This is equivalent to imposing an elastic boundary condition at the edge where the two plates are joined together. An experimental demonstrator of the aforementioned structure has been built and its equilibrium configurations are shown in Fig. 3.5.

Let A be the domain representing the whole structure so that $A = A_1 \cup A_2$ where

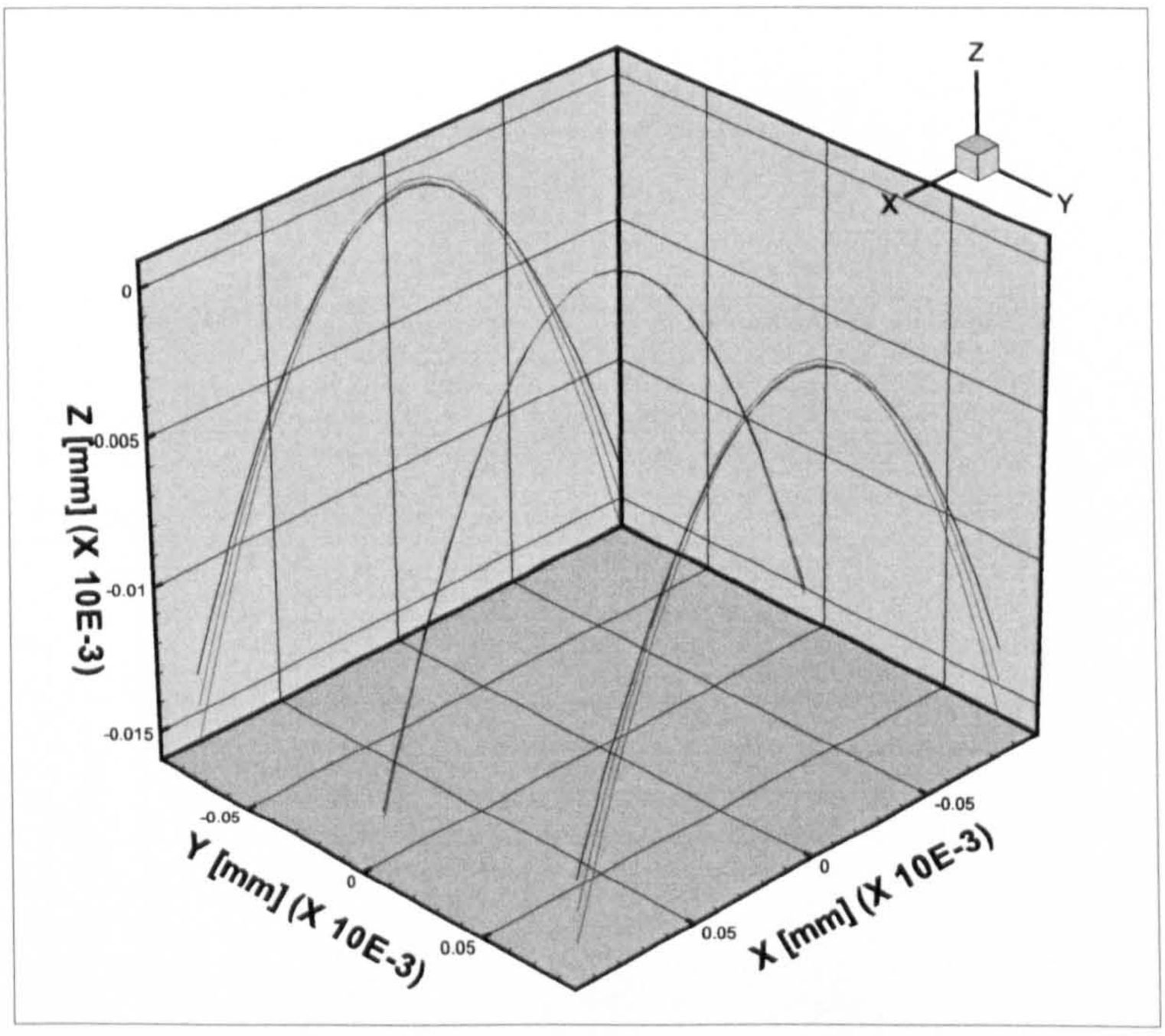

Figure 3.2: Cross-section comparison at different stations

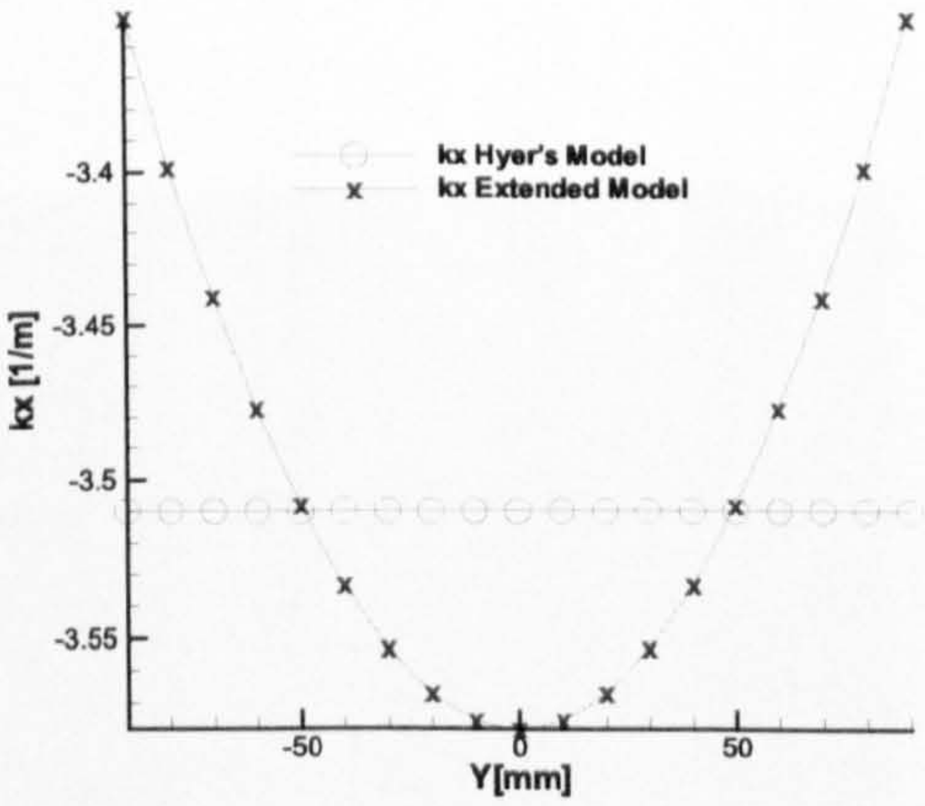

(a) k_x curvature

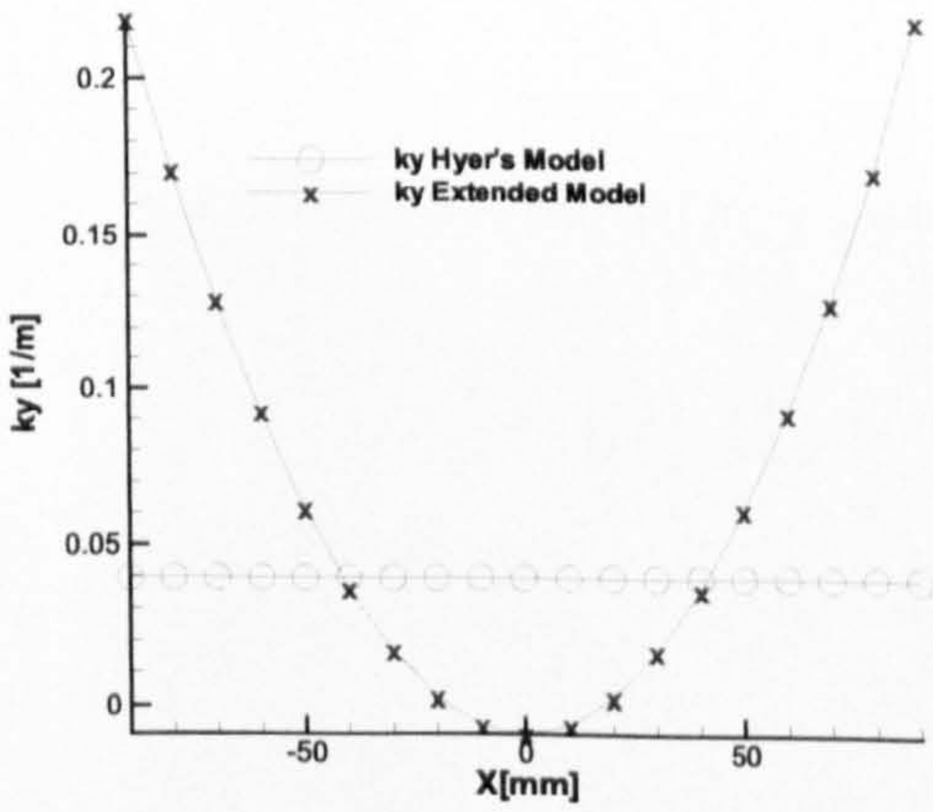

(b) k_y curvature

Figure 3.3: Principal curvature comparison

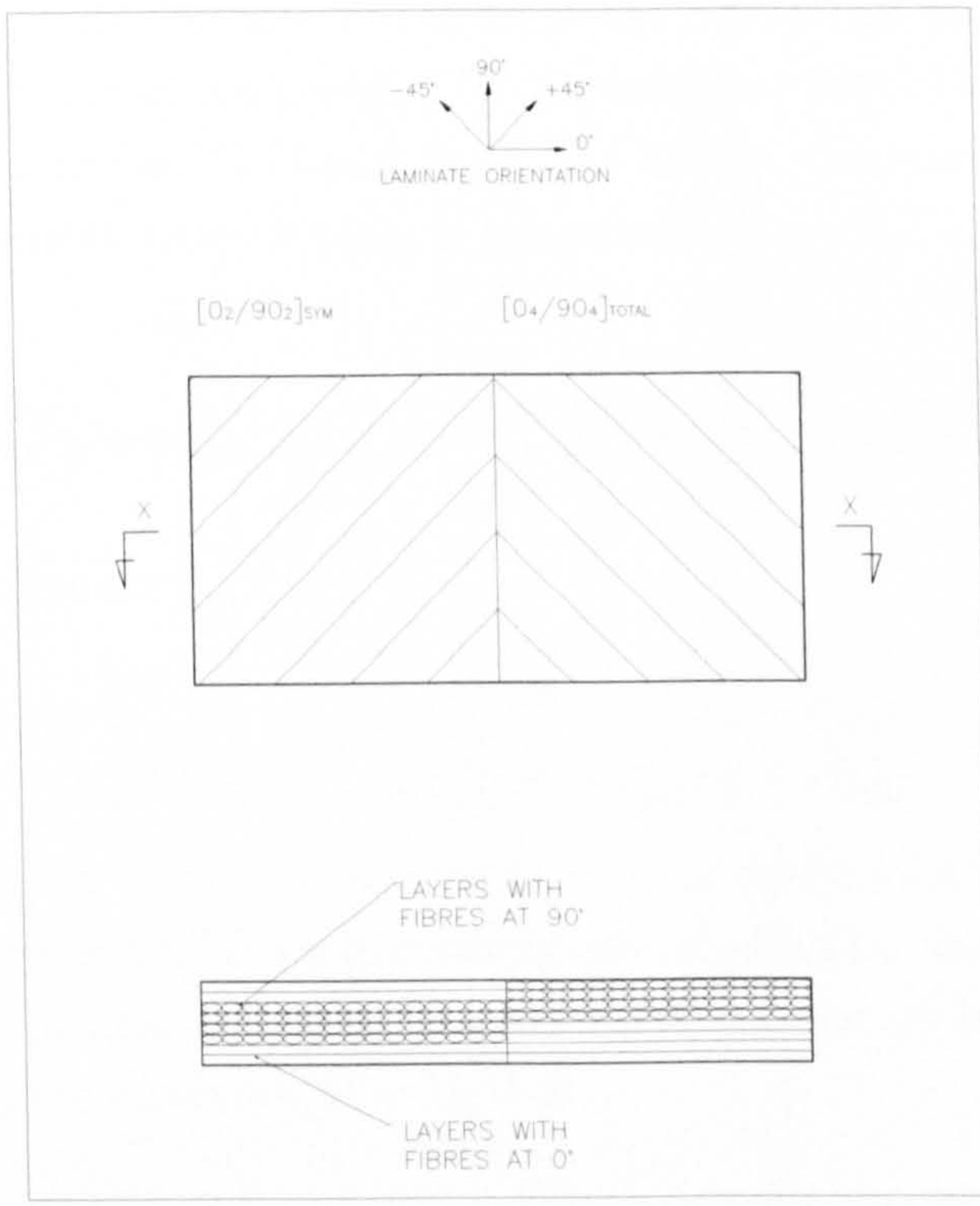

Figure 3.4: Geometry and reference system for the test model

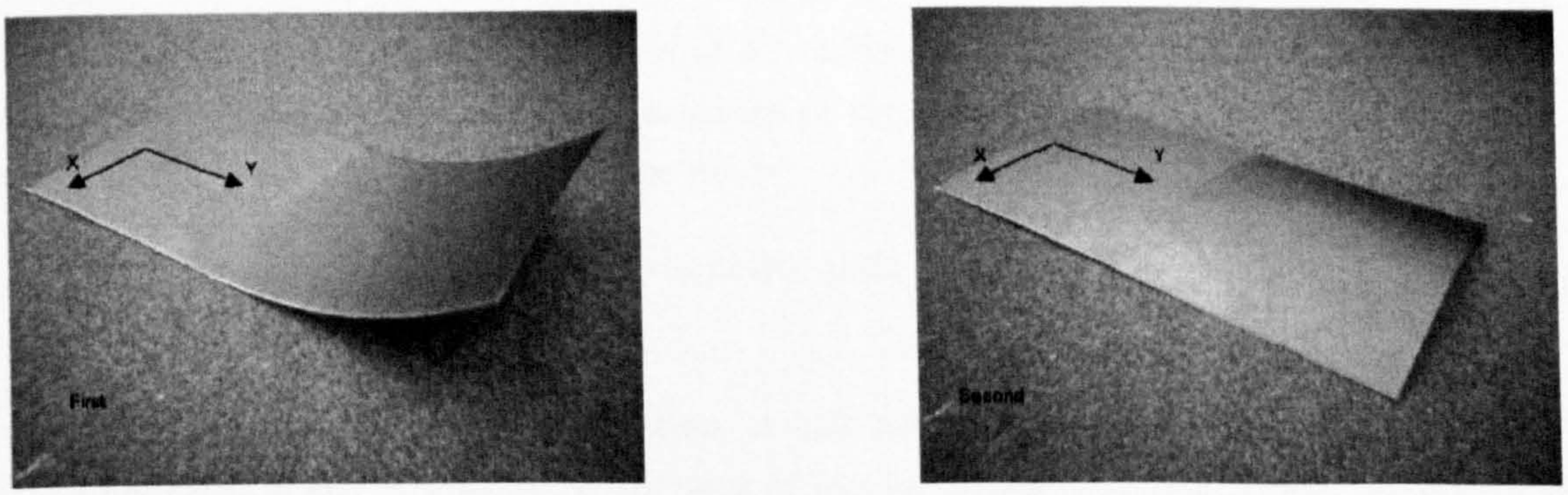

(a) First equilibrium shape (b) Second equilibrium shape

Figure 3.5: Experimental model

A_1 represents the symmetric plate and A_2 the unsymmetric plate. Using a domain decomposition, if the functions that describe the displacements are piecewise smooth over the domain A, it is possible to take into account the interaction between the symmetric and unsymmetric portions of the panel. The displacement field of each part of the plate is modelled according to Eq. (3.7) and (3.9). For clarity, the function for the assumed out-of-plane displacement for each plate is presented

$$w^{(i)}(x,y_i) = w_{00}^{(i)} + w_{01}^{(i)} y_i + w_{02}^{(i)} y_i^2 + w_{10}^{(i)} x + w_{11}^{(i)} x y_i + w_{12}^{(i)} x y_i^2 + w_{20}^{(i)} x^2 + w_{21}^{(i)} x^2 y_i + w_{22}^{(i)} x^2 y_i^2 \tag{3.13}$$

The strain functions are

$$\begin{aligned} \varepsilon_x^{0(i)} &= \epsilon_{x00}^{(i)} + \epsilon_{x20}^{(i)} x^2 + \epsilon_{x11}^{(i)} xy + \epsilon_{x02}^{(i)} y^2 \\ \varepsilon_y^{0(i)} &= \epsilon_{y00}^{(i)} + \epsilon_{y20}^{(i)} x^2 + \epsilon_{y11}^{(i)} xy + \epsilon_{y02}^{(i)} y^2 \end{aligned} \tag{3.14}$$

where the index i refers to the symmetric ($i = 1$) or unsymmetric ($i = 2$) part. The strain energy is formulated for each substructure separately, thus accounting for the different stacking sequences and then, the two contributions are summed to obtain the energy for the complete structure, $\Pi = \Pi_1 + \Pi_2$

$$\begin{aligned} \Pi = & \int\int_{A_1} \left(\frac{1}{2} \begin{bmatrix} \underline{\varepsilon}^{(1)} \\ \underline{k}^{(1)} \end{bmatrix}^T \begin{bmatrix} \underline{\underline{A}}^{(1)} & \underline{\underline{B}}^{(1)} \\ \underline{\underline{B}}^{(1)} & \underline{\underline{D}}^{(1)} \end{bmatrix} \begin{bmatrix} \underline{\varepsilon}^{(1)} \\ \underline{k}^{(1)} \end{bmatrix} - \begin{bmatrix} \underline{\varepsilon}^{(1)} \\ \underline{k}^{(1)} \end{bmatrix}^T \begin{bmatrix} \underline{N}^{th} \\ \underline{M}^{th} \end{bmatrix}^{(1)} \right) dxdy + \\ & + \int\int_{A_2} \left(\frac{1}{2} \begin{bmatrix} \underline{\varepsilon}^{(2)} \\ \underline{k}^{(2)} \end{bmatrix}^T \begin{bmatrix} \underline{\underline{A}}^{(2)} & \underline{\underline{B}}^{(2)} \\ \underline{\underline{B}}^{(2)} & \underline{\underline{D}}^{(2)} \end{bmatrix} \begin{bmatrix} \underline{\varepsilon}^{(2)} \\ \underline{k}^{(2)} \end{bmatrix} - \begin{bmatrix} \underline{\varepsilon}^{(2)} \\ \underline{k}^{(2)} \end{bmatrix}^T \begin{bmatrix} \underline{N}^{th} \\ \underline{M}^{th} \end{bmatrix}^{(2)} \right) dxdy \end{aligned} \tag{3.15}$$

The strain energy Π is now a function of 42 unknown coefficients and its local minima correspond to the equilibrium configurations of the plate. To simplify the minimisation process, the following assumptions are made

- The geometric centre of the symmetric part is clamped to eliminate rigid body translation (i.e. $w_{00}^{(1)} = 0$)
- From the experimental observation, it has been noticed that the equilibrium configurations are symmetric with respect to the y-axis (i.e. $w_{10}^{(i)} = w_{11}^{(i)} = w_{12}^{(i)} = 0$ for $i = 1, 2$)
- The drilling degree of freedom is eliminated in both parts (i.e. $u_{01}^{(i)} = v_{10}^{(i)}$ for

$i = 1, 2)$

With this approach, the number of unknown coefficients is reduced to 33. To account for the interaction between the symmetric part and the unsymmetric part of the panel, it is necessary to impose the continuity of the displacement across the whole domain A, and therefore the following conditions must hold

$$\begin{aligned} u^{(1)}\left(x, \tfrac{L}{2}\right) &= u^{(2)}\left(x, -\tfrac{L}{2}\right) \\ v^{(1)}\left(x, \tfrac{L}{2}\right) &= v^{(2)}\left(x, -\tfrac{L}{2}\right) \\ w^{(1)}\left(x, \tfrac{L}{2}\right) &= w^{(2)}\left(x, -\tfrac{L}{2}\right) \\ \tfrac{\partial w^{(1)}}{\partial x}\left(x, \tfrac{L}{2}\right) &= \tfrac{\partial w^{(2)}}{\partial x}\left(x, -\tfrac{L}{2}\right) \end{aligned} \tag{3.16}$$

The continuity on $\frac{\partial w}{\partial y}$ is not imposed since this is implicitly satisfied from within the continuity of the out-of-plane displacement. The solutions have been found with the same technique as for the square plate. The analytical model successfully captures the behaviour of the multi-stable structure as shown in Fig. 3.6. It must be pointed out that Eq. (3.16) are assumed to be valid on a macroscopic basis (i.e. at laminate level). The understanding of what happens at ply level requires a different approach. Because of the particular stacking sequence, fibres and matrix continuity at ply level can only be obtained for those layers with fibres at 0^0 (i.e. parallel to the y-axis), which are continuous through the symmetric and the unsymmetric laminates. For the layers at 90^0, such continuity relies entirely on the matrix since the fibres are parallel to the boundary. This creates resin-rich zones that also induce stress-concentrations that might cause cracks to develop when the load axis is along the 0^0 direction. To reduce this, it is possible to modify the interface between the two parts by offsetting the position of the ply drop for the layers at 90^0. This would create a transition zone rather that an abrupt change as it is now, but could also modify the stiffness of the constraint introducing further difficulties for the analytical model. For these reasons and for engineering modelling purposes, the assumption of structural continuity at laminate level is considered acceptable. A detailed comparison with the numerical and experimental configurations is presented in the next section.

3.1.5 Finite element analysis and experimental results

In this section, the results obtained with the analytical model and their comparison with numerical and experimental data is presented. Residual stresses are generated by the temperature difference and no external force is applied to the specimen. For the time being, the results obtained through the numerical analysis (performed with the

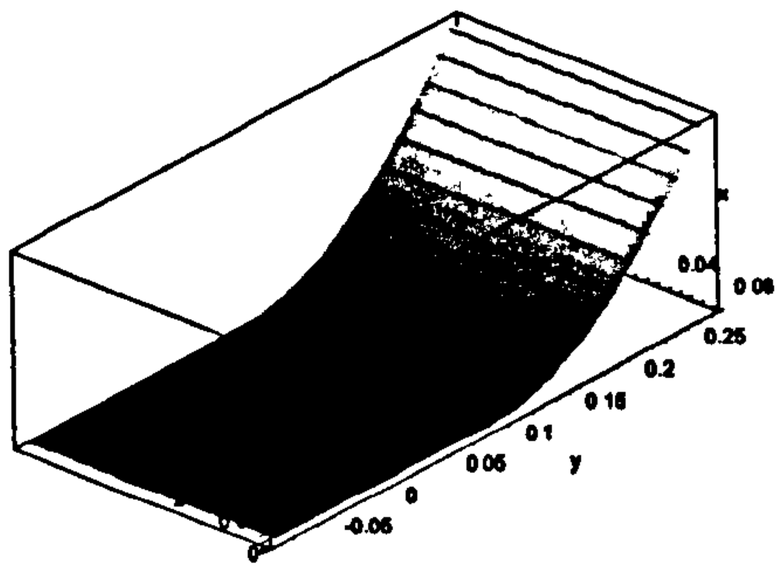

(a) First shape

(b) Second shape

Figure 3.6: Equilibrium shapes obtained with the analytical model

commercial software ABAQUS) will be assumed correct; the numerical analysis itself and the difficulties related to it will be dealt with in the next section. The panel is modelled using 800 four-node-square shell elements ($S4R$) with a total of 861 nodes and 5166 degrees of freedom. The cool-down is simulated by applying an initial temperature of 140^0C and a final temperature of 0^0C to all the nodes of the model. To capture the different equilibrium shapes, a pseudo-dynamic analysis is used. This analysis adds viscous forces to damp local instabilities, when convergence is difficult to achieve, and allows the system to jump to the different branches of the solution (i.e. converge to the different shapes).

Figs. 3.7 and 3.8 show an overall comparison between the FEA and the analytical data for the 4 and the 8-layered panels. The comparison is carried out according to the system of reference shown in Fig. 3.4. The markers represent the analytical data whereas the mesh represents the FEA results. As can be seen, the two models have a satisfactory overall agreement, the greatest difference being towards the unsymmetric edge. The 8-layered panel shows a better agreement compared to the 4-layered one. The analytical model, because of its reduced number of degrees of freedom, is in a sense stiffer and therefore it better captures the reduced displacements of the 8-layered panel. Figs. 3.10 and 3.11 show a similar comparison but the results are also compared against experimental data. This latter comparison highlights the effect that the FEA is also stiffer with respect to experimental data, presumably due to the mesh density chosen as a compromise between accuracy and computational efficiency.

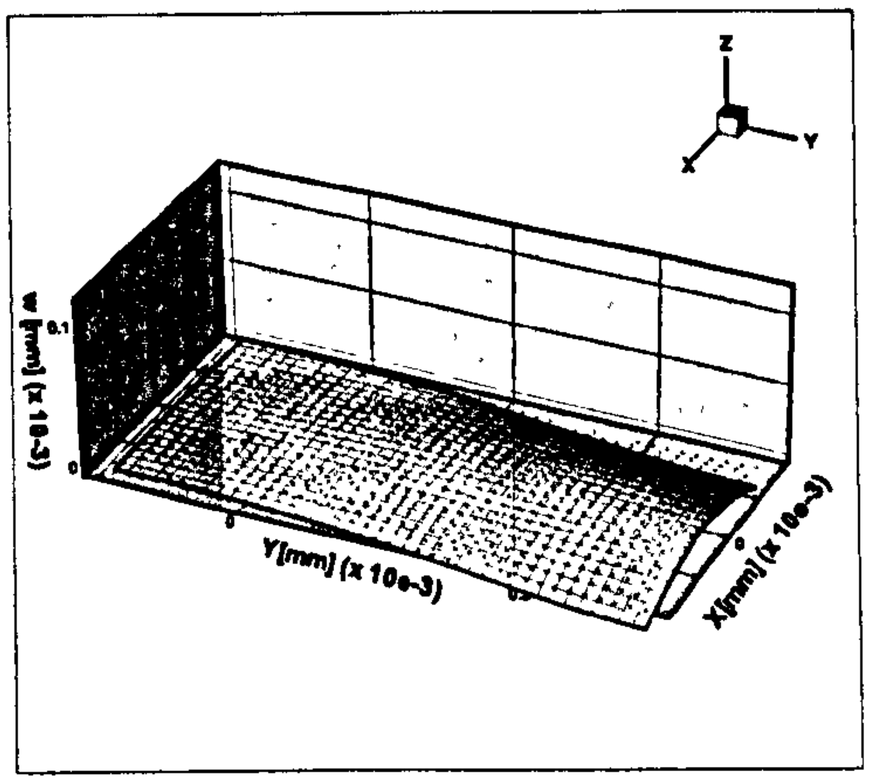

(a) Flat configuration

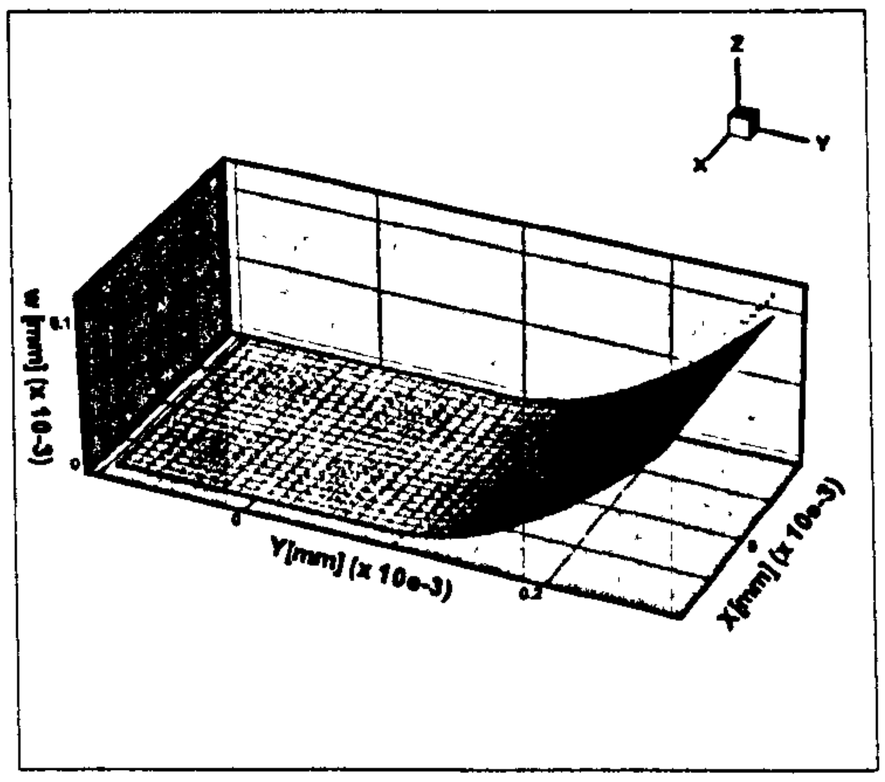

(b) Curled configuration

Figure 3.7: Analytical vs FE shape for the 4-layered plate

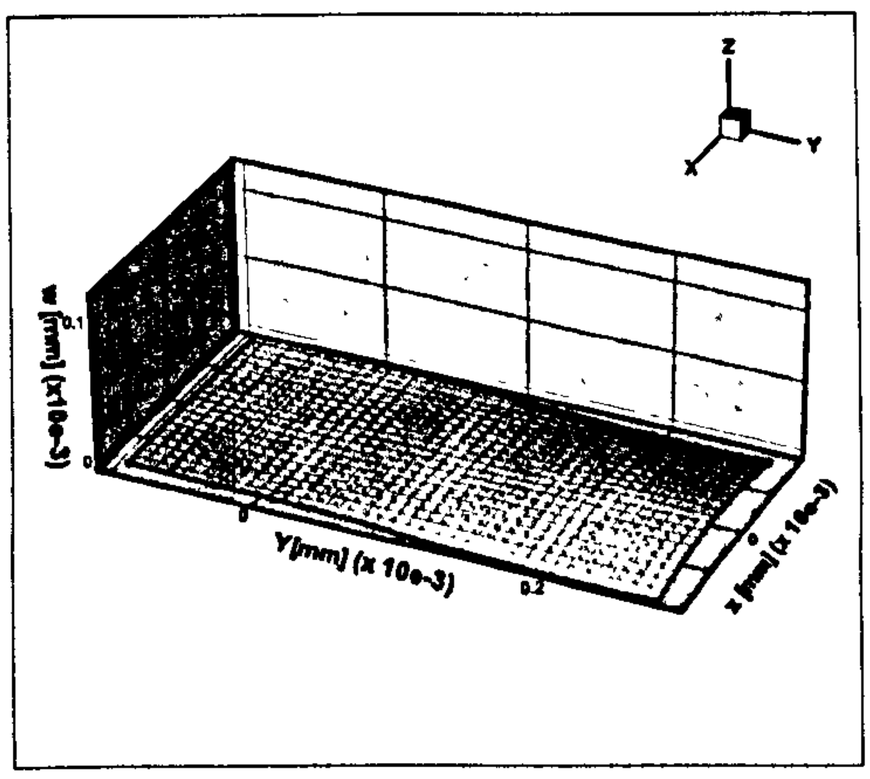

(a) Flat configuration

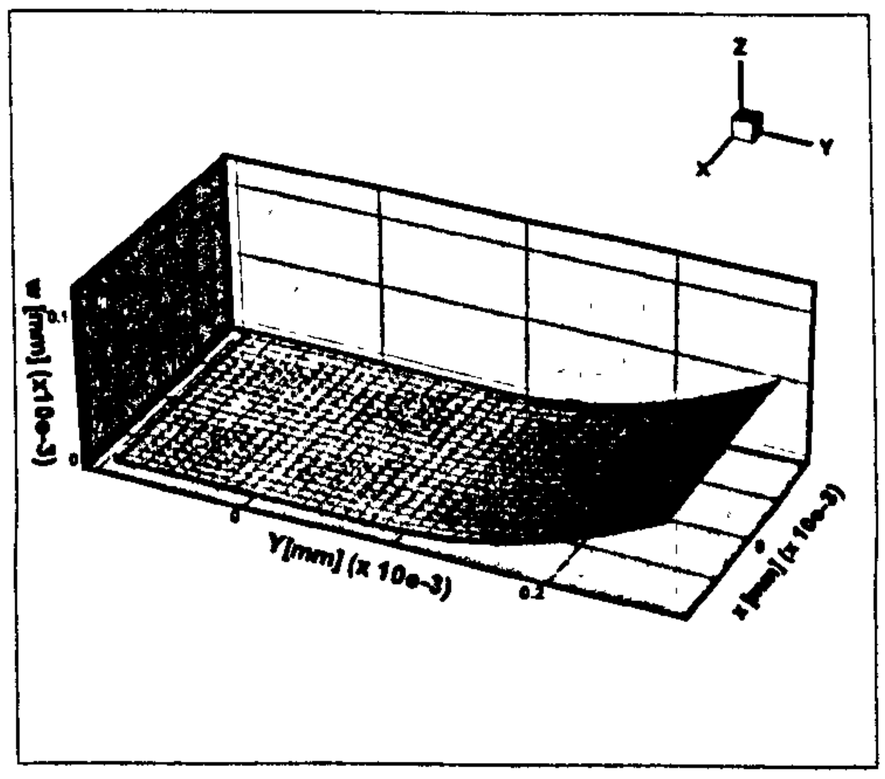

(b) Curled configuration

Figure 3.8: Analytical vs FE shape for the 8-layered plate

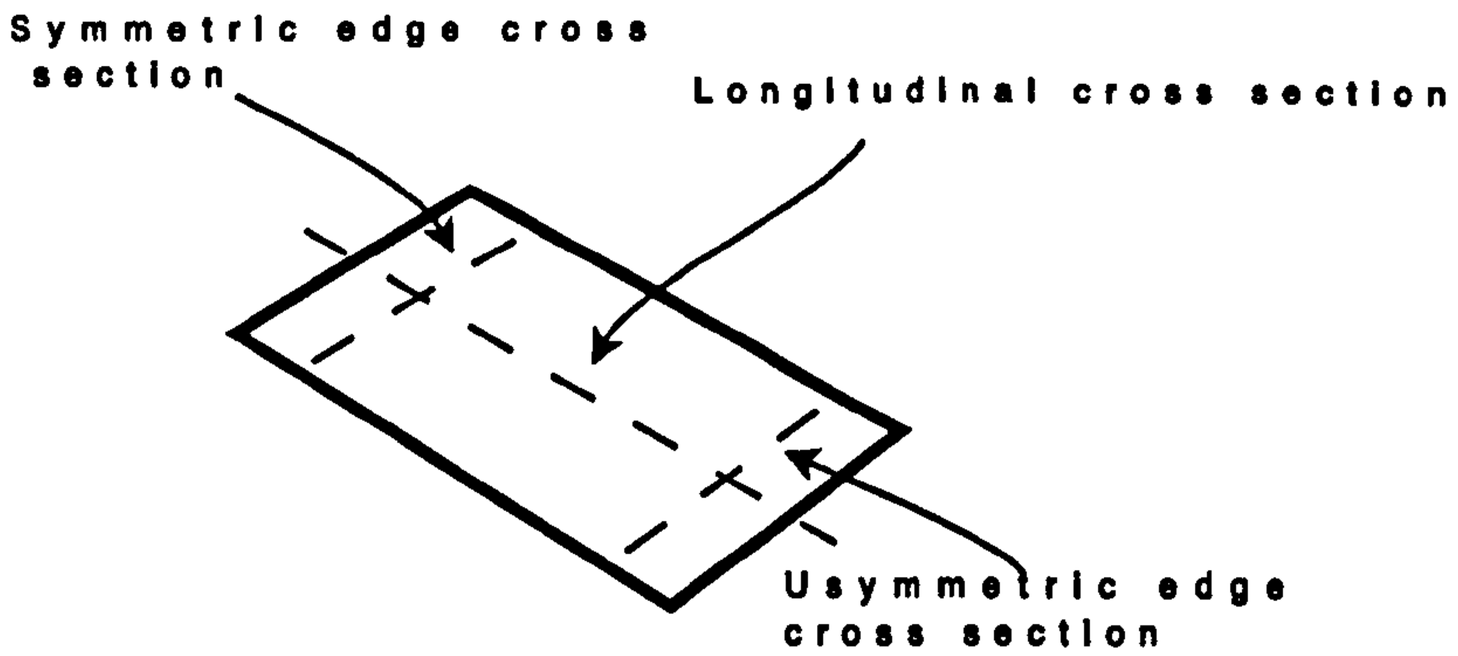

Figure 3.9: Test model geometry and coordinate system

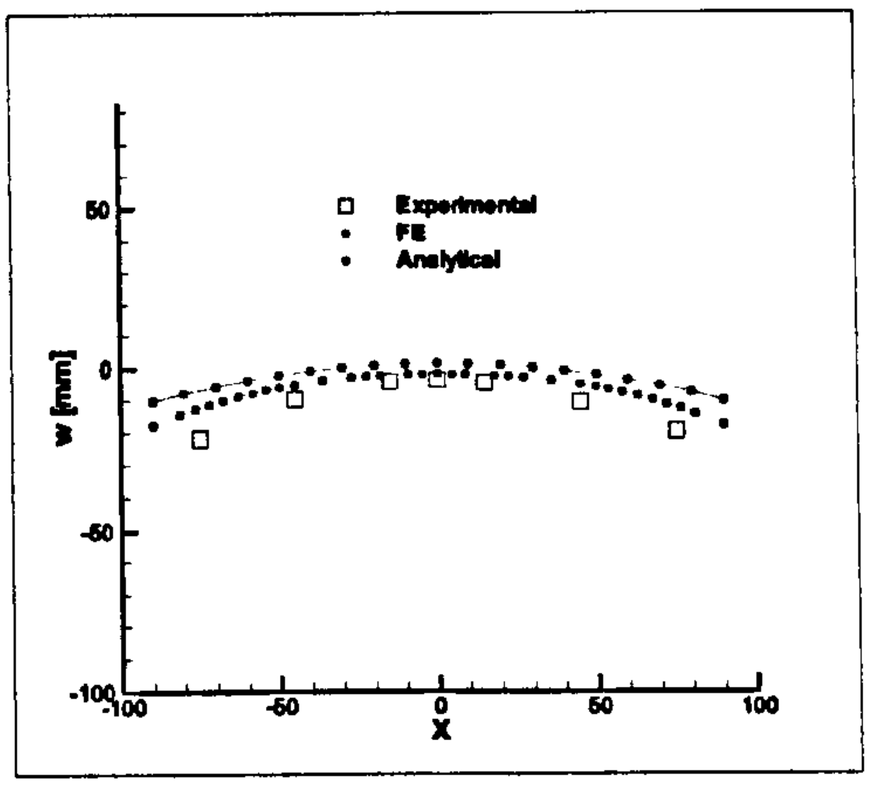

(a) Unsymmetric edge cross-section

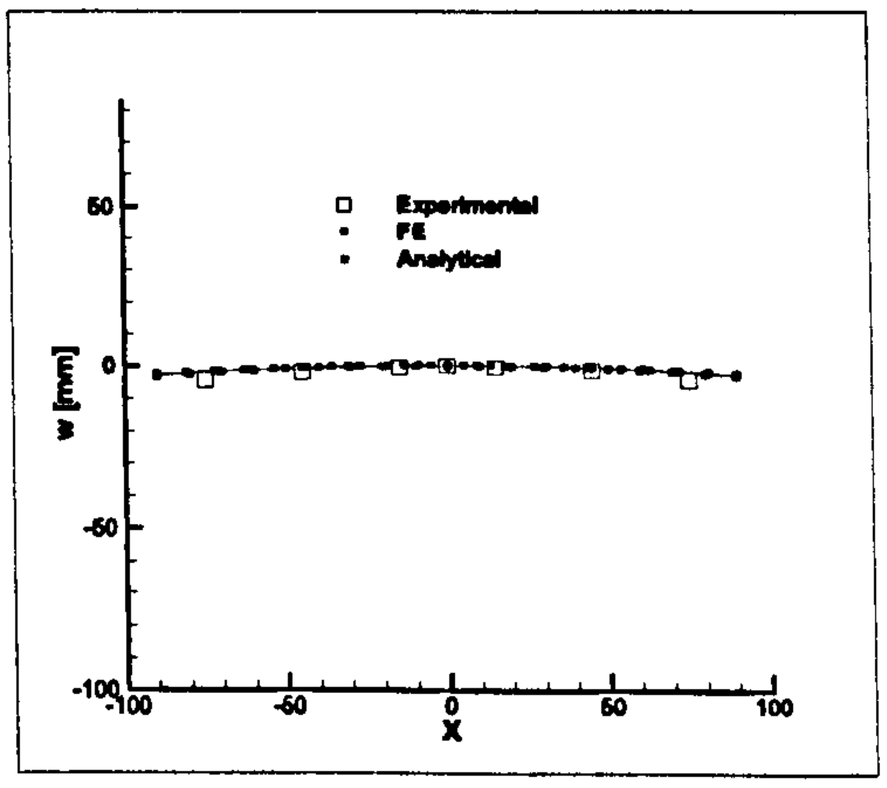

(b) Symmetric edge cross-section

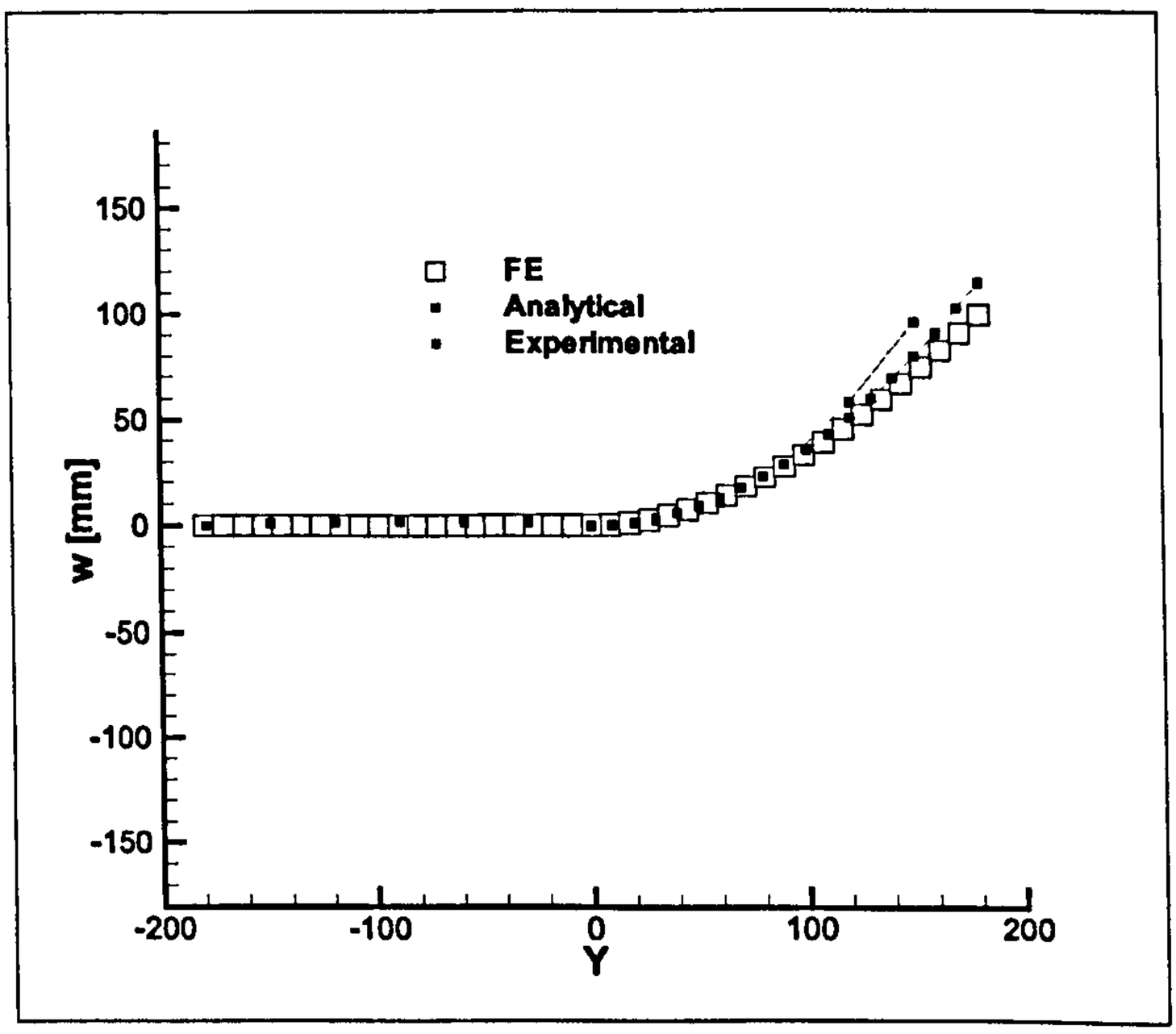

(c) Longitudinal cross-section for the curled configuration

Figure 3.10: Analytical vs. FEA and experimental section for the 4-layered plate

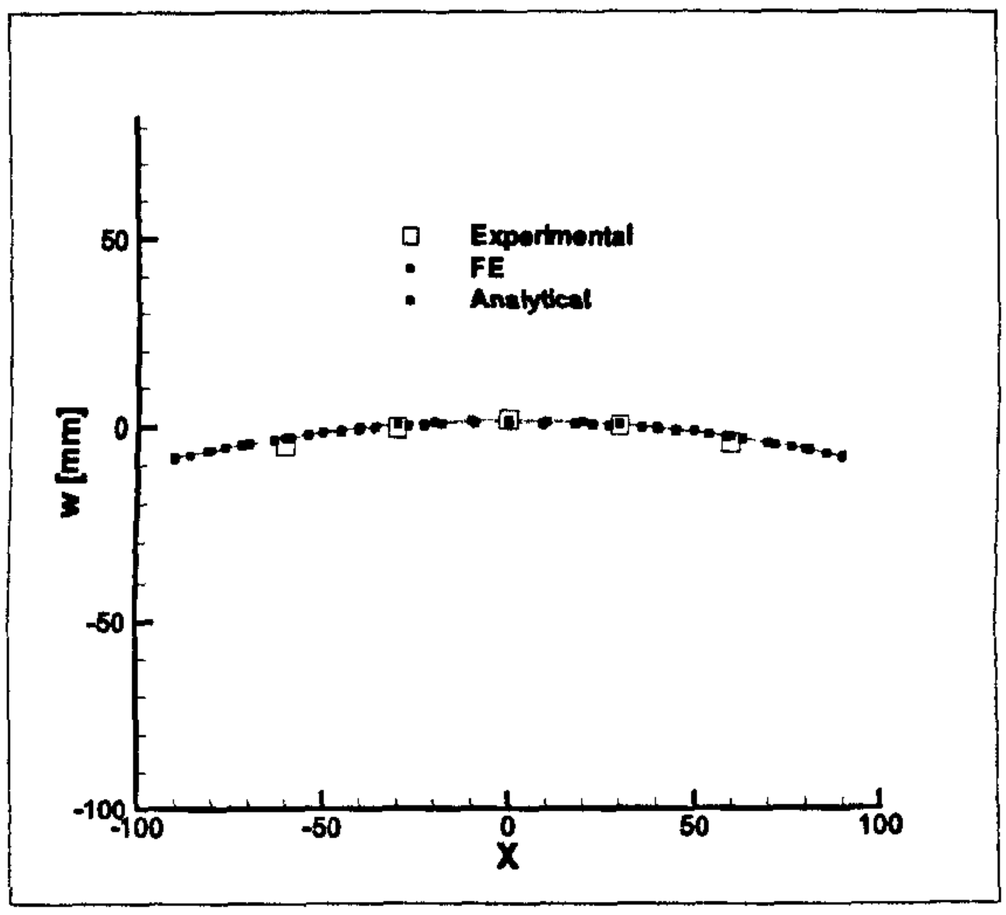

(a) Unsymmetric edge cross-section

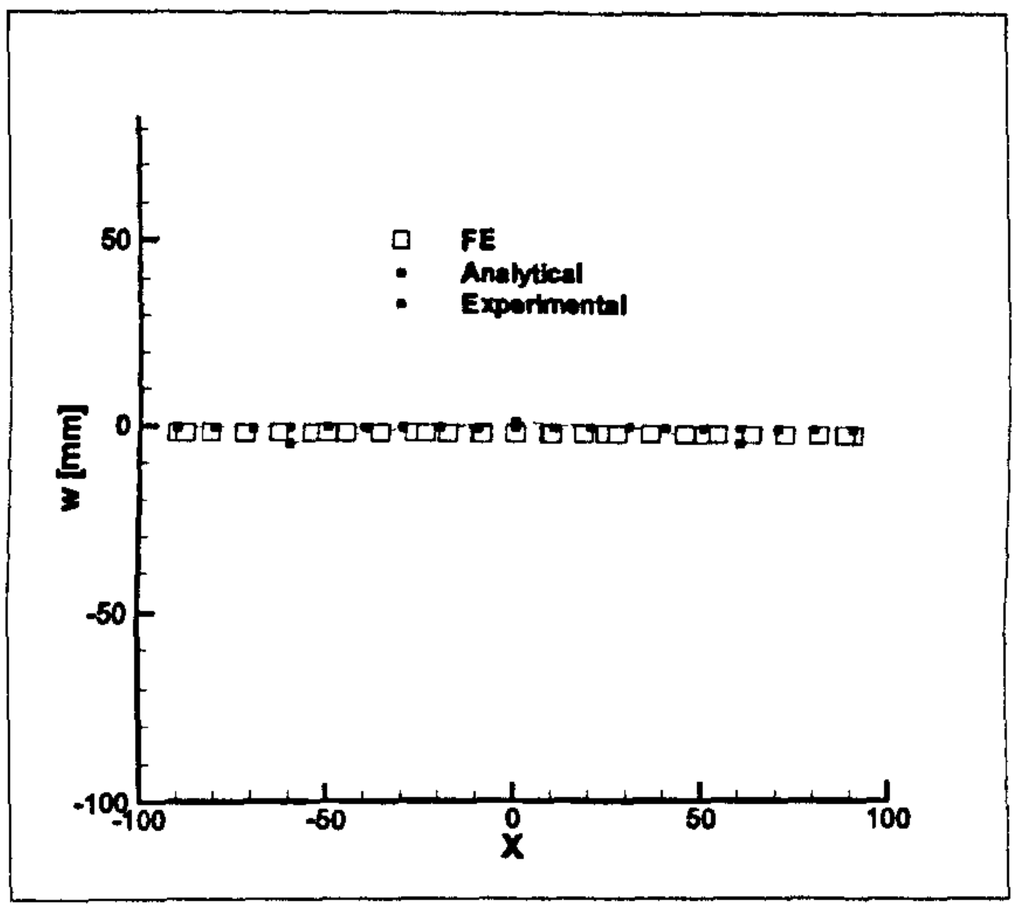

(b) Symmetric edge cross-section

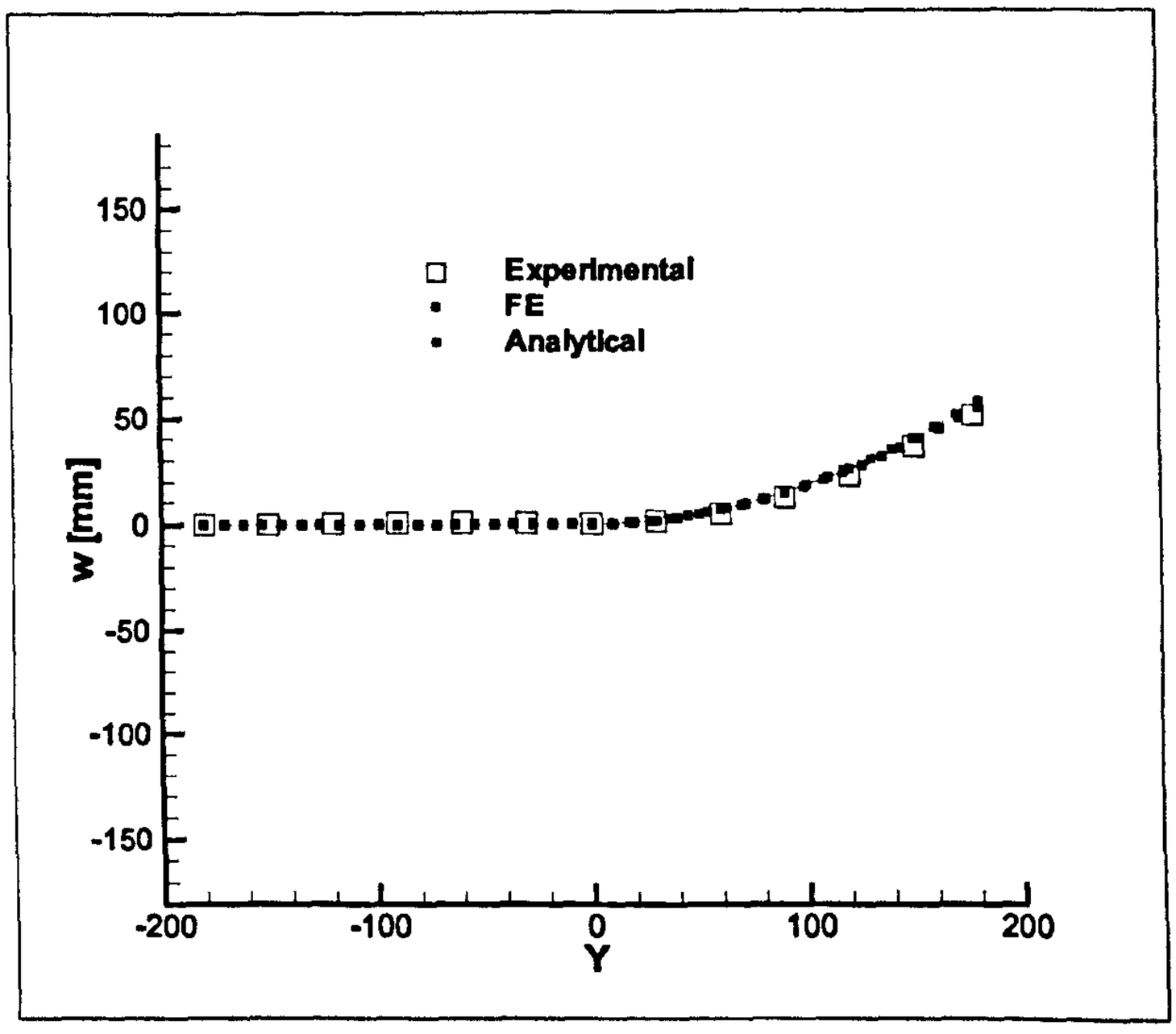

(c) Longitudinal cross-section for the curled configuration

Figure 3.11: Analytical vs. FEA and experimental section for the 8-layered plate

3.1.6 Parametric studies: effects of boundary conditions

In this section the analytical model is used to investigate the effects of different lay-ups and thicknesses of the symmetric part of panel. The scope of this section is to highlight the effect of the boundary conditions on the bi-stable properties of the unsymmetric part of the panel. The base state is represented by the 8-layered unsymmetric panel without any constraint. As observed in the previous sections, the two cylindrical configurations that are obtained with a square unsymmetric panel are identical in terms of curvature values. By constraining one of the edges of the panel, the curvature along the constrained edge is considerably reduced, as expected. At the boundary between the two 8-layered plates, the transverse curvature is 37% of the unrestrained panel curvature. Moving away from the restrained edge, the effect of the constraint diminishes and the curvature is gradually recovered. At the maximum distance from the constraint (i.e. the "unsymmetric-edge"), the curvature reaches approximately 60% of the unrestrained plate curvature. By examining the longitudinal curvature (i.e. perpendicular to the constrained edge), the curvature is 99% of the value achieved by the free panel (i.e. it is almost unaffected by the presence of the symmetric panel). This effect is explained by the fact that the constraint increases the stiffness in the transverse direction and therefore the associated curvature changes. Along the longitudinal direction, the shape is almost perfectly cylindrical, there is little transverse curvature and therefore a very small effect is observed. In fact, the shape is never exactly cylindrical but has a small anticlastic component that is highly dependent on the thickness/side-length ratio. For plates with geometry similar to those analysed here, it is expected that this response does not affect the global behaviour of the panel and therefore as a first approximation, the effects of the anticlastic curvature are neglected. The parametric study was done using seven different panels with different lay-ups for the symmetric part:

- 8 layers: $[0_2^0, 90_2^0]_{SYM}$
- 16 layers: $[0_4^0, 90_4^0]_{SYM}$
- 24 layers: $[0_6^0, 90_6^0]_{SYM}$
- Ninety dominant laminate: $[90_3^0, 0^0]_{SYM}$
- Zero dominant laminate: $[0_3^0, 90^0]_{SYM}$
- Quasi isotropic laminate: $[45^0, -45^0, 90^0, 0^0]_{SYM}$
- Antisymmetric angle ply: $[45^0, -45_2^0, 45^0]_{ANTISYM}$

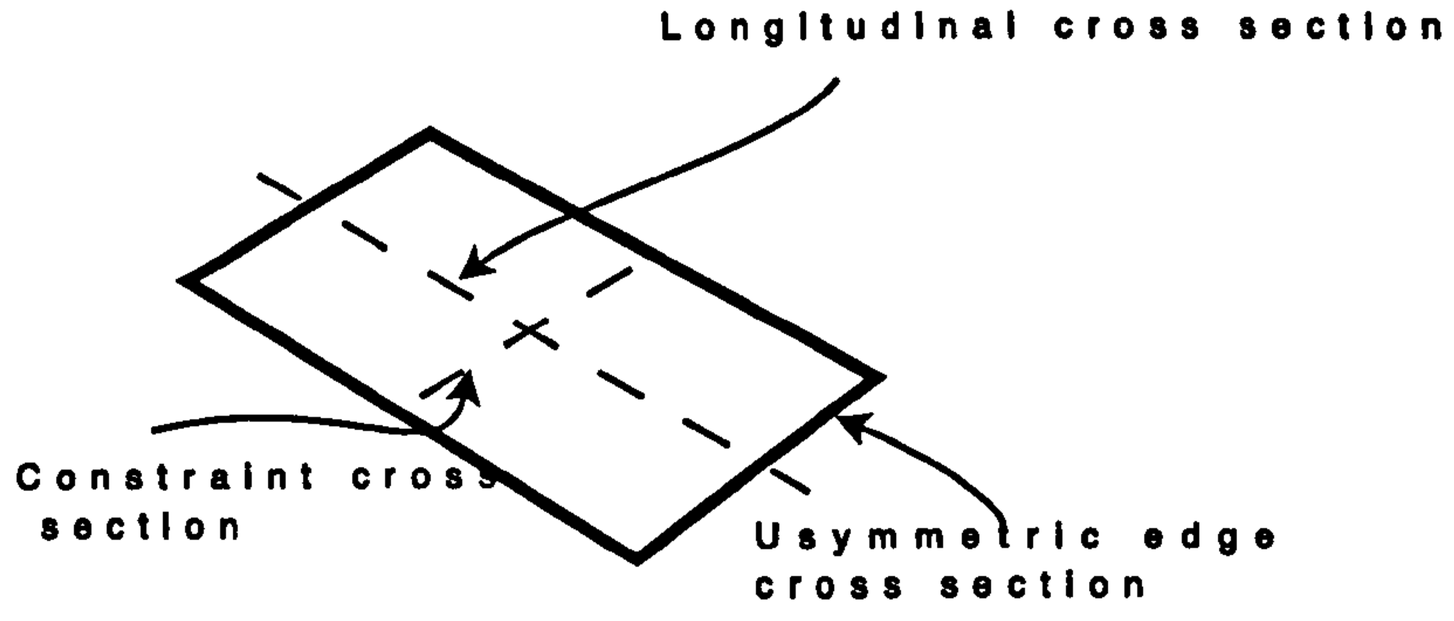

Figure 3.12: Parametric study geometry and cross-sections

The principal difference between the laminates tested is the transverse stiffness. For the first three stacking sequences, the driving factor is the thickness, while for the last four it is the fibre orientation. Throughout the analysis the unsymmetric part remains unchanged, with stacking sequence $[0_4^0, 90_4^0]_T$, as this maximises the bi-stable behaviour. The values of the transverse curvature k_x and the difference with respect to the free-free square plate are shown in Tables 3.2 and 3.3. From a physical point of view it is easier to understand the differences by examining Figs. 3.13 and 3.14 where the different cross-sections (see Fig. 3.12) of the plate are shown. Figure 3.13 presents the results obtained by varying the number of layers. As expected, an increase in thickness results in a reduction of the transverse curvature of the flat configuration as shown by Figs. 13(a) and 13(b). Figure 13(c) shows almost identical values for all configurations and this result confirms the reduced sensitivity of the longitudinal curvature with respect to a variation of the constraint characteristics. The effects of using different stacking sequences with the symmetric panel are summarised in Fig. 3.14. Figures 14(a) and 14(b) show the same result as above but with a much smaller range of variation since the thickness of the two plates is the same. Figure 14(c) shows (Fig. 13(c) likewise) that the longitudinal curvature is not affected by the constraint. In both cases, the curvature at the unsymmetric edge is very similar and reaches approximately 60% of the unrestrained panel. These results highlight the robustness of the bi-stable behaviour of unsymmetric laminates. Even if one of the edges is constrained, almost 60% of their bi-stable behaviour is retained and moreover it is possible to tailor the final geometry with reasonable accuracy.

3.1.7 Remarks on the analytical model

A non-linear analytical model to predict the equilibrium configurations of multistable composite with piecewise variation of the laminate in the planform has been presented.

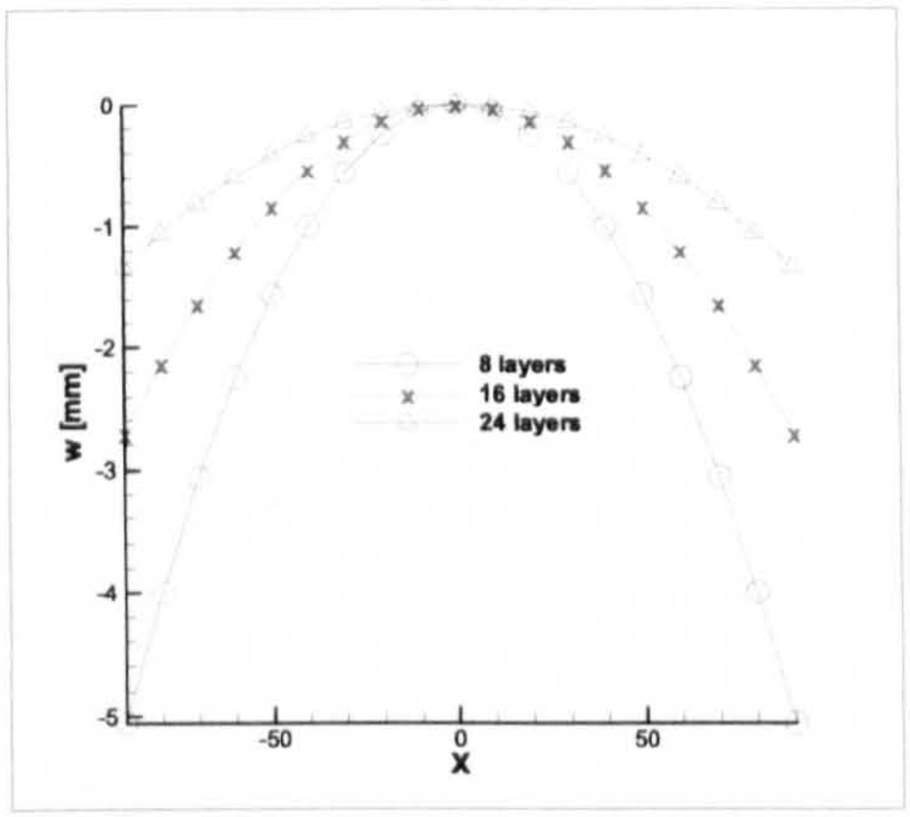

(a) Constrainded cross-section

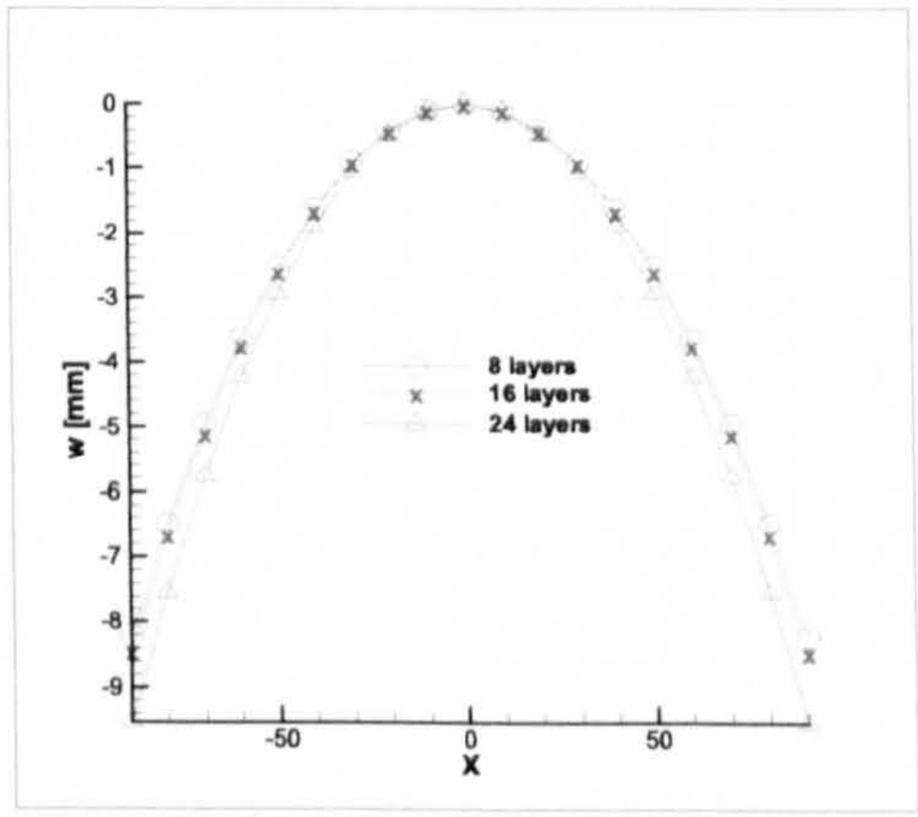

(b) Unsymmetric edge cross-section

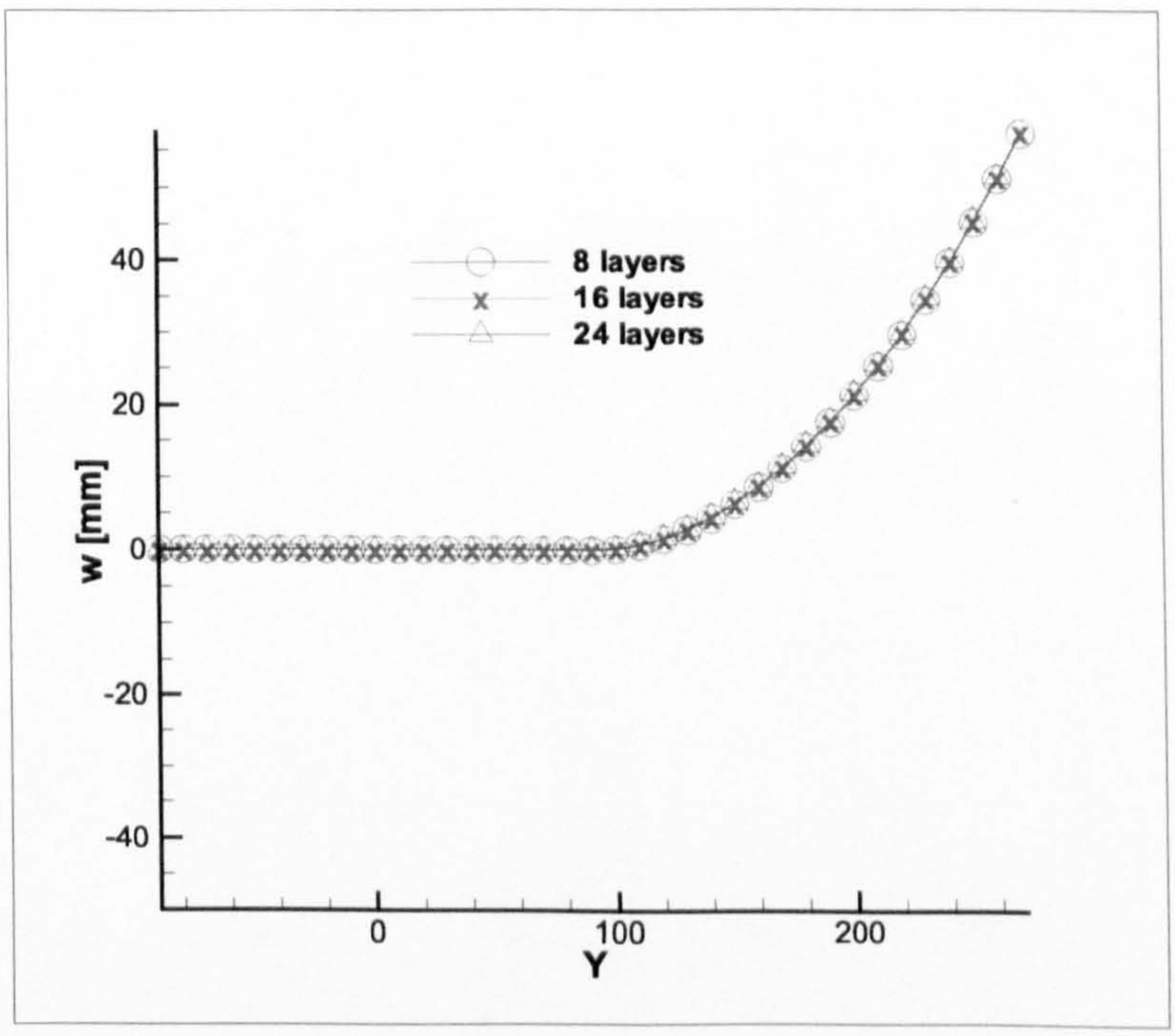

(c) Longitudinal cross-section for the curled configuration

Figure 3.13: Effects of the thickness variation for the symmetric part

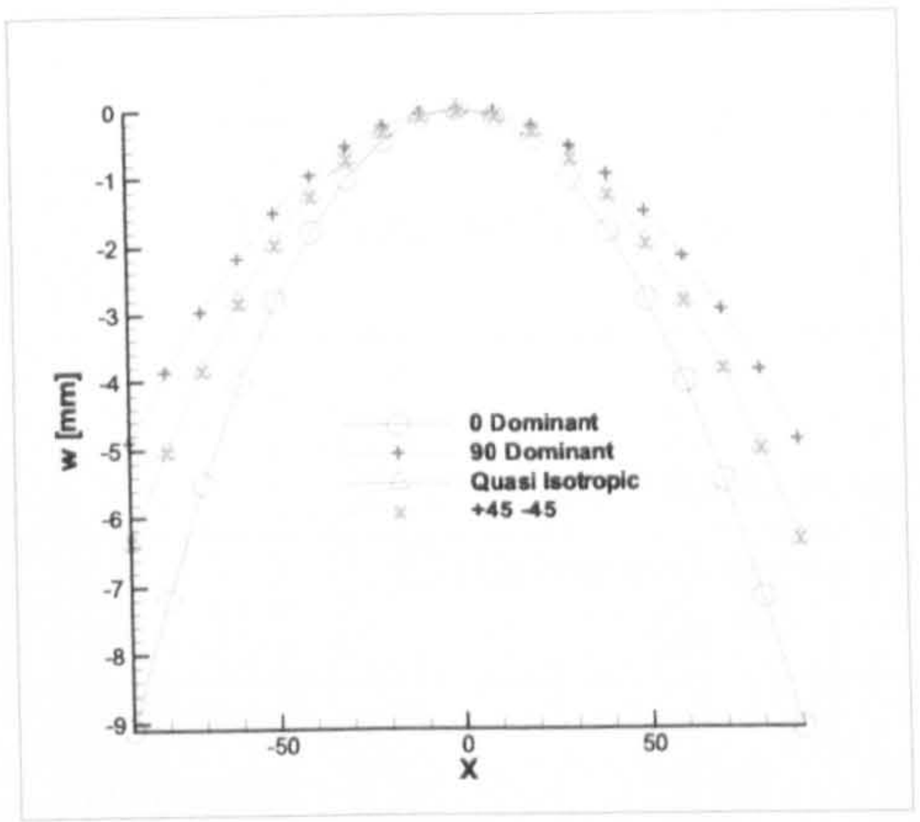

(a) Constrained cross-section

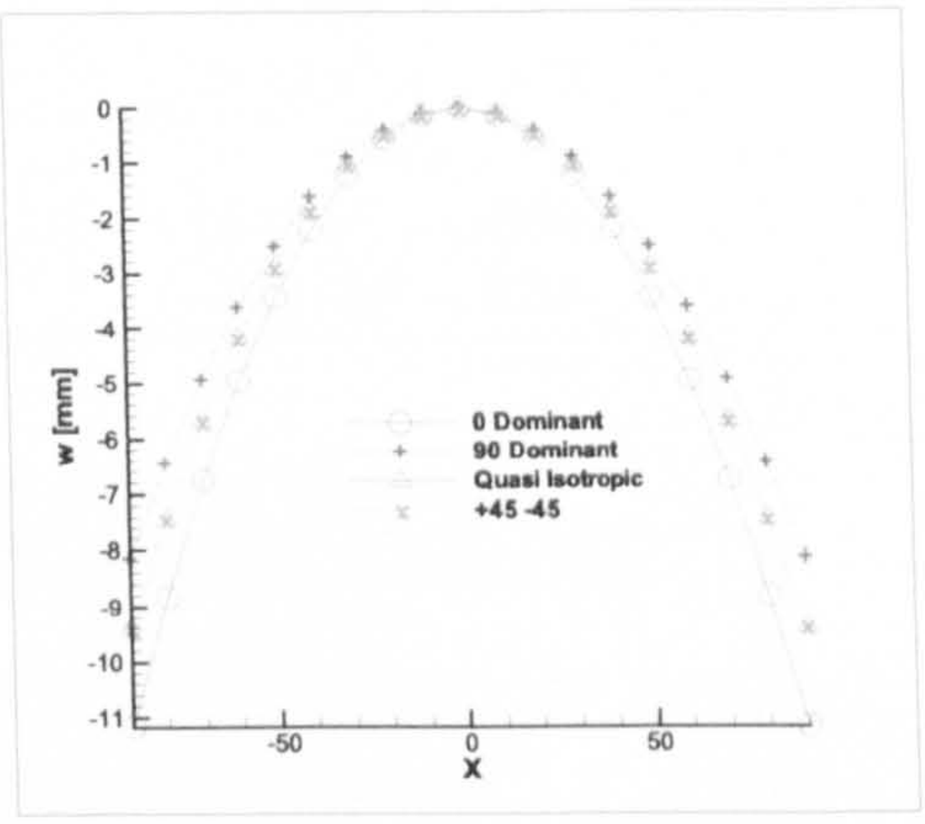

(b) Unsymmetric edge cross-section

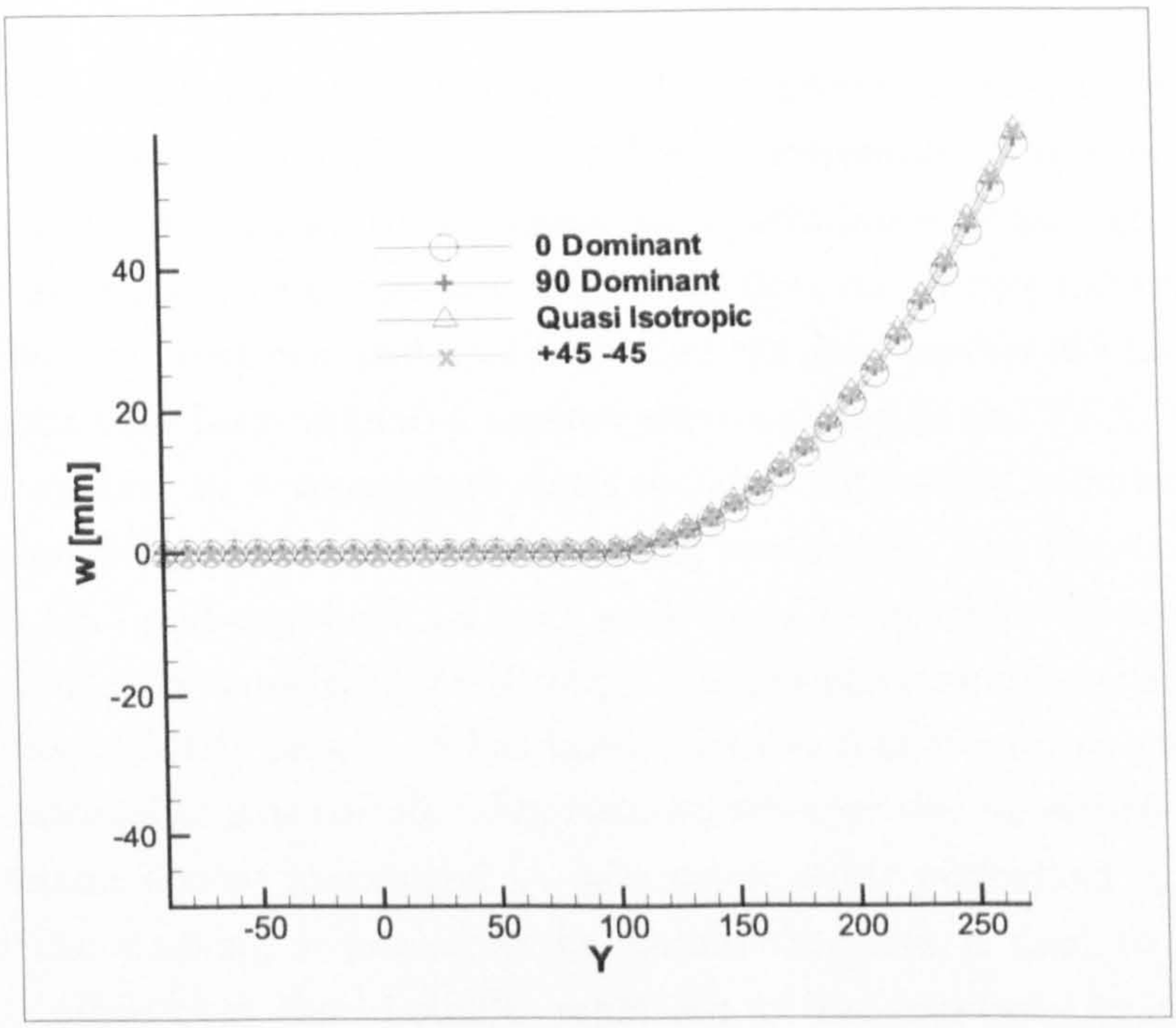

(c) Longitudinal cross-section for the curled configuration

Figure 3.14: Effects of different laminates for the symmetric part

Table 3.1: Curvature and strain energy value comparison for the square plate

		Hyer's Model $[m^{-1}]$	Extended Model $[m^{-1}]$
Configuration 1	Π	-0.874	$-.878$
	k_x	-3.52	$-28.02y^2 - 3.58$
	k_y	0.04	$-28.02x^2 + 0.0089$
Configuration 2	Π	-0.874	$-.878$
	k_x	0.04	$-28.02y^2 + 0.0089$
	k_y	-3.52	$-28.02y^2 - 3.58$

Table 3.2: Transverse curvature k_x for different thicknesses

	Constrained cross-section $[m^{-1}]$	Δ %	Unsymmetric cross-section $[m^{-1}]$	Δ %
8 layers	-1.25	37.2	-2.03	60.5
16 layers	$-.67$	20	-2.04	60.9
24 layers	-0.33	9.8	-2.03	60.5
Reference:	***Square plate*** k_x		-3.351	

The model is aimed at helping the preliminary design phases of unsymmetric laminates and is based on an empirical approach that relies on experimental tests to validate the results. The goal was to extend previous analytical techniques by adding the capability to map curvatures that are non-constant within the domain. A new formulation for the displacement field is undertaken and used to predict the deformation of a bi-stable square plate. The results have been validated against previous models and FEA. The extended model is then applied to a compound plate obtained by joining together two square plates with symmetric and unsymmetric stacking sequences. The results obtained are compared with FEA and experimental tests achieving a satisfactory agreement. Finally, the technique is used to investigate the effects of the boundary conditions on the bi-stable behaviour of unsymmetric panels. It has been observed that if one edge is constrained, the curvature parallel to it is considerably reduced whereas the curvature perpendicular to the edge remains almost unchanged. A parametric study performed by changing the thickness and the stacking sequence of the symmetric plate is used to confirm these results and to prove that the bi-stable behaviour of unsymmetric laminates is quite robust. This confirms that the integration of bi-stable patches within bigger structures could be a potential solution for the realisation of new structural systems where the requirement of flexibility and stiffness must be combined together.

Table 3.3: Transverse curvature k_x for different laminates

	Constrained section $[m^{-1}]$	Δ %	Unsymmetric section $[m^{-1}]$	Δ %
$[0_2^0/90_2^0]_{SYM}$	−1.25	37.2	−2.03	60.5
$[0_3^0/90^0]_{SYM}$	−2.25	67.1	−2.76	82.2
$[90_3^0/0^0]_{SYM}$	−1.21	36.1	−2.01	60.1
$[45^0/-45_2^0/45^0]_{ANTISYM}$	−1.56	46.6	−2.32	69.2
$[45^0/-45^0/90^0/0^0]_{SYM}$	−1.56	46.6	−2.32	69.2
Reference:	***Square plate*** k_x		−3.351	

3.2 Numerical modelling

This section presents a numerical procedure to model the non-linear flexural response of laminates that have piecewise variation of lay-up in the planform, using finite element analysis. Attention is focused on the effects that thermal stresses have on the potential multiple shapes of a composite structure. As addressed in previous sections, the multiple equilibrium configurations which unsymmetric laminates exhibit may present difficulties in the analysis. In static analyses, numerical solutions are often coaxed to converge into one or the other branch of the solution. A methodology to overcome this problem is presented. Such modelling is necessary to allow for the application of multistable composite within morphing aircraft structures as multistable composites could provide a viable solution for the realisation of shape-adaptable structures.

3.2.1 Cool-down and equilibrium shapes

The presence of multiple equilibrium states implies that during the cooling process a singular point in the equilibrium path of the structure is encountered. Within ABAQUS^{TM} the incremental formulation of the finite element approach to non-linear analysis (as shown in Fig. 3.15) is [Bathe, 1982], [Fujikake, 1985]

$$K(t)\Delta U = P(t+\Delta t) - I(t) \tag{3.17}$$

where $K(t)$ is the tangent stiffness matrix of the finite element model at time t (which is a function of the stress and displacement in the structure), $\Delta U = U(t+\Delta t) - U(t)$ is the vector of nodal incremental displacements, $P(t+\Delta t)$ is the vector of externally applied nodal loads at time $t+\Delta t$ (in this particular case, it is a function of the temperature) and $I(t)$ is the vector of nodal forces corresponding to the internal stress at time t. If the structure is in a state of stable equilibrium, $K(t)$ is positive definite (i.e. all of its

eigenvalues will be real and positive) whereas it is non-positive definite if the structure is in a state of unstable equilibrium (i.e. it allows the possibility of a zero eigenvalue). If a negative eigenvalue is found during the numerical simulation, the solution has jumped over a singular point and found an unstable equilibrium configuration. This may not affect the accuracy of the solution, but means that between two successive increments there exists a configuration for which the tangent stiffness matrix is singular, which is a condition typical of limit and bifurcation points. There are various strategies for dealing with this issue. For snap-through problems a dynamic scheme is the most suitable because this approach accounts for the inertial effects. However dynamic schemes can be expensive from the computational point of view and, as explained later, require a detailed description of the damping characteristics of the structure. For these reasons a different strategy, based on a modified static simulation, has been employed to perform the analysis, as detailed in Section 3.2.2.

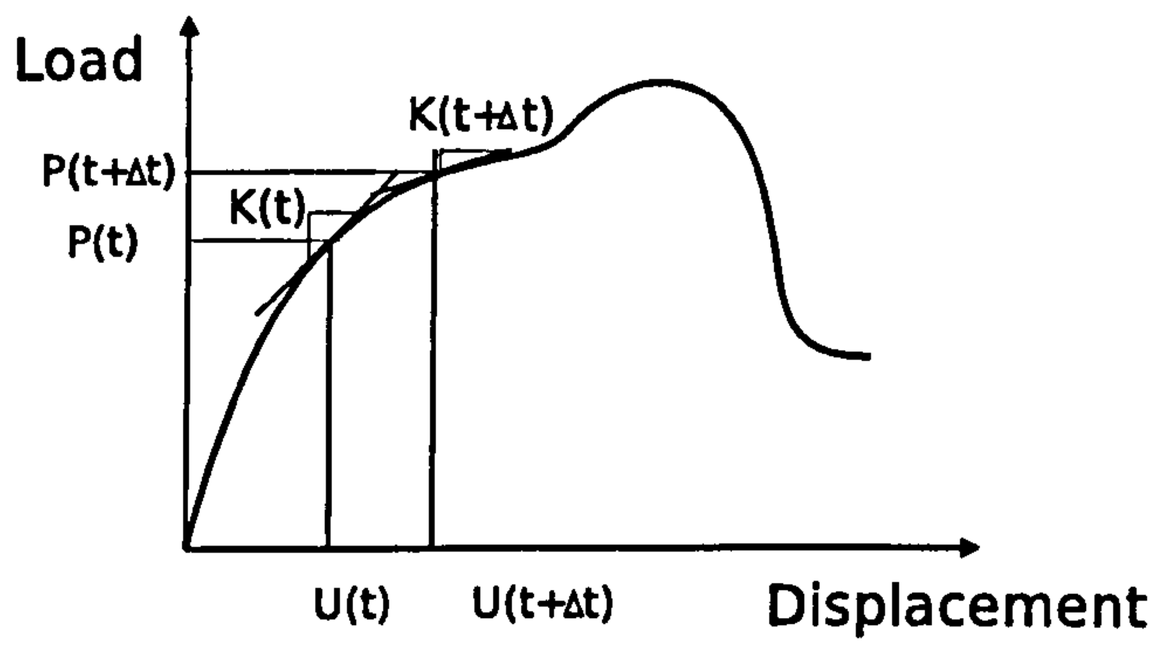

Figure 3.15: Incremental solution method

3.2.2 Solution strategies

The test panel analysed in Fig. 3.4, is now considered as a basis for the numerical analysis. The material properties used are still those shown in Table 2.1 while Fig. 3.5 shows the two stable shapes. The numerical simulation does not take into account irregularities in the internal structure due to the local variation in fibre tow thickness, direction and local resin content. For these reasons very thin laminates have been avoided as such effects are more evident and 4 and 8 layered plates have been chosen as a basis for the analysis. The numerical simulation is divided in two sections: the first reproduces the cool-down after the curing process and the second simulates the transition between the stable shapes obtained.

"Cool-down" simulation

The "cool-down" analysis predicts the various equilibrium configurations. The physical process itself takes a considerable time to complete (a few hours depending on the curing cycle that the material requires) and therefore it can be considered as a quasi-static process. The finite element analysis was performed with the commercial software ABAQUS^{TM}. A "`*Static`" step was used to perform a non-linear static analysis and a "`*Static stabilize`" step was used to perform the pseudo-dynamic non-linear analysis. The cool-down was simulated by applying an initial temperature of $140\,°C$ and a final temperature of $0\,°C$ to all of the nodes of the model. Mechanical loads are generated by the temperature difference and no external force is applied to the specimen. For this reason no significant velocities are developed and therefore this step can be modelled either statically or dynamically without a detailed definition of the damping properties of the material. The main difficulty, during the cool-down simulation, is presented by the existence of a bifurcation point given by a value for the temperature beyond which two solutions are possible. The general approach is to impose a geometric imperfection on the structure to coax the solution to converge to one configuration rather than the other. This approach generally works well for square plates where removing the double symmetry eliminates the bifurcation. However, for the chosen configuration there is no such symmetry and the sensitivity with respect to imperfections is smaller. Therefore a different method was required. It has been observed that the static algorithm converges to one equilibrium shape whereas the dynamic algorithm always converges to the other shape. This difference is due to the inertia contribution which the dynamic analysis accounts for and requires further explanation. Figure 3.16 shows the potential energy as a function of the temperature during the cool-down. Note that the potential energy of the flat configuration at the equilibrium is slightly higher than that of the curled configuration at the equilibrium ($2,322\ J$ for the flat configuration and $2,244\ J$ for the curled configuration). Since the initial conditions of the two analyses are exactly the same, a bifurcation in the diagram is expected. If the cool-down is simulated with a static algorithm, the potential energy of the plate is coincident with the strain energy as there is no other contribution.

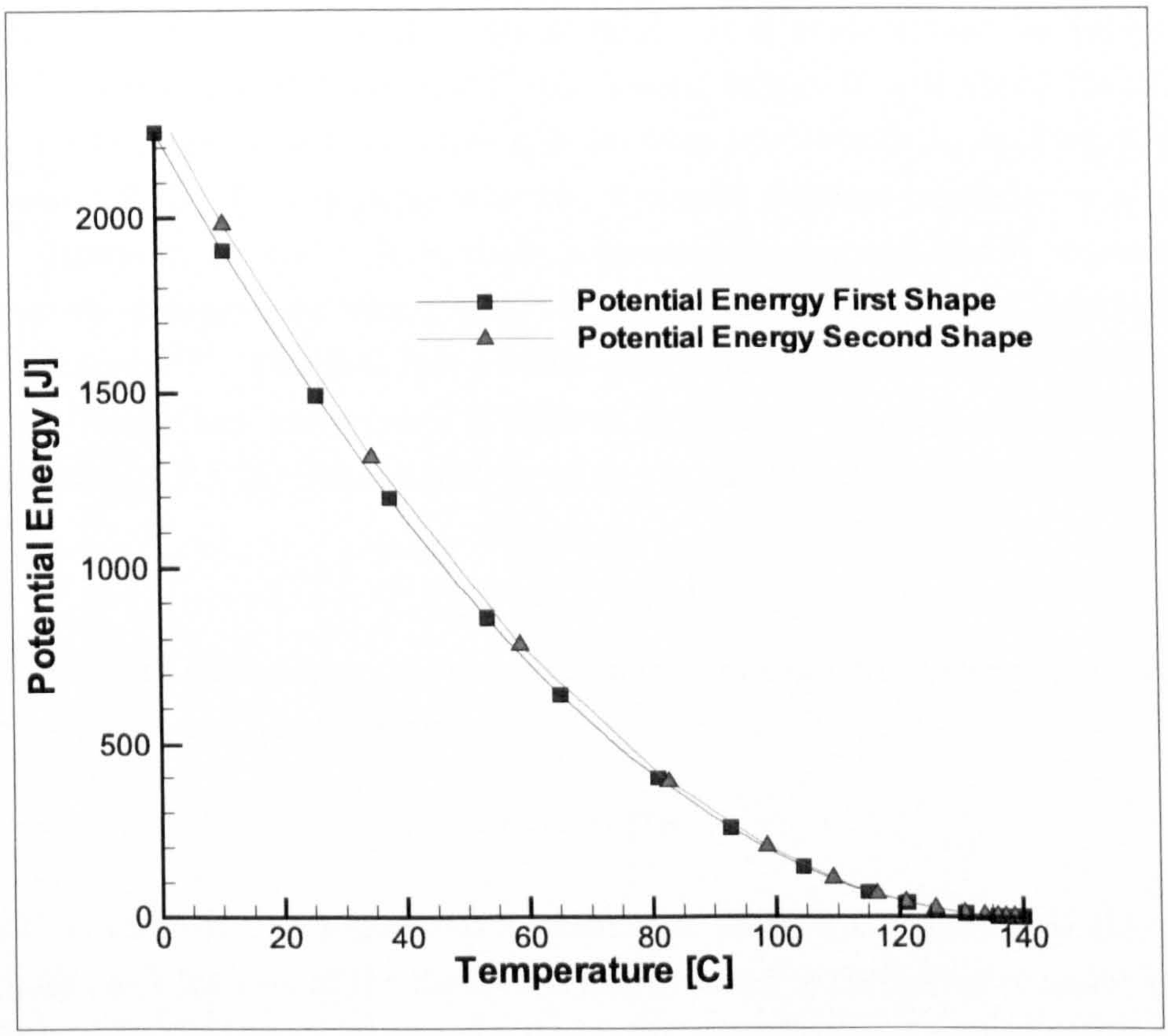

Figure 3.16: Potential energy versus temperature for the two equilibrium configurations

If the dynamic algorithm is used, the potential energy results from the strain plus the kinetic energy. In this way, two separate energy curves (that lead to the two different states) are obtained, the static curve always being below the dynamic one that converges to the higher equilibrium configuration because of the kinetic energy contributions. This is confirmed by the fact that when the dynamic algorithm is used, it is possible to coax the numerical scheme to converge to either shape by varying the mass density of the model. The final value of the potential energy in each configuration does not depend on the mass density. If the mass density is below a critical value, then the curled shape is always obtained since the kinetic energy is not sufficient to trigger the jump between the two solution branches. If the mass density is above the critical value, the kinetic energy will then be greater than the difference in the energy curves and a switch is then possible. This is clearly shown in Fig. 3.17 where the dashed line represents the difference between the potential energies (i.e. the potential energy of the flat shape minus the potential energy of the curled shape). The lines with circles and those with triangles represent, respectively, the kinetic energy for values of the

mass density below and above the critical value. It is evident that for values of the temperature between $130°C$ and $135°C$, the kinetic energy is well above the difference between the two curves and therefore a jump from one branch to another is possible (see Section 3.2.3). This explains why the dynamic schemes converge to a different solution. However, as said before, these schemes are computationally expensive and an alternative strategy was found with the pseudo-dynamic solution implemented in Abaqus/Standard^{TM}. This is in fact a static algorithm that adds viscous forces to damp local instabilities when convergence is difficult to achieve. The automatic stabilisation, implemented in ABAQUS/Standard^{TM}, adds viscous forces to the global equilibrium equation:

$$P - I - F_v = 0 \tag{3.18}$$

where P and I are respectively, the external and the internal force vectors. F_v represents the viscous forces and has the form of

$$F_v = cM^*v \tag{3.19}$$

where M^* is the artificial mass matrix calculated with unit density, c is the damping factor chosen as a fraction of the dissipated energy and v is the vector of nodal velocities. In this way, since the mass density is fixed to unity, the additional control on the potential energy is obtained by the viscous forces. It is then possible to converge to either of the equilibrium states by modifying the amount of artificial damping used. Differently from the dynamic schemes, the accuracy of the pseudo-dynamic approach can be affected by the amount of damping used. To ensure accuracy it is important to choose c as the smallest value that suppresses the local instabilities (values of the damping coefficients are shown in Table 3.4). This is done by increasing its value until the 'negative eigenvalue warnings' disappear (i.e. no singular point is encountered). The contour plots in Fig. 3.18, show the distribution of the viscous dissipation energy and the total strain energy of the model. Figure 3.19 shows a comparison of the two energies for an element on the top left corner of the plate, where the viscous forces reach their maximum value. It can be observed that this value does not exceed 4% of the total strain energy and therefore it can be stated that the artificial damping is not affecting the global accuracy of the solution. The dynamic analysis, whether it uses the explicit or the implicit integration scheme, has been shown to converge to the same equilibrium shape as in the pseudo-dynamic analysis.

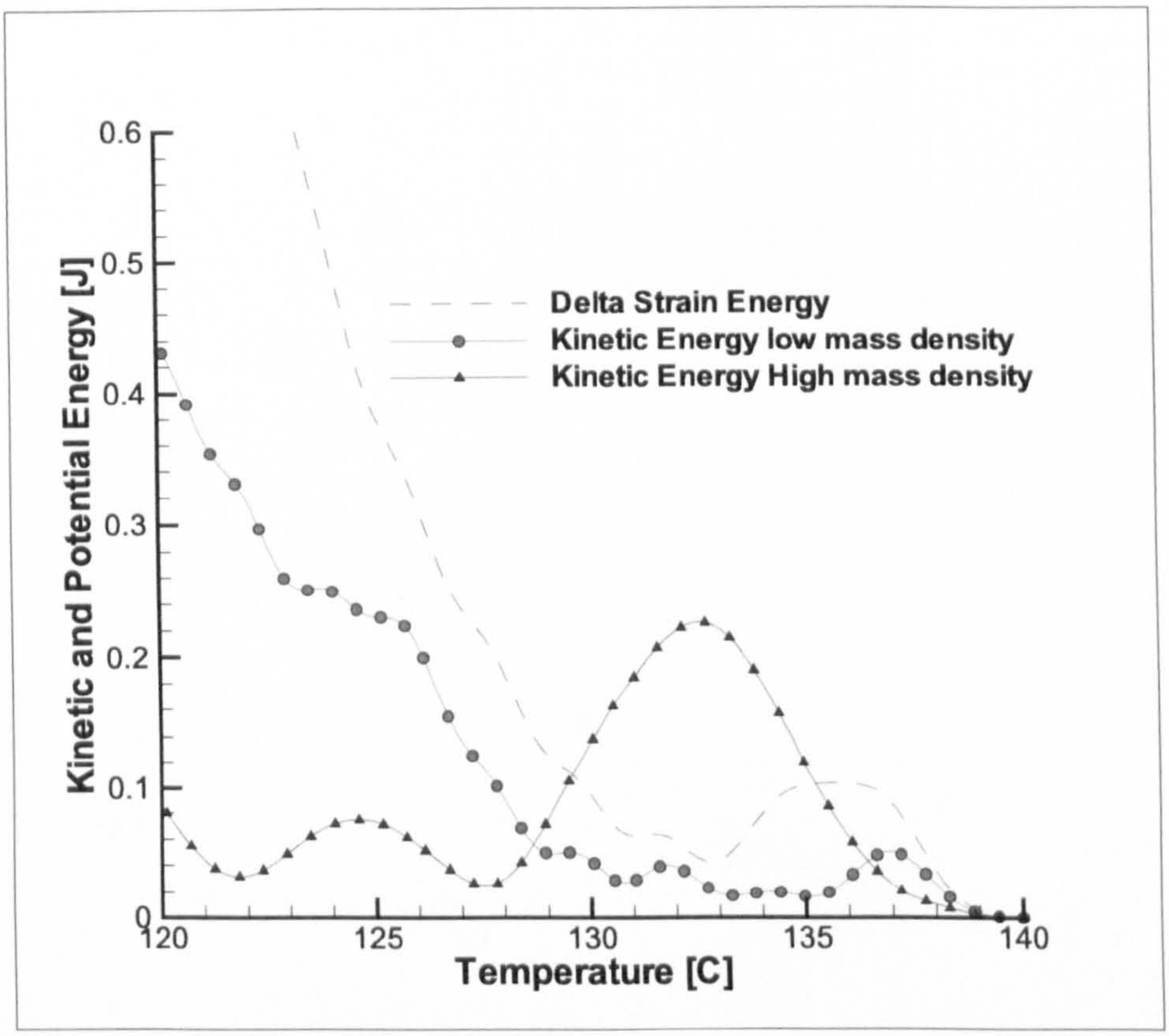

Figure 3.17: Effects of the inertia on the kinetic energy contribution

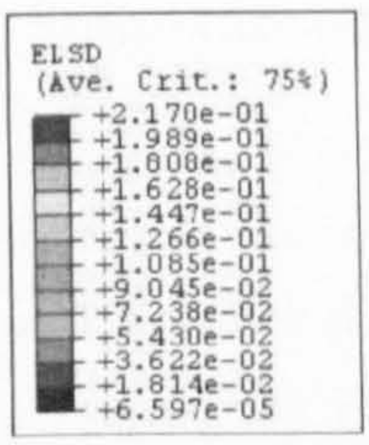

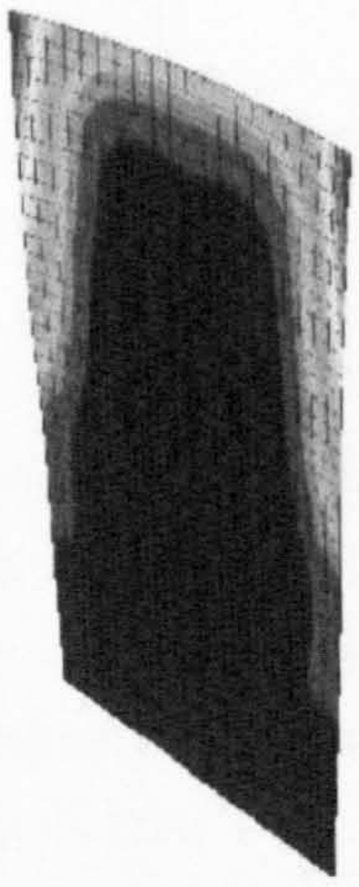

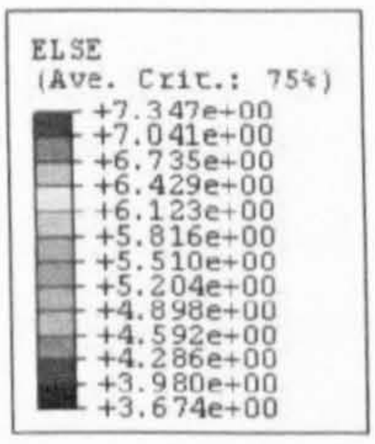

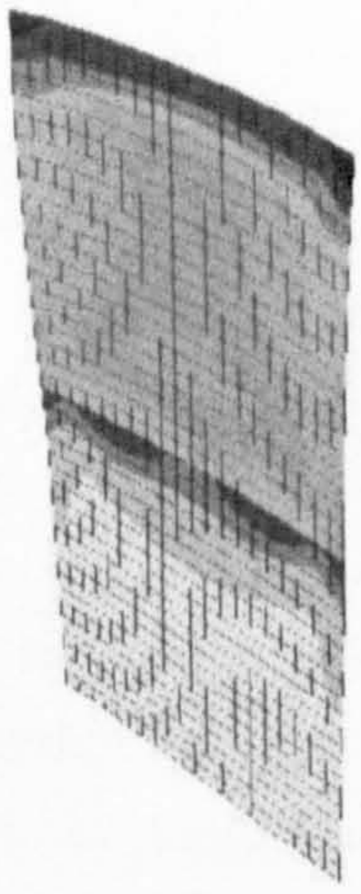

Figure 3.18: Contour plot of the viscous dissipation energy and of the total strain energy

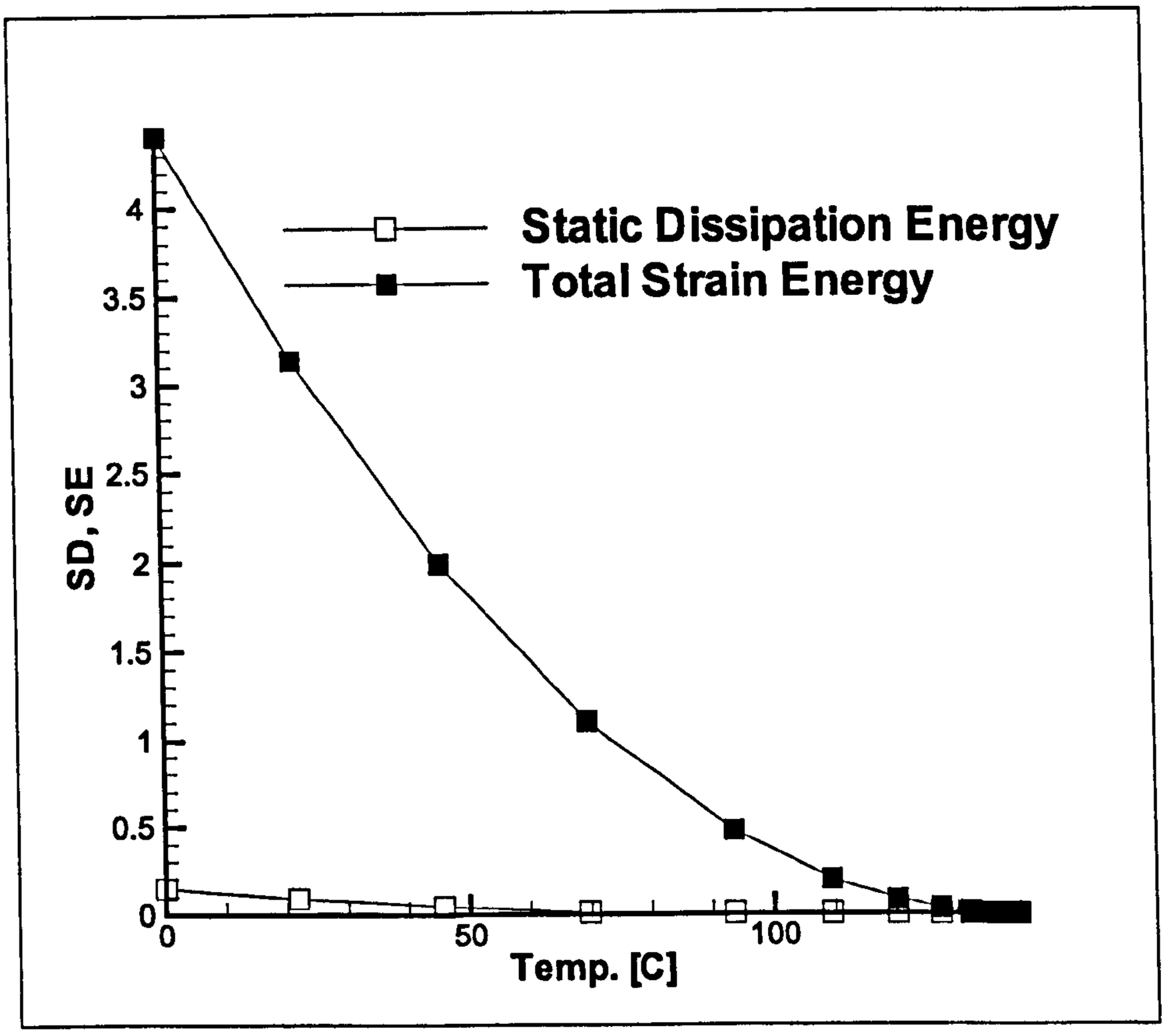

Figure 3.19: Viscous damping energy and total strain energy comparison

"Snap-through" simulation

The "snap-through" analysis describes the elastic response of the structure when loaded with a concentrated force. The plate is now simply supported at the four corner nodes and a vertical force is applied at the centre of the unsymmetric part to simulate the actuator, as shown in Fig. 3.20. During the application of the load, the structure will first deform elastically (i.e. a linear relationship between force and displacement). When the force reaches a critical magnitude, the structure will buckle and eventually rest in the other stable configuration once the load is removed. From the static point of view this problem represents an unstable collapse and "arc-length" methods are often considered to be the preferred tool. The arc-length method considers the magnitude of the applied load as an additional unknown whose value is determined together with the displacement, by solving a modified Newton-Raphson scheme. The approach is equivalent to a displacement-controlled analysis test and it has been successfully applied to describe the response of structures such as shallow arches [Cerini and Falzon, 2005].

However, for the panels analysed in this paper, the presence of the bifurcation and the relatively low stiffness of the plate, meant that the version of "arc-length" methods implemented in ABAQUS, did not prove sufficiently robust. More details on the results obtained with arc-length methods are provided in Appendix A. The pseudo-dynamic solution algorithm provided good results and good agreement was found when these results were compared with those from the explicit dynamic analysis. The next section presents a selection of the numerical results obtained.

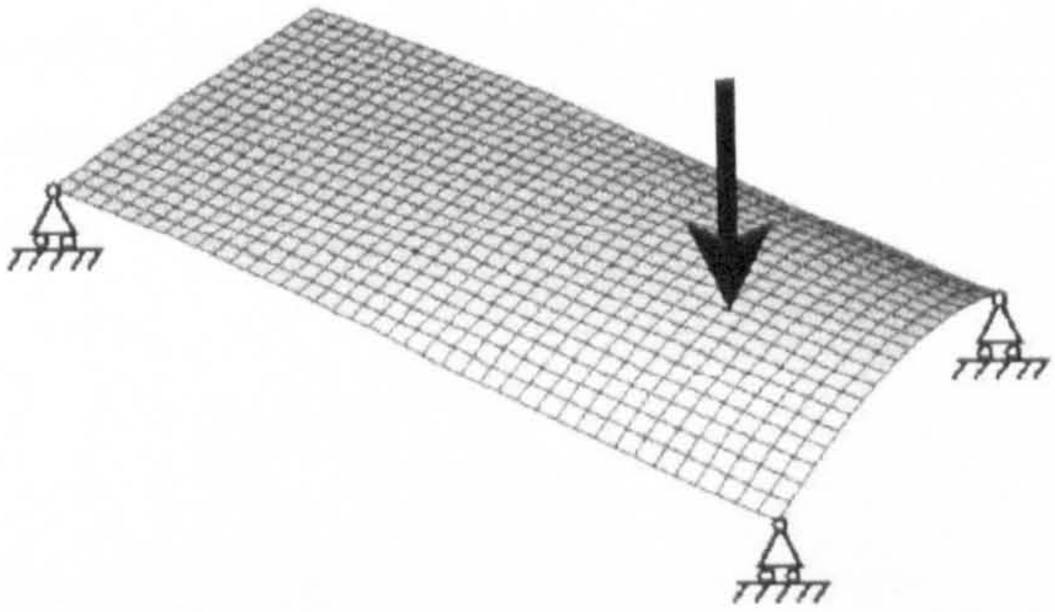

Figure 3.20: Boundary conditions for the 'snap-through' analysis

3.2.3 Prediction of equilibrium configurations with FEA

For static analysis the panel is modelled using 800 four noded shell elements ($S4R$), the number of nodes is 861 and the total number of degrees of freedom is 5166. To reduce the highest natural frequency and reduce the computation time, the dynamic analysis has been performed with a coarser mesh where the number of elements has been reduced to 200 elements ($S4R$), with 231 nodes and 1386 is the total number of degrees of freedom. The stacking sequence, for the different number of layers tested, is shown in Table 3.5. The plate is clamped in the geometric centre to suppress rigid body motions and to reproduce free-free boundary conditions. The predicted equilibrium configurations at room temperature are shown in Fig. 3.21a and Fig. 3.21b. A comparison with Fig. 3.5 shows an overall good agreement with the experimental shapes for the 8 layered plate. The finite element analysis and the experimental data are compared along the lines shown in Fig. 3.22. Figure 3.23 shows a comparison between the longitudinal cross-sections for the first and the second equilibrium configuration. The maximum difference reaches a local value of 8% for the curled configuration in the region close to the unsymmetric free-edge (right hand side of Fig. 3.23a). For the second equilibrium configuration the most critical area is the one close to the boundary between the symmetric and the unsymmetric part. Here the error reaches a maximum value of 8.5% (central part of

Fig. 3.23b). Figure 3.24 shows a comparison between the transverse cross-sections in the second shape. The same results for the 4 and 8 layered plates are shown from Fig. 3.25 to Fig. 3.27. In the deformed configurations, the unsymmetric portion of the panel exhibits a cylindrical deformation with generators either parallel to the x-axis (second shape) or to the y-axis (first shape). As explained previously, this is due to the unsymmetric stacking sequence that causes the structure to buckle under the thermal load. During the first few incremental iterations of the analysis, when the temperature change remains small (approximately 10 °C) and the displacements are within the linear range, the shell always deforms into a saddle configuration first (displacements are shown in Fig. 3.28). The equilibrium path then bifurcates and the two solution schemes converge to the different geometric shapes. This point is further clarified in the following section.

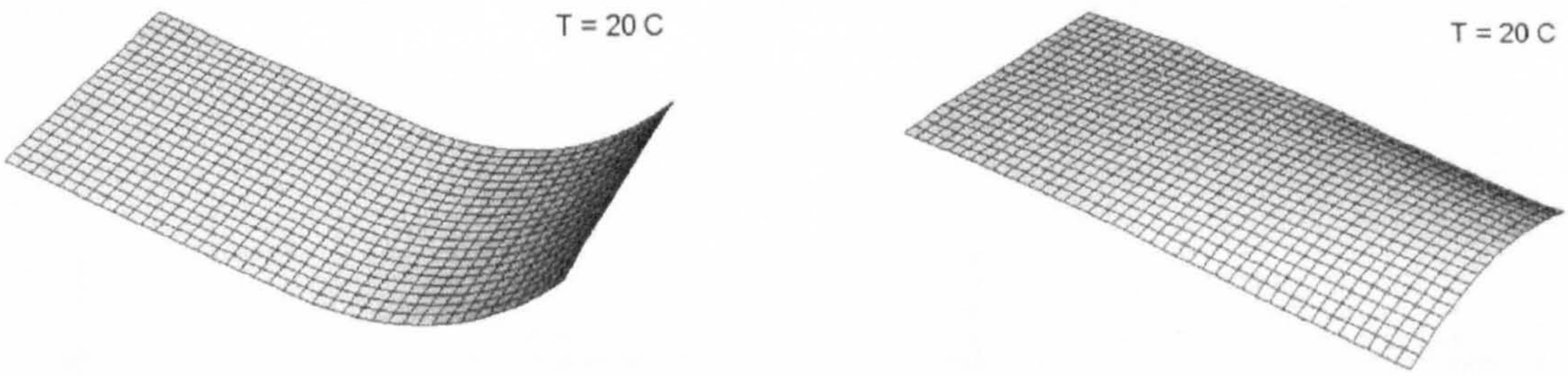

(a) First stable shape

(b) Second stable shape

Figure 3.21: Numerical equilibrium shapes

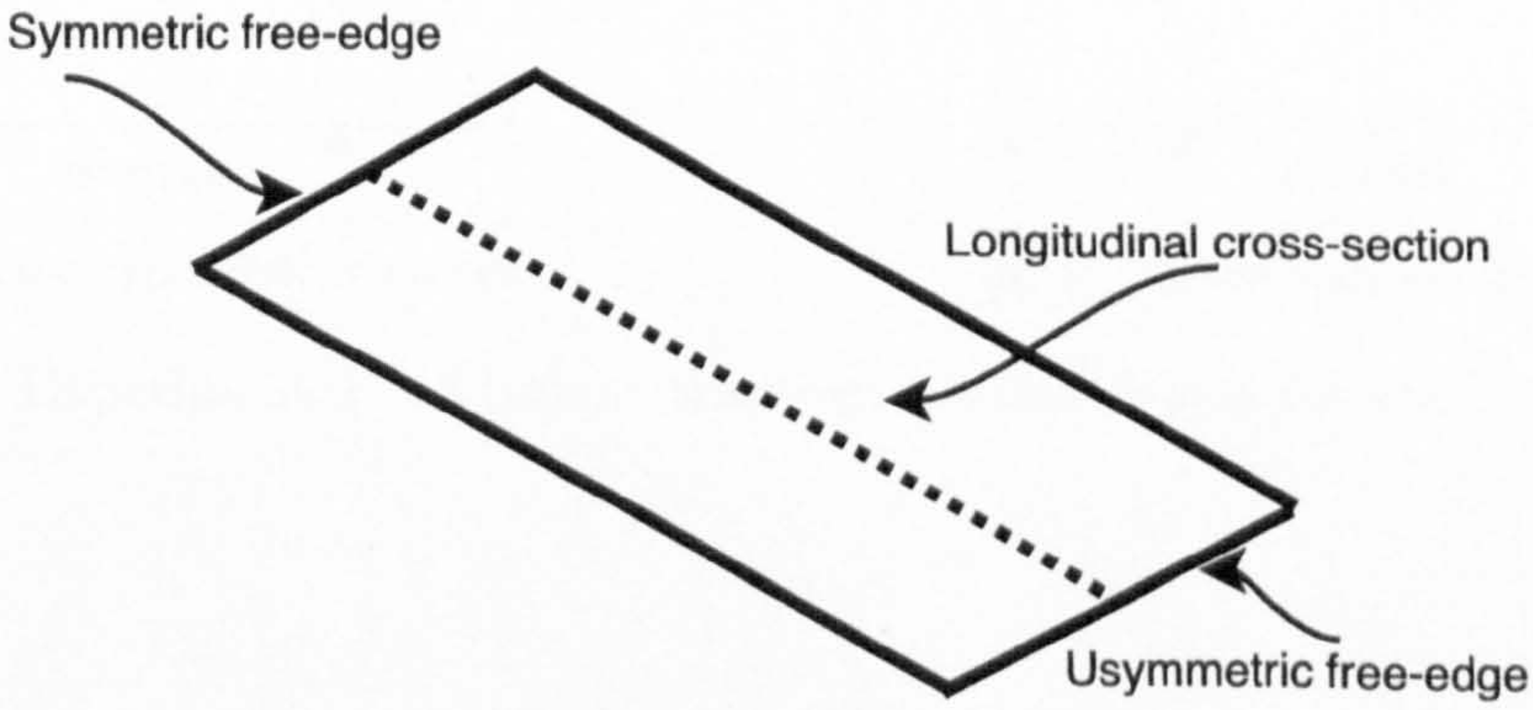

Figure 3.22: Position of the longitudinal and transverse cross-sections

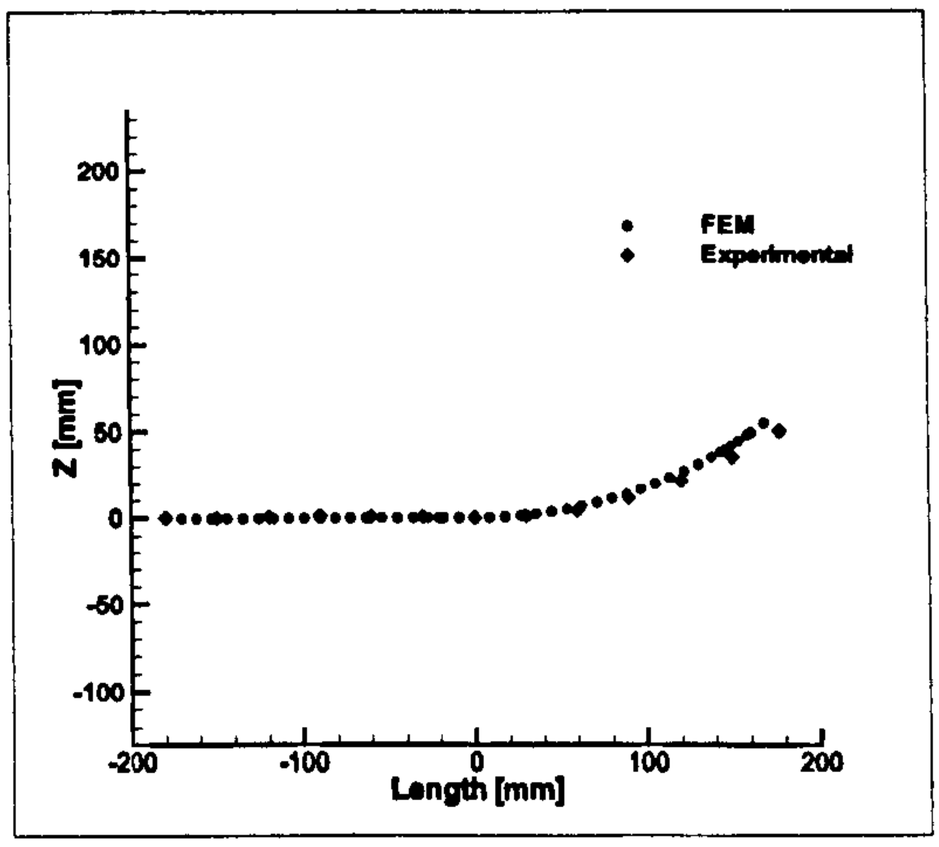

(a) 1^{st} shape

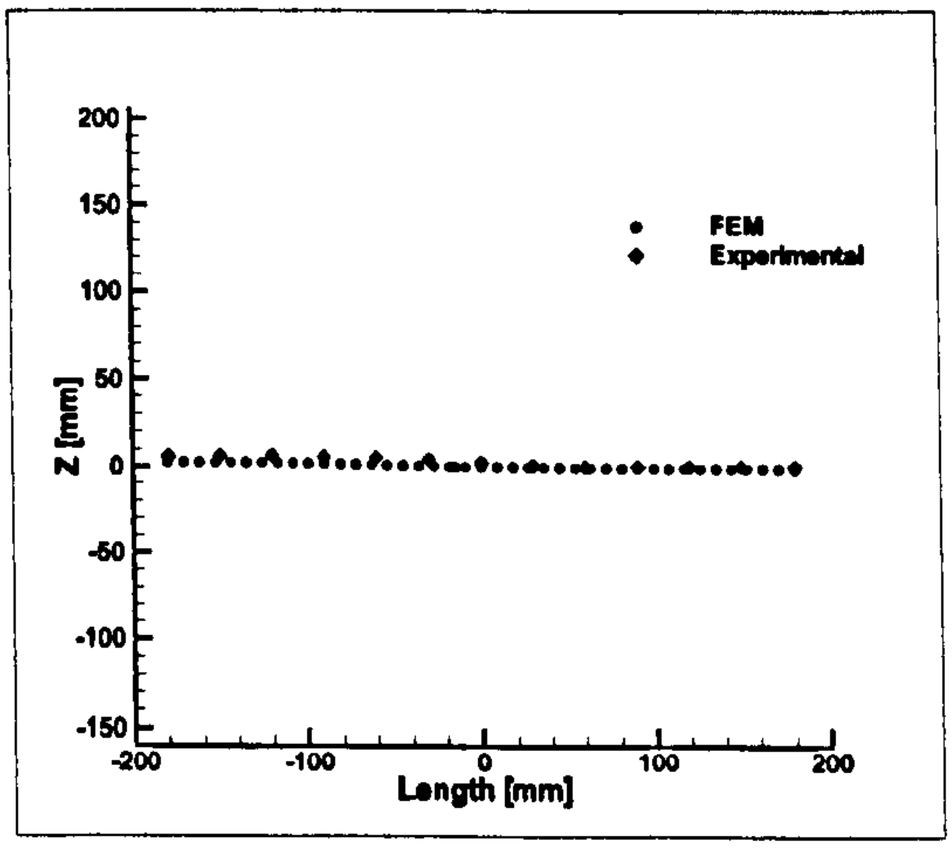

(b) 2^{nd} shape

Figure 3.23: Experimental validation: longitudinal cross-section for the 8-layered plate

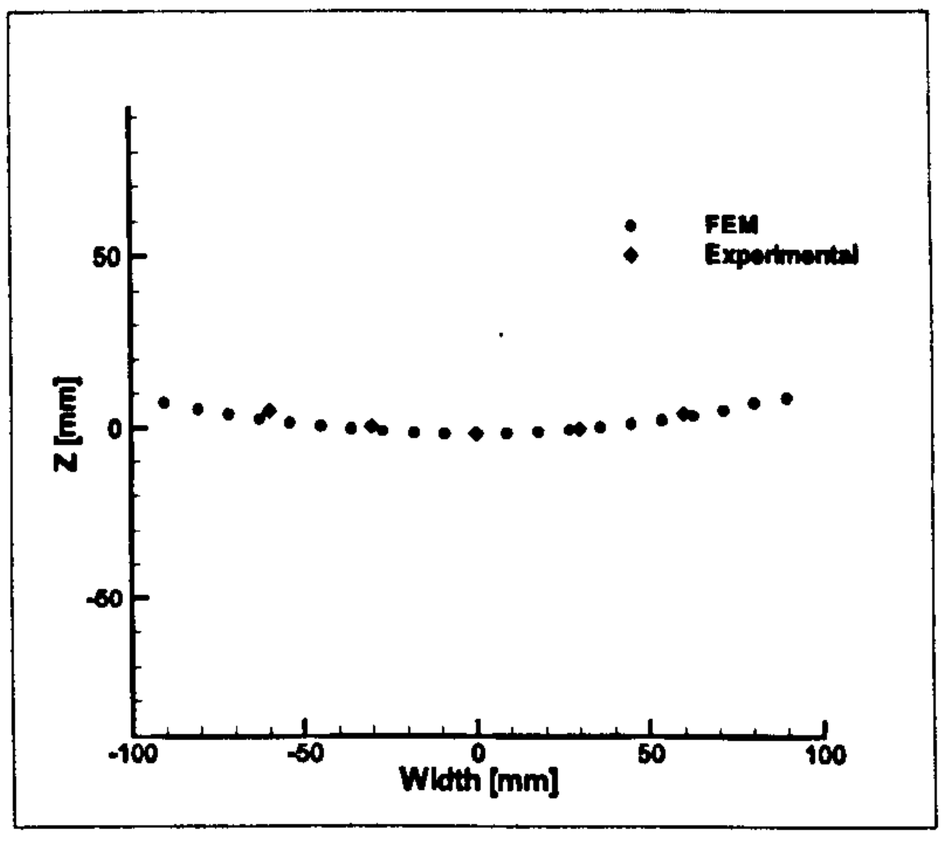

(a) 2^{nd} shape symmetric free-edge

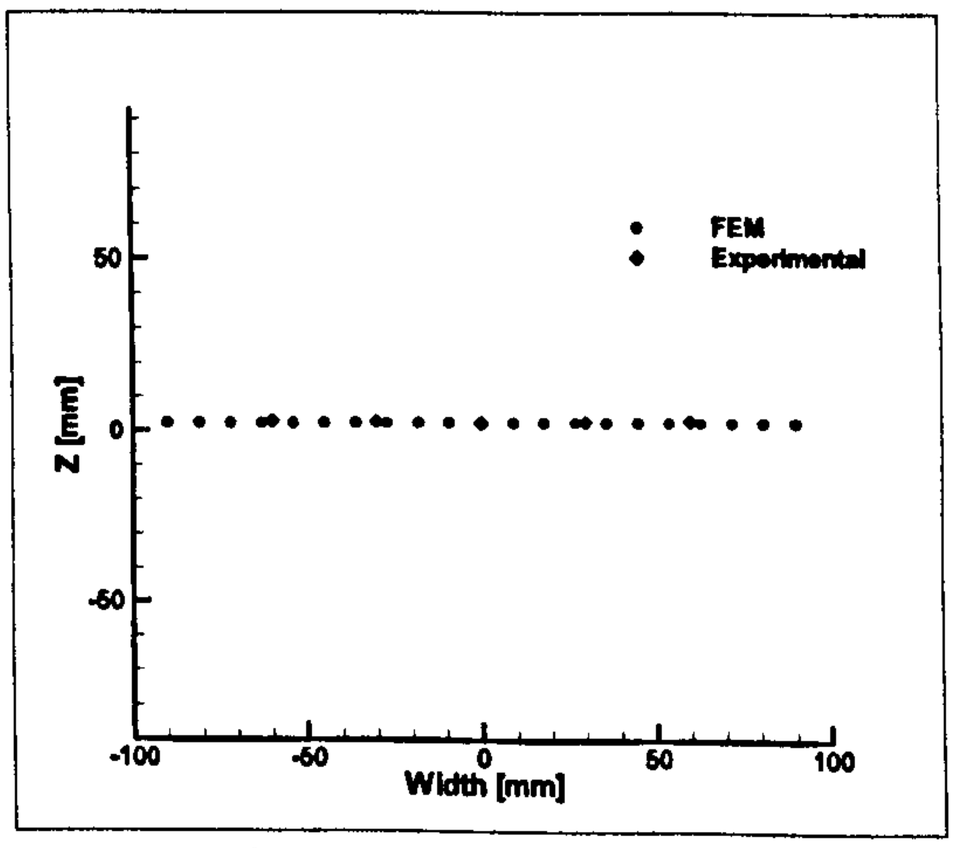

(b) 2^{nd} shape unsymmetric free-edge

Figure 3.24: Experimental validation: transverse cross-section for the 8-layered plate

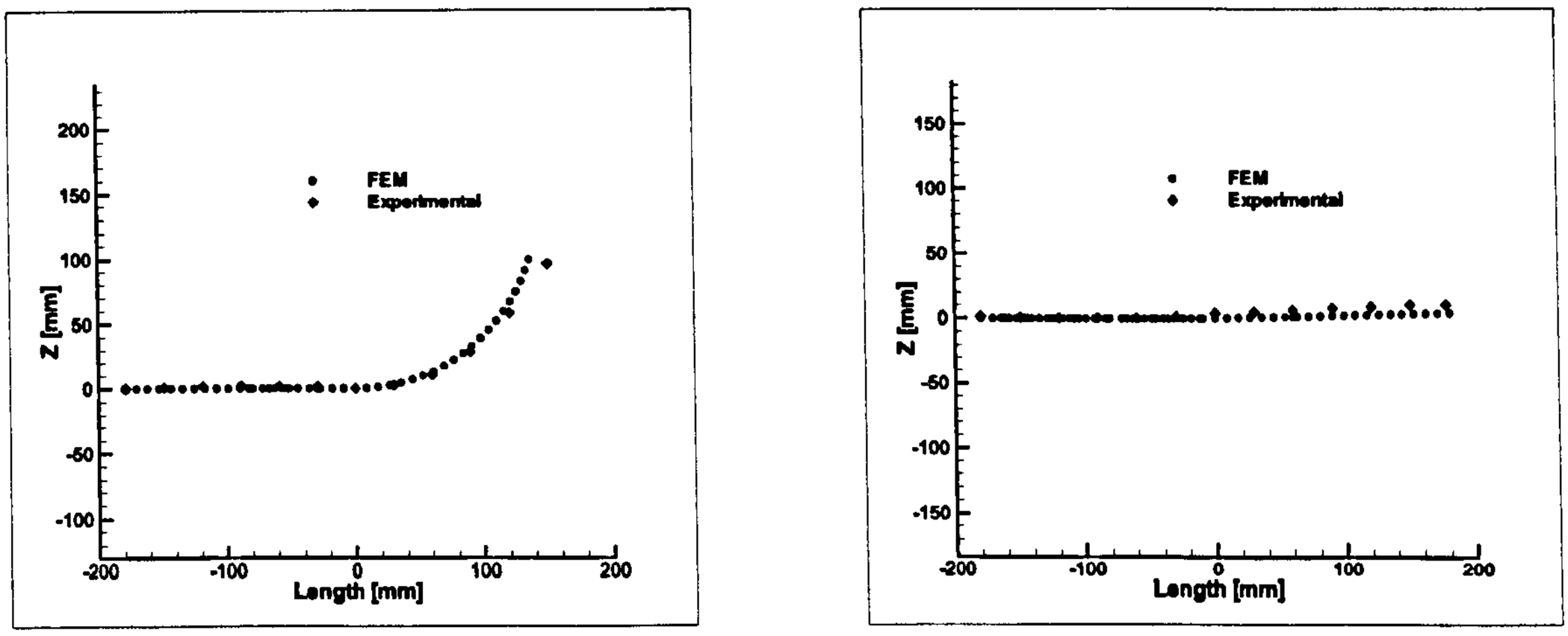

(a) 1^{st} shape (b) 2^{nd} shape

Figure 3.25: Experimental validation: longitudinal cross-section for the 4-layered plate

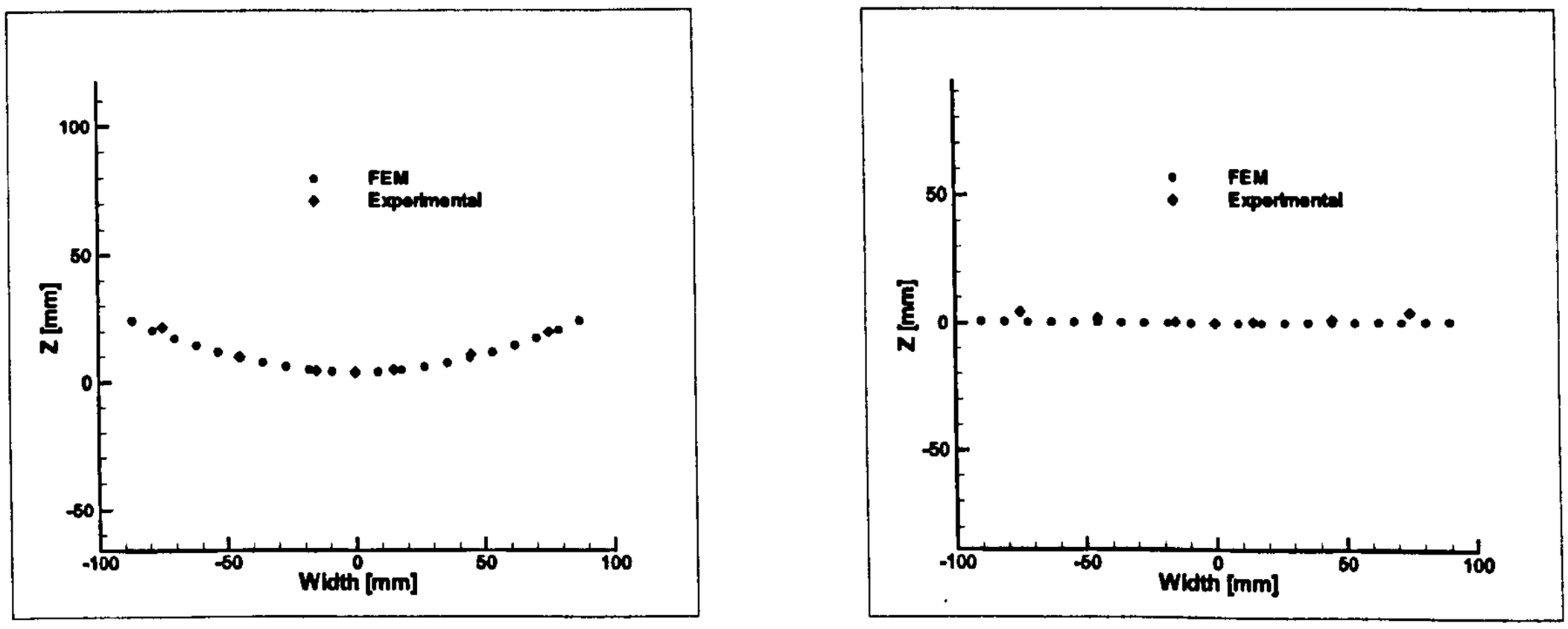

(a) 2^{nd} shape symmetric free-edge (b) 2^{nd} shape unsymmetric free-edge

Figure 3.26: Experimental validation: transverse cross-section for the 4-layered plate

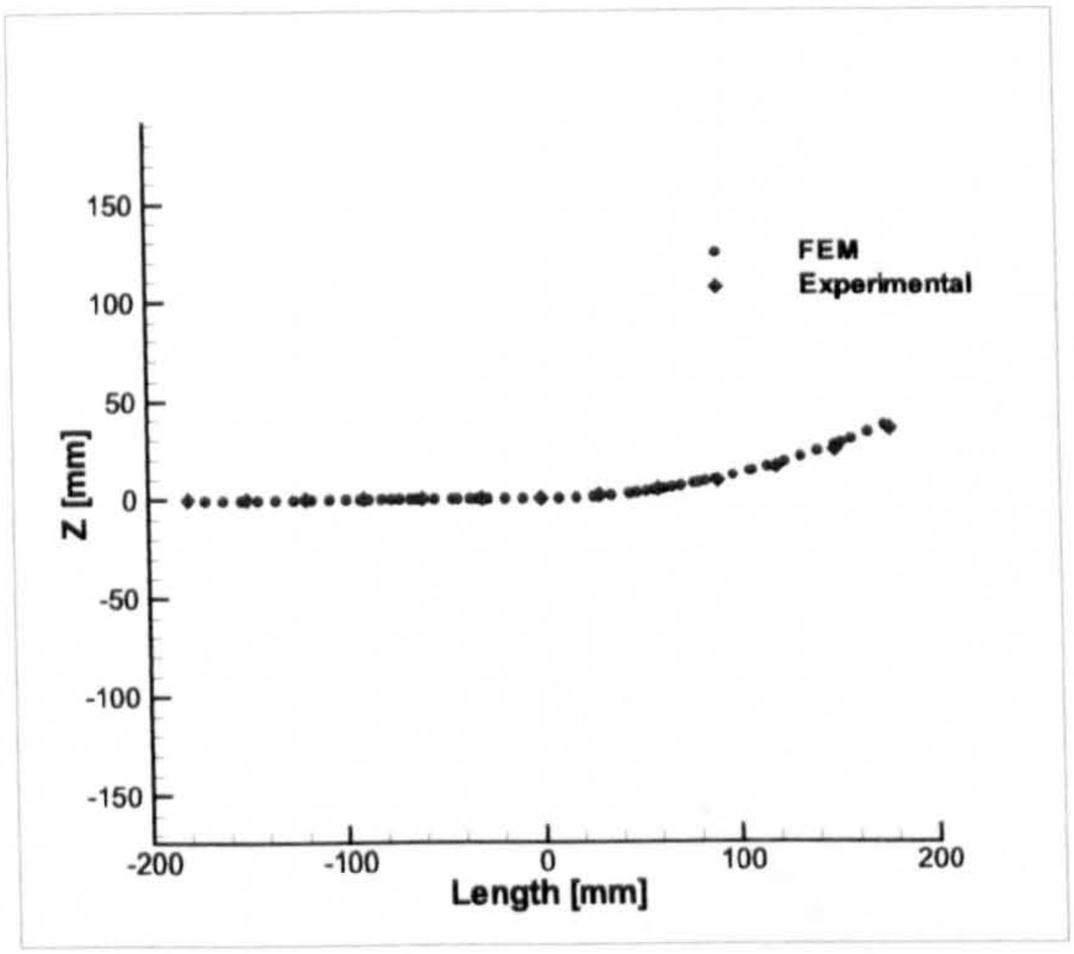

Figure 3.27: Experimental validation: 1^{st} shape longitudinal cross-section for the 12-layered plate

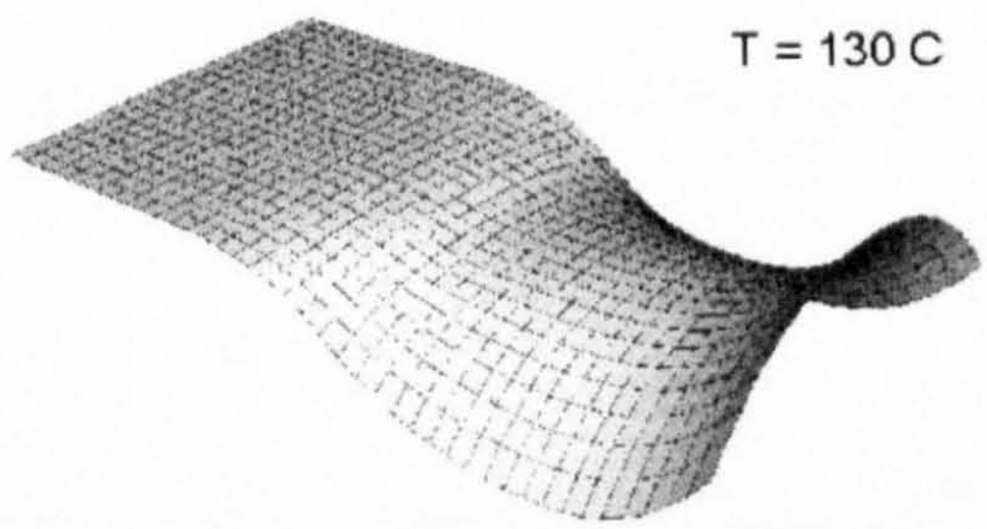

Figure 3.28: Initial saddle shape (displacements x 100)

Curvature - Temperature diagram

The temperature difference generates out-of-plane displacements in the plate that can be quantified in terms of principal curvatures (k_x and k_y). It is instructive to examine the principal curvatures of the unsymmetric portion of the panel. Fig. 3.29 and Fig. 3.30 show the curvature-temperature diagram for the 180×360mm panel, with different number of layers (4 and 8 respectively).

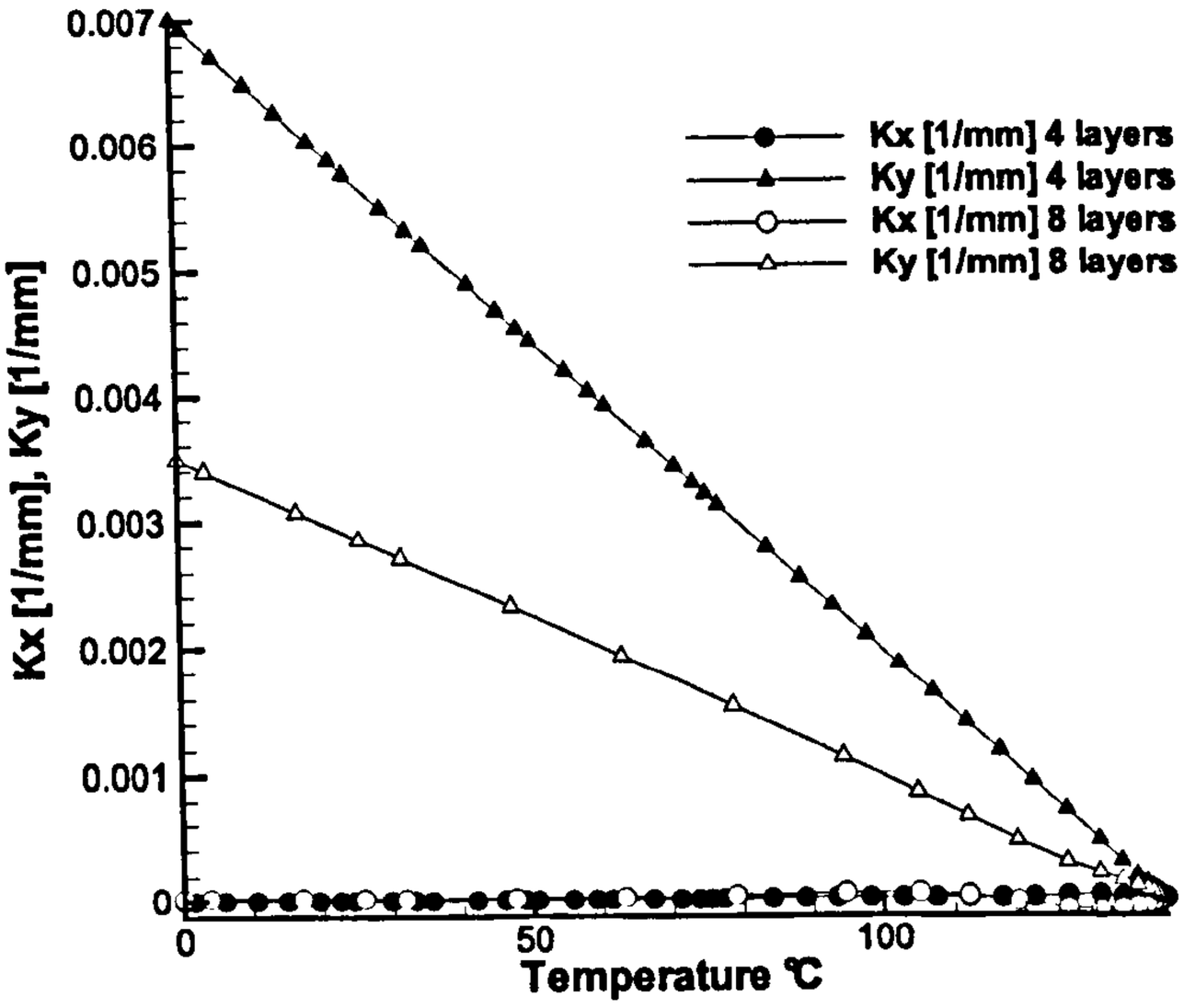

Figure 3.29: Principal curvature for the first shape

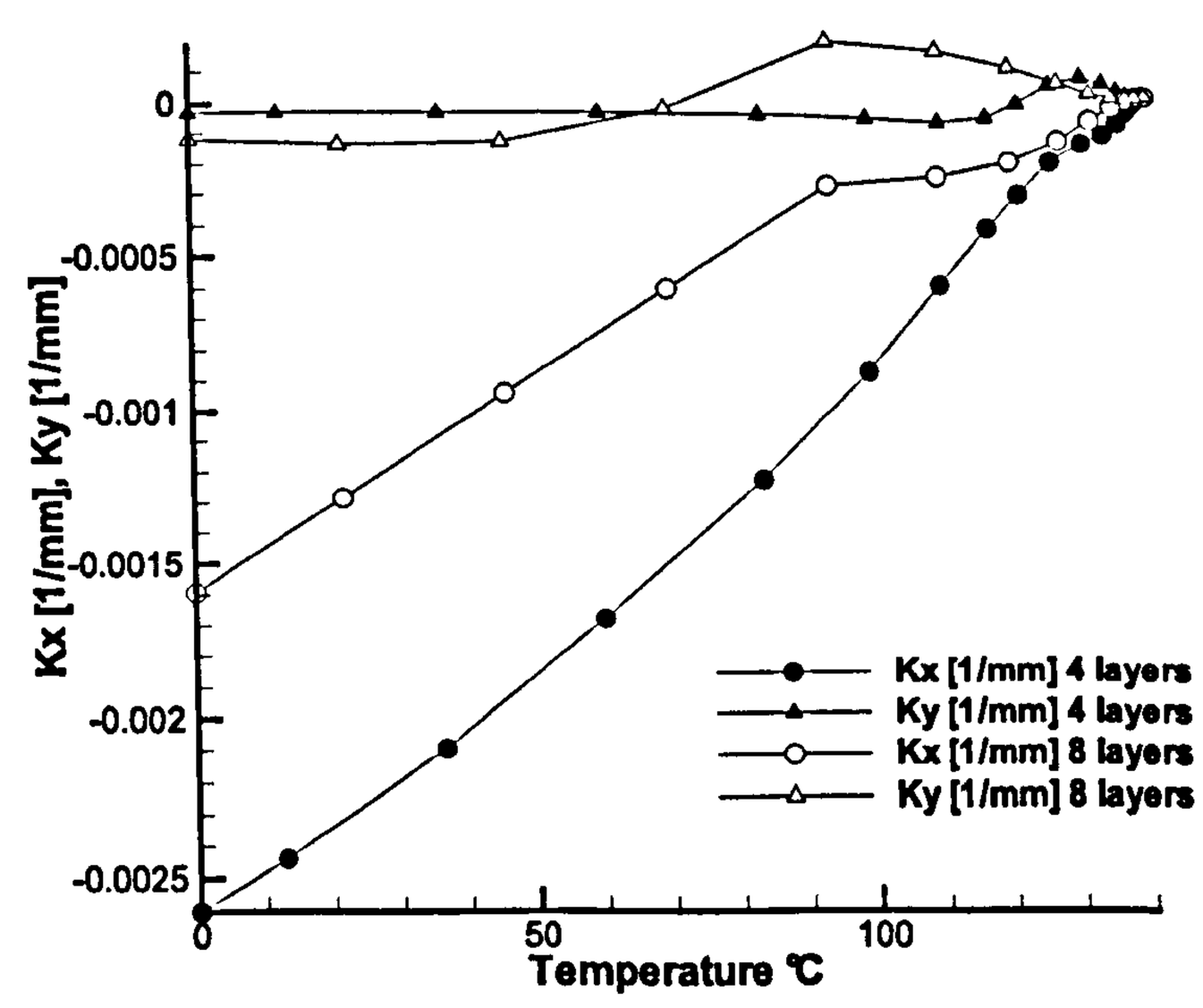

Figure 3.30: Principal curvature for the second shape

At 140 °C (right hand side of the diagram), the plate is flat; as soon as the temperature decreases, the deformations (i.e. the curvatures) start to develop; the final state is obtained when the temperature reaches 0 °C (left hand side of the diagram). The magnitude of the curvature depends greatly on the thickness of the plate and it decreases as the number of layers increases. The values shown in the diagrams are average values; however they are sufficient to describe the geometry in the two different states of equilibrium. Fig. 3.31 shows k_x and k_y versus temperature for the only configuration of the 12-layered plate, as it is too thick to have two equilibrium states. There is a critical value for the non-dimensional thickness t^*, (defined as the ratio between the thickness and the width of the plate) above which the shell does not have a bi-stable behaviour. The 8-layered plate is bi-stable and has a value for t^* of $\frac{1}{180}$ (5.5e-3). The 12-layered plate has t^* equal to $\frac{1}{120}$ (8.3e-3) and it is not bi-stable, therefore t^*_{cr} is an intermediate value between $\frac{1}{120}$ and $\frac{1}{180}$. Similar considerations regarding the non-dimensional thickness have been reported by Gigliotti et al. [2004]. Another important parameter, that can be obtained from the curvature-temperature diagrams, is the critical temperature T_{cr}: for $T > T_{cr}$, k_y is nearly equal to $-k_x$ and for each value of the temperature there will be only one possible configuration (i.e. the saddle configuration). For $T < T_{cr}$, there will be two solutions for each value of T, either $k_y \gg k_x$ (first cylindrical shape) or $k_x \gg k_y$ (second cylindrical shape). The value of T_{cr} is most easily identified in Fig. 3.32, where for convenience $-k_x$ is plotted. For the 8-layered plate T_{cr} is 93 °C whereas for the 4-layered plate T_{cr} is 130 °C. For values of the temperature above T_{cr}, the principal curvatures are nearly equal and opposite as expected for a saddle shape configuration. Below T_{cr} the difference between k_x and k_y diverges until an almost perfect cylindrical shape is achieved. Fig. 3.29 also shows a linear dependency of the principal curvatures with temperature when $T < T_{cr}$. This suggests that excluding the initial non-linear region of the diagram, the linear theory gives a good approximation of the major curvature of the unsymmetric part in the 1^{st} shape, where the constraint imposed by the symmetric part of the panel seems to have a marginal effect on the overall behaviour of the rectangular plate. When considering the first configuration, the displacements of the unsymmetric part match closely those of a 180 × 180mm unsymmetric plate with free edges and the same stacking sequence. Therefore the effect of the symmetric part is only to rigidly rotate the unsymmetric portion and when considering the curvature its effects can be neglected. This point is important as it suggests that stable "bi-stable states" may be represented in terms of a relatively simple, linear model. To show this possibility, values of the principal curvatures for a square unsymmetric plate are obtained with classical lamination theory and compared with those of the unsymmetric part obtained with the

non-linear finite element analysis. According to classic lamination theory, the stress resultants are related to the mid-plane strains and curvatures through (ref. to 2.1.3)

$$\begin{bmatrix} N + N^{th} \\ M + M^{th} \end{bmatrix} = \begin{bmatrix} A & B \\ B & D \end{bmatrix} \cdot \begin{bmatrix} \varepsilon^0 \\ k^0 \end{bmatrix} \tag{3.20}$$

By rearranging Eq. 3.20 and imposing zero mechanical loads N and M, the principal curvature vector may be expressed in terms of the thermal forces and moments as

$$k^0 = \left(-\left(D - BA^{-1}B\right)^{-1} BA^{-1}\right) \cdot N^{th} + \left(D - BA^{-1}B\right)^{-1} \cdot M^{th} \tag{3.21}$$

where the dependency on temperature change is contained within the terms N^{th} and M^{th} as shown by Eq. 2.25. All the other quantities are determined by the material properties and the stacking sequence and therefore are constant for a given laminate. From a closer inspection of Eq. 3.21 the curvature vector k^0 is linear with respect to ΔT and the slope can be computed as

$$\frac{dk^0}{d\Delta T} = \frac{d}{d\Delta T} \begin{bmatrix} k_x \\ k_y \\ k_{xy} \end{bmatrix} = \left(D - BA^{-1}B\right)^{-1} \left(-BA^{-1} \frac{dN^{th}}{d\Delta T} + \frac{dM^{th}}{d\Delta T}\right) \tag{3.22}$$

The $i-th$ component is

$$\frac{dk_i^0}{d\Delta T} = \sum_{k=1}^{N_l} \sum_{j=1}^{N} \left(Q_{ij}^{(k)}(h_k - h_{k-1}) + \frac{1}{2} Q_{ij}^{(k)} \alpha_j^{(k)} (h_k^2 - h_{k-1}^2)\right) \tag{3.23}$$

The values for k_x and k_y obtained with Eq. 3.21 and those of their slopes obtained with Eq. 3.23 are equal and opposite, as expected from the linear theory. However the analytical value of k_y closely matches the non-linear, numerical solution (a comparison is shown in Table 3.6). If a system of hypothetical external loads is imposed that eliminates the anticlastic curvature k_x =-k_y leaving the other curvature unchanged, then the resulting deformed shape would be very similar to that predicted with the non-linear FEA analysis. In this way the hypothetical external loads would represent the correction required to the linear theory to agree with the experimental observation. This simple result allows linear classical lamination theory to model deflections in the large displacement regime. Effectively, once the flat plate bifurcates upon cool-down into one of the cylindrical shapes, this shape responds linearly with temperature, and complicated non-linear modelling (to capture the bifurcation) is not required. Finally, it is noted that the small difference in computed values of the curvature's slope may be

attributed to localised non-linear effects, particularly those occurring in the vicinity of the critical temperature.

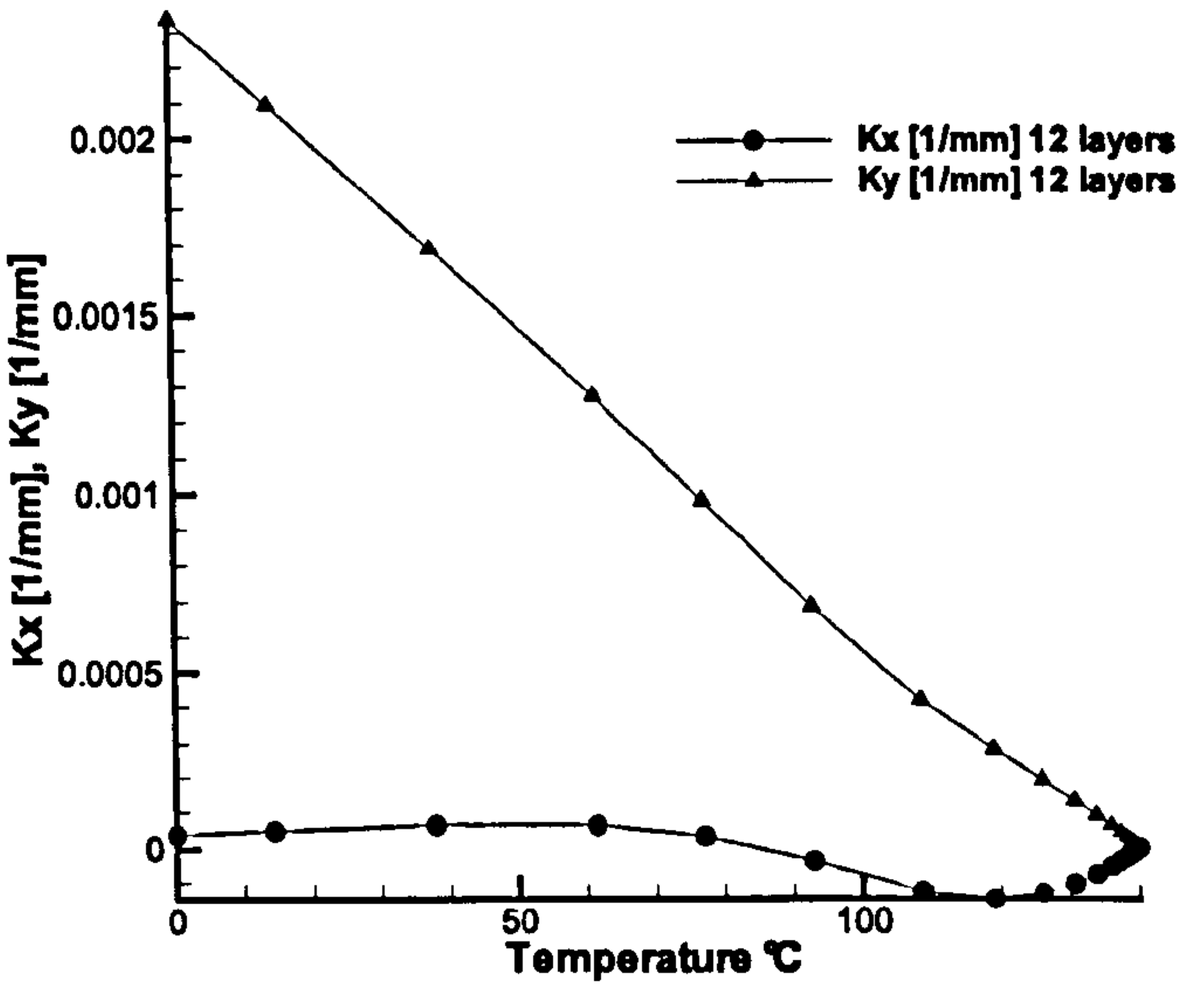

Figure 3.31: Principal curvature for the 12-layered plate

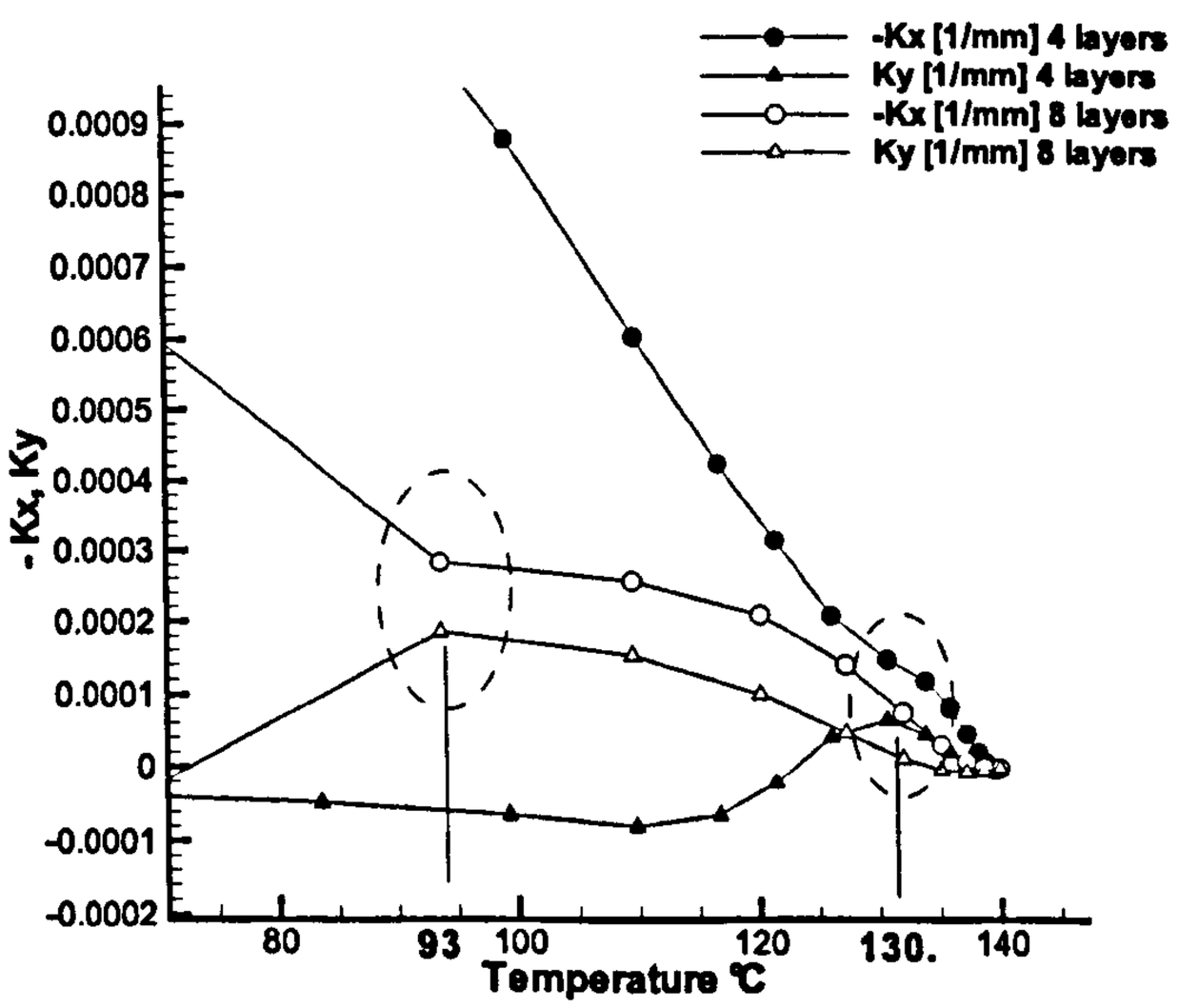

Figure 3.32: Identification of T_{cr}

3.2.4 Load - Displacement diagram

In this section the results of the snap-through analysis are presented. The aim of this analysis is to compute the maximum out-of-plane load that the panel can withstand before changing configuration. To obtain the load corresponding to the limit point, the cool-down of the plate is modelled first. Then in a second step, the following boundary and loading conditions are applied (see Fig. 3.20)

1. The four corner nodes of the shell are restrained from moving along the vertical axis.

2. The geometric centre of the unsymmetric part of the shell is constrained to move along the vertical axis.

3. A concentrated force, again parallel to the vertical axis, is applied to the centre of the unsymmetric part.

A '`*Static, stabilize`' step is then performed. This methodology is equivalent to the one used by Tawfik et al. [2007]. From the experimental point of view, this technique corresponds to a "load-controlled" test. A set of experiments were carried out to validate the numerical prediction of the loads. The Instron 3343 Single Column System was used to perform the snap-through. The load was applied through a steel rod connected to a 1 kN force transducer with a controlled speed ranging from $0.01m/s$ to $0.1m/s$. The load - displacement (i.e. reaction force - displacement) curves were then measured and compared against the numerical prediction. Fig. 3.33 shows the numerical load-displacement plot for the 180 × 360mm panel with different number of layers. It is noteworthy to mention that, during the mechanical tests, it is quite difficult to replicate the friction-less condition at the four corners, which is present during the numerical analysis. The friction between the corners of the panel and the metallic support can considerably affect the accuracy of the measured loads. Using lubricant oil considerably reduce this drawback but it is also very important to choose an appropriate speed for the application of the load. The speed needs to be low enough to minimise the inertial effects that are generated during the motion of the panel. During the tests, however, it has been noticed that if the speed was too low, the effects of the surface imperfection were somehow, amplified. It was found that for each test there was a speed for which the friction effects were minimised.

As expected, the critical load increases considerably with the thickness. In Table 3.7 the value of the numerical and the experimentally measured loads are reported. It must be noted that despite having a single stable equilibrium configuration, the 12-layered

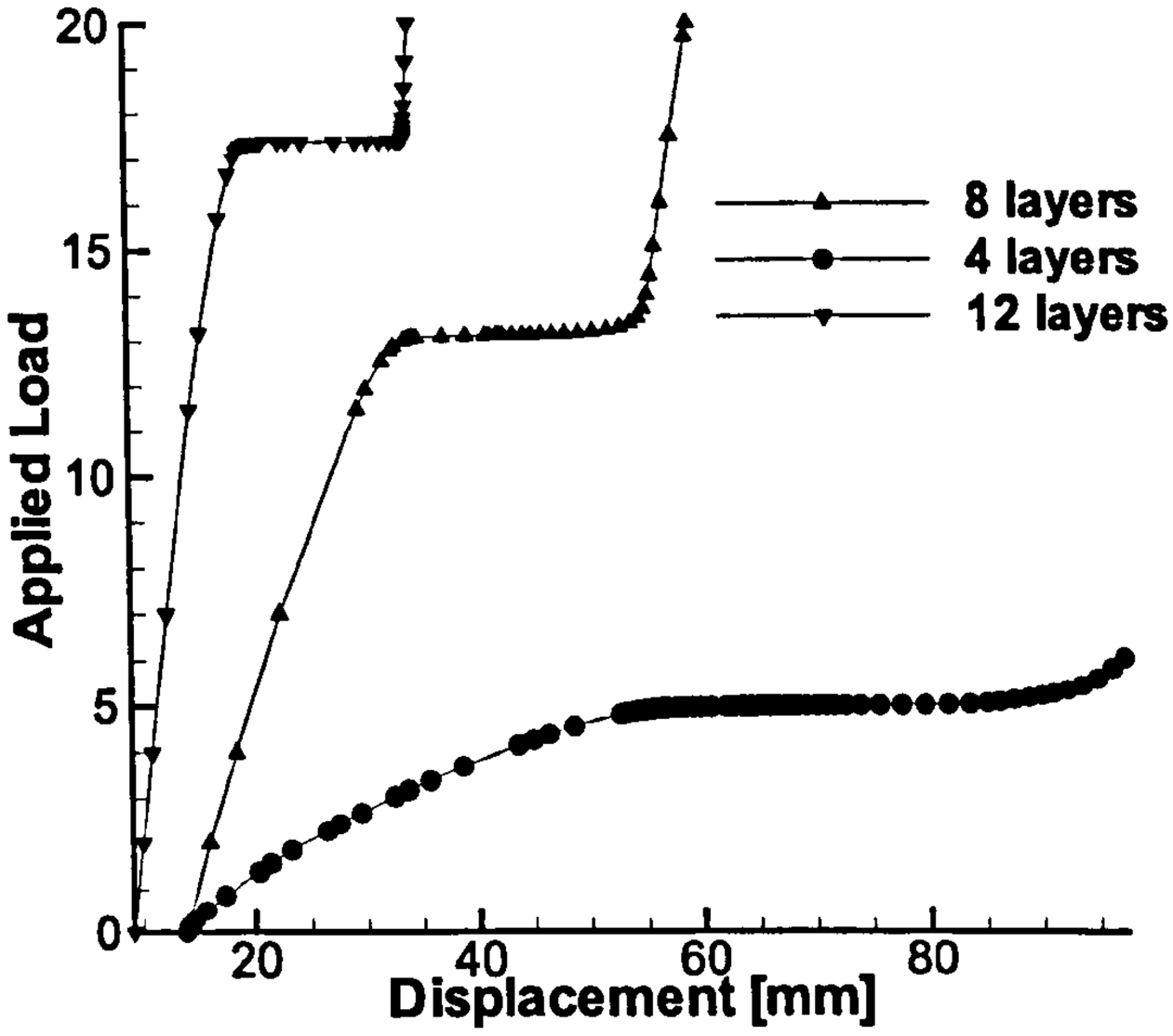

Figure 3.33: Stabilised load-displacement diagram for different number of layers

plate still exhibits a non-linear structural response. After the critical load is reached, the plate snaps into the second configuration. However soon after the load is removed the plate snaps back in to the original shape.

Fig. 3.34 shows a comparison between the applied load and the sum of the reaction forces at the four corner nodes for the same plate (8 layers). These curves are then compared against the experimental data in Fig. 3.35.

During the experiments, data were measured from the beginning of the test until the snap through. After this the specimen is disconnected from the load cell and therefore the tests were stopped to avoid inaccuracies. The same numerical results, but for a bigger panel (300 × 600 mm) are reported in Fig.3.36.

The difference between the two curves (i.e. the applied load and the sum of the reaction forces) can be regarded as a measure of the effect of the viscous damping during the analysis. For loads less than the limit load the behaviour of the two analyses is identical. Once the limit load is exceeded, the structure becomes unstable and while the curve with circular markers continues horizontally due to stabilisation, the one with triangular marker follows the unstable equilibrium path. Eventually the curves meet again in the new stable portion of the diagram since the vertical equilibrium of forces must be satis-

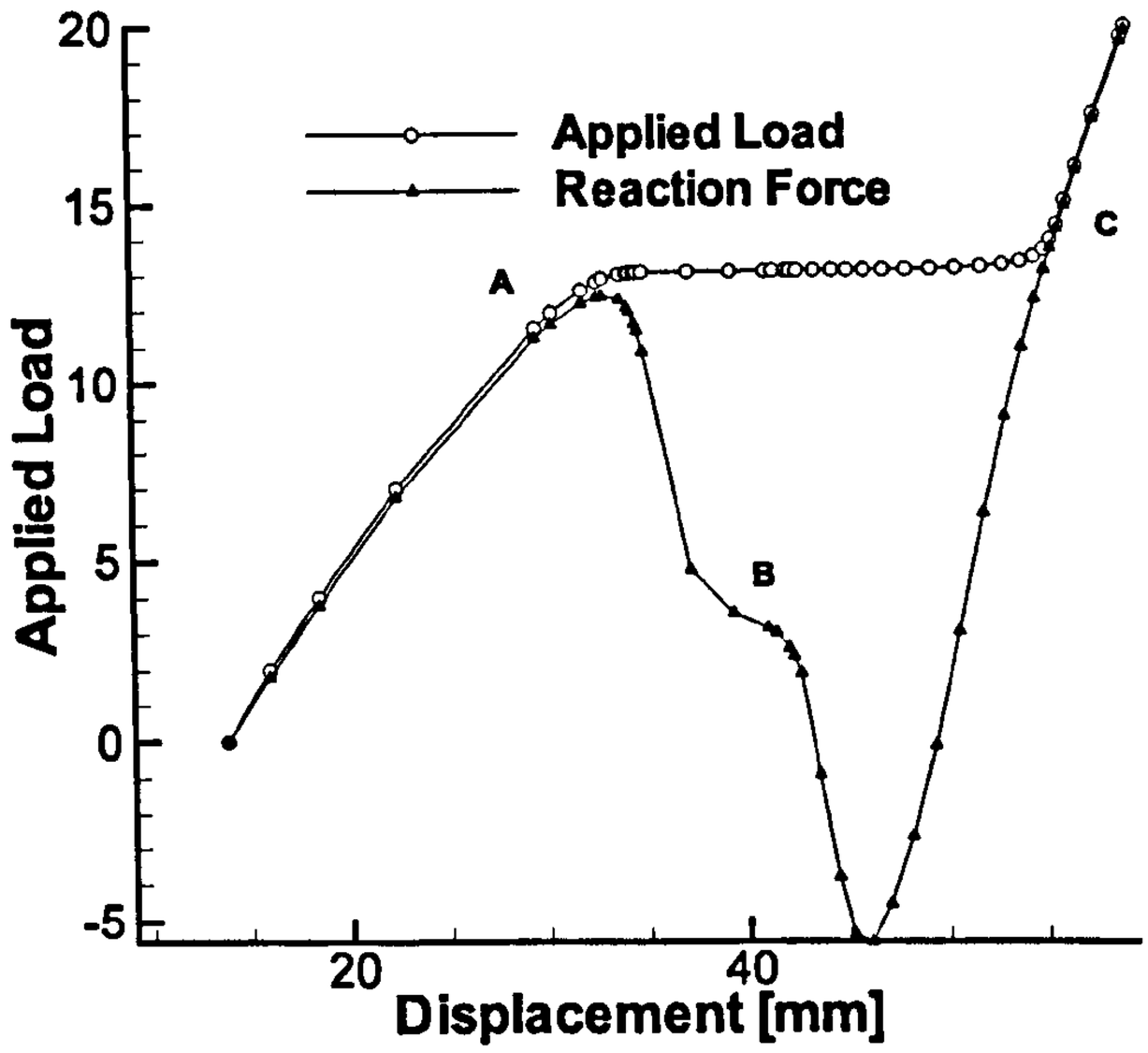

Figure 3.34: 'Snap-through' diagram from shape 1 to shape 2 for the 180 x 360 mm panel

fied. The "Reaction Force" curve is a measure of the force required to maintain the static equilibrium at a given position. Clearly the points on the curve segment between points A and C are configurations of unstable equilibrium. Point B highlights an intermediate state of unstable equilibrium already described experimentally by Potter and Weaver [2004]. It seems that the snap-through does not occur symmetrically but first one side of the unsymmetric part is reversed, and then the other side follows the curvature reversal. This phenomenon has been encountered mainly when trying to snap the plate from the first shape to the second shape. During the inverse transformation, the snap-through follows a more direct path and the intermediate states are more difficult to identify. Fig. 3.37 shows the intermediate deformation state corresponding to point B, where half of the unsymmetric part has its curvature reversed while the other not.

Fig. 3.38 shows the "snap-through" diagram as Fig. 3.34 but for the inverse transformation (from the second shape to the first one). Once the limit load is reached the reaction force drops almost linearly until the next configuration is reached. This difference is explained by the internal constraint that the symmetric part of the plate introduces. The constraint acts principally during the transition from the first shape to the second shape because its main effect is to prevent the curvatures along the x-axis

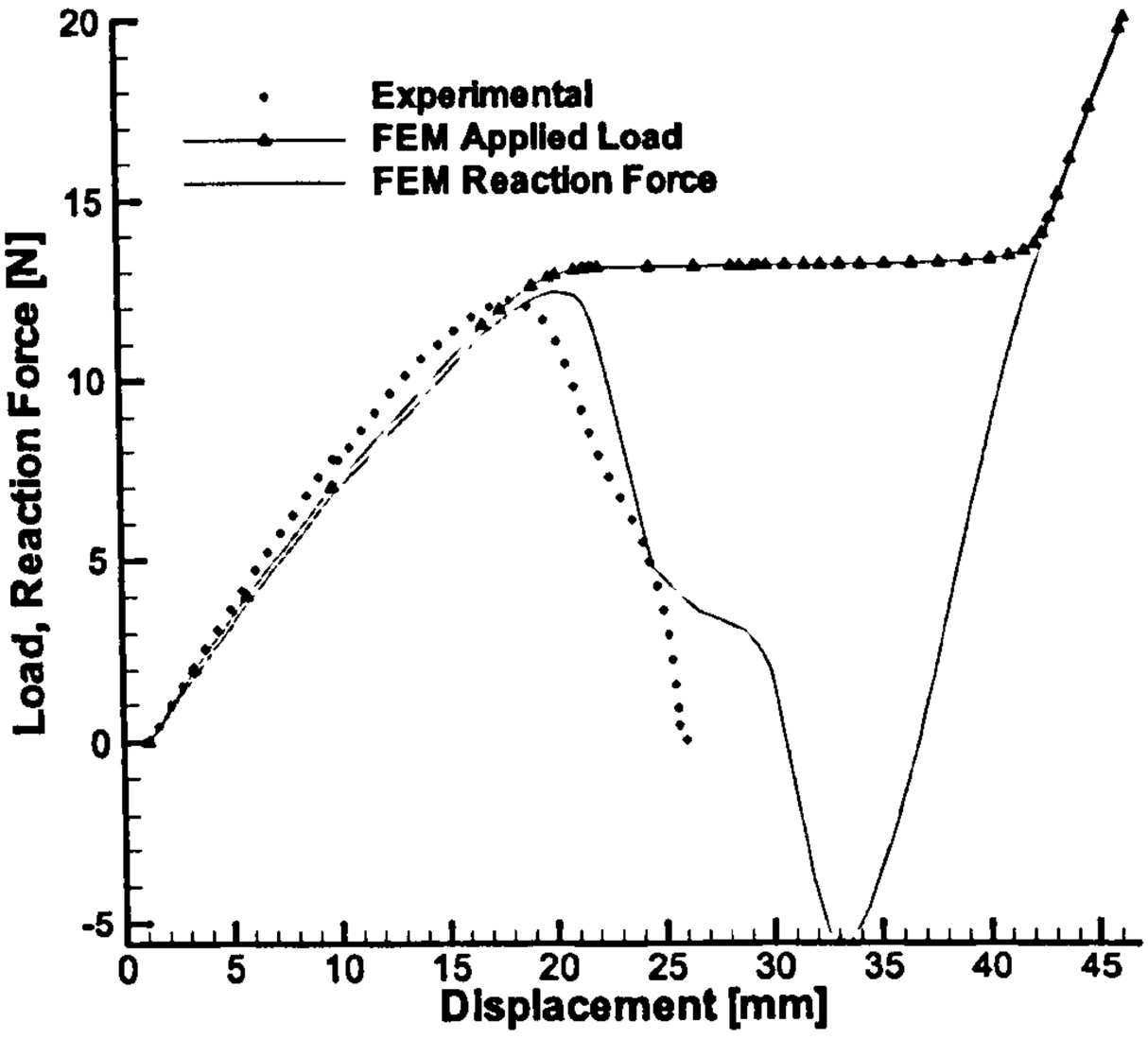

Figure 3.35: Comparison of the 'Snap-through' diagram with the experimental data

to develop freely. The same diagram computed for the 300 × 600 mm panel is shown in Fig. 3.39.

3.2.5 Explicit integration analysis

As mentioned in the previous section the explicit analysis can provide a complete description of the snap-through because it takes into account the effects of inertia [Crisfield, 1997a, Vol.1], [Crisfield, 1997b, Vol.2]. However a more detailed characterisation of the material properties is essential and therefore more user inputs are required. Both the explicit-dynamic analysis and the stabilised algorithm always converge to the same shape as expected since their objective is to reach the closest stable equilibrium for a given load, as quickly as possible. The steady state response of the dynamic analysis can be compared with the results of the static analysis. However, the oscillatory part of the dynamic analysis (i.e. the transient when the plate changes configuration) and the incremental iteration of the static analysis are two completely different problems and therefore not comparable. Matching the results (i.e. especially forces) obtained with the static method presents some difficulties since the two type of analysis are intrinsically different: the static analysis is dominated by the stiffness properties of the model

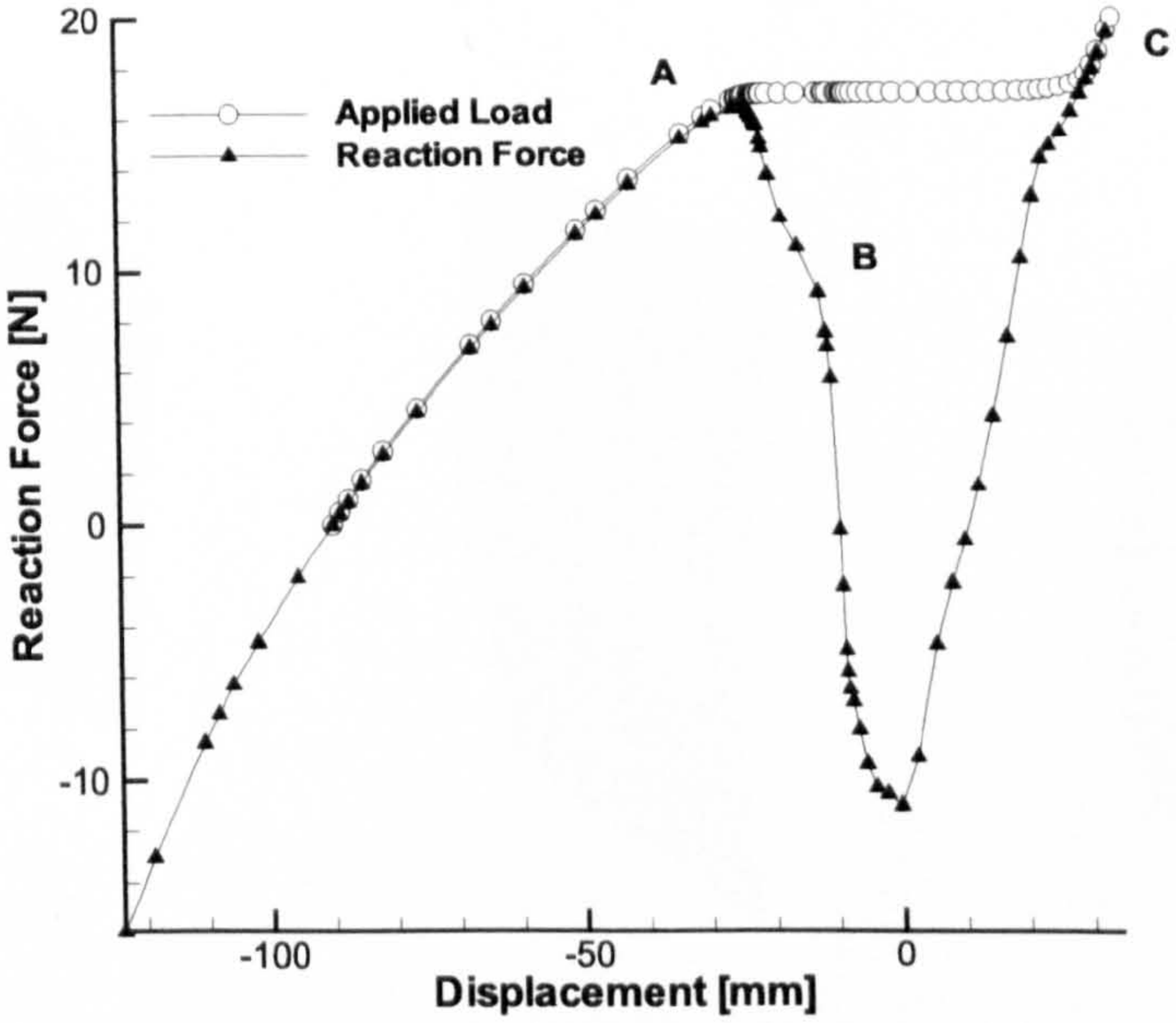

Figure 3.36: 'Snap-through' diagram from shape 1 to shape 2 for the 300 x 600 mm panel

whereas the dynamic analysis is heavily dependent on the mass and damping characteristics. Monitoring the reaction forces during the snap-through process required accurate modelling of the transient process during which the plate jumps from one shape to the other and is further complicated by the method of load application which also influences the solution. For this study the load has been applied as a step function but this excites the higher modes which proved difficult to damp out and different methods are currently under investigation. Having a good representation of the physical damping also presents difficulties as the damping models available are approximate and difficult to verify experimentally. Abaqus/Explicit^{TM} implements a Rayleigh damping model that introduces a damping matrix of the form:

$$C = \alpha M + \beta K \tag{3.24}$$

where M is the mass matrix of the model, K is the stiffness matrix of the model, and α and β are user defined factors. Fig. 3.40 presents a comparison between the dynamic and static simulation of the response during the snap-through process. Despite some high frequency oscillations shown in the first and second part of the diagram, the stiffness of the structure after the snap-through (i.e. after a displacement of 90mm) shows a good

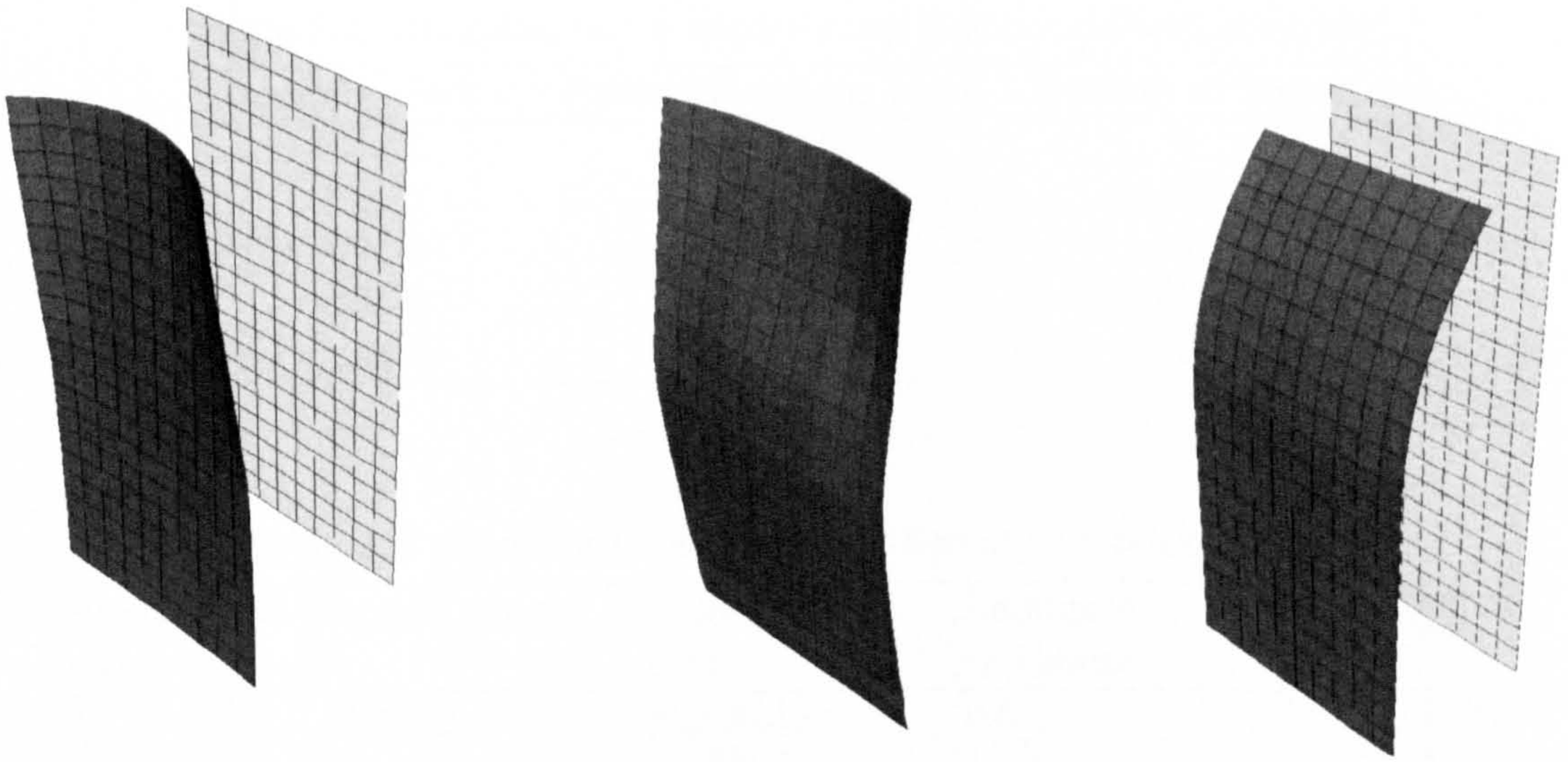

(a) Start (b) Unstable state (c) Finish

Figure 3.37: Intermediate deformations during snap-through from shape 1 to shape 2

agreement. The diagram also shows that the reaction forces reach considerably higher values during the transient, suggesting the existence of dynamic amplification of the loads during the snap-through.

3.2.6 Remarks on the numerical analysis

The possibility of tailoring the deformations caused by residual stress fields relies on the accurate prediction of the post-cured shape of unsymmetric laminates. This section presented a methodology to provide a numerical estimate for the equilibrium configurations of unsymmetric laminates that show multiple equilibrium states. Three different approaches are described and they all show good agreement with each other. Values for the critical temperature and the critical load to induce bifurcation are obtained. By monitoring the reaction forces, it is also possible to obtain the full equilibrium path that brings the structure from one stable configuration to the other. These results are compared with explicit-dynamic analysis. A further feature which may prove useful in design is the linear dependence of curvature with temperature which appears to be captured adequately using classical laminate theory for temperature significantly cooler than the critical temperature. The methodology contained in this paper may be used in

the application of multistable composite plates to morphing aircraft.

Table 3.4: Damping factor used during static stabilised analyses

Damping Factor	Plate dimensions [mm]	Number of layers
2.5e-7	180 x 360	4
3.5e-5	180 x 360	8
3.9e-6	300 x 600	4
8.3e-6	300 x 600	8
2.5e-5	300 x 600	12

Table 3.5: Stacking sequences for different number of layers

Number of layers	Symm. part.	Unsymm. part.	Laminate thickness	$t^* = \frac{thickness}{width}$
4	$[0/90]_S$	$[0_2/90_2]_T$	0.5	1/360
8	$[0_2/90_2]_S$	$[0_4/90_4]_T$	1	1/180
12	$[0_3/90_3]_S$	$[0_6/90_6]_T$	1.5	1/120

Table 3.6: Analytical and numerical k_y-curvature of the unsymmetric part of the 180x360 plate

Number of layers	Analytical - linear $\left[\frac{1}{m°C}\right]$	Numerical - non linear $\left[\frac{1}{m°C}\right]$	Δ %
4	0.053	0.05021	5.6
8	0.0246	0.0265	7.7
12	0.0177	0.0173	2.3

Table 3.7: Critical load for different number of layers

Number of layers	Numerical [N]	Experimental [N]	Δ %
4	4.92	4.65	5.8
8	12.9	12.18	5.9
12	17.98	22.2	19

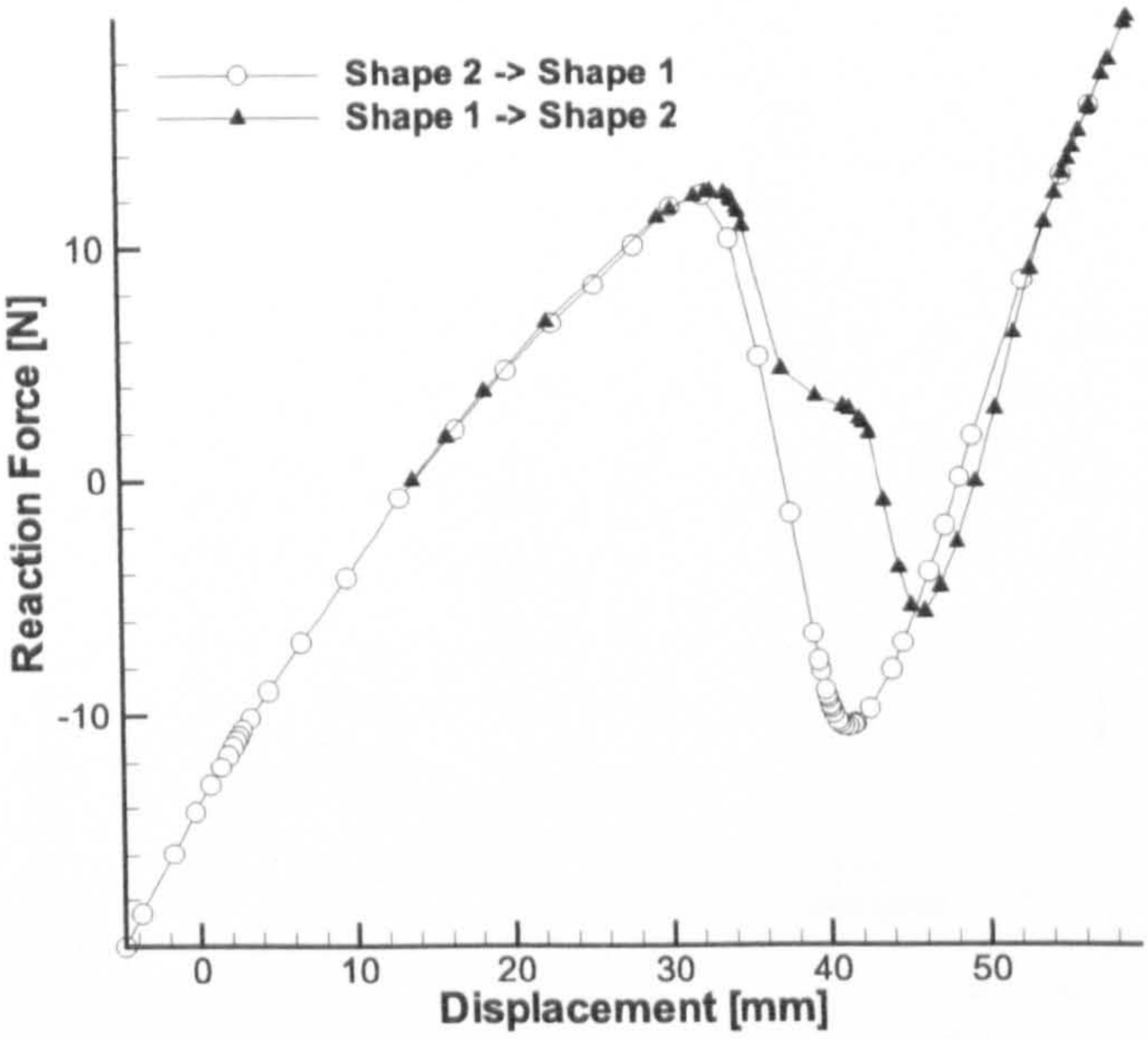

Figure 3.38: 'Snap-through' shape 1 to shape 2 and vice versa, 180 x 360 mm.

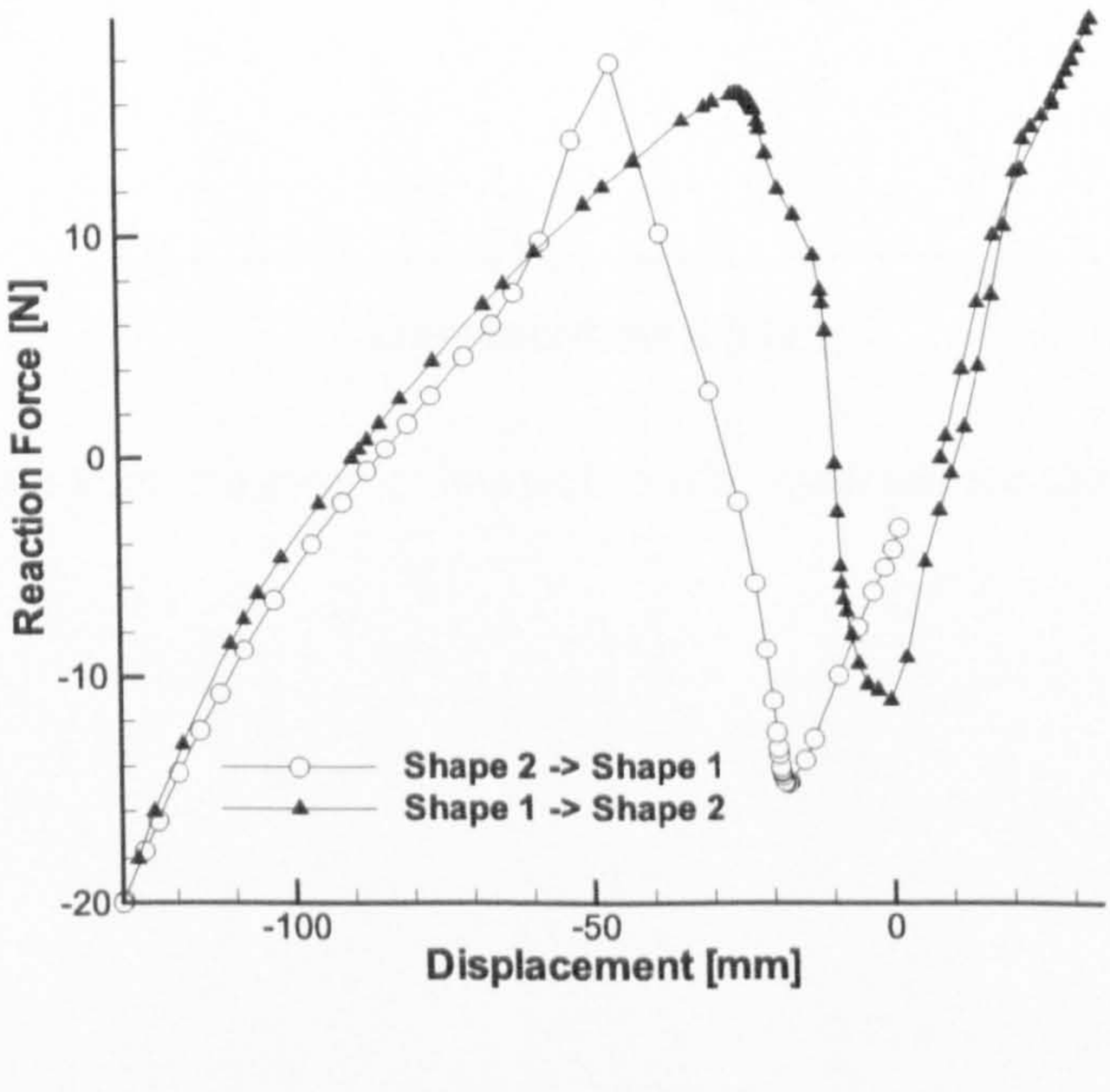

Figure 3.39: 'Snap-through' shape 1 to shape 2 and vice versa, 300 x 600 mm.

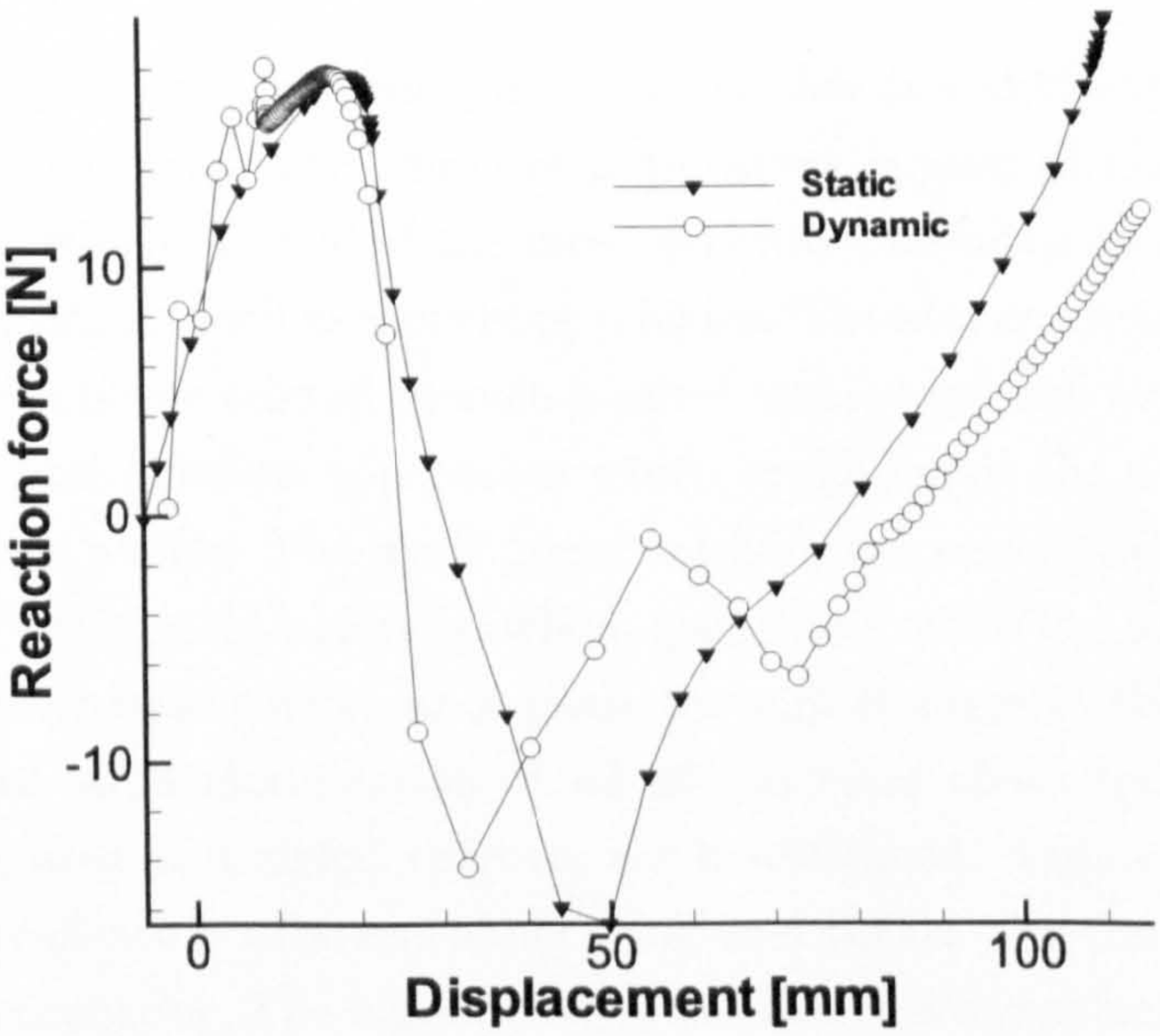

Figure 3.40: Static versus dynamic "snap-through" diagram for the 300 x 600 mm panel

Chapter 4

Concepts for applications

This section will present some concepts for the application of the technologies discussed in the previous chapters. The frame of application is that of the UAVs (Unmanned Aerial Vehicles), which are one of the most versatile platforms to experiment new and unconventional systems such as morphing vehicles. The aim is not to propose a definitive solution to the problems related to such a novel technology but rather, it is to open up the way to new and different approaches which could enable the shape-adaptability for aircraft to become reality. The work presented here is a contribution to the "Morphing aircraft project" at Bristol University, whose goal is to explore the possibility of achieving "significant aerodynamic performance gains through changes in the aircraft geometry". For this purpose large modification of all of the main characteristics of wings, such as sweep angle, area and airfoil camber, are investigated. Figure 4 outlines the basis for a possible realisation of a morphing wing and points out the areas of interest for the application concepts. The baseline wing consists of a swept-back tapered wing with curved cross-section spars used to obtain sweep variation. Large portions of the wing skin are made of elastomeric material to allow for aspect ratio and area variation [Thill et al., 2008]. The rib will be a combination of the "shear web" design and "truss" type to allow for additional degrees of freedom. Sections of the trailing edge are engineered to obtain a continuous variation of the airfoil camber without the use of concentrated hinges. Compliant sections of the leading and trailing edges will ensure a smooth transition between the deformable and the undeformable parts. Finally, the wing tip is designed to have a multi-functional behaviour as explained in the next paragraphs. Three main "active" areas for the shape adaptability have been identified: the spar, the trailing edge and the wing tip. The remainder of the wing components, namely the covers, the leading edge and part of the ribs, were not directly the subject of this study and

therefore for these components simple compliant surfaces or conventional solutions have been adopted, the only purpose being to address a possible system integration. The wing-box structure is responsible for the most significant geometric changes and therefore has deeper structural implications. The trailing edge and the wing tip on the other hand are dedicated to smaller shape changes which affect mainly the aerodynamic field and therefore their impact in the overall structure is more limited. The following paragraphs will give a detailed description of each component.

One important aspect, which must be considered during the design and engineering phase, is the manufacturing of any proposed solution. For a new concept to be successful, it is indeed important that performance gains are achieved. However, many proposals that in principle offer very good performance gains, are still discarded because of the added cost due to manufacturing complexity or excessive maintenance requirements. Ease and economy of manufacturing is of paramount importance, especially in a competitive sector such as the aeronautical sector.

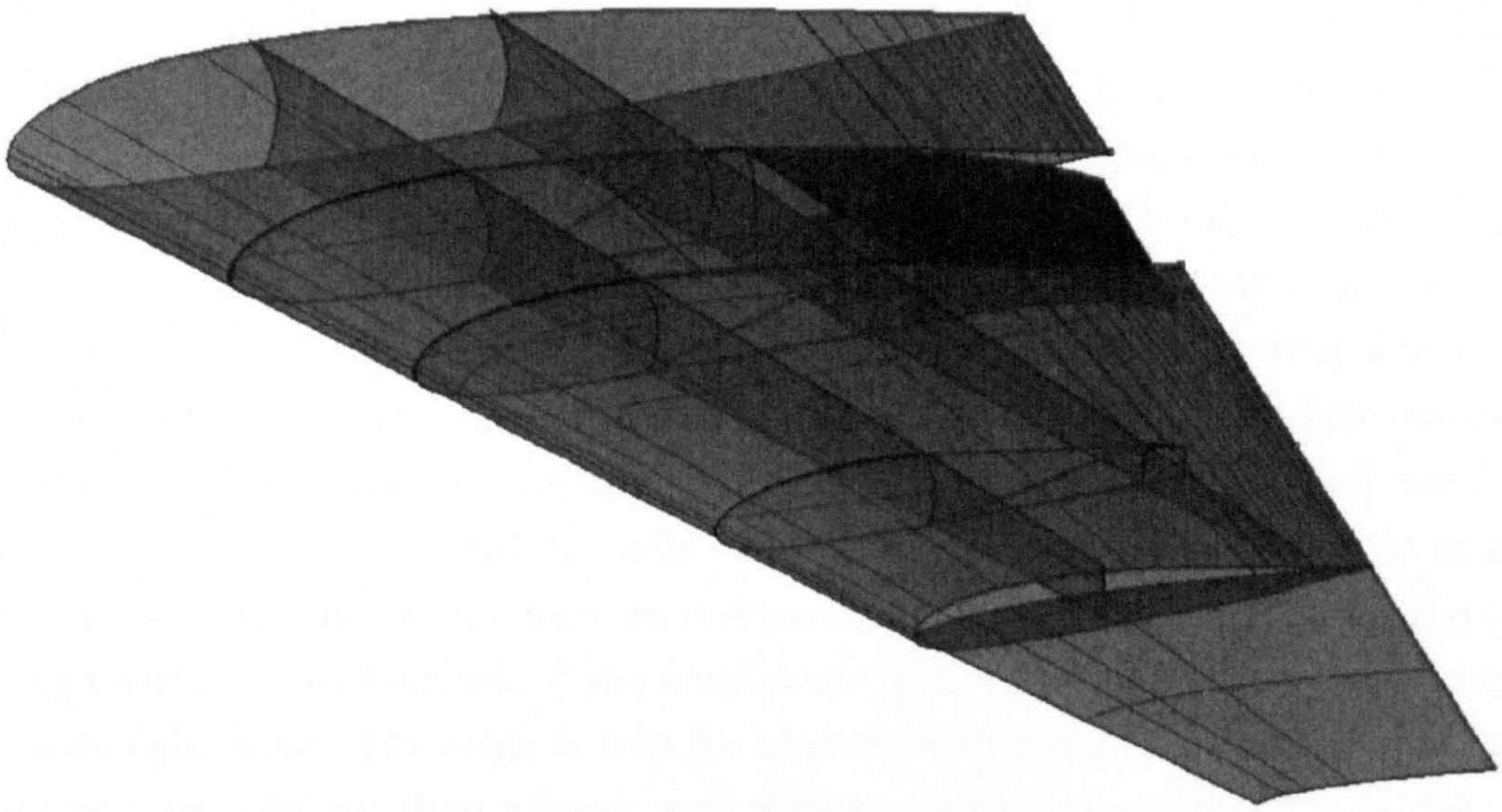

(a) High-lift configuration

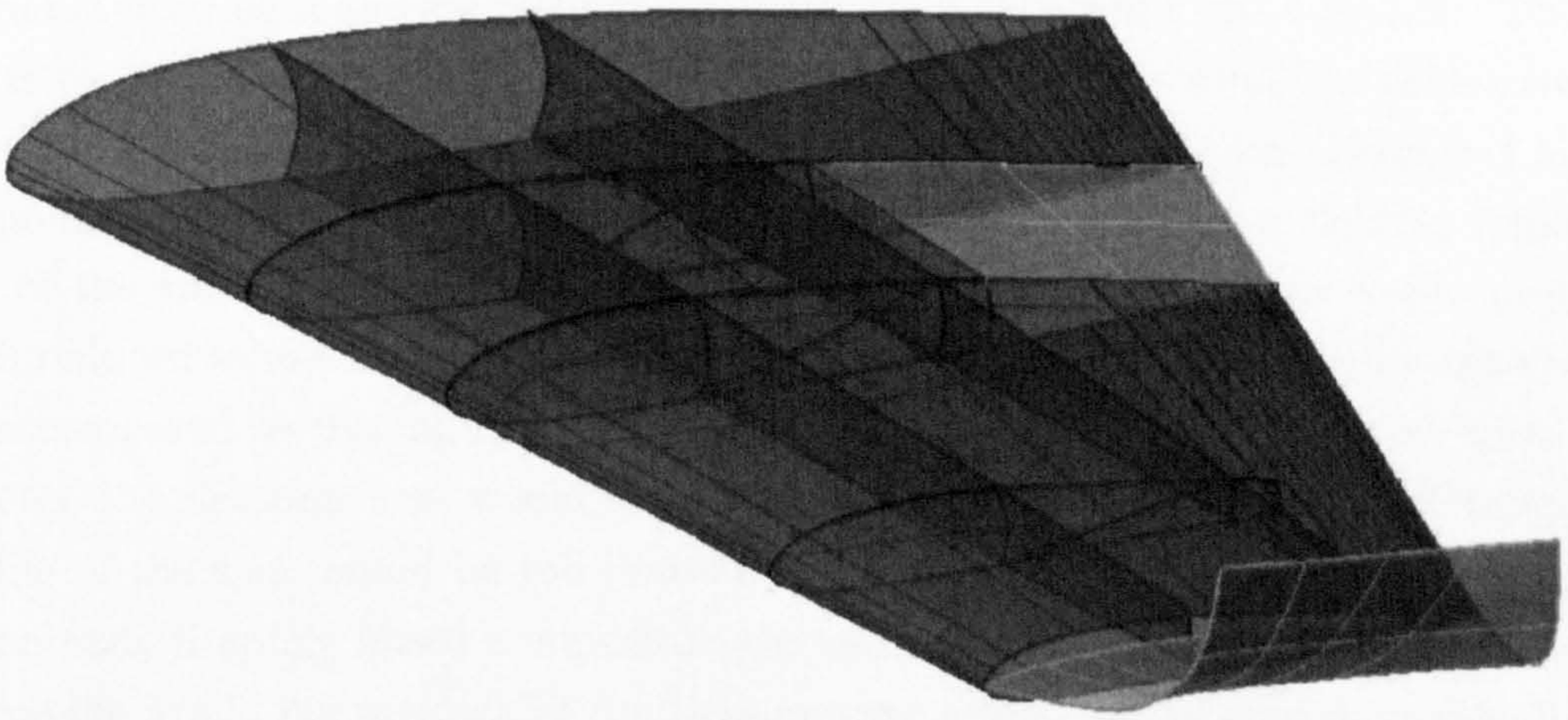

(b) Cruise configuration

Figure 4.1: Morphing wing assembly concept

4.1 Variable sweep wing-box

A wing with a variable sweep angle offers several benefits from the aerodynamic point of view such as the delay in the rise in drag at Mach numbers close to unity and buffet onset [Anderson, 1999]. From the structural point of view, there are the advantages when flying at higher speed obtained by changing the sweep angle, since structural loads are redistributed along the span reducing the bending moment requirements at root sections. The drawback is that variable sweep wings also pose significant disadvantages. The most common design for a variable sweep angle consists of a rigid wing that rotates around a pivot: this constrains all of the aerodynamic loads through the pivot producing a significant concentration of stresses. As a result, the large metal pivot needed to move the wings is complicated to build and install [Niu, 1999a]. This may increase maintenance requirements and decrease fuel performance. An aircraft capable of moving its wing forward for fuel-efficient flight could never be as efficient as an airplane equipped with a straight wing. The same is true for aircraft with swept-back wings; they would always be more efficient than aircraft with swing-wings. If on one hand it is clear that a variable sweep wing offers significant advantages, on the other hand the trade-off in terms of performance gains is quite consistent and the use of such a technology is allowed only if strictly necessary. The variable sweep wing technology would therefore greatly benefit from improvements in the structural configuration and reducing the structural drawbacks would increase the range of applicability. The wing-box concept proposed in this section is aimed at a lightweight composite structure which relies on the geometric characteristics to create an easily deformable system. The geometry of the preliminary design in the straight and swept-back configuration is shown in Figs. 4.2a-4.2b. The main idea is to use purposely designed tape-springs as spars. This would to take advantage of the properties of the tape spring that have been discussed on Chapter 2.5. The key point is that with this system the hinge point is replaced by a "folding region", an area of the spar that acts as a hinge. This structural configuration would produce a much reduced stress concentration and consequently lower reinforcements requirement, when compared to pin-lug systems. Tape-spring spars could be designed with metal, however the deformations would impose severe requirements in terms of fatigue and the life of the spar would be too limited, especially with a "fail safe" design approach. In contrast, if epoxy based composites are used and the strain level is controlled, the fatigue life would be, practically, limitless making a tape-spring spar economically more viable. This design, however, has a direct implication on the requirements for the ribs. A conventional configuration, in fact, would not allow the required degrees of freedom

of the tape-spring spars. This is clear by examining Figure 4.3 where a cross section of the spar in the straight and in the swept-back mode, is shown. The spar section changes from curved to flat and therefore for this to be possible, the rib must allow a height change of the spar cross-section. For these reasons, the part of the rib between the spars, has been realised with three rods hinged at the spars and arranged in a Z-type truss structure.

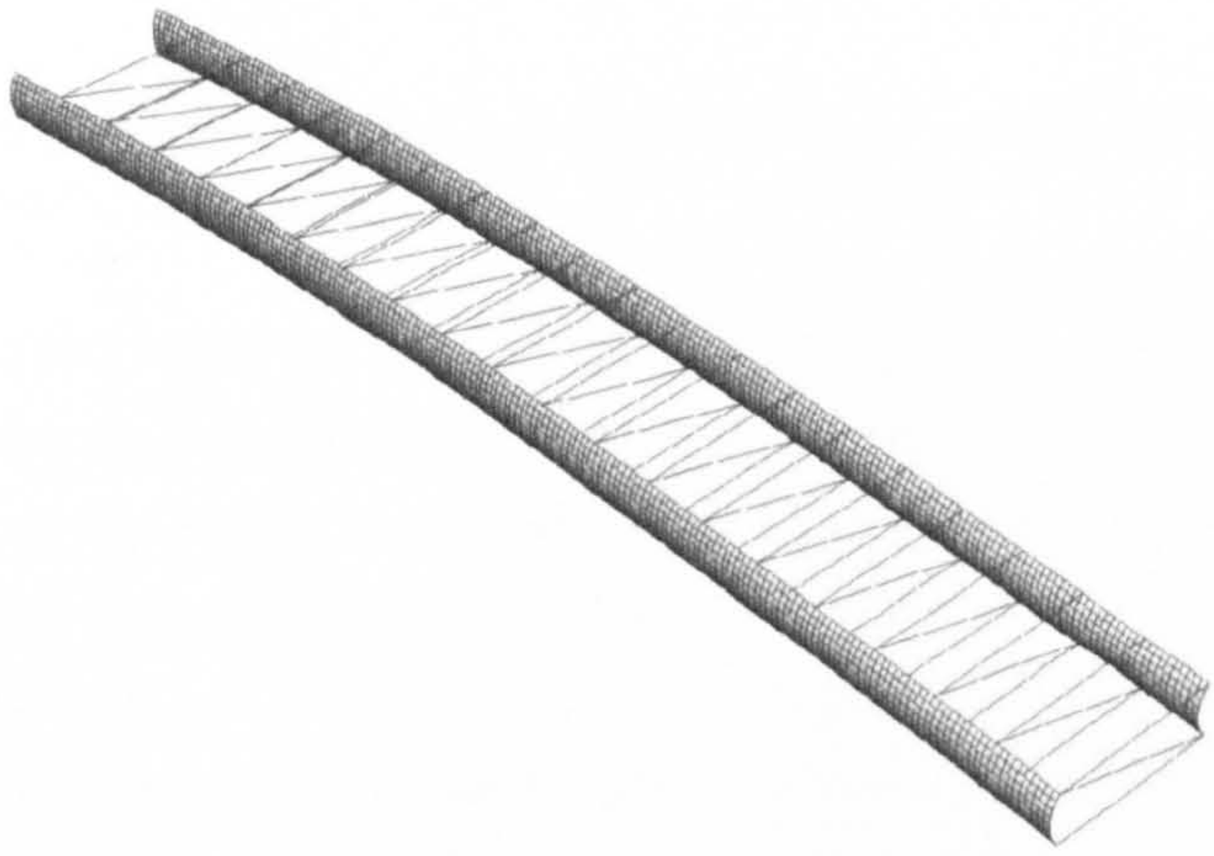

(a) Straight configuration

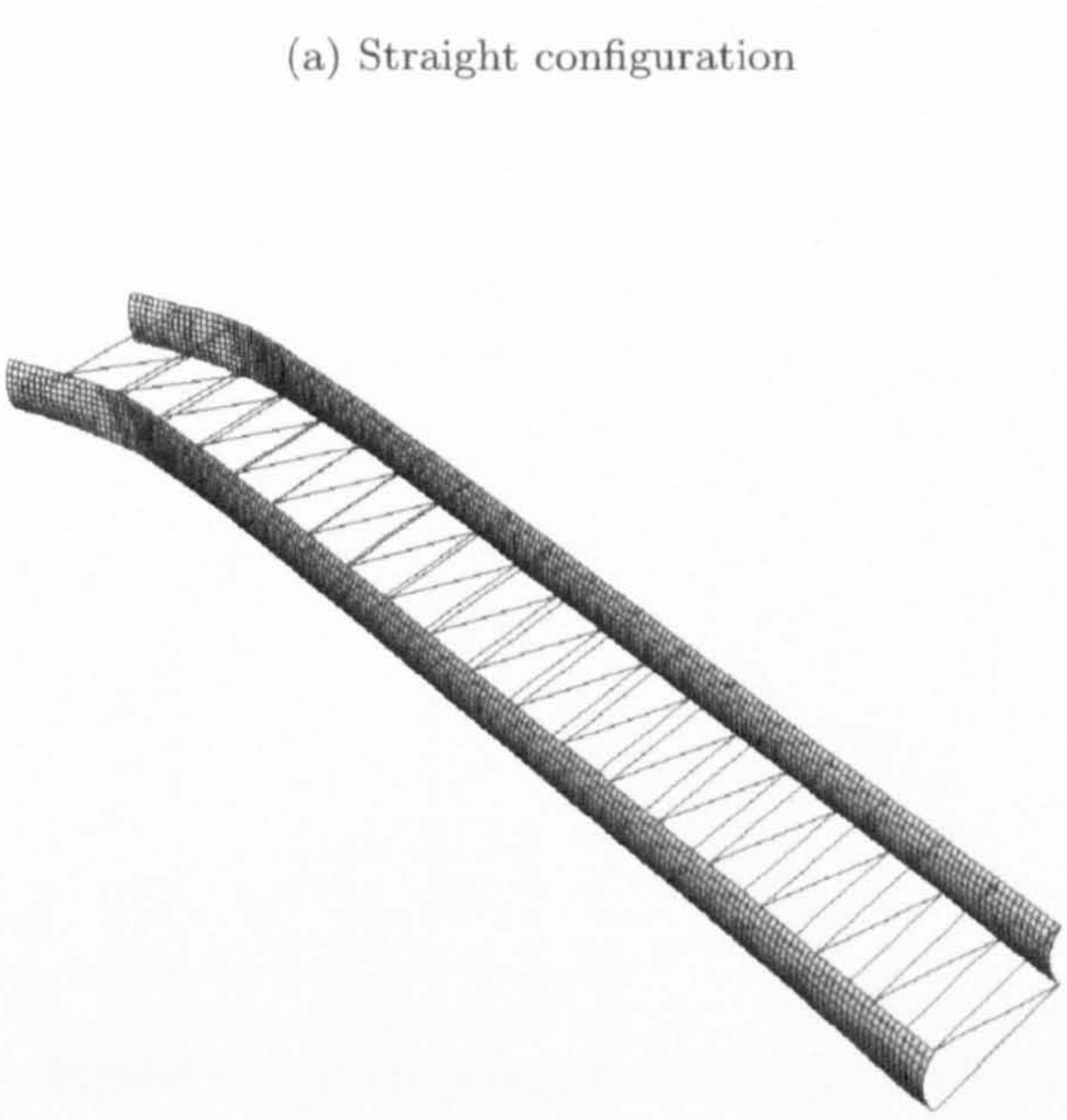

(b) Swept configuration

Figure 4.2: Variable sweep wing-box structure

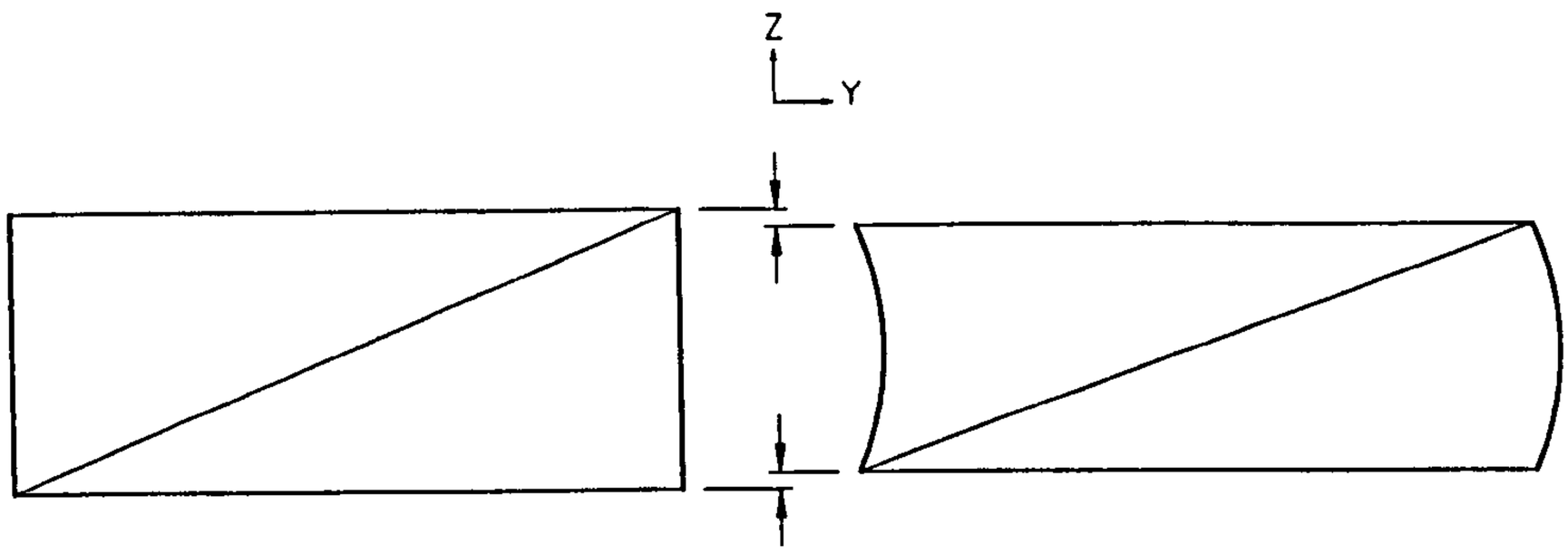

Figure 4.3: Wingbox geometry in the swept (left) and straight configuration (right) at the deformed location

Deformable spars to realise the sweeping mechanism, have an additional benefit. The relative rotation, between the spars and the ribs, couples the sweep angle with the wing area so that increasing the sweep angle reduces the wing area and vice-versa (ref. to Fig. 4.4). By changing the sweep angle from 0° to 20° and 39° the wing area between the two spars, reduces from 0.149 m^2 to 0.141 m^2 and finally 0.129 m^2, which corresponds to a variation of 13%. The sweep angle is increased with speed and so is the wing area required to produce a given lift; consequently substantial drag reductions is achievable with such a system.

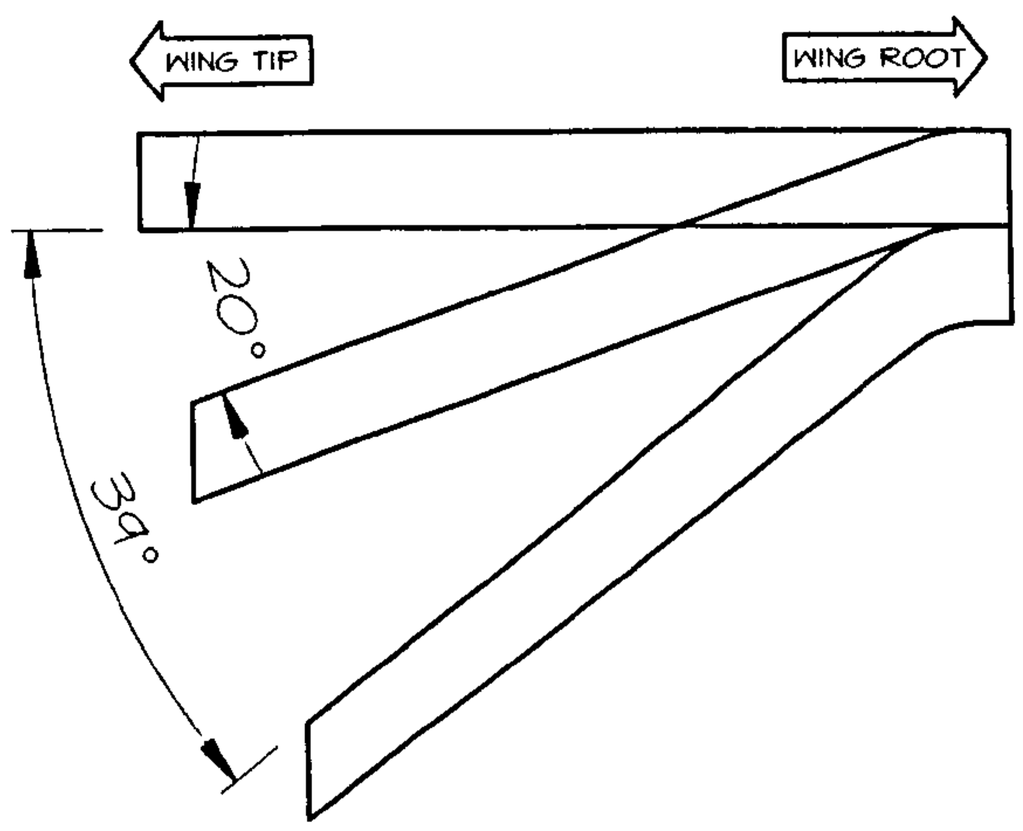

Figure 4.4: Sweep angle and area variation

The wing skin also presents some problems: during the transition between the two configurations, the wing plan-form changes from rectangular to rhomboidal requiring a consistent shear deformation of the wing skin. A comprehensive review of the problems related to the design of morphing skins has been given by Thill et al. [2008]. At present, no definitive design for a proposed skin has been investigated. However, from the current

research in this area, membrane skins based on silicon rubber seem to provide an effective solution [Gandhi and Phuriwat, 2008, Love et al., 2007]. Considering this as the most likely solution, it was proposed that the spars are designed to support all the aerodynamic and structural loads and no significant support is provided by the skins in terms of shear and bending moment capacity.

4.1.1 Spars' analysis

The wingbox was designed for the structural requirements imposed by a small UAV with a maximum take-off weight of 18kg and 1.2m semi-span. The spars are designed around their main feature i.e. the transverse curvature. This enables two advantageous properties for the wing: it increases the moment of inertia considerably improving the bending performance and it confers a hinge-like behaviour to the spar. The main characteristics of this behaviour are shown in the diagram presented in Fig. 2.12. One important parameter to consider is the magnitude of the bending moment M^* to induce bifurcation in the structure. This is linked to the radius r of the folding region as shown in Eqs. (4.1) and (4.2) [Yee et al., 2004]:

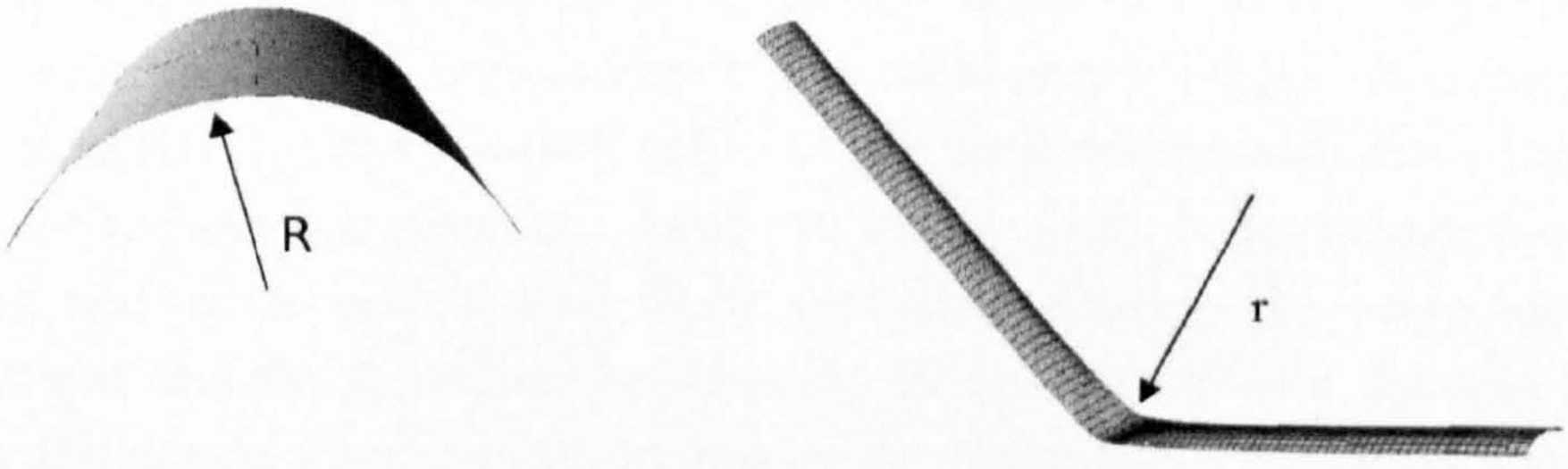

(a) Undeformed transverse curvature radius

(b) Folding region radius

Figure 4.5: Geometric characteristics of the shell

$$r = \sqrt{\frac{D_{11}^*}{D_{22}^*}}\, R \tag{4.1}$$

$$M_y = \frac{D_{22}}{R} \tag{4.2}$$

where D^*_{ii} are the components of the reduced flexural matrix of the laminate, R and r are the undeformed transverse curvature and the deformed longitudinal curvature of the shell respectively. In Eq. (4.2), D_{22} is a component of the flexural matrix and M_y is the bending moment per unit width required to produce the curvature $k_y = \frac{1}{R}$. Through these relationships it is possible to match the actuation moment M^* to the drag produced at a given speed. A spar designed with these features, has the advantage that if the speed of the aircraft is below a given value, then the equivalent moment produced by the drag force will not be enough to snap the spars, resulting in the wing behaving like a conventional straight wing. With increasing speed, the wing can be snapped into the swept configuration through a combined action of the actuator system and the drag force. The actuation force is only needed to overcome the peak moment required for the snap and once in the swept configuration, the wing adjusts the sweep angle to a position representative of the equilibrium between the internal elastic reactions and the drag force (the sweep angle increasing or decreasing along with flight speed). It may also be possible to achieve both positive and negative sweep angle if required (i.e. forward swept wing for increased manoeuvrability).

A combined experimental and numerical (FEA) approach was adopted to analyse this novel type of structure. In order to understand which parameters are more important for the proposed application, a number of different stacking sequences, aspect ratios and curvature radii for the shell were tested numerically. At first, a single spar was analysed through numerical simulation of the cool-down and snap-through processes. The analysis confirmed that, besides from the material properties (i.e. stacking sequence and reinforcing fibre), the curvature radius of the shell determines most of the useful properties for the sweep application. As shown by Eq. (4.2), it determines the bending strength as well as the critical load to be applied to activate the sweep mechanism. Initially, it was thought to realise the structure by making use of a flat tool only and relying on the deformation induced by unsymmetric laminates to obtain the required transverse curvature. This was not possible because of the high aspect ratio of the spars which, as explained in the previous chapters, prevents the bi-stability to exist. In addition to this, by making use of unsymmetric laminates on a flat tool, the equilibrium shape with curvature along the longitudinal dimension was mostly observed and only rarely transversely curved shells were obtained. For these reasons, a slightly curved tool was used to coax the specimen to cool-down in the transversely curved configuration (i.e. with greater curvature along the short edge) rather than in the longitudinally curved configuration (i.e. greater curvature along the longitudinal dimension). This method worked well and long rectangular shells were always obtained. A few specimens have been

realised with this technique by using a semicircular extruded aluminium bar as tool. The tool curvature radius was 53.5mm and because of the unsymmetric stacking sequence, the final curvature radius for the shell was 28.5mm. According to Eq. (4.2), this would produce a maximum bending moment per unit length of 3.2N, which corresponds to total moment of 0.13Nm, clearly not enough for the proposed application. To overcome this problem, it was decided to add 5mm wide reinforcement strips along the longitudinal axis so to obtain a conventional capping layer. Adding the reinforcement strips eliminates the possibility of having two equilibrium states, however this was considered an acceptable trade-off since the bi-stable behaviour was already limited by the high aspect ratio of the spar. The final stacking sequence is shown in Fig. 4.6: the web consists of an unsymmetric laminate ($[0° / 90°]_T$) while the spar caps have an additional reinforcement of five 5mm-wide layers at 0° on top of the basic web laminate. Note that the residual stress field introduced with the unsymmetric laminate potentially increases the energy content stored in the structure which is then released during the snap-through, making the transition between the straight and the swept configuration more efficient.

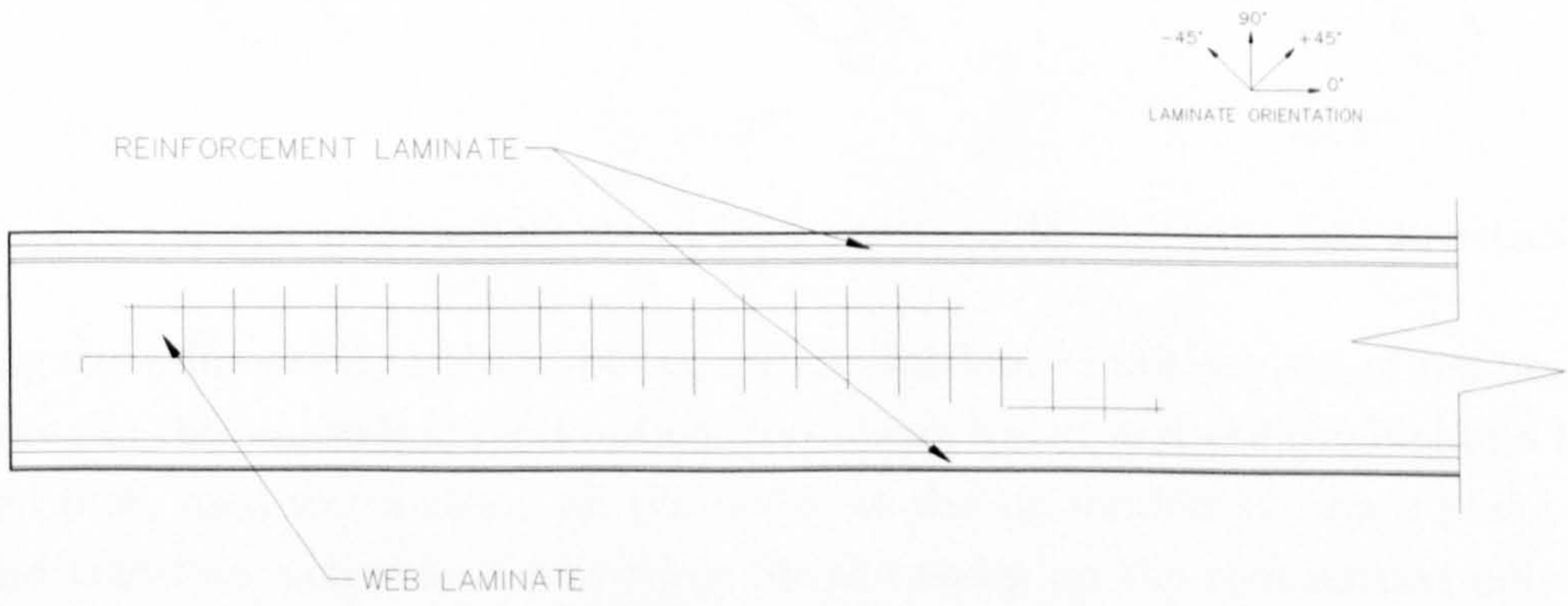

Figure 4.6: Stacking sequence regions for the spar structure

The rib spacing was determined on the basis of Euler buckling and shear buckling considerations for the spar caps and the whole spar respectively. To consider Euler buckling, the spar-caps were considered as pinned columns with the length equal to the distance between two successive ribs, whereas for the shear buckling the whole spar-web panel was subjected to the shear load produced by a maximum lift of 200N with a factor of safety of 3. This produced a theoretical rib spacing dominated by the Euler buckling for 2/3 of the wing's span and by the shear buckling for the remaining outboard part. Since the differences between the two distributions were found to be quite small (the minimum was 56mm for the Euler buckling and 88mm for the shear buckling) and to

increase the margin of safety during the experimental analysis, it was decided to space the ribs evenly every 56mm.

All of the FEA were carried out using ABAQUS®. To model the spar structure `S4R` shell elements were used, while for the truss-rib structure `T3D2` rod elements were chosen. The ribs were modelled free to rotate while their displacements were constrained to follow those of the spars through multi-point constraints (MPC). The FEA model used is shown in Fig. 4.2a. To simulate the cool-down process a non-linear static analysis was performed, while for the snap-through process, a stabilised Newton - Raphson scheme was used. To ensure accuracy the stabilisation factor was set equal to 5×10^{-11}, representing the lowest value where convergence was still achieved. Figure 4.7 shows a series of snapshots from the straight to the swept-back configuration.

(a) 1^{st} (b) 3^{rd} (c) 4^{th}

Figure 4.7: Various intermediate swept-back positions for the wing-box structure

During the bifurcation analysis, boundary and loading conditions are of paramount importance. In this analysis several options have been tested and the combination that performed best, used to constrain all the nodes at the tip section to rotate about the y-axis and translate along the x-axis while for the nodes on the root section only the translation along the z-axis was allowed.

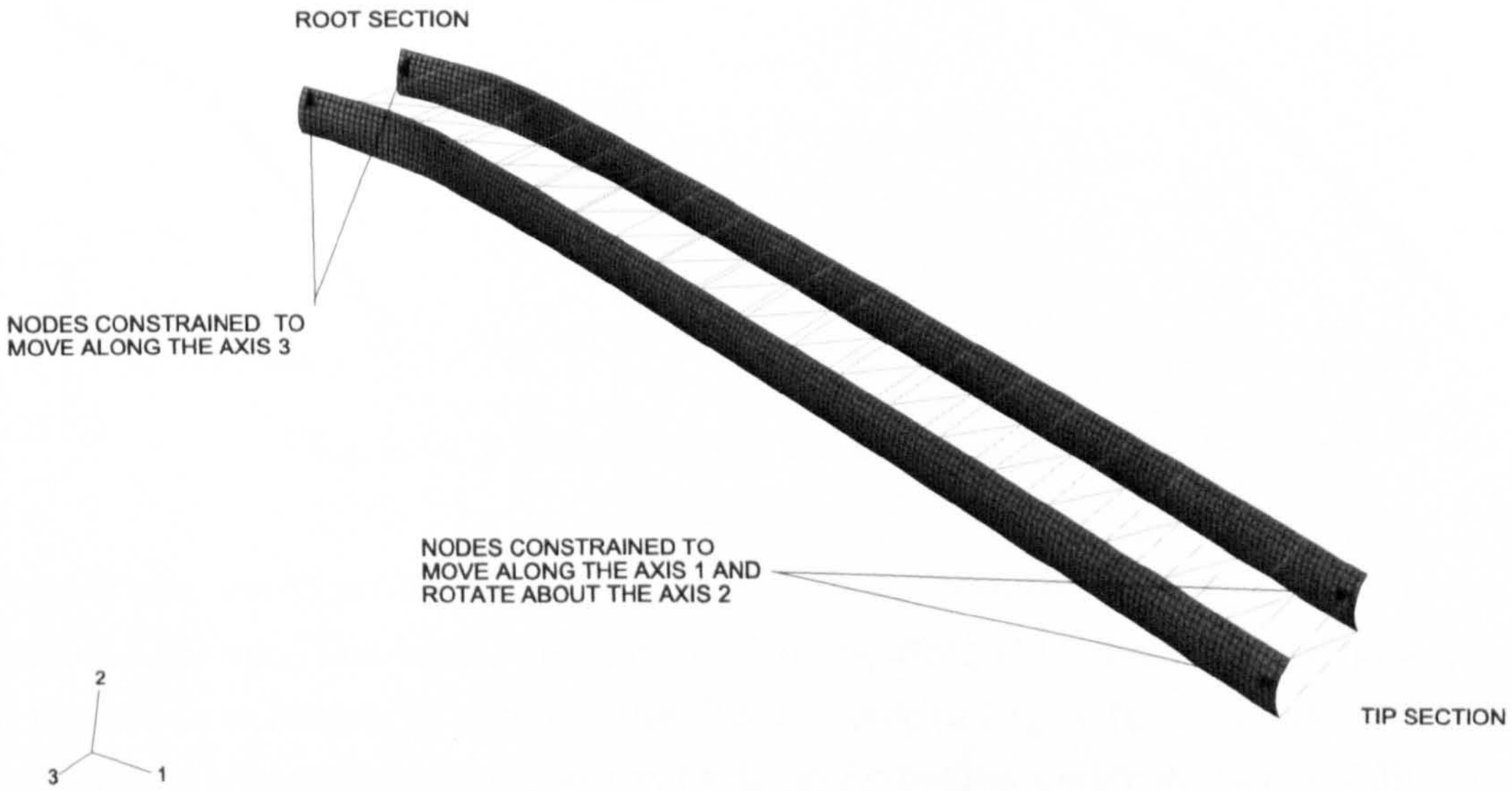

Figure 4.8: Boundary conditions

To induce the buckling of the wing-box two concentrated forces parallel to the z-axis were applied at two nodes on the root section. Loads and boundary conditions are shown in Fig. 4.8.

Tailoring of the sweep point position

Theoretically, the wing structure can snap (i.e. bend) at every span location between the root and the tip. This is because the transverse curvature of the spar is uniform along its length and therefore no preferential location for the snap exists. However, considering the in-flight loading conditions of the wing, the highest stresses will occur towards the root and therefore the snap will be more likely to happen in the region closer to the root. If different stacking sequences are used for different regions of the spar, the corresponding critical load can be increased or decreased accordingly and therefore other locations along the span can become more likely to snap. An example FEA confirmed this showing two spars, with the same geometry and loading conditions but different stacking sequences, snap at different locations as shown in Fig. 4.9a and Fig. 4.9b.

4.1.2 Experimental analysis

A preliminary wing-box structure, with the same characteristics as that discussed above, was manufactured and tested. The spar was manufactured using unidirectional pre-preg

(a) Laminate 1

(b) Laminate 2

Figure 4.9: Snap position for different laminates

carbon fibres, cured on an aluminium tool with a curvature radius of 53.5mm and a length of 1300mm. The truss-ribs were built using 2mm threaded steel rod with plastic ball-cup joints as hinges. A detail of the ribs is shown in Fig. 4.10. The spar successfully snapped from the straight to the swept back configuration under its own weight plus an additional load of 5N at 220mm from the root section. The swept configuration showed a good agreement with the one computed with the FEA, as shown by comparing Figs. 4.11a and 4.11b. In addition, the FEA prediction of the snap position was found to agree with that measured experimentally; both occurring in proximity of the second rib as shown in Figs. 4.12a and 4.12b

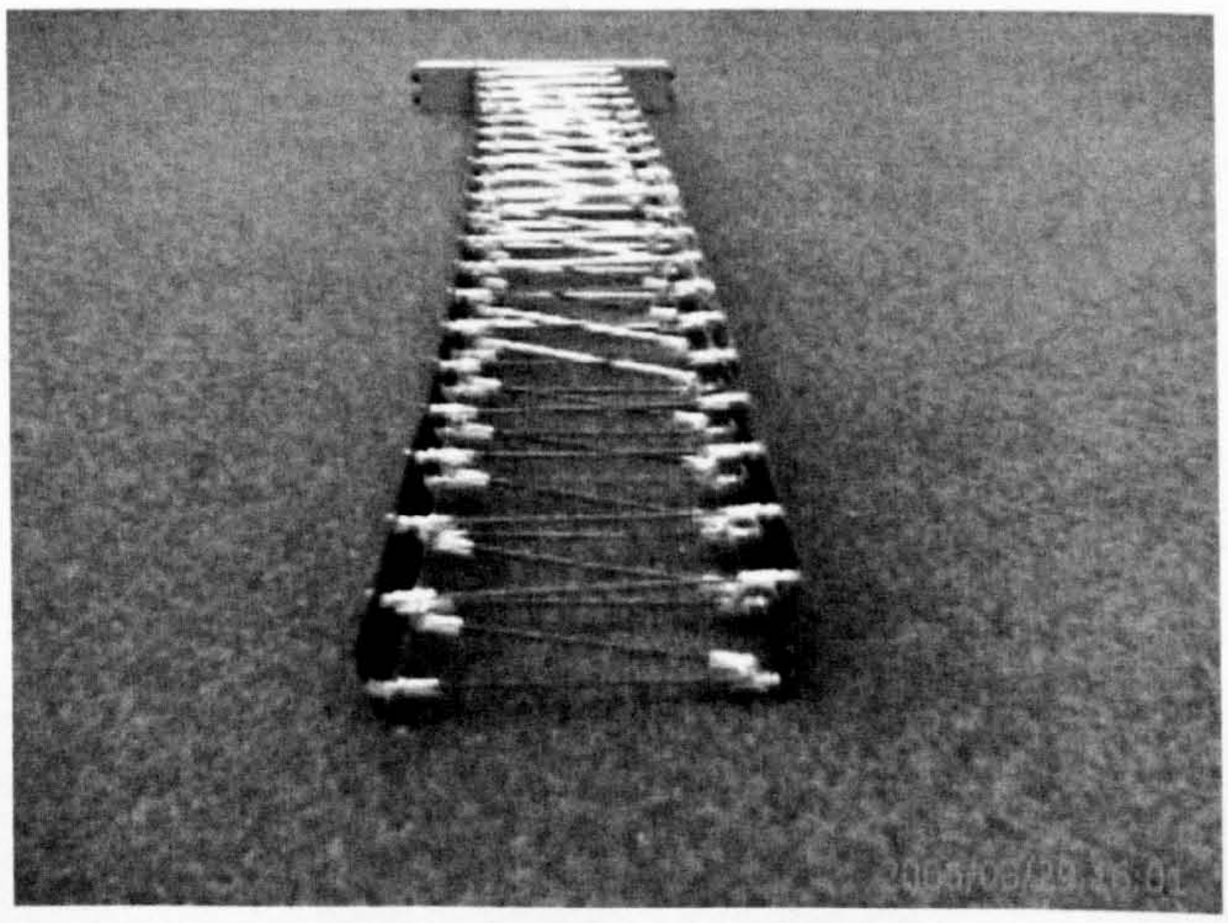

Figure 4.10: Experimental wing boxl

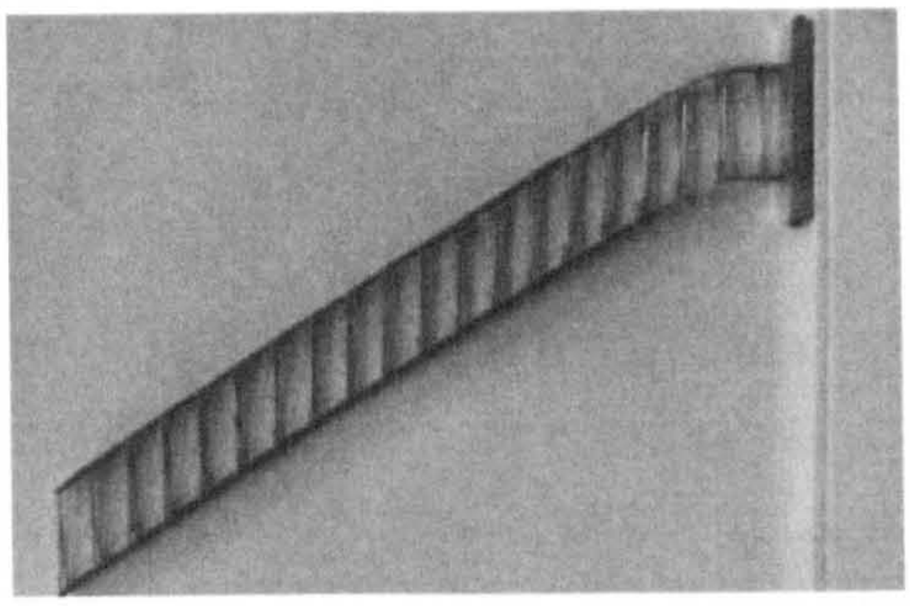

(a) Swept configuration: experimental model

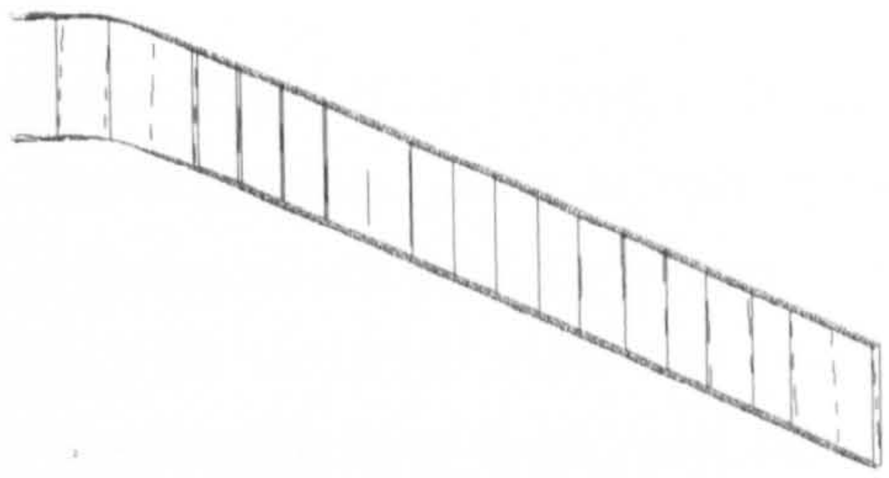

(b) Swept configuration: FE model

Figure 4.11: Swept configuration comparison

(a) FE model

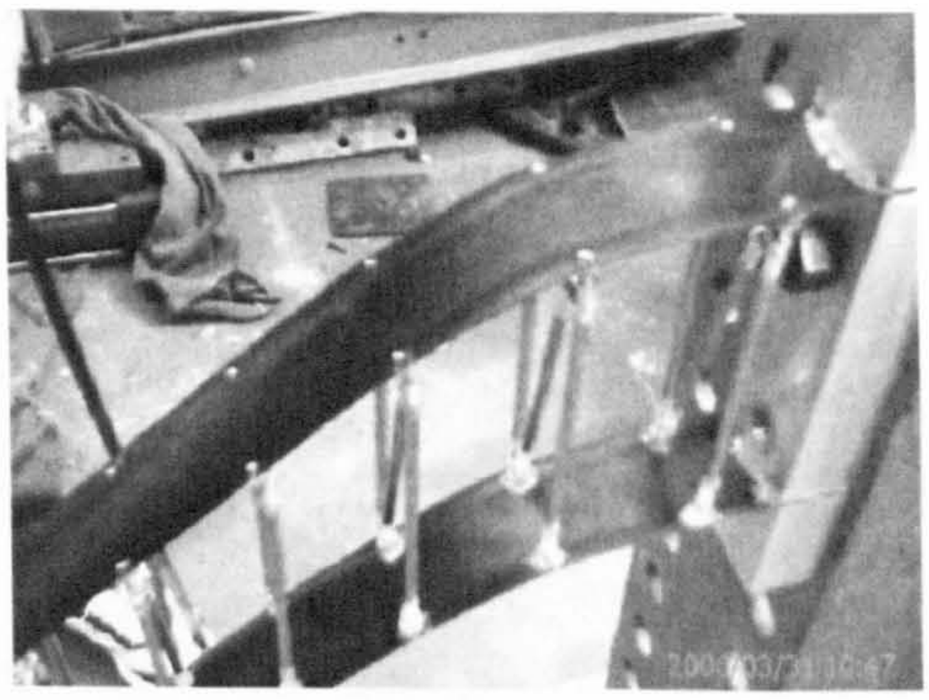

(b) Experimental model

Figure 4.12: Snap area

The experimental model was tested statically to investigate the maximum load that the structure could withstand and the critical failure modes. The wing-box was clamped to a rigid support and loaded with a force applied at 40% of the total length (i.e. the centre of effort of an elliptical lift distribution). The first buckling instabilities were observed in the section close to the root (ref. to Fig. 4.13) with a load magnitude of $70.3\,N$.

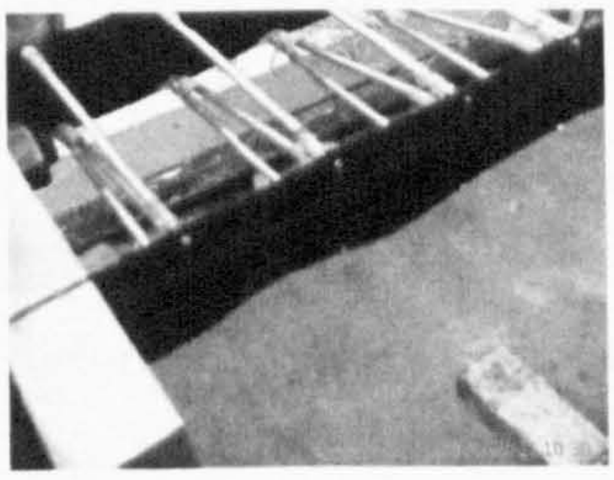

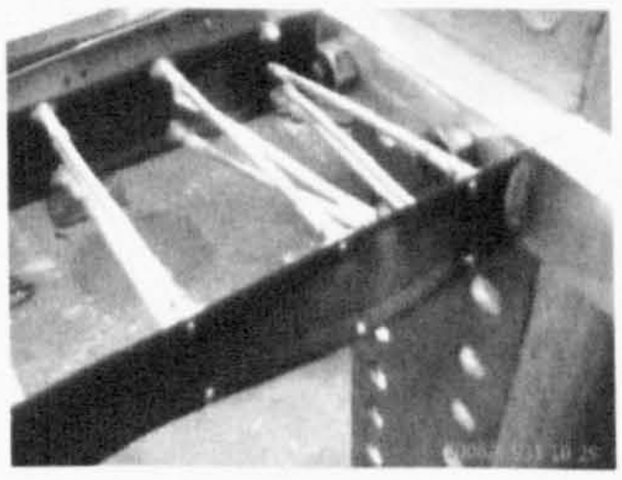

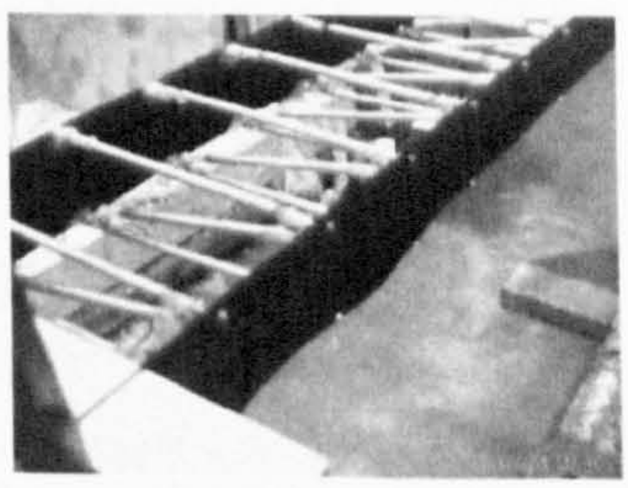

Figure 4.13: Local buckling of the spar

4.1.3 Re-design of the variable sweep wing-box

The demonstrator was entirely built with off-the-shelf materials. This proved to be and enormous constraint in terms of optimisation of its characteristics. As it is well know, carbon-epoxy laminate offer very high performance in terms of strength to weight ratio and therefore it is not surprising that the ribs, made with threaded steel and plastic ball joints were the weakest link. To limit this, only two layers have been used for the spar webs thus obtaining webs with a nominal thickness of 0.25mm. The rib joints determined to a great extent the load bearing capability of the spars and therefore the overall performance of the proposed wing-box. In addition, the spherical joints of the ribs posed a few difficulties because they relied on a plastic locking system to hold the ball-cap in place. In several occasions, this proved to be unreliable since the pop-out force (i.e. the force required to pop the ball-joint out of its fitting) could not be determined with sufficient reliability. Despite this, the overall system was satisfactory for the purpose of the demonstrator and large improvements will be obtained by using purposely designed joints. Considering that the truss-ribs are loaded in tension and compression, compliant hinges made of composite fibre with a high elongation matrix, will considerably improve the performance. Their use might potentially limit the range of sweep angles achievable, but this seems to be an acceptable trade-off. The best candidate for the wing covers is, as already mentioned, silicone elastomeric skins, which can stretch up to 100% and have successfully been tested for similar in-plane morphing by Hypercomp and NextGen Aeronautics reaching wind tunnel testing speeds close to the transonic regime [NextGen, 2007]. To provide enough support for the skin, additional rigid ribs need to be mounted at the fore and aft edge of the truss-rib. The rigid part of the rib would be designed to withstand the shear loads transmitted from the covers and therefore, as a first approximation, simple panels with fibres at $\pm 45°$ would be suitable. A concept sketch for the ribs is shown in Fig. 4.14.

Fig. 4.15 also shows a concept for an improved design of the spar structure together with the wing planform shape based on elastomeric skins and leading edge. For the new concept the forward spar must have a curvature radius in the snapped configuration larger than that of the rear spar. This is determined by the geometry of the swept configuration and can be achieved by using different laminates for the spar as show by Eq. (4.1). The spar's height needs to be re-designed to adapt to the profile thickness in different areas of the wing.

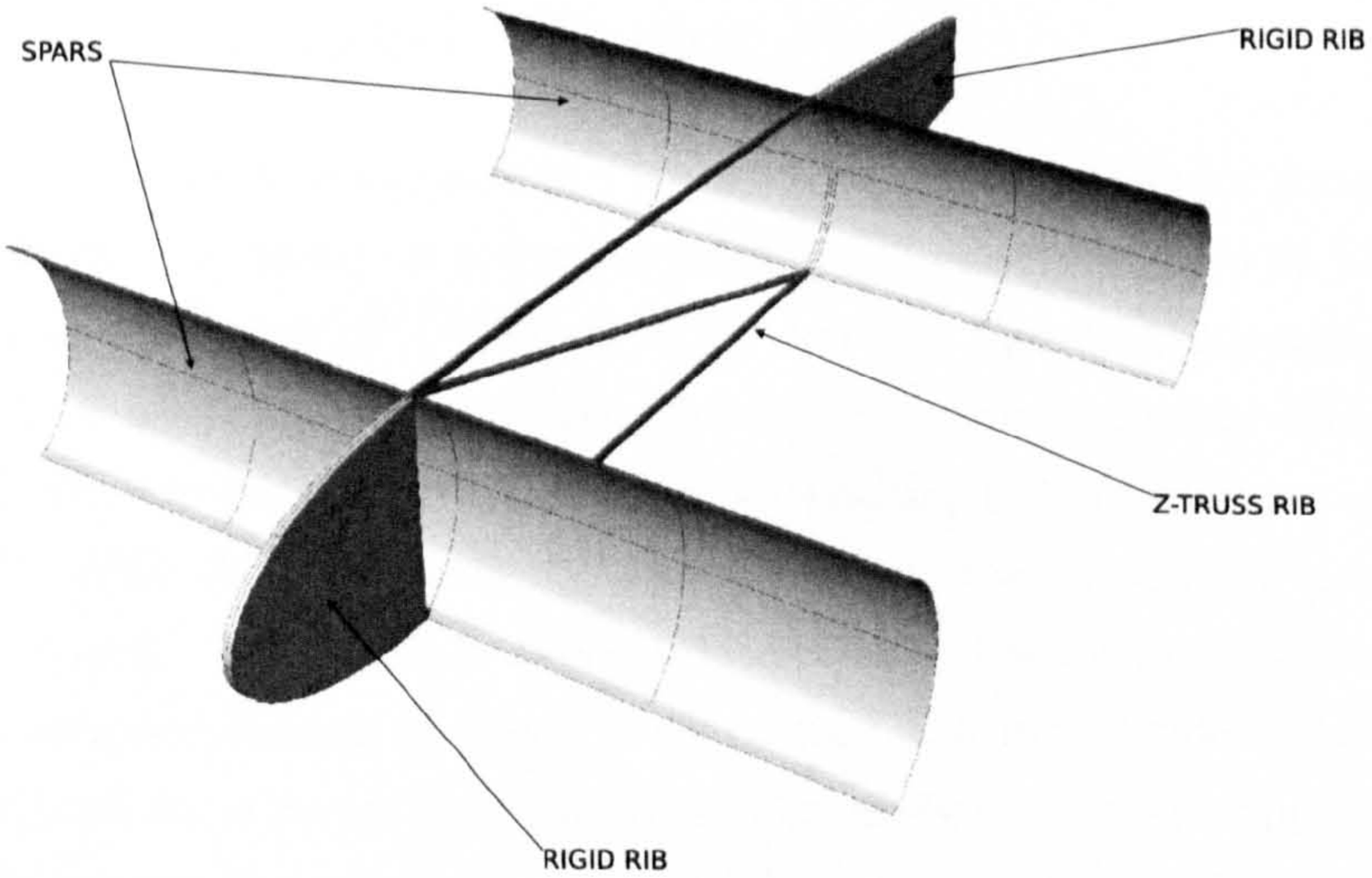

Figure 4.14: Improved rib design

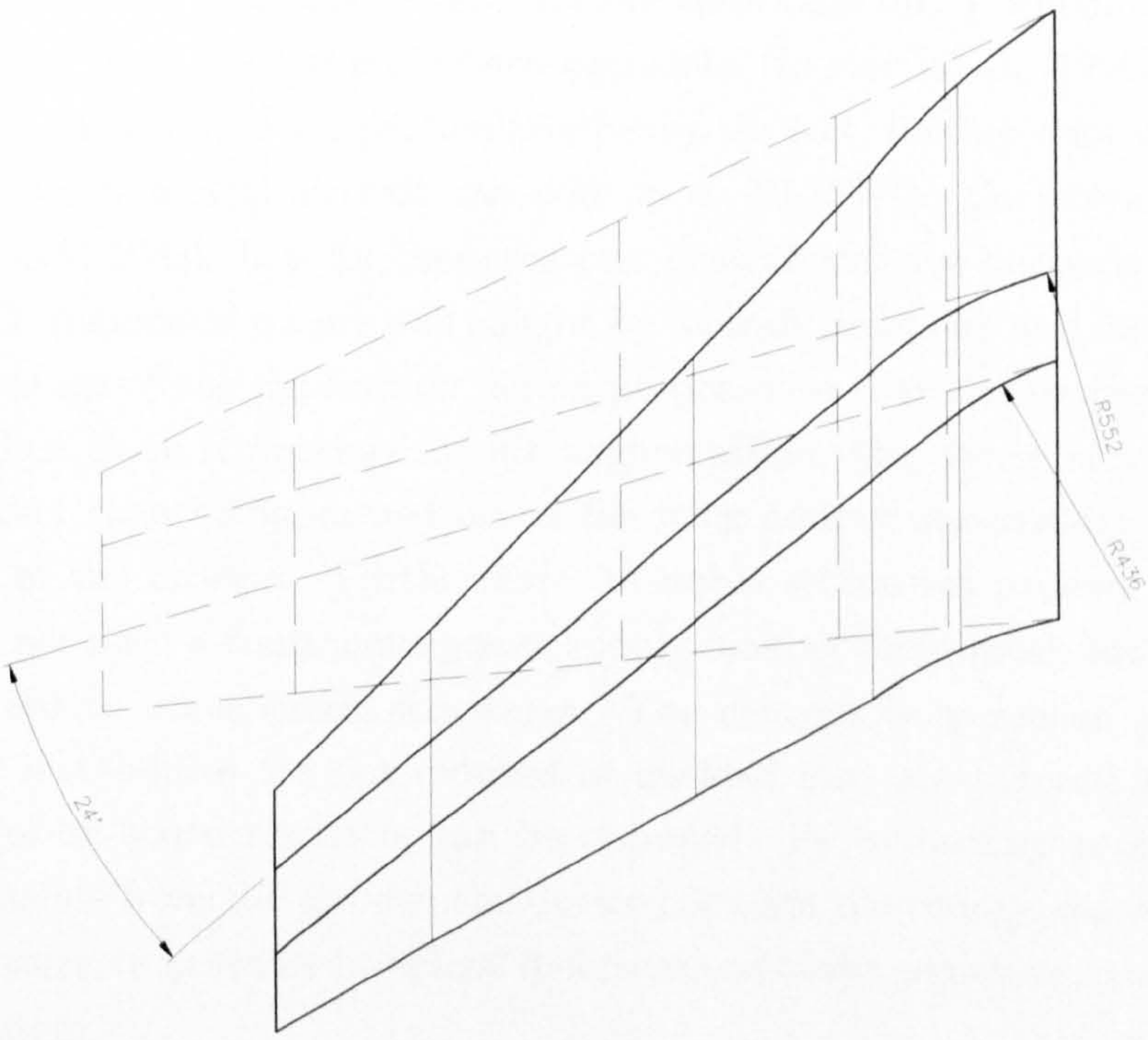

Figure 4.15: Improved wing-box design

4.2 Bi-stable Blended Winglet

This section presents an investigation in the use of bi-stable panels for the realisation of a shape adaptable device, based on bi-stable panels, which can be used as high-lift devices during low speed operation of *UAVs*. The device has two configurations: "extended" and "deployed". A bi-stable panel, derived from the compound plate shown in Fig. 3.5, is mounted on the tip of a rigid wing, thus extending the wing span (i.e. "extended configuration"). With the increasing dynamic pressure, the "extension panel" snaps into the second "deployed" configuration which is similar to a traditional winglet design. This application is designed having in mind the fact that the initial take-off configuration is particularly critical for aircraft performance. For a given aircraft, the maximum take-off weight, determines the take-off speed and hence the length of runaway, which has a considerable impact on the usability of the vehicle. Modern aircraft, optimised for cruise flight, require a considerable increase of lift at this stage and generally they make use of deployable slats and flaps to generate the additional lift. Unfortunately, however, systems such as these need complex arrangements [Englar et al., 1994] and multiple redundancies and therefore are particularly heavy. In fact, the inclusion of one of these systems into a commercial aircraft can add up to 10-15% to the overall wing weight alone [Torenbeek, 1982]. It is for these reasons, that alternative methods for temporary generating lift augmentation are still sought by aircraft designers and manufacturers.

The advantage of the application herein proposed, is that during the cruise part of the flight, when there is no need for lift augmentation, the device is actively used as a winglet rather than being stowed inside the wing adding unnecessary weight for the longest part of the mission. Furthermore, bi-stable structures present the advantage that they do not need a continuous power supply making them much less power-hungry when compared to other smart structures. The concept is to realise a device whose aerodynamic instabilities are not reduced or avoided but, are tailored so that a more efficient use of on-board resources can be obtained. By extracting as much actuation energy as possible from the airflow, the device converts the energy, associated with the dynamic pressure, to generate beneficial deformations of the structure, realising a passive actuation system.

The planform of the winglet and the baseline wing, chosen as a basis for the design, are shown in Fig. 4.16. The geometric dimensions are

- span b, 300mm
- root chord C_{root}, 185mm

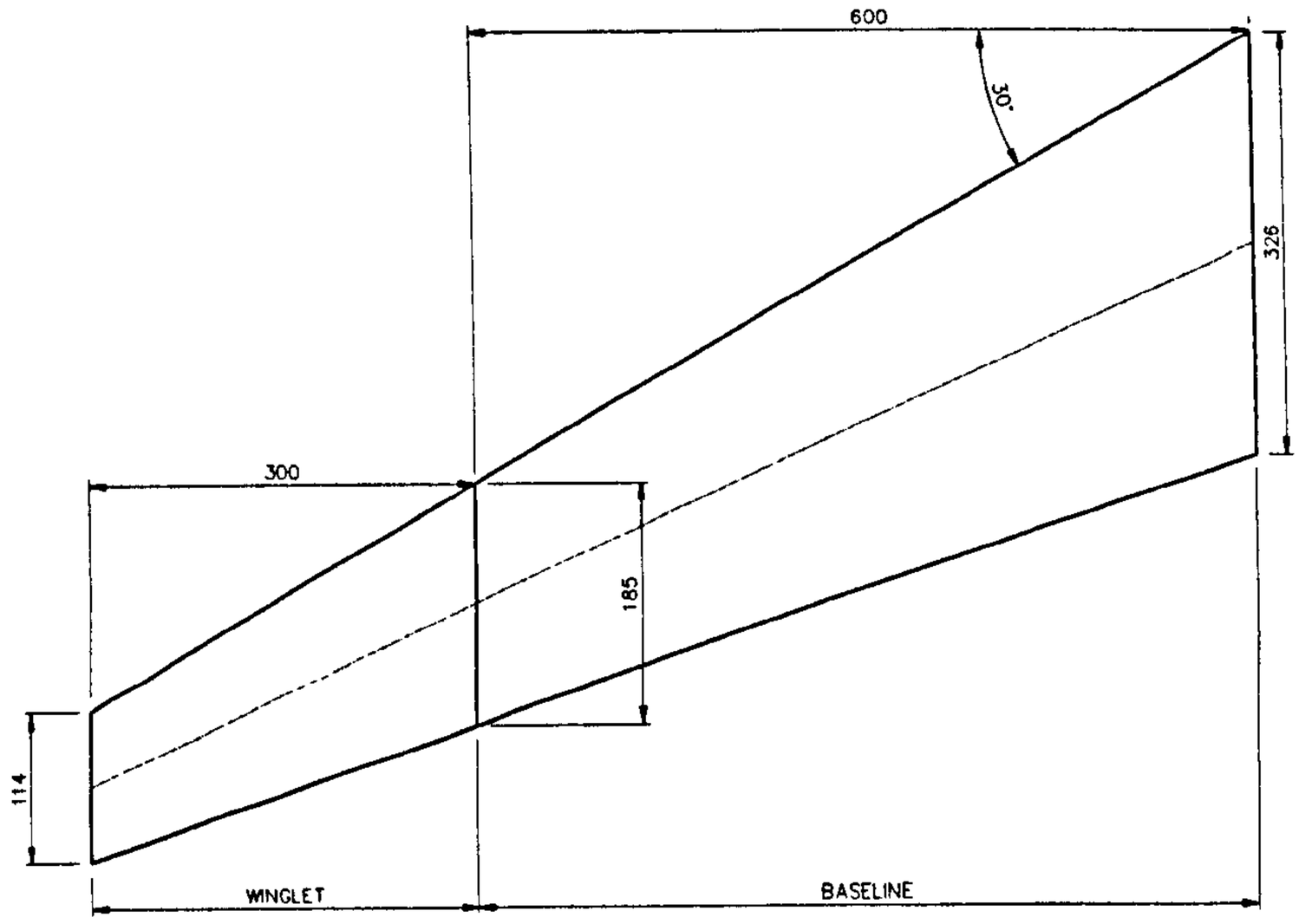

Figure 4.16: Baseline wing planform

- tip chord C_{tip}, 105mm
- sweep angle Λ, 30°

The baseline swept wing used throughout the testing is a Zagi 12 wing section, with the following geometry

- 30° sweep angle at the leading edge
- 600mm span
- zero washout
- root chord of 326mm
- tip chord 185mm

This type of baseline wing was the same chosen for several other tests within the Morphing Aircraft Research Project, of which this study was part.

The winglet planform is divided into two regions, a first one which has an unsymmetric laminate (and is therefore bi-stable) and a second one where the laminate is symmetric. The reason for this is that the symmetric part is used to tailor that shape of the unsymmetric part (as shown in Section 3.1) and also to ease the transition into the baseline wing. Different extents for the symmetric part have been tested and the triangular shape chosen proved to be the best compromise in term of shape tailoring

and compatibility with the baseline wing. To select a model for the wind tunnel testing, several configurations have been analysed numerically, of these the three shown in Fig. 4.17 were found to have best characteristics.

The first configuration had the 0° fibres aligned with the leading edge, the second one had 0° fibres parallel to the centreline while the last configuration had the 90° fibres parallel to the boundary between the symmetric and the unsymmetric parts. The shapes obtained with each configuration were predicted with FEA, using "cool-down" and "snap-through" analysis as described in Section 3.2. To ensure accuracy 336 8-noded double curvature shell elements (S8R) and 1089 nodes have been used for the FEA mesh. The cool-down simulation was performed by clamping the geometric centre of area of the planform in order to eliminate rigid body motion and the midpoints at the root and the tip where restrained from in-plane translation. The snap-through was simulated by applying a concentrated vertical force at the tip midpoint and clamping the nodes at the root (i.e. to simulate the interaction with the baseline). This last boundary condition was justified by the fact that in the real model, the symmetric part is almost entirely inserted into the baseline wing and therefore "fixed" boundary conditions were considered appropriate. The amount of curvature which can be obtained from unsymmetric panels is heavily dependent on the thickness of the plate and therefore 2, 4, 8 and 12 layers were tested. Two and four layers produced out-of-plane displacements which were considered too extreme for the proposed application. Conversely 12 the layered panel was too stiff and often did not show bi-stable behaviour. The 8-layered winglet was the only one to give configurations comparable to generic winglet cant angles in the deployed state and sufficient camber in the extended configuration.

The choice of the final configuration was determined through several criteria. Firstly, in the extended configuration, the transverse curvature should be sufficient to produce a significant increase in the lift generated, ideally in-line with the current high lift systems. This was particularly difficult to obtain and in practice attention should be paid to avoid flow separation. Another important aspect, considered through the snap-through analysis, was that the magnitude of the load required for the transition into the winglet shape, should be achievable within the range of pressure achieved during take off conditions and more importantly within the capabilities of the experimental test rig. Finally, the deployed configuration should match as closely as possible a traditional winglet design, allowing the possible exploitation of the aerodynamic benefits of common winglets. These criteria where used to help the selection process between the three proposed configurations. Fig. 4.18 and Fig. 4.21 show how the first configuration produced shapes not suitable for the proposed application. The extended configuration exhibits a negative

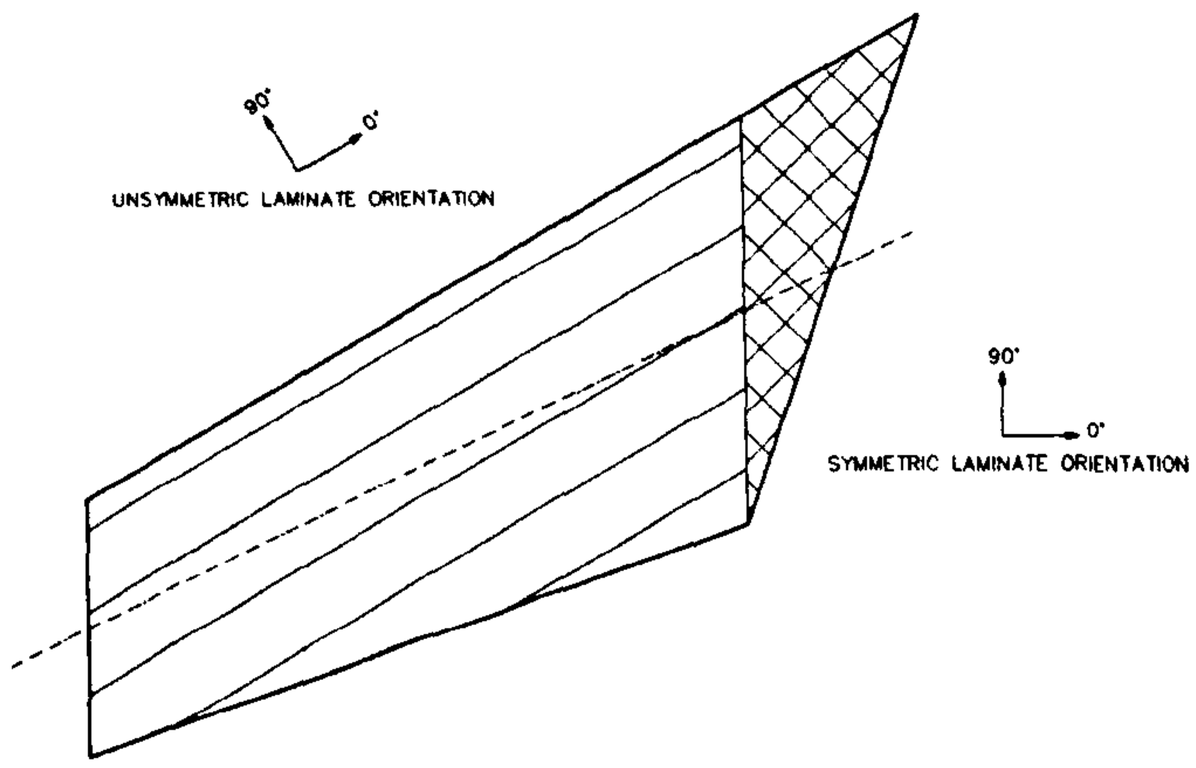

(a) Laminate parallel to LE

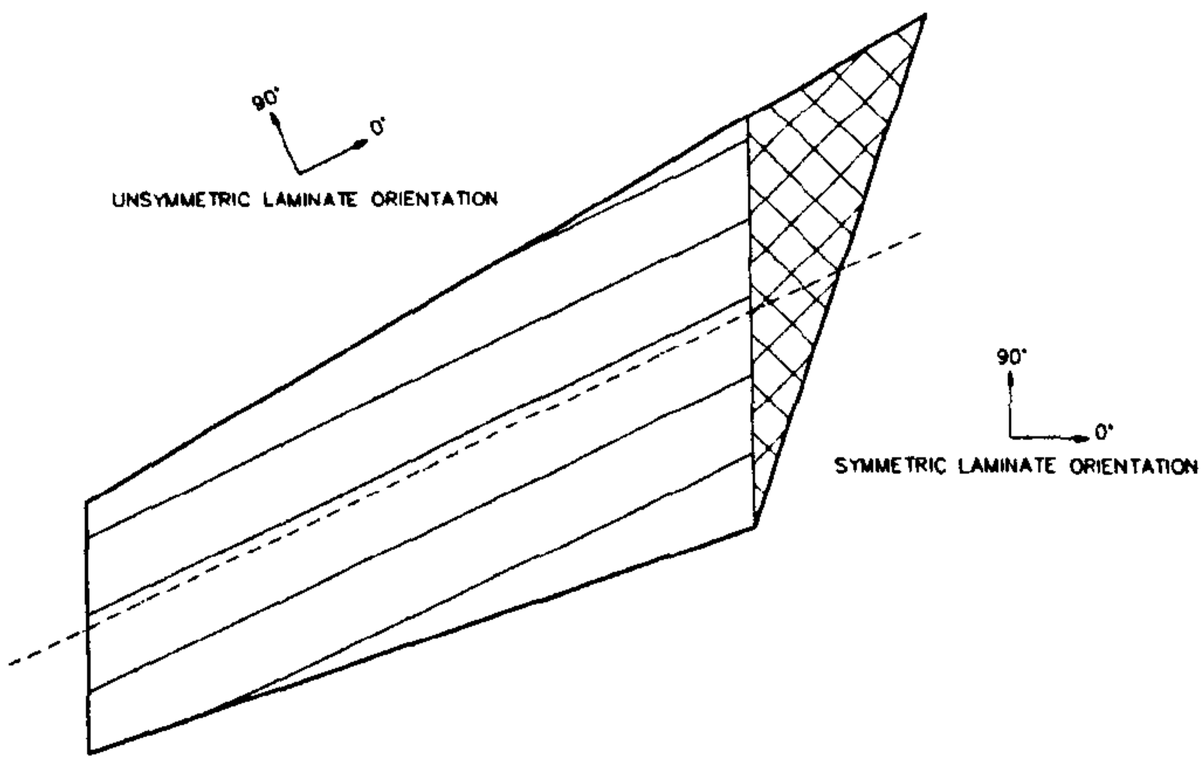

(b) Laminate parallel to centre-line

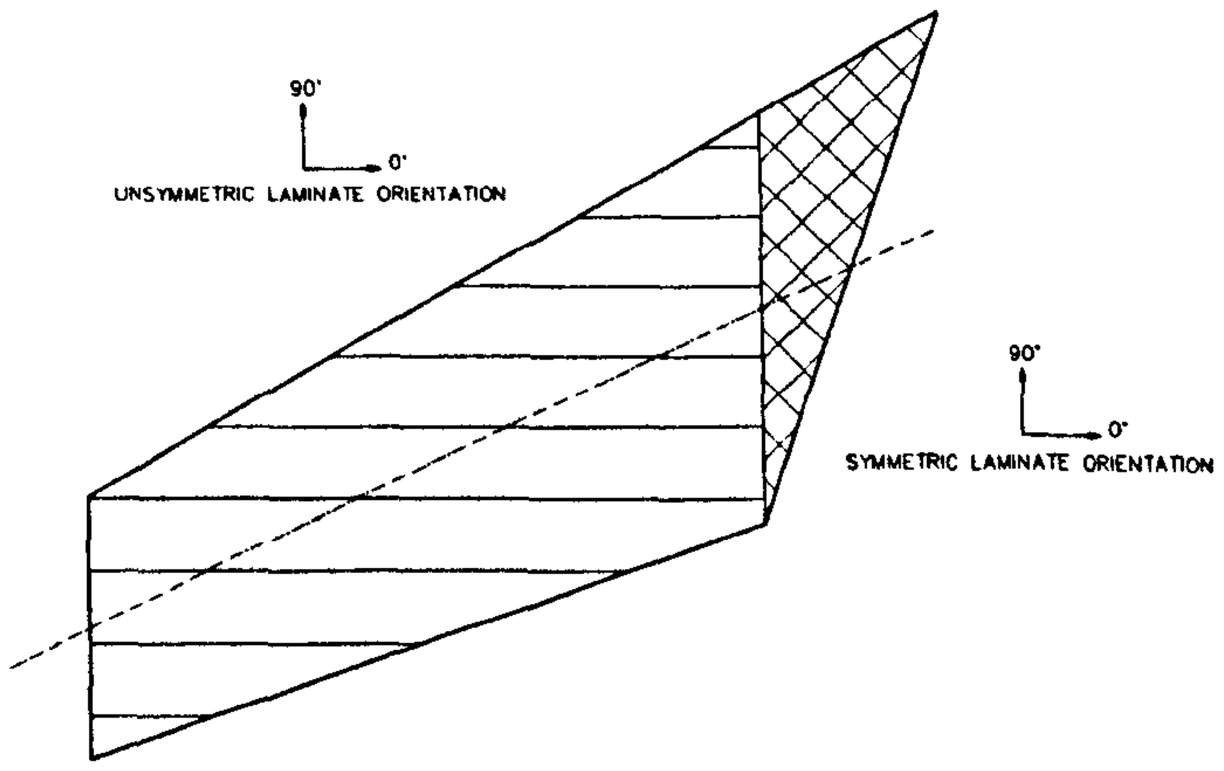

(c) Laminate parallel to the horizontal axis

Figure 4.17: Composite winglet laminate's configurations

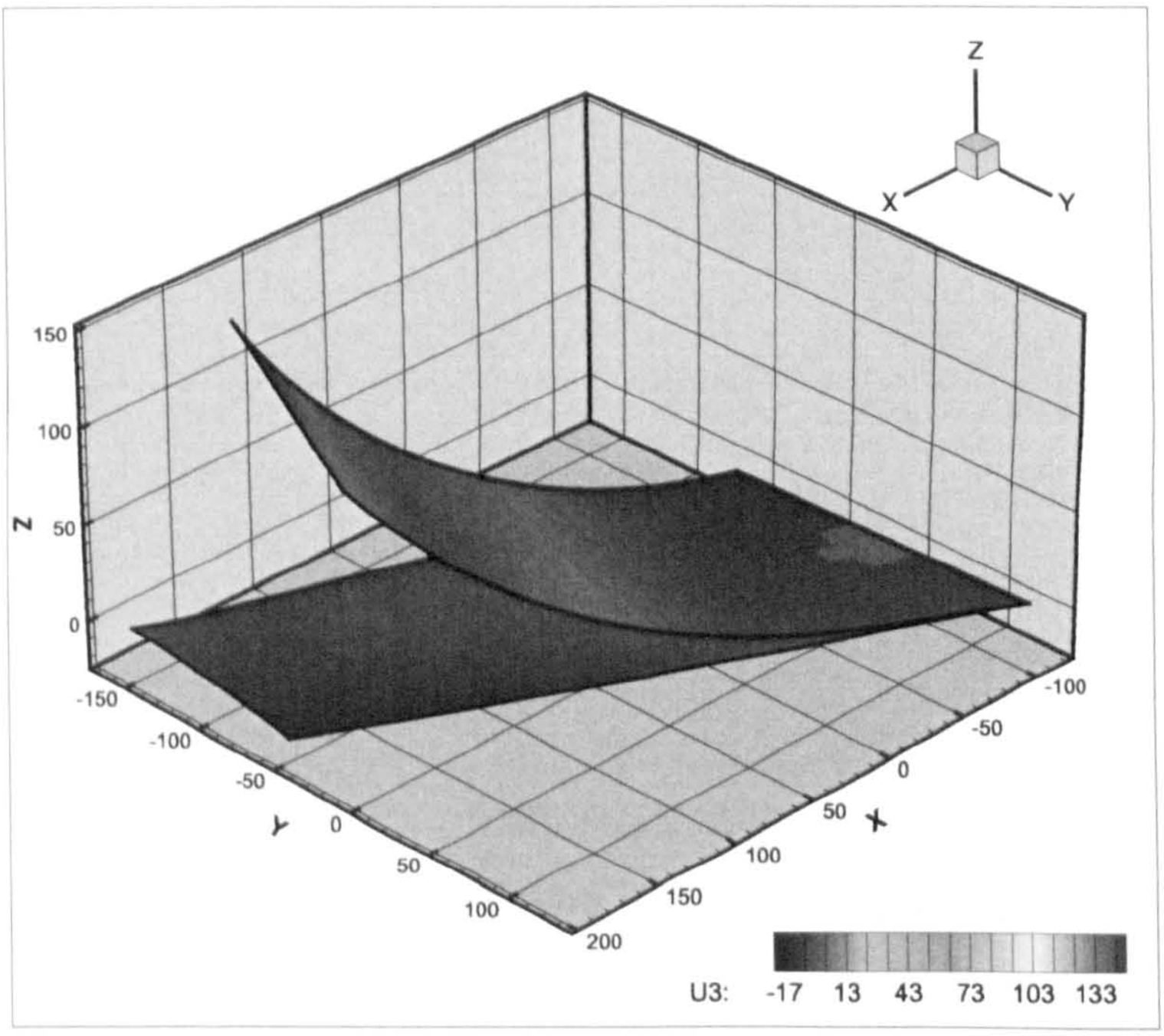

Figure 4.18: Isometric view for the fibres parallel to the leading edge configuration

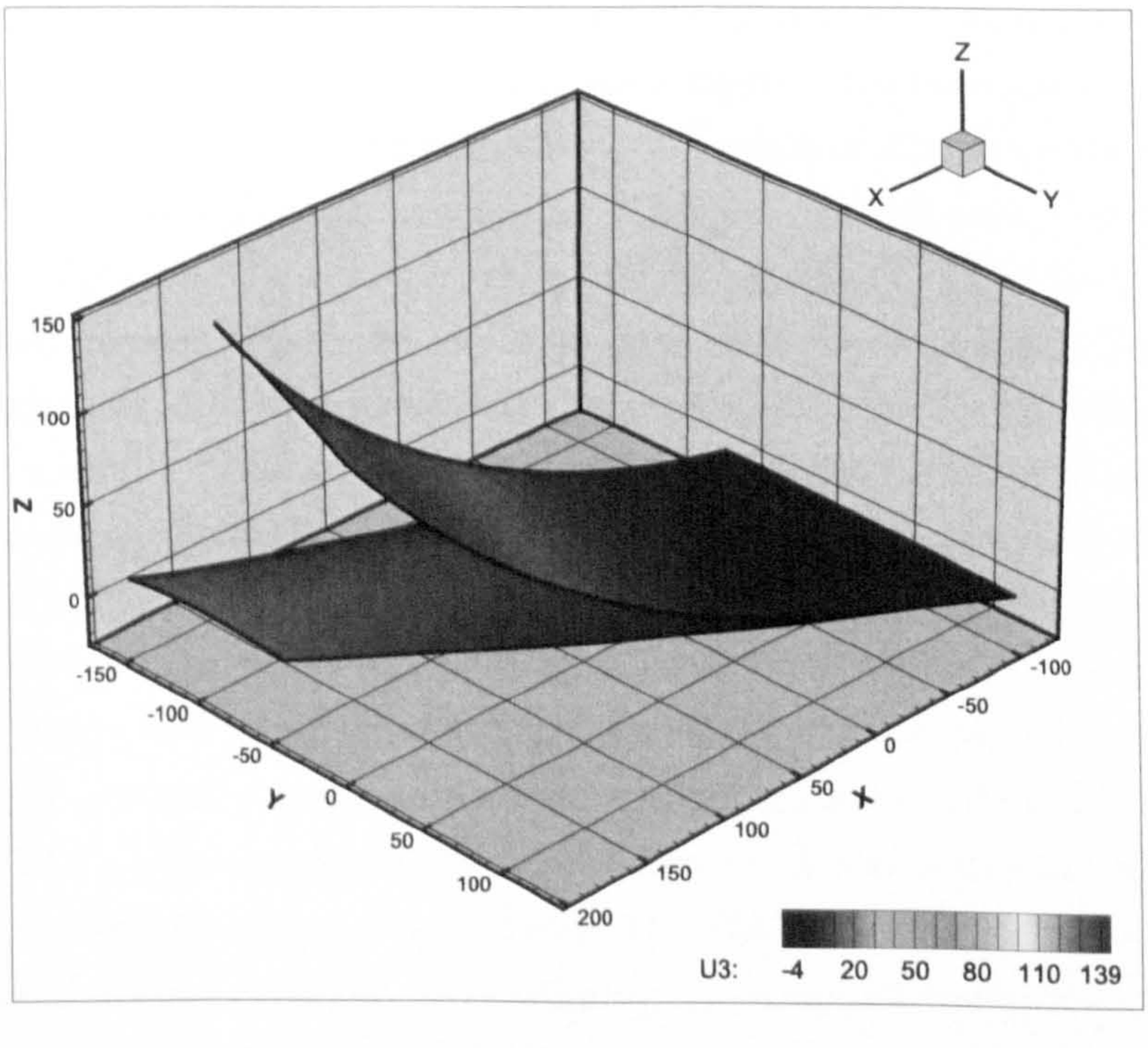

Figure 4.19: Isometric for the fibres parallel to the centreline configuration

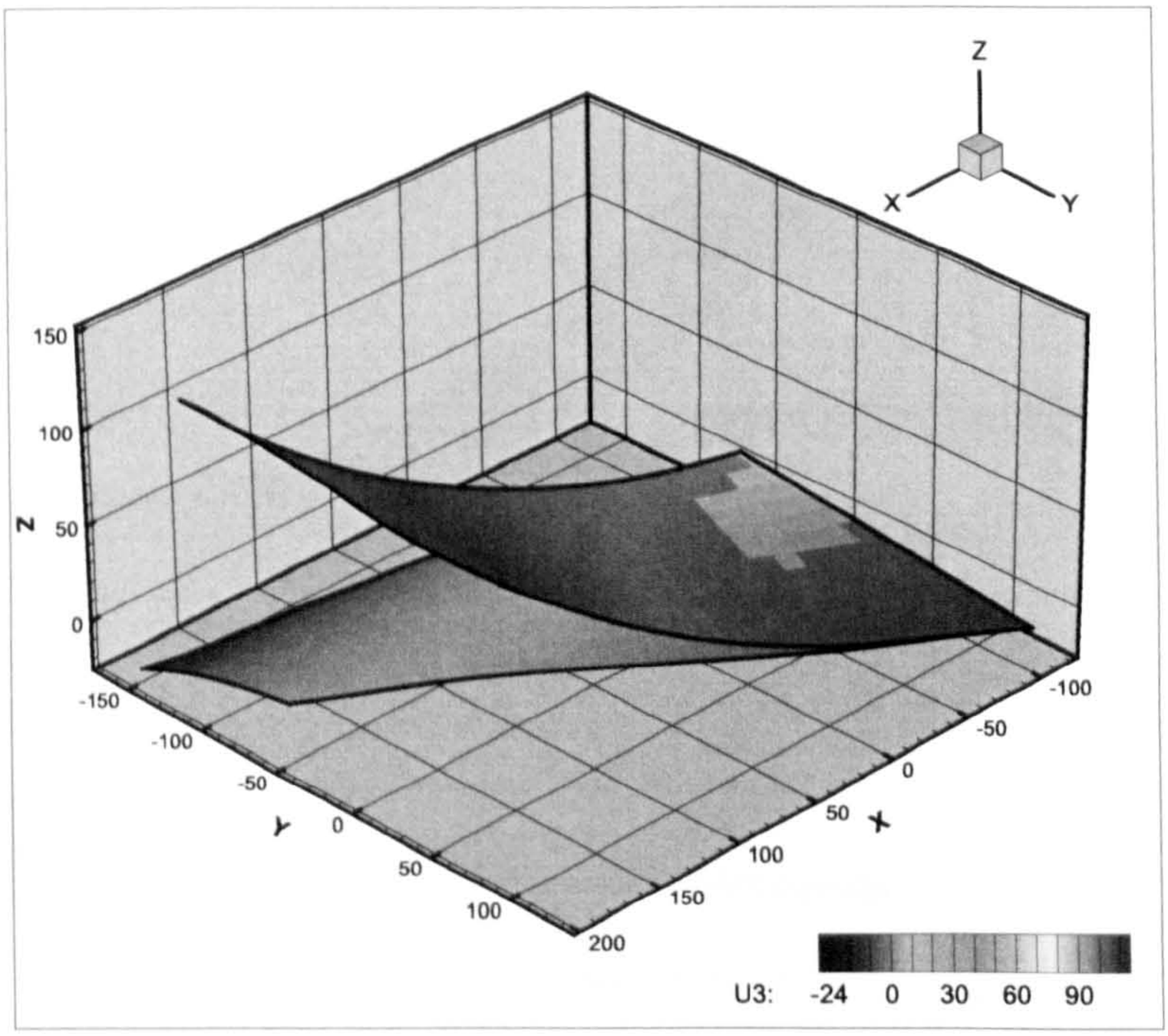

Figure 4.20: Isometric view for the fibres parallel to the horizontal axis configuration

twist producing an angle of attack at the tip of $\approx -6°$ and no noticeable camber can be observed. (ref. Fig. 4.21, side view). In the same figure a negative twist in the snapped configuration is observed with approximately $-21°$ angle of attack at the tip. This configuration would not produce any increase in the total lift and also, due to the twist in the snapped configuration, the side force would be significant. The third configuration can be examined through Fig. 4.20 and Fig. 4.23. For this case the laminate 0°-axis is rotated approximately 20° clock-wise with respect to the previous configuration. This produces effects almost opposite to those observed in the first configuration: there is still a large twist along the span, but this time the local angle of attack at the tip is $\approx +22°$, certainly useful for the generation of extra lift. Considering that the winglet is essentially a thin airfoil, such a high value for the local angle of attack suggests the development of large areas of severe flow separation towards the outboard portion of the winglet. This situation remains virtually unchanged at the winglet midspan where the angle of attack is reduced to 10.2°, approximately the level where stall conditions are well established on most thin airfoils [Abbott and von Doenhoff, 1959]. These results were particularly unfortunate for this configuration, as examining the snapped configuration revealed the predicted geometry to be quite suitable for the application, with a small local angle of

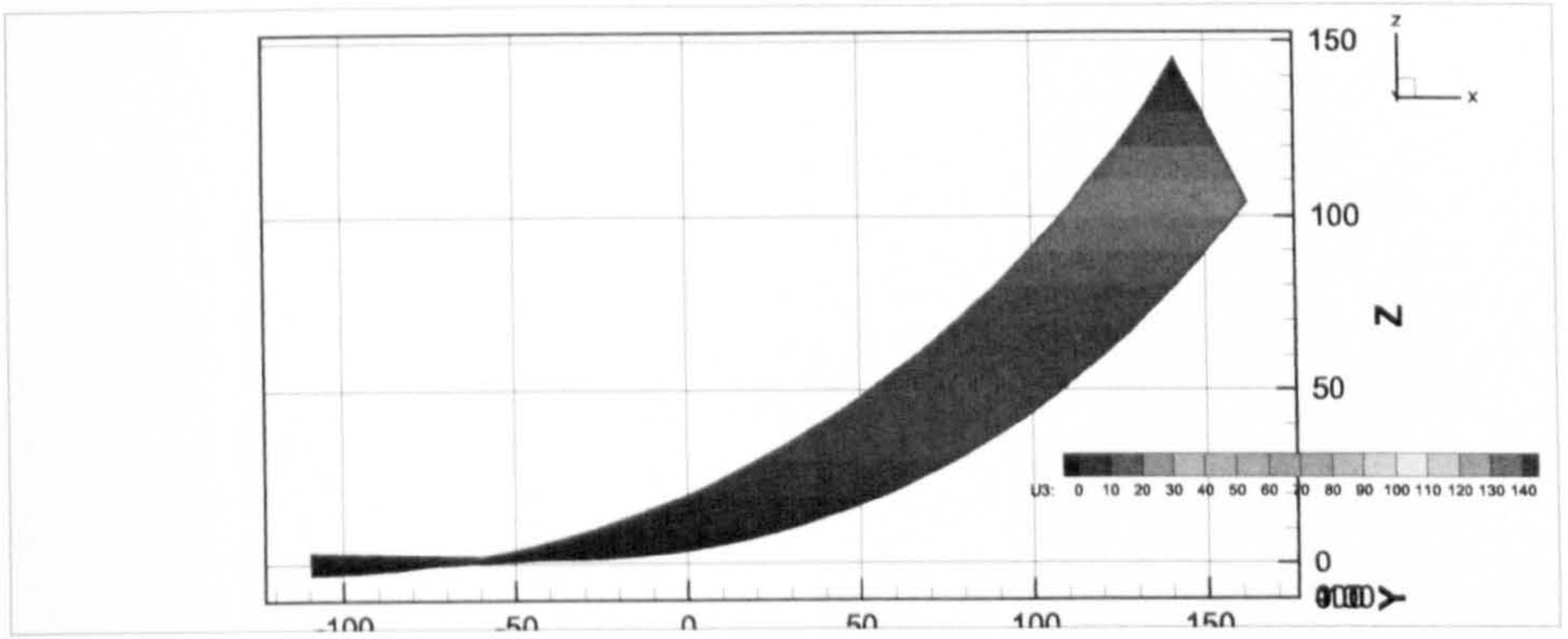

(a) Rear view

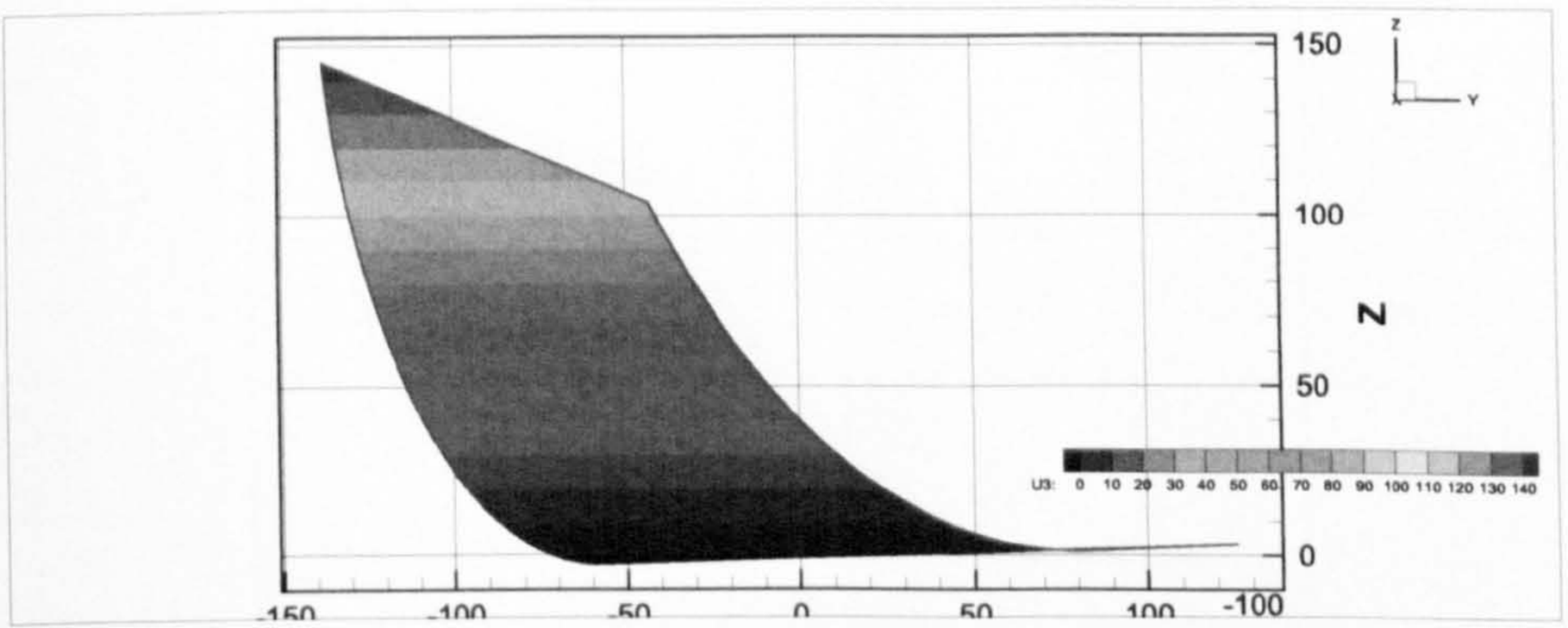

(b) Side view

Figure 4.21: Views for the fibres parallel to the leading edge configuration

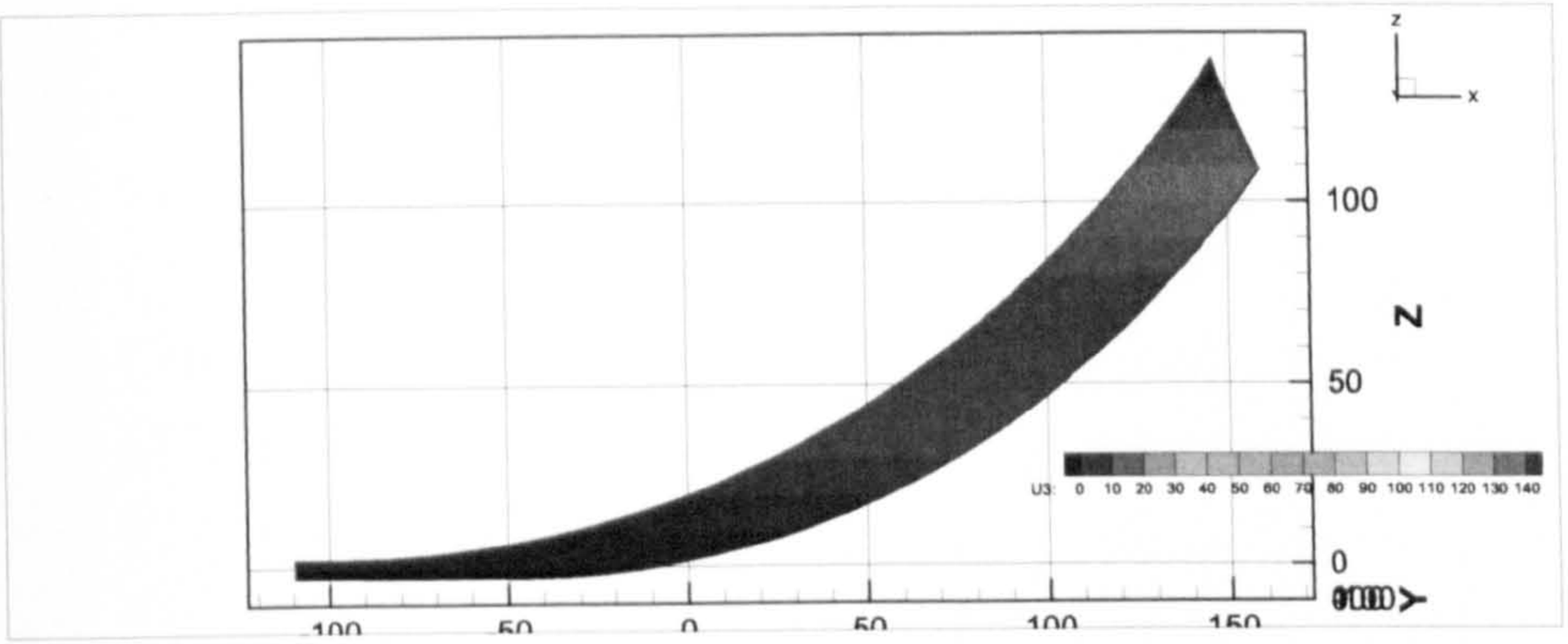

(a) Rear view

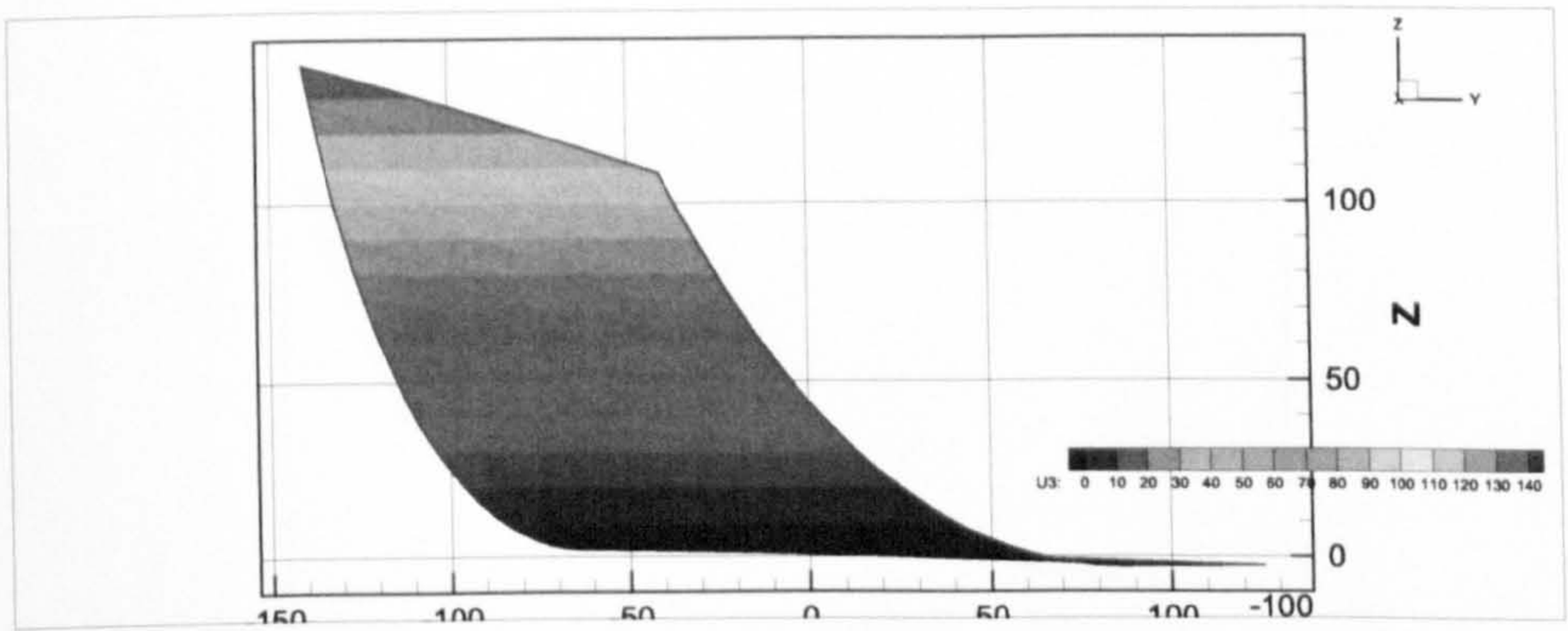

(b) Side view

Figure 4.22: Views for the fibres parallel to the centreline configuration

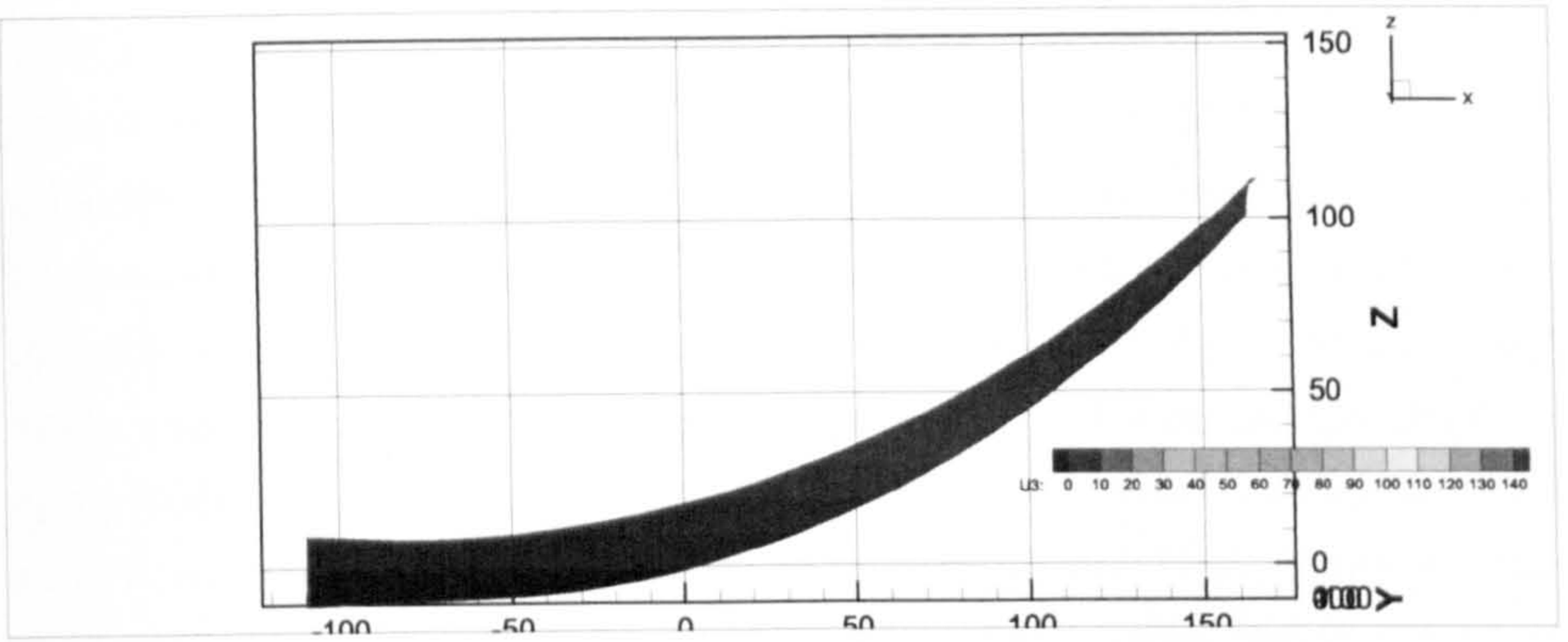

(a) Rear view

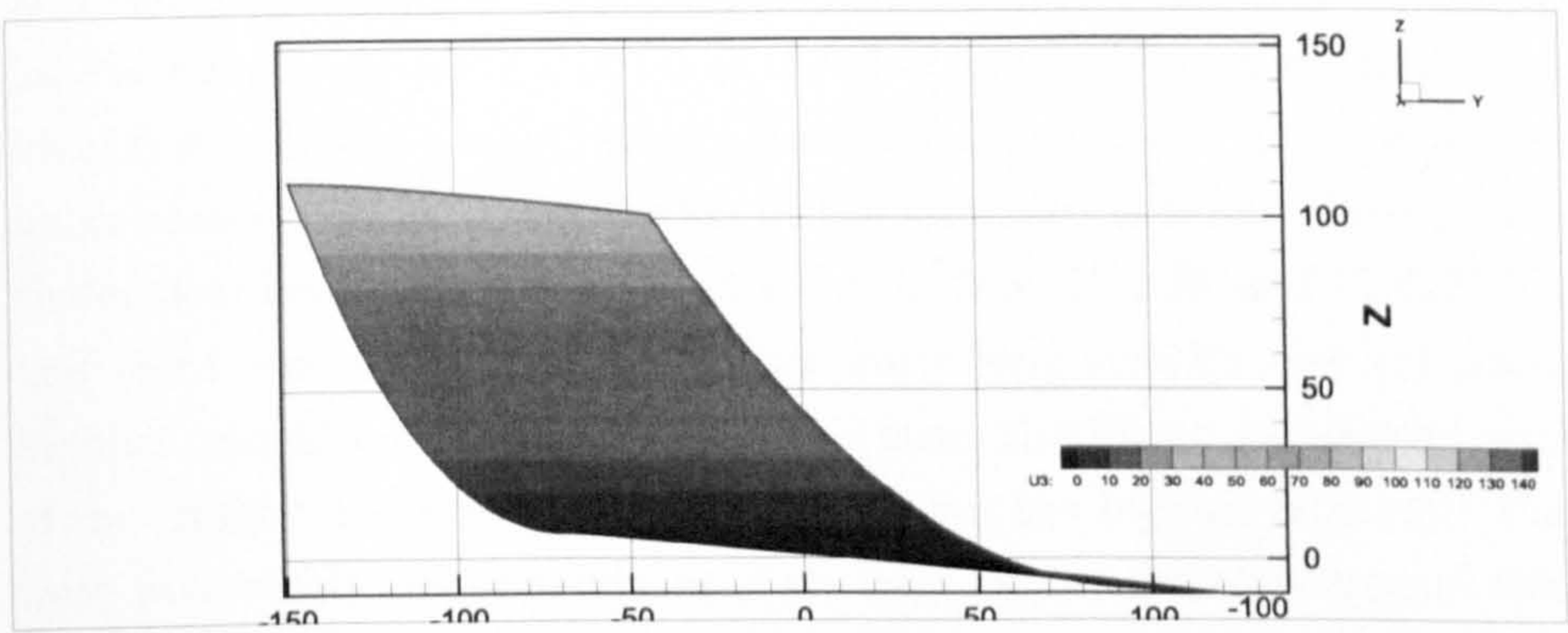

(b) Side view

Figure 4.23: Views for the fibres parallel to the horizontal axis

attack $\alpha = 1.2°$ of negative twist, a value that is in agreement with the "classical" winglet design requirements of $\alpha = 4°$ [Whitcomb, 1976]. The last case to be examined (ref. Fig 4.19 and 4.22) had the laminate 0°-axis aligned in an intermediate position with respect to the two previous cases . The unsnapped configuration exhibited a moderate camber of 3.2% and 6.1% at the tip and mid-span of the winglet respectively. Also the twist angle was found to be negligible along the span. These results were considered encouraging because, if on one side they are enough to produce lift augmentation, they are still sufficiently moderate not to cause flow separation. Unfortunately this had a trade-off with the snapped configuration in which the twist angle measured 10.2° at midspan and 15.7°at the tip section. The cant angle also, was found to have increased from 45.3° in the previous configuration, to 53.1°. This level is significantly lower than the classical recommendation for winglet design [Whitcomb, 1976], but it is still within more modern winglet design philosophies ($45° < \gamma < 75°$) [ESDU, 1998]. From the comparison between the three cases, it appears quite clearly that the orientation of the 0°-axis of the laminate is of great importance for the final shape and hence the performance of the winglet.

The results for the "load - displacement" diagrams are shown in Fig. 4.24, where "LE", "CL" and "Horizontal" refer to the fibre axis parallel to the leading edge, the centre line and the horizontal line respectively. The diagrams are very similar to those obtained for the compound plate and all of the characteristics of a bi-stable laminate are clearly identifiable: linear-elastic regime, critical load, snap-through (negative stiffness), second linear-elastic region. The rotation of the laminate axis has a less pronounced impact on the critical load, which was found to be 22.75N, 25.20N and 18.62N for the first, second and third case respectively. It is not surprising that the second configuration has the highest critical load since, only for this case, the fibres are aligned with the elastic axis of the winglet and therefore this laminate has the highest strength. The values obtained were well within the capabilities of the test rig for the wing tunnel analysis.

Further to these considerations, the second configuration was considered to meet the requirements for the proposed application best and was chosen for manufacturing and testing.

To manufacture the specimen for the wind tunnel testing phase, eight rectangular laminae, measuring 300mm×200mm of standard T300/914 carbon-epoxy pre-preg were laminated accordingly to Fig.4.17b. After assembly of the lay-up, the panel was trimmed to match the planform of the winglet and then cured in an autoclave according to the manufacturer specifications (ref. Fig. 2.2). The resulting composite winglet was then removed, inspected, cleaned and readied for wind tunnel testing (ref. Fig. 4.25).

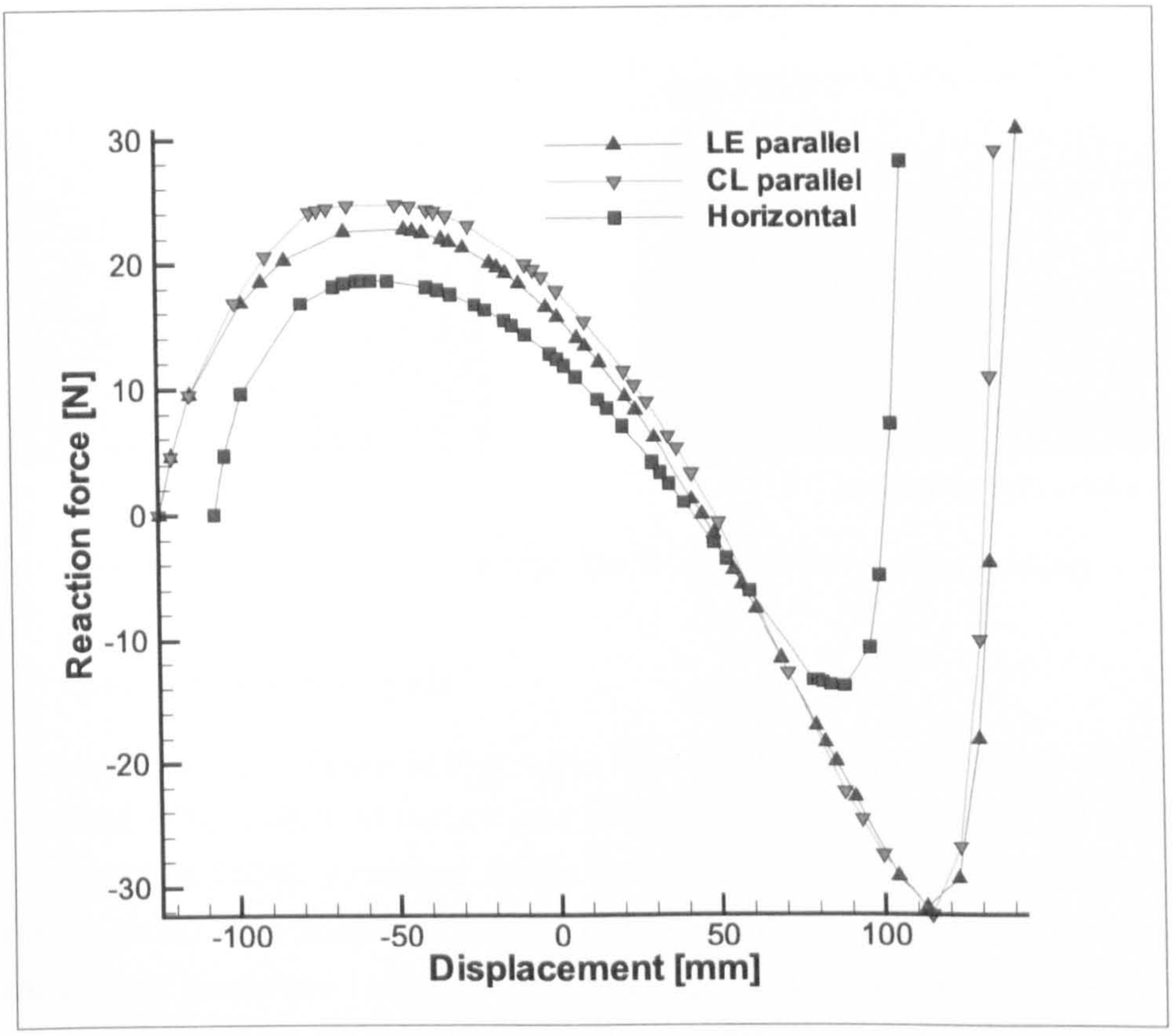

Figure 4.24: Bistable winglet comparison: snap loads

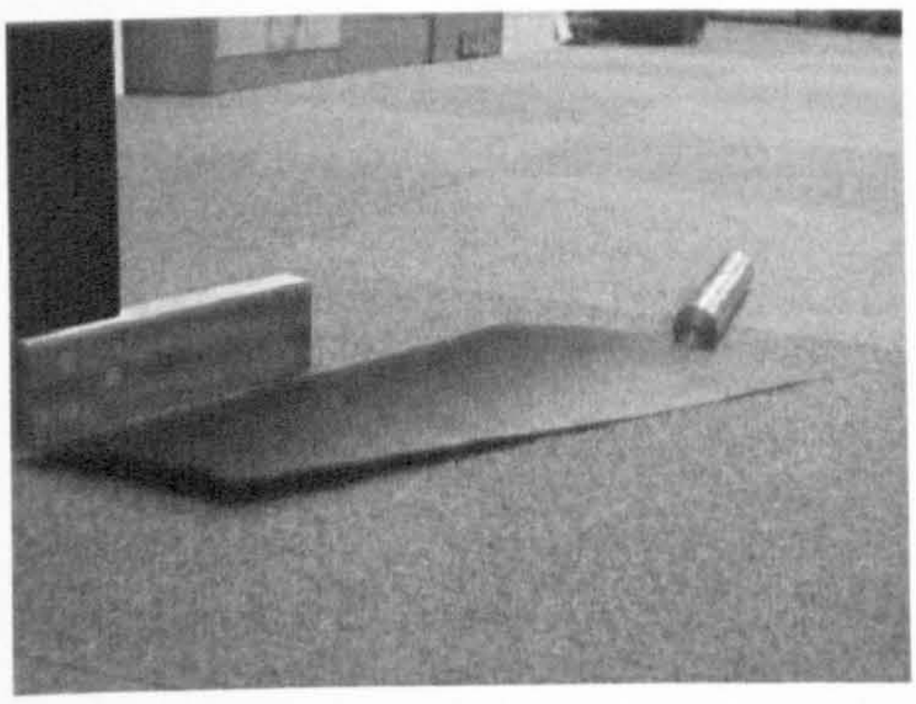

(a) Extended configuration

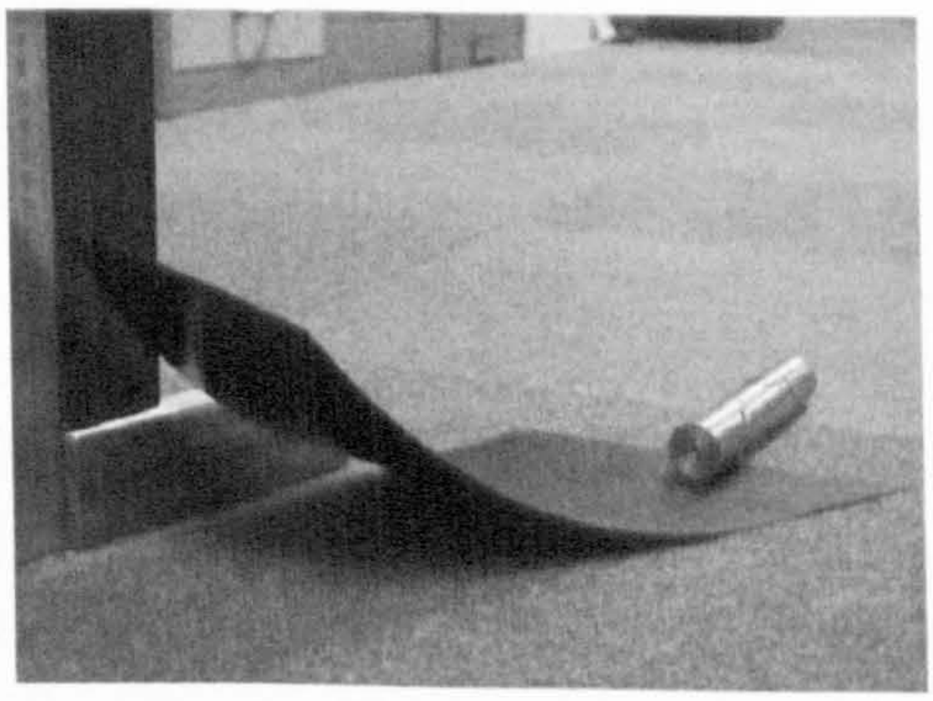

(b) Deployed configuration

Figure 4.25: Experimental model

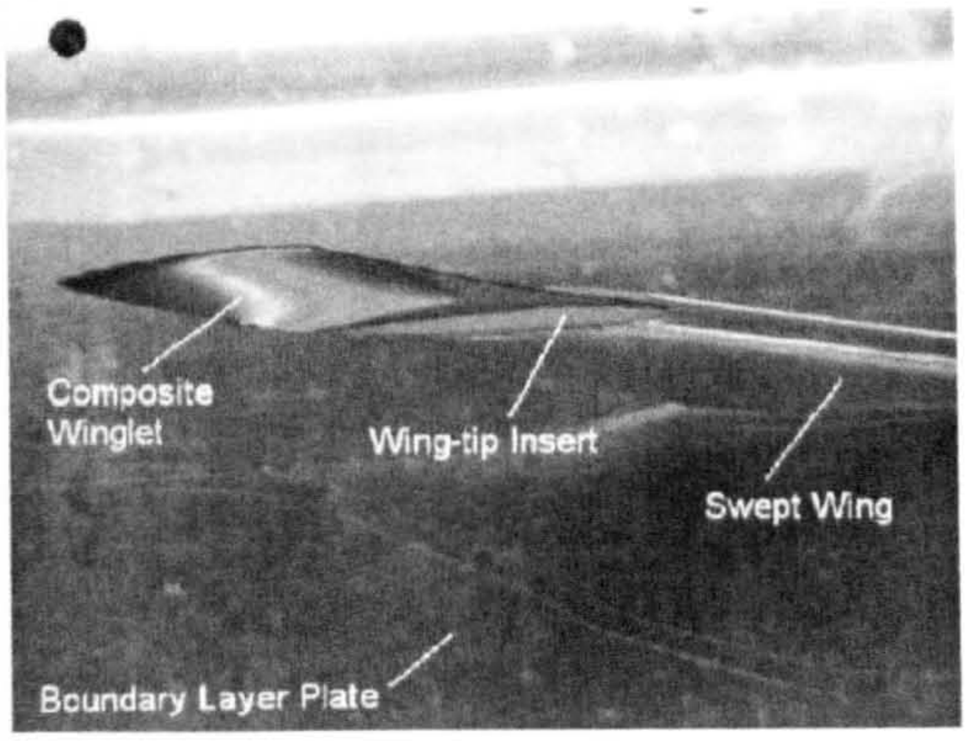

(a) Extended configuration

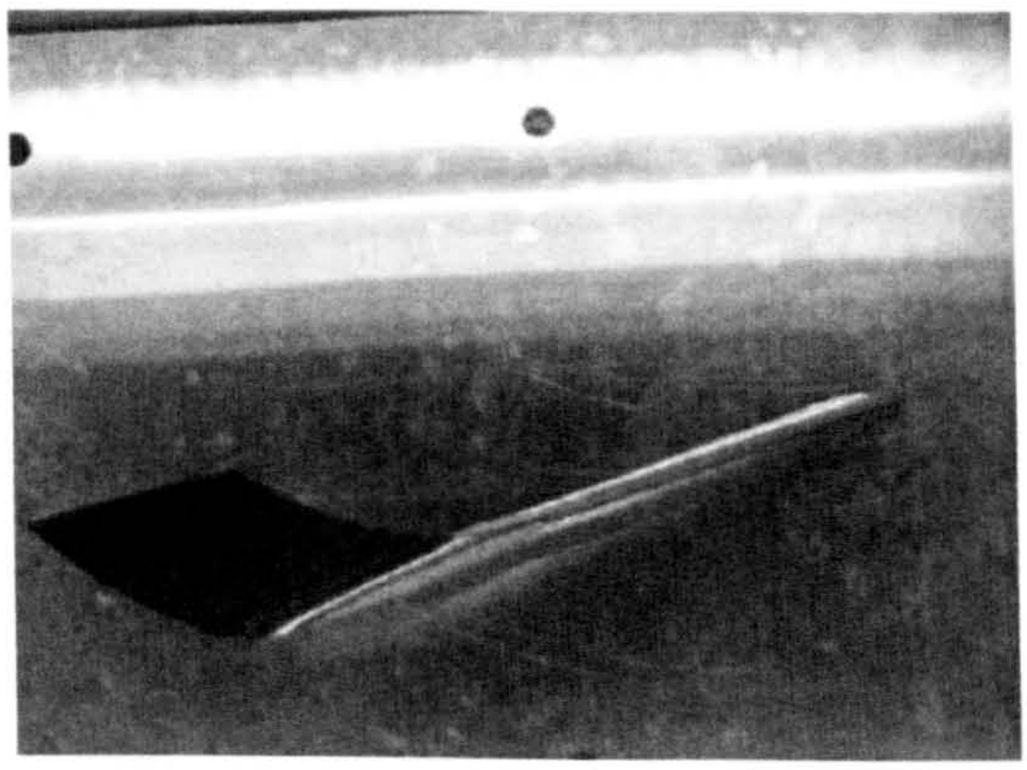

(b) Deployed configuration

Figure 4.26: Test rig assembly for winglet wind-tunnel testing

4.2.1 Experimental analysis

The experimental setup is shown in Fig. 4.26. The baseline wing was made of polyurethane foam laminated with a layer of carbon and wooden veneer to maintain an aerodynamically robust surface finish. Attached at the quarter chord point of wing root, a purpose built support metal bar, 26mm in diameter, was rigidly fixed to the internal structure of the wing via a machined insert bedded with epoxy adhesive and secure with metal fasteners. A removable plate, measuring 1100mm×760mm, was fixed 50mm off the side-wall test section for the purpose of minimising the interaction between the boundary layer of the wall and the flowfield around the wing. The swept wing was then anchored to a six-axis load cell, through a 30mm cut-out in the removable plate.

The load cell used to measure the response of the test rig to aerodynamic loading was an AMTI MC3A-500. The maximum lift, drag and side force capabilities of this cell were rated at ±2kN, ±1kN and ±1kN with pitching, rolling and yawing moments specified at ±56Nm, ±56Nm and ±28Nm respectively. After calibration, maximum differences for all six components returned prior to the wind tunnel testing was less than ±2.5%. Assessment of the maximum observed non-linearity as well as zero drift after a rigourous pre-testing programme were found to be better than ±0.5%. All data obtained from the load cell was digitised through a 16-bit dSpace data acquisition system, at 1000Hz, over a period of 60s. The swept wing was installed at mid-test-section height inside a closed test section, closed circuit wind tunnel with a maximum operating freestream velocity was $40\text{ms}^{-1} \pm 1\text{ms}^{-1}$. The freestream turbulence level at the model station was approximately 0.2%. Under test conditions, measurements of all six forces and moments

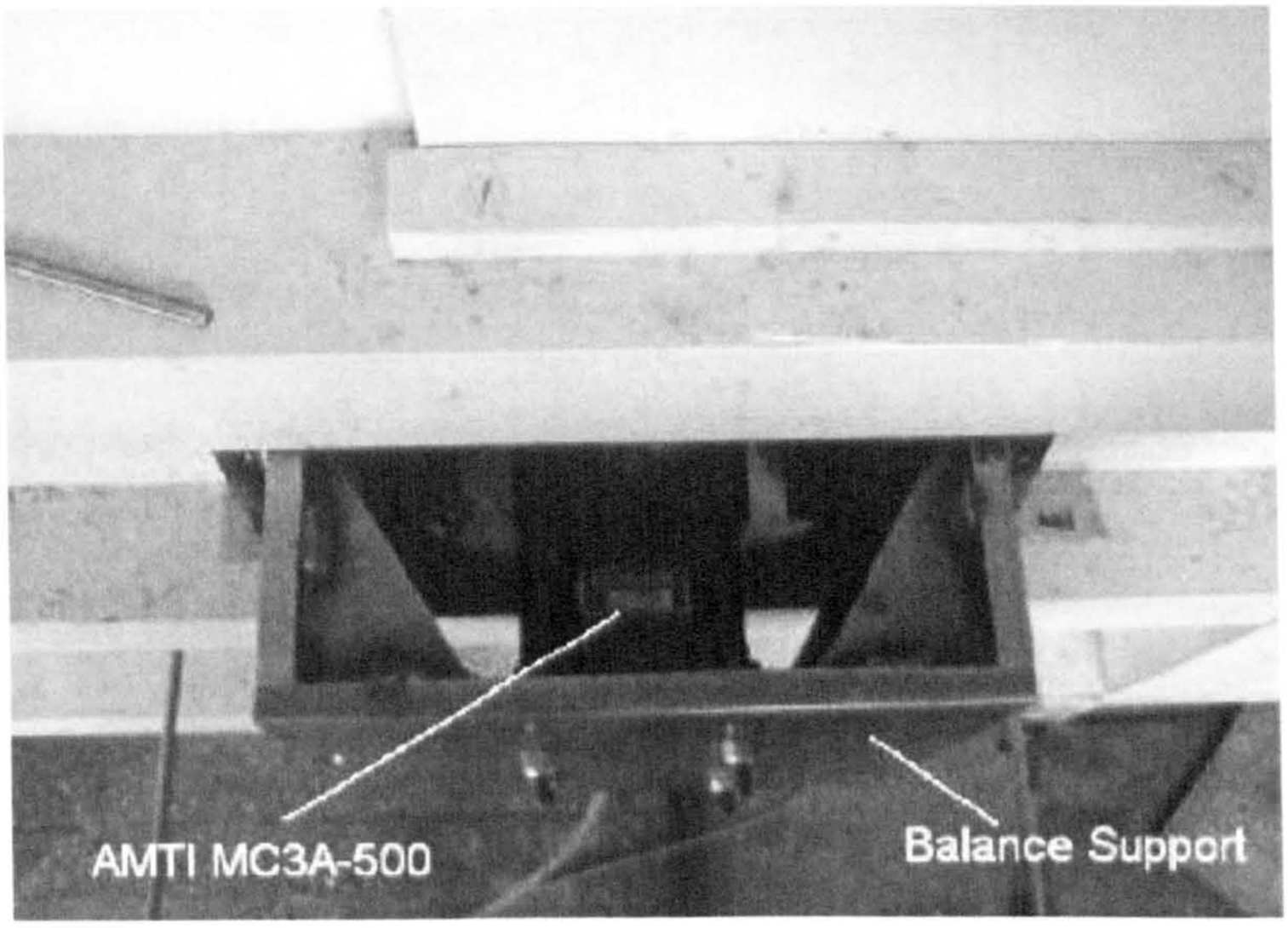

Figure 4.27: Details of balance setup

were taken prior to increasing the wind speed, which allowed the compensation of the final test results for these initial conditions. To increase the aerodynamic loading on the winglet, the wind tunnel was brought up to speed manually and steadily by the operator until winglet snap was achieved. This process was repeated at several different angles of attack ranging from 0° to 27.5° (position error ±2°). For each of these angles of attack, the freestream velocity at the point of winglet snap was calculated and recorded giving a test Reynolds Number range between 2.8×10^5 to 4.8×10^5. The support bar was attached to an externally mounted rotation stage, which allowed manual adjustment of the angle of attack of the swept wing. This was mounted directly to the force and moment balance, which was also connected to a support frame fixed to the outside test section wall (Fig. 4.27). The composite winglet was mounted, on the tip of the baseline wing, through a machined Nylon 6 insert, moulded to match the camber line of the winglet. Once mounted into the insert, the winglet was slotted into a recessed area of the wingtip.

4.2.2 Results

Figure 4.28, shows a summary of the aerodynamic forces (lift L, drag D, rolling moment l, pitching moment m and yaw moment n) before and after the snap. The results are consistent with usual data found in literature [Raymer, 1992], including a 'drag bucket', where the drag is at a minimum for small values of angle of attack (thereafter increasing

angle of attack [°]	Lift increase [%]
0	438
2.5	58
12.5	6
> 12.5	8.3-11

Table 4.1: Lift augmentation generated by the winglet

non-linearly) and an initial linear increase in lift, with increase in angle of attack. In this particular case of swept wing, this linear lift increase was found to persist up to a maximum at $\alpha = 22.5°$, decreasing marginally thereafter as the wing stalls. As expected, side force and yawing moment both show trends significantly different from those already discussed. For side force, the results tend to indicate a substantial and curious degree of inconsistency, firstly increasing up to $\alpha = 17.5°$, then linearly decreasing thereafter up to the maximum angle of attack tested. At the two highest angles of attack tested, side force is shown to reverse direction suggesting unsteady stall conditions [Orlik-Ruckemann, 1983]. For yawing moment, results show a similar trend to that already discussed for lift, pitching moment and rolling moment for $\alpha \leqslant 17.5°$. After this angle of attack, the yawing moment deviates, increasing significantly to magnitudes almost double that observed at $\alpha = 17.5°$.

For all angles of attack tested, most aerodynamic force and moments show a measurable decrease in mean magnitude after winglet snap. From the results of lift force, the extra lift augmentation generated by the bi-stable winglet, was found to range as shown in Table 4.1. Considered that, for existing advanced high-lift system, the increase in lift is around 50% of the maximum lift [Raymer, 1992], only the values obtained for angle of attack below 2.5°compare well. However, the consistency in the lift generation indicates that the proposed concept performs better than wings with traditional flap [Abbott and von Doenhoff, 1959]. For $2.5° \leq \alpha \leq 27.5°$, all moments after snap were found to decrease in the range of $15\%-55\%$ when compared to results before snap. Pitching moment results, in particular, compared well with the deployment of double slotted trailing edge flaps (DSTEF). Between deployment and retraction the typical correction required for the pitching moment are $\Delta C_m \cong -0.3$ at C_{Lmax} [Abbott and von Doenhoff, 1959]. The values measured during the test reached a maximum of $\Delta C_m \approx 0.14$ with the winglet in the extended configuration ($\alpha = 2.5°$ and $V = 23\text{ms}^{-1}$).

Table 4.2 and Fig. 4.29 show the freestream velocity at which the winglet snapped for the different angles of attack tested. The speed dimished with increasing angle of attack and the maximum measured value was 27ms^{-1} at $\alpha = 0°$. Under these circumstances, the

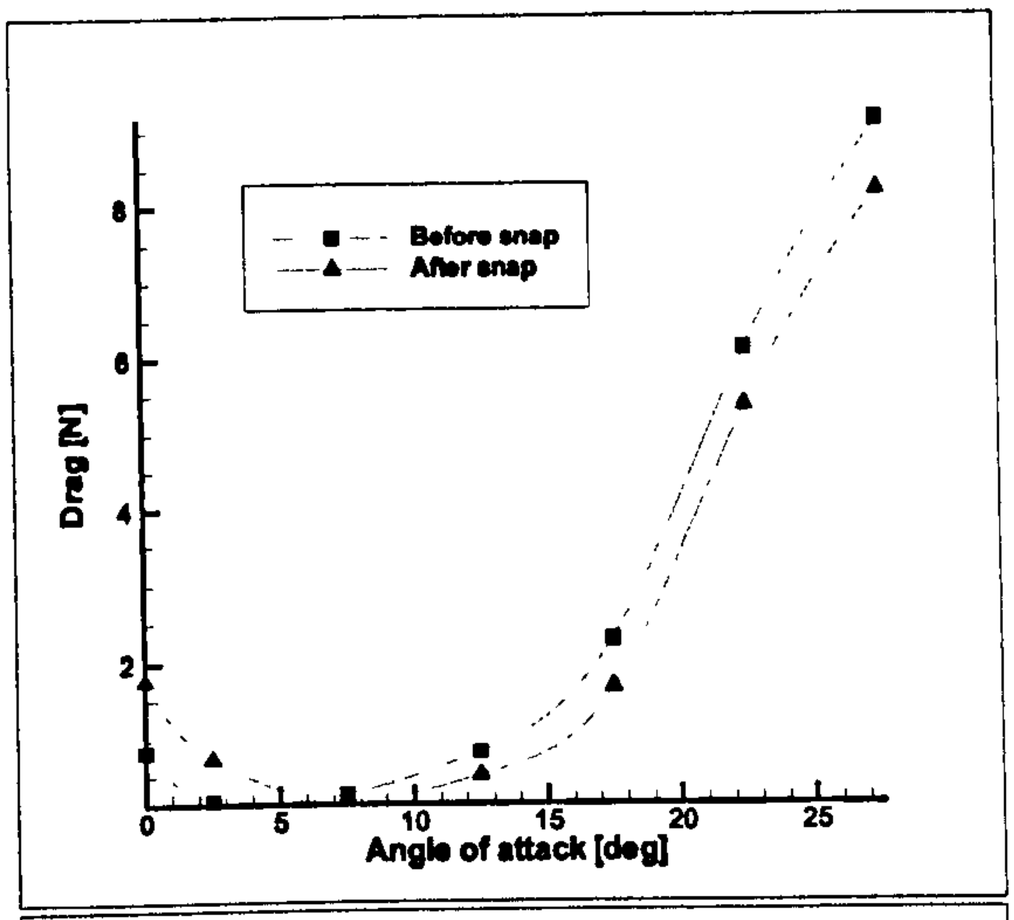

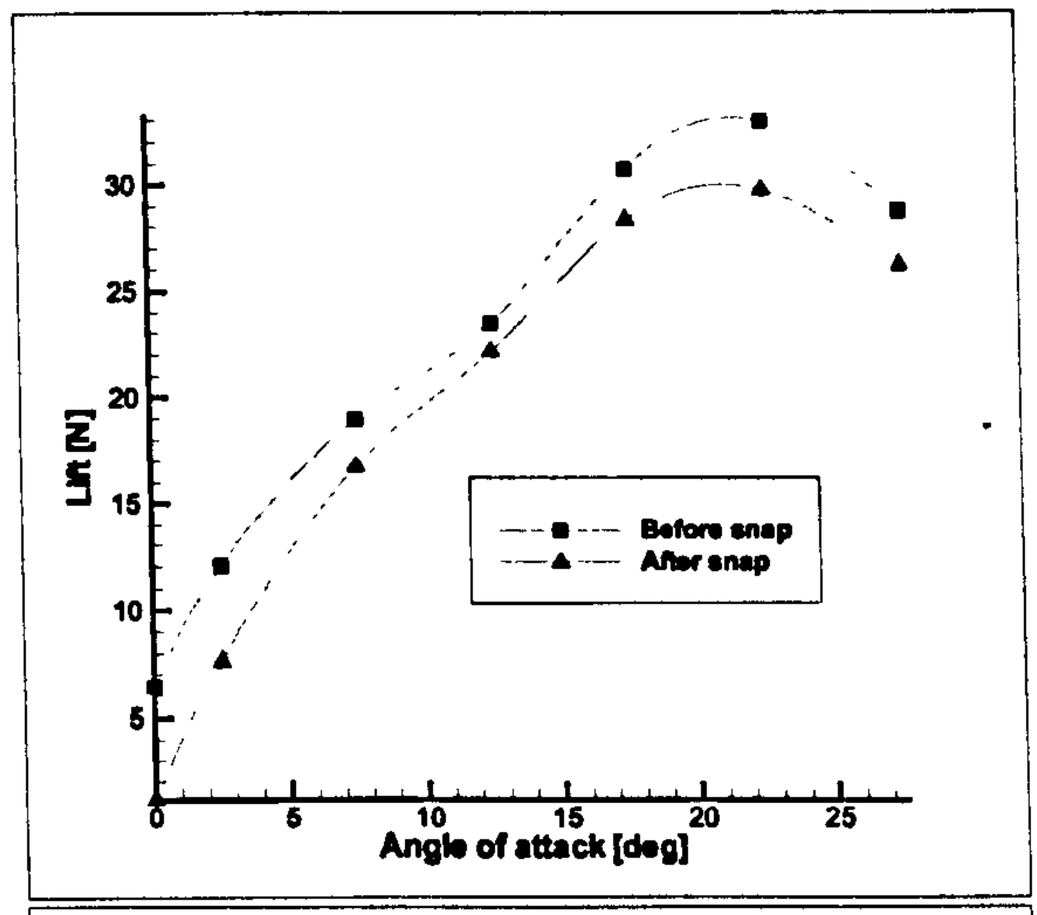

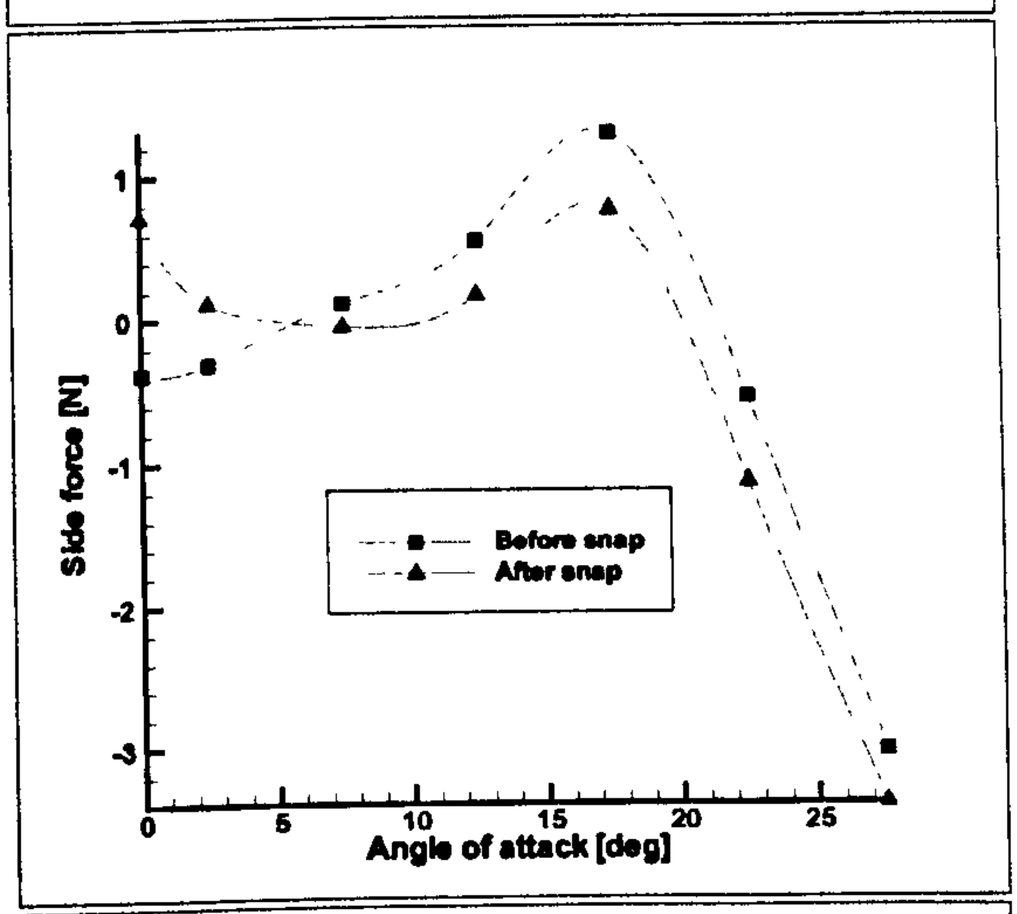

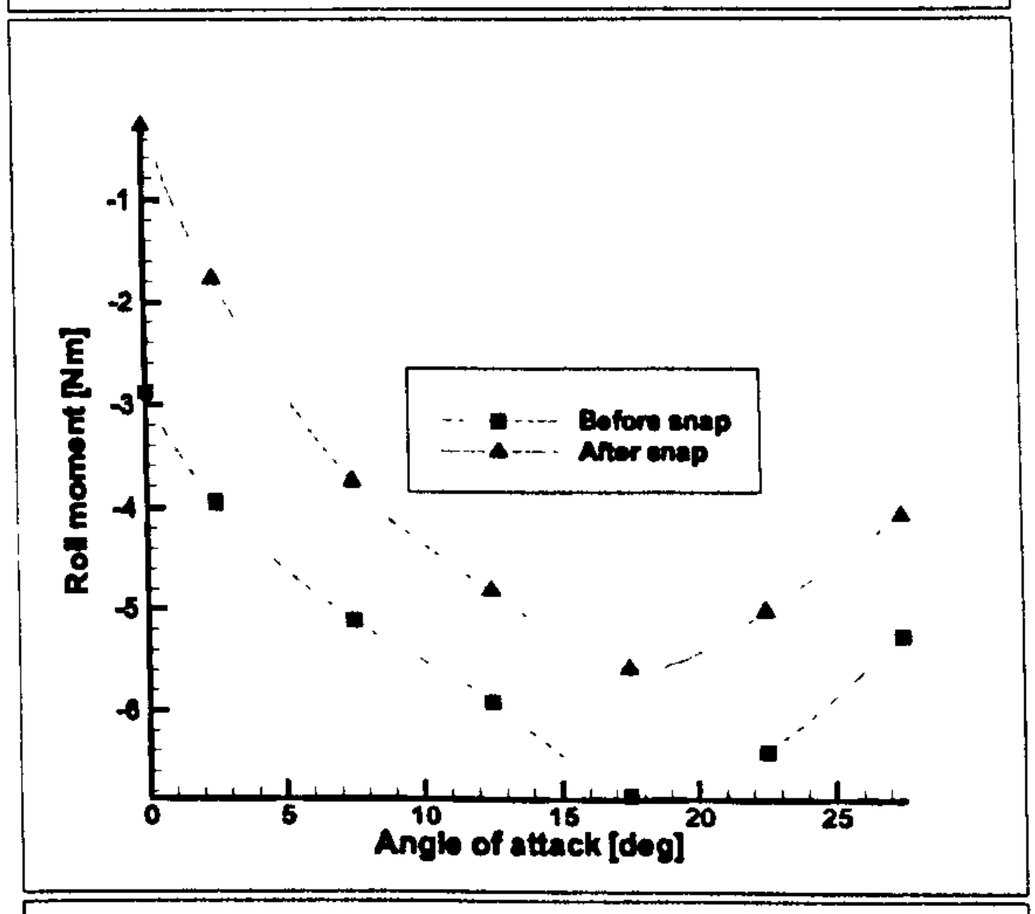

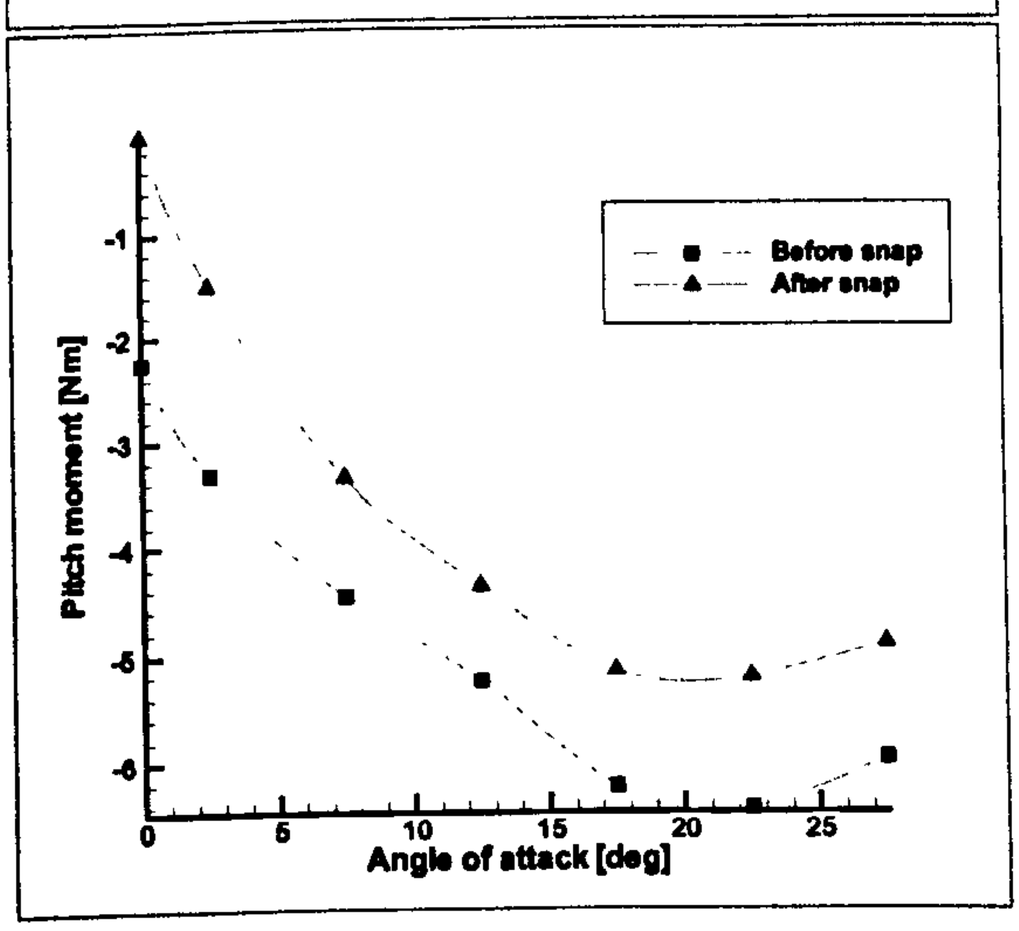

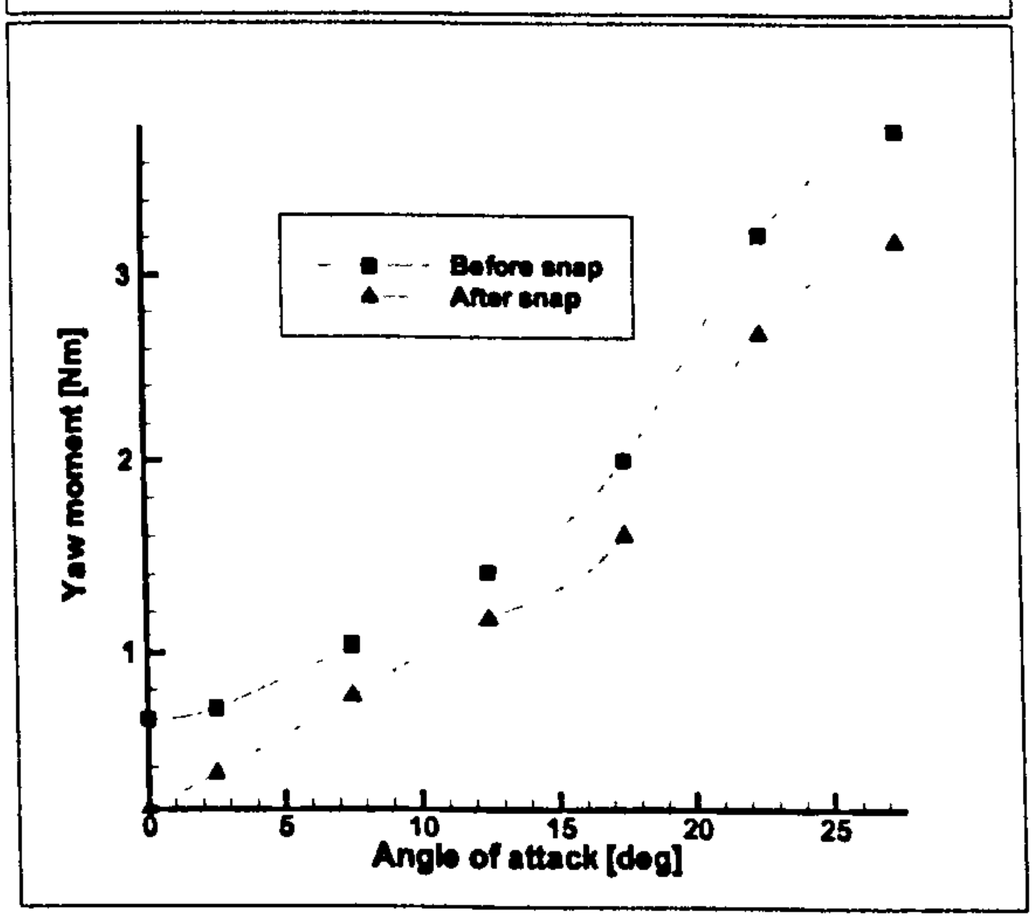

Figure 4.28: Aerodynamic forces before and after the snap

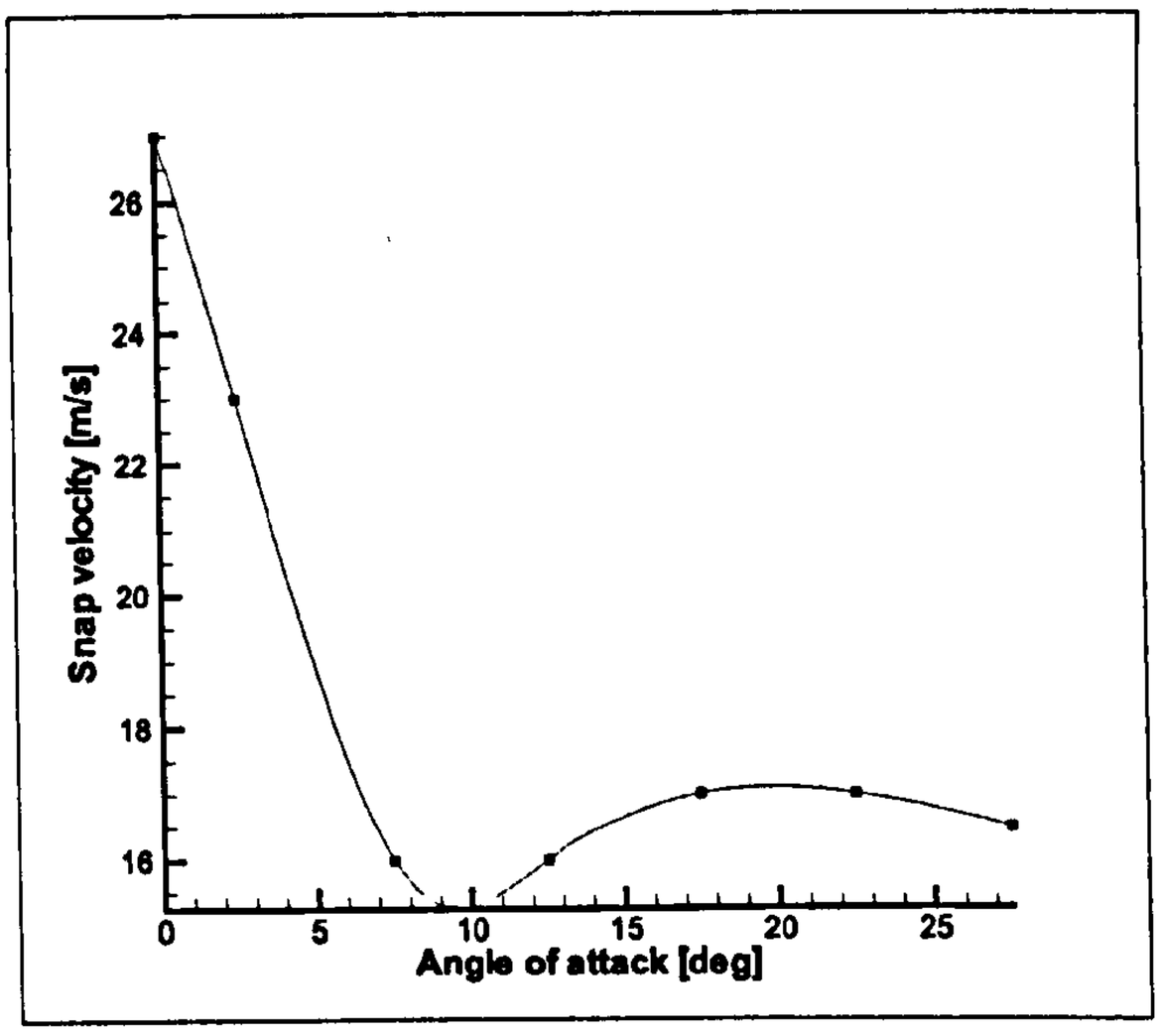

Figure 4.29: Snap velocity vs. angle of attack for the winglet

Table 4.2: Angles of attack and snap velocities for the winglet

Angle of attack [°]	0	2.5	7.5	12.5	17.5	22.5	27.5
Snap velocity $[ms^{-1}]$	27	23	16	16	17	17	16.5

resultant of the aerodynamic forces generated is almost vertical. With increasing angle of attack, the required speed decreased rapidly reaching a minimum value of 16ms^{-1} at $\alpha = 7.5°$. This is explained by the fact that for these values of the angle of attack, the increase in dynamic pressure is translated into an increase of vertical force contributing to the snap, hence a rapid decrease in snapping speed. With higher angles of attack, however, the situation is more complex as the aerodynamic resultant is no longer in line with the vertical and therefore both the lift and the drag contribute to the force required to snap. In addition, unsteady oscillations of the winglet indicate that flow separation might have occurred. This explains why the snapping velocity remains relatively constant at $16 - 17\text{ms}^{-1}$.

Figure 4.30 shows an example of the dynamics of the aerodynamic forces as measured by the load cell. The values are sampled over a period of 60s, which was considered sufficient for the transient to decay. There is an increasing degree of unsteadiness which is clearly identified by the sharp peak in the response. After the snap, the unsteadiness remains present and it seems to be marginally increased. This might be explained by the interaction between the flow field and the curved configuration of the winglet, which is considerably more flexible when compared to the shape before the snap.

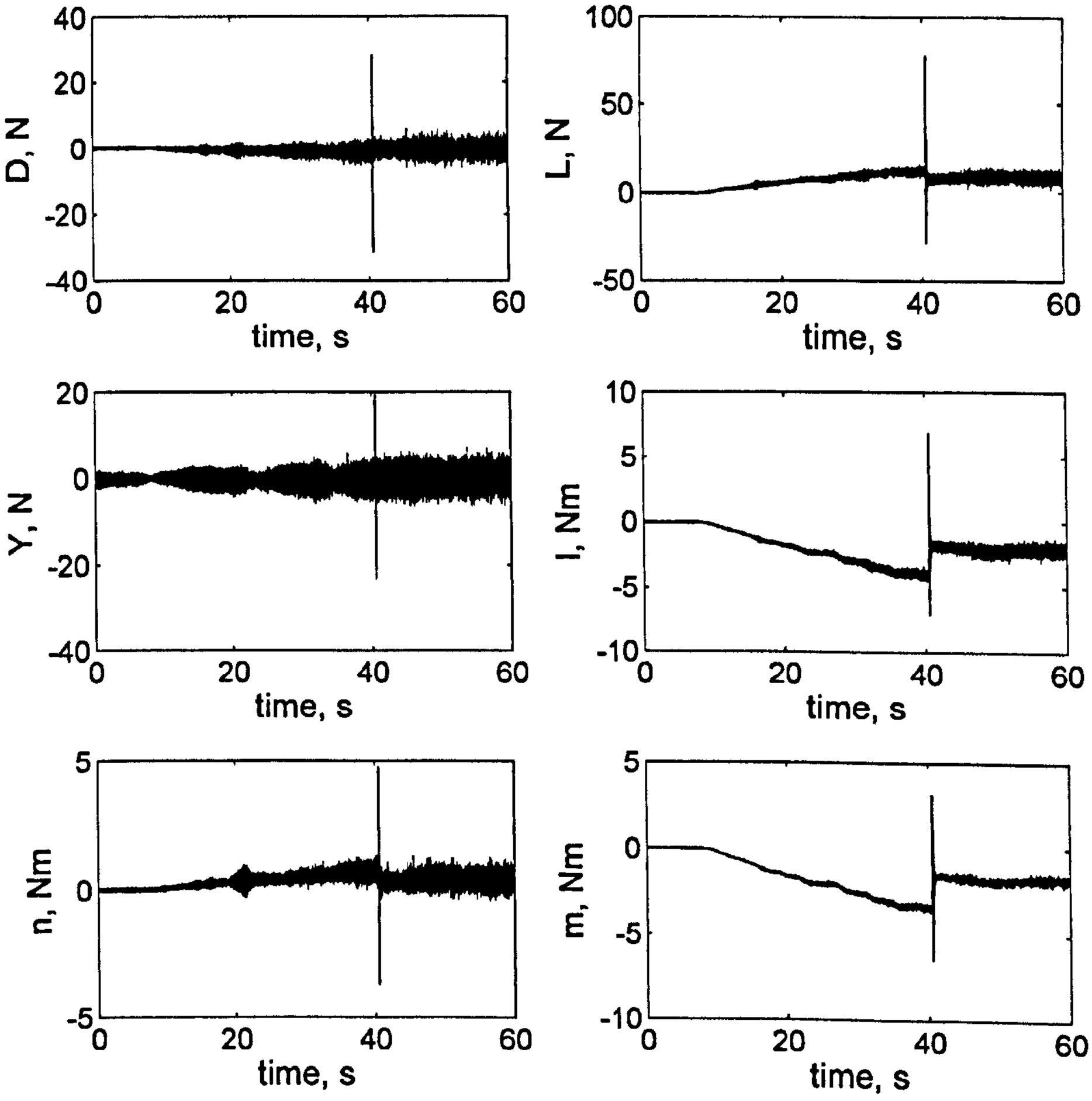

Figure 4.30: Response of the composite winglet and swept wing combination at $\alpha = 2.5°$

Figure 4.31 gives a more detailed view of the snap dynamics for the lift and the three associated moments. Immediately before the winglet snaps, the diagrams show a reduction in magnitude to levels consistent with those after the snap. Then, at approximately 40.51s, the large peak in the dynamic loads occurs and after a further $0.3 - 0.4$s of oscillatory transient, the steady response is re-established at the new value. The duration of the dynamic snap was found to last approximately for half a second, though more accurate measurements are required to obtain an estimate of the time constants involved.

The maximum and minimum loads experienced during the snap-through are presented in Fig. 4.32. With the increasing dynamic pressure, elastic energy is stored in the winglet until the winglet snaps. The snap is quite abrupt and the transient load measured by the load cell can reach up to 200% of the steady-state values values. From a design point of view, it is clear that these are the loads to be used for the design phase of the winglet. Furthermore, the winglet behaviour poses great problems if a control system was to be designed to comply with such sharp peaks. However, piezoelectric active systems [Portela et al., 2008, Schultz, 2008, Ren, 2007] could be used to counteract, at least partially, these effects.

A detailed analysis of the snap-through dynamics is therefore important and it is certainly part of the work that need to be carried out for future developments of the device.

4.2.3 Remarks on the Bi-stable Blended Winglet

The Bi-stable Blended Winglet introduced a novel concept to generate lift augmentation for low subsonic flows. The winglet was obtained through composite panels with a tailored unsymmetric stacking sequence. This demonstrated the great level of shape tailoring that is possible to achieve by modifying the fibre orientation and using unsymmetric laminates. Experimental tests were performed to show a significant increase in the lift generated in the first equilibrium shape. The second equilibrium shape, similar to a conventional winglet design, showed significant dynamic loadings during the snap-through process, suggesting the need for more in-depth dynamic analysis of bi-stable structures.

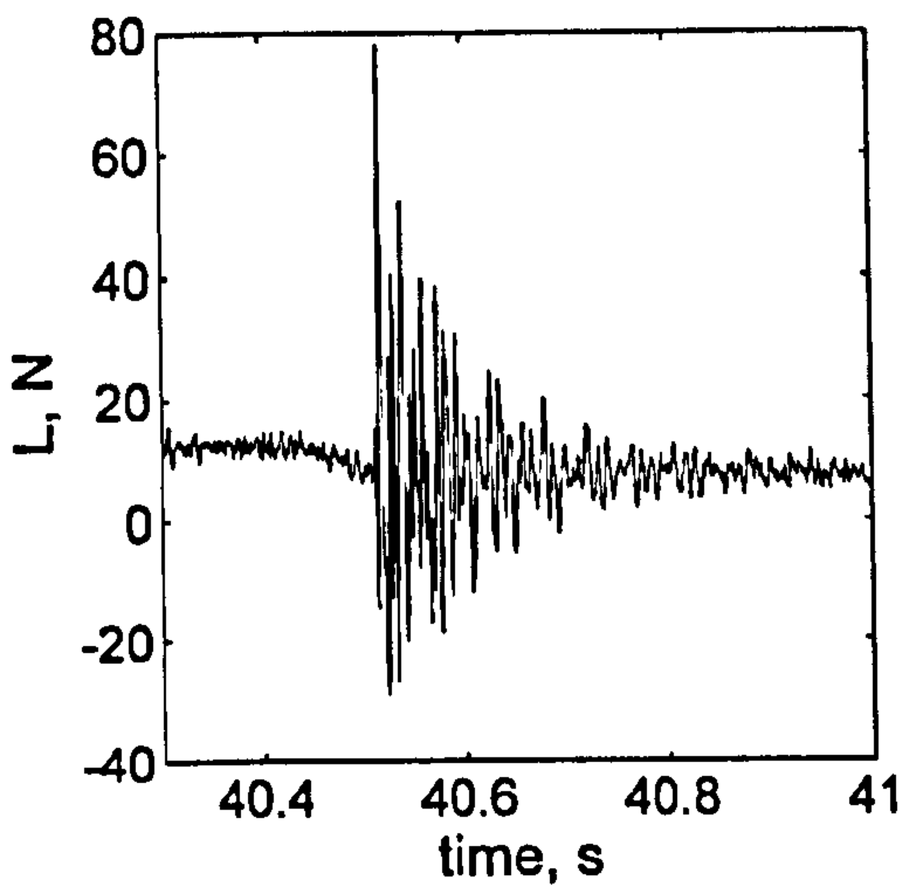

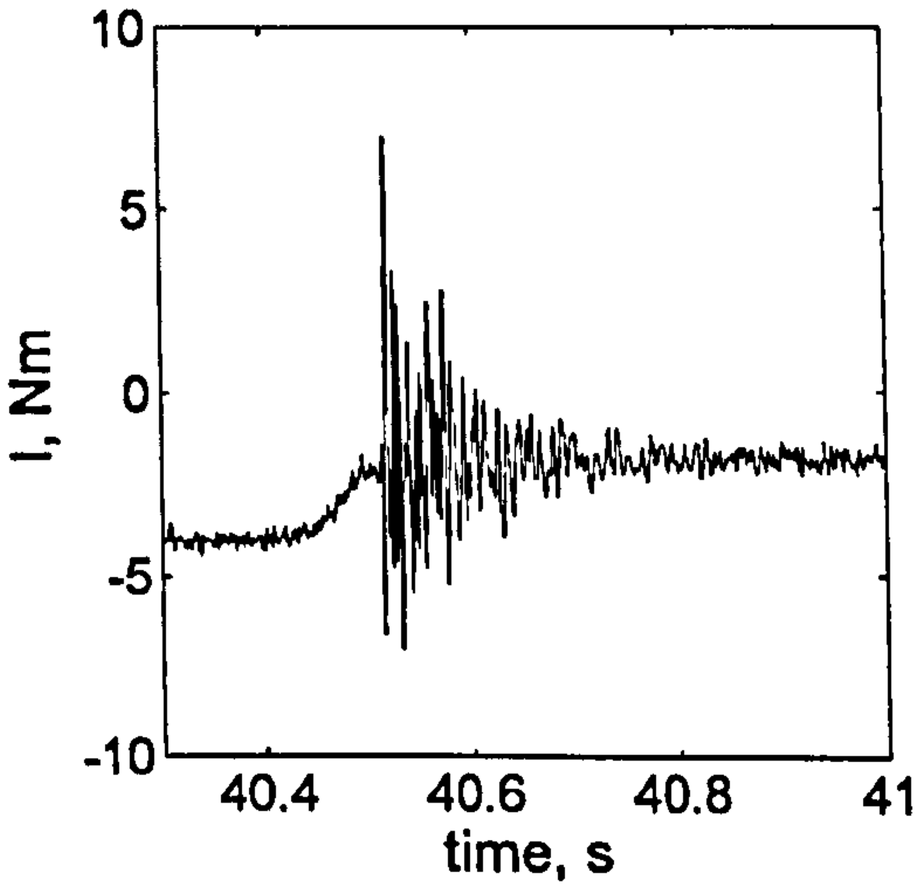

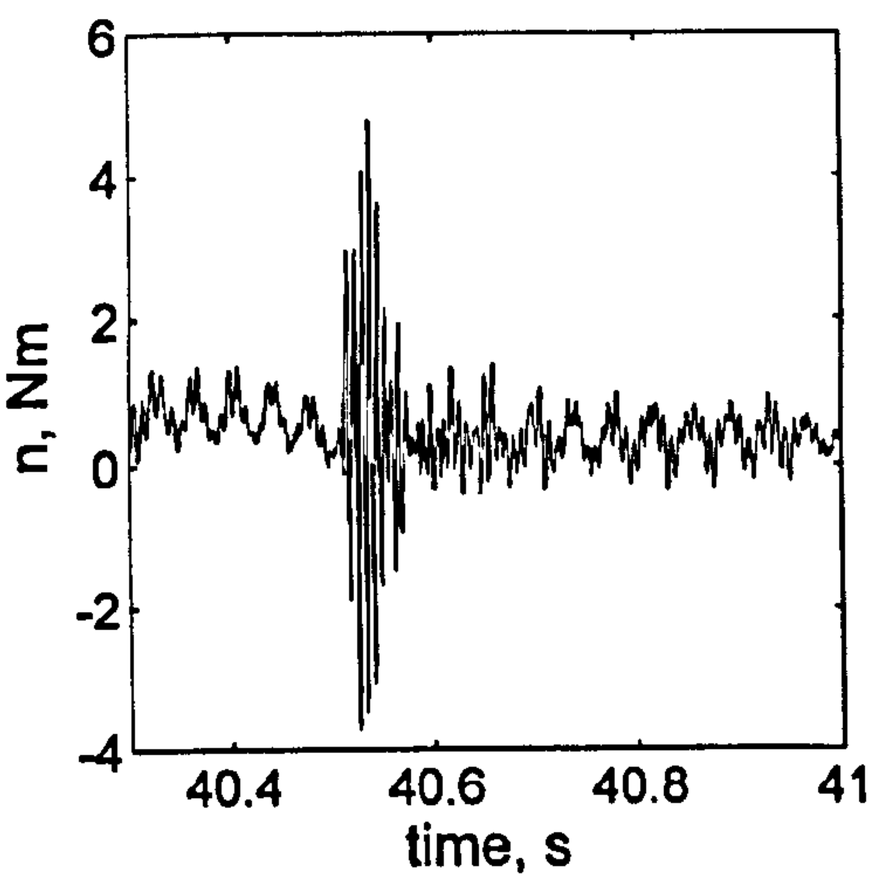

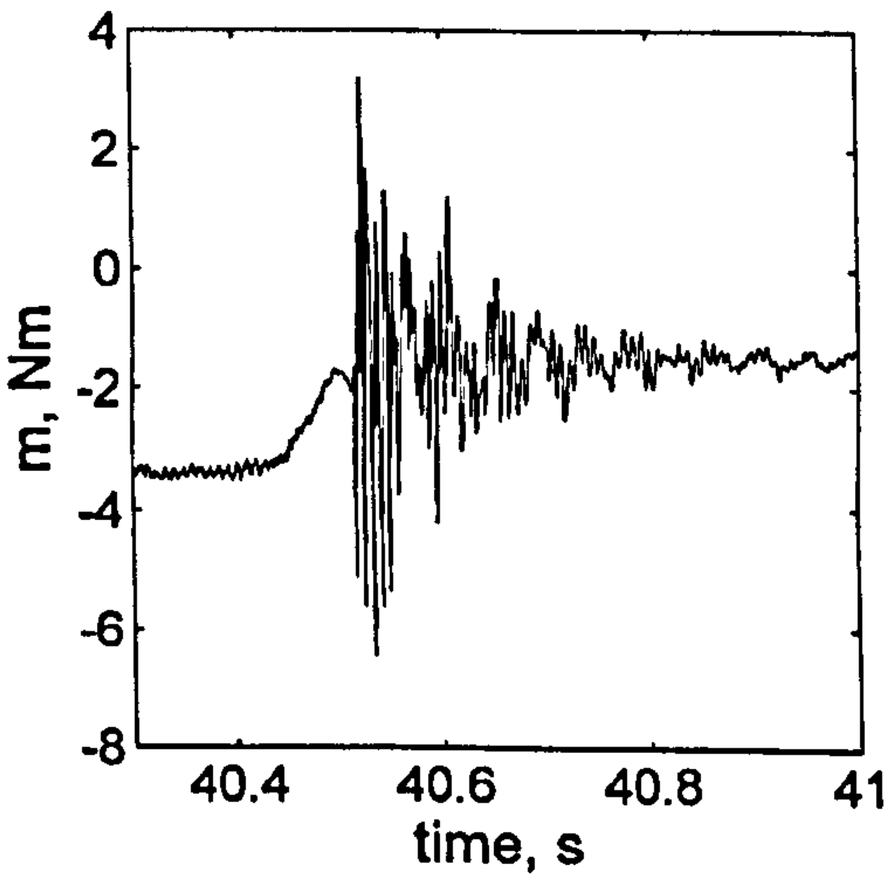

Figure 4.31: Detailed response of lift force and all moments during snap at $\alpha = 2.5°$

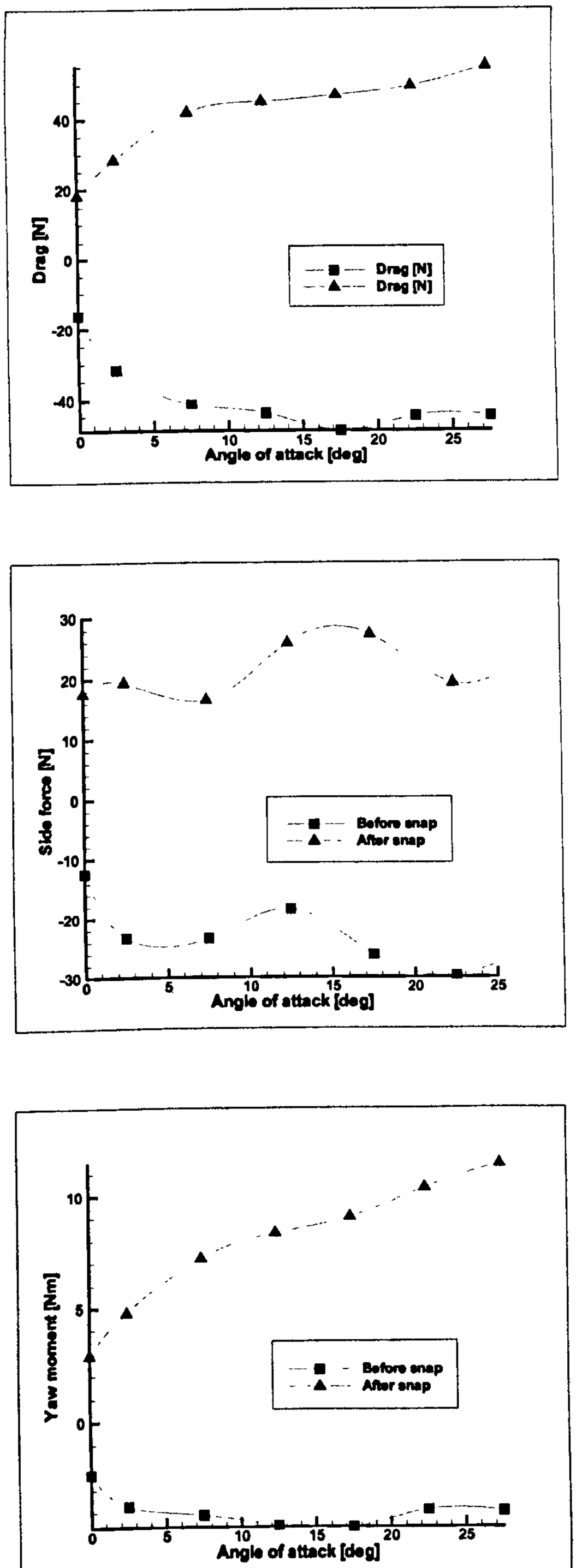

Figure 4.32: Aerodynamic forces during the snap-through

4.3 Variable Camber Devices

An efficient way to allow aircraft to perform efficiently over a wide range of airspeeds can be realised by cambering and de-cambering the airfoil. When soaring, for example, aircraft must be trimmed for high C_L and for low drag should have a highly cambered wing. For the high speed part of flight, low cambered airfoil are preferable. Plain flaps widen the speed range by modifying the angle of attack at which the best combination of C_L and C_D are obtained [Simonis, 1989]. A true variable camber wing, which can smoothly increase or decrease the curvature of the profile, is aerodynamically superior to a wing with flaps [Spillmann, 1992]. Variable camber, potentially, allows the minimisation of the wing drag, an aspect that is critical for mission efficiency. Long endurance flight, for example, can experience weight variations as much as 50% during a typical mission. In these cases, significant benefits are possible through the ability of reconfiguring the airfoil to suit different airspeed and lift-to-drag ratio requirements. According to aerodynamic investigations, the camber variation concentrates on the trailing edge since because of aerodynamic as well as structural considerations, this region has the highest efficiency [Szodruch, 1985]. Currently, this is accomplished using articulated trailing edge flaps [McKinney, 1982, Statkus, 1984, Cole, 1976]. The relative rigid motion is obtained through mechanical joints and bearings that, even if optimised for lightweight, induce a weight penalty. This can be acceptable as long as the number of the joints is small, although it is in contrast with the need for a smooth camber variation. The greater the angle between two discontinuous surfaces, the higher the chance of flow separation, especially if large angles of attack are considered. The goal of realising a variable geometry wing profile through a hinge-less flap that can effectively change wing camber and minimise drag, have been extensively sought by both industries and researchers. Relying on compliant surfaces can, in principle, reduce the drawbacks produced by a non smooth surface. However, the load required to deform a compliant structure capable of both withstanding considerable aerodynamic loads, is not negligible and therefore the size of the actuator could offset the potential benefits. For these reasons it seemed desirable to look for an alternative solution relying on the characteristics of unsymmetric laminates. The main idea is to realise a trailing-edge-mounted device to change the camber of an airfoil by morphing its geometry. Since bi-stable laminates are often made of thin laminates, they still present some of the drawbacks of compliant structures (due to the well known relationship between bending stiffness "D" and thickness "t", $D \propto t^3$). However, in some of the stable configurations, this flaw is much reduced and the load bearing capability along certain directions can be quite considerable. In addition, it is possible

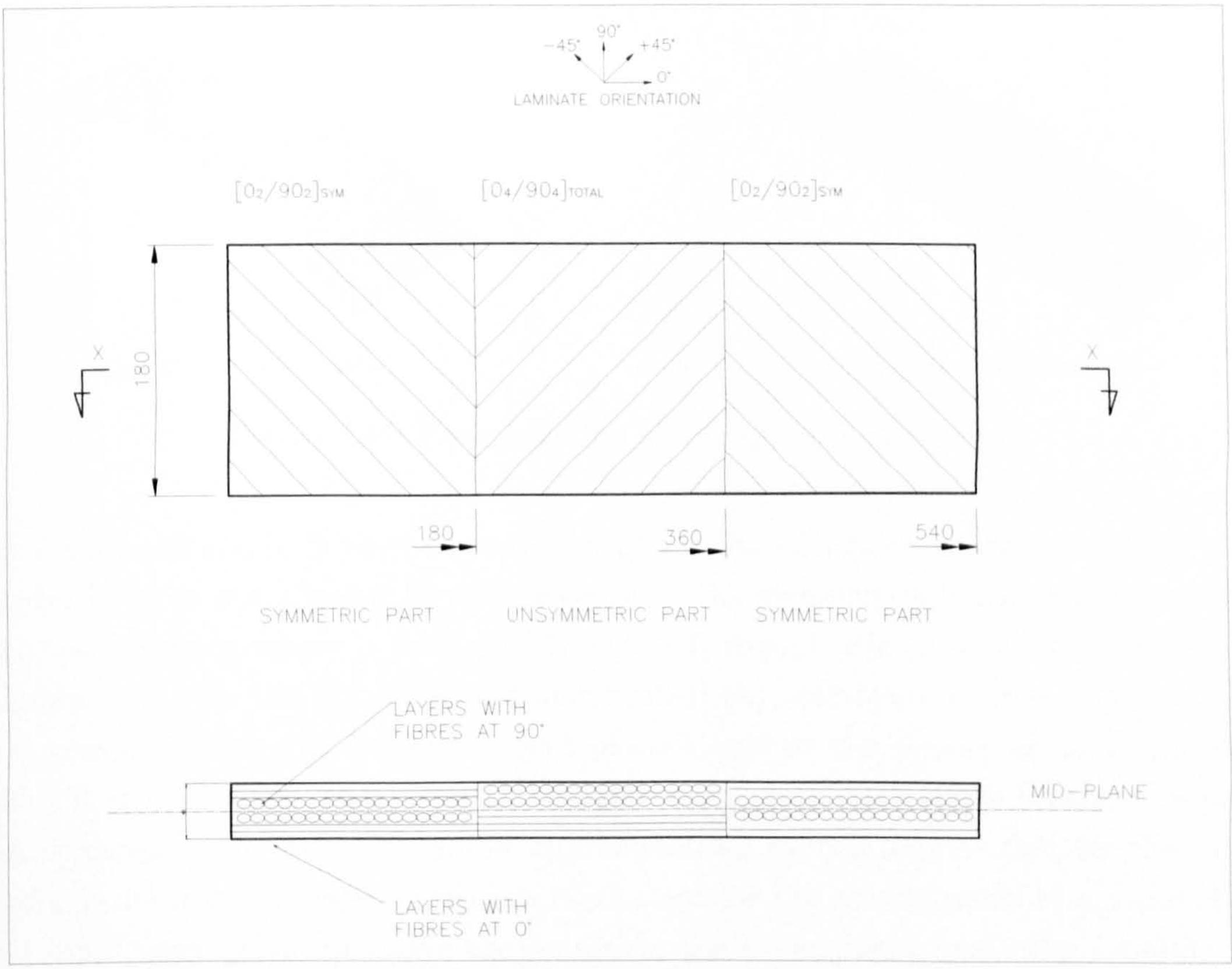

Figure 4.33: Stacking sequence and principal dimensions for the basic building block

to compensate (at least partially) for the lack of structural stiffness, by engineering the laminated structure with a geometric configuration that can be very stiff even if made of thin laminates. This is indeed achievable with any type of material, however bi-stable laminates have the additional possibility of "snapping" the component into a different configuration by means of a relatively low actuation load. This, in fact, represents the capability of temporarily reducing the stiffness to obtain large deformations with low energy consumption. The basic building block for the application proposed, consists of a strip of CFRP which can be considered as an extension of the compound plate described in Chapter 3.1. The only difference is having symmetric laminate patches on both the left and the right end side on the unsymmetric part. An example of the stacking sequence is shown in Fig. 4.33.

A panel laminated in this way, retains most of the bi-stable properties highlighted for the compound plate and the two stable configurations achieved are shown in Fig. 4.34. Both configurations are symmetric with respect to the longitudinal and the trans-

(a) Curved configuration

(b) Flat configurations

Figure 4.34: Basic building block equilibrium shapes

verse axes and similarly to the compound plate, the curvature in the y-direction (i.e. longitudinal) is not affected by the presence of the symmetrically laminated patches. The transverse curvature is considerably reduced, though still present. The transverse curvature (k_x) for the flat shape and longitudinal (k_y) curvature for the curved shape, are measured along the centre line and plotted against the y-axis, as shown in Fig. 4.35. It is noteworthy that for each configuration, both short edges present virtually zero transverse curvature. To a first approximation, we can assume that for the "flat" configuration the transverse curvature is constant for the central panel at a value close to 1.4m^{-1}, and quadratic along the y-axis, in the outer panels (ref. Fig. 4.35a). In fact, values $< 0.1\text{m}^{-1}$, are already reached at 100mm from each edge ($\sim$ 16% of the total length). In the curved configuration (ref. Fig. 4.35b), the longitudinal curvature is only present for the central panel and the two outer panels are left undeformed. These deformation patterns suggested that the residual stresses, away from the boundaries between the symmetric and the unsymmetric portion of the laminate, are very small and therefore embedding such a component into another structure, should not modify its basic properties. In fact, a finite distance (i.e. boundary layer) exists beyond which both configurations are unaffected by the neighbouring structure, a conclusion which may seem trivial for structure with linear behaviour, but it is not so for these type of composites structures.

4.3.1 Trailing Edge Device

This compound plate offered a good opportunity for the realisation of a multi-stable trailing edge by joining two panels like those shown in Fig. 4.33 along one edge at an angle, forming a wedge shaped structure. Fig. 4.36 shows the geometry and the stacking sequence areas for the device: the dark areas have an unsymmetric stacking sequence

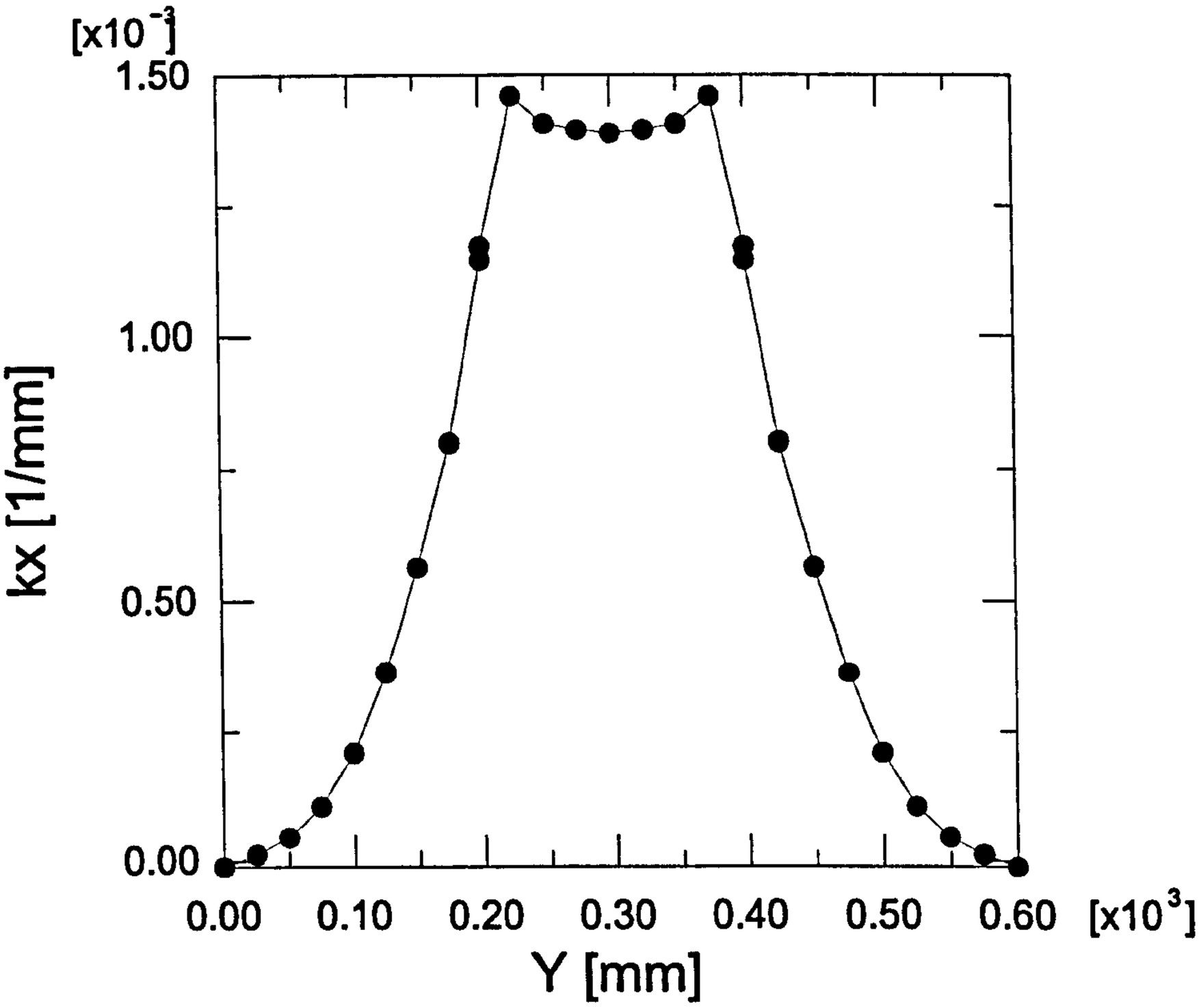

(a) k_x curvature

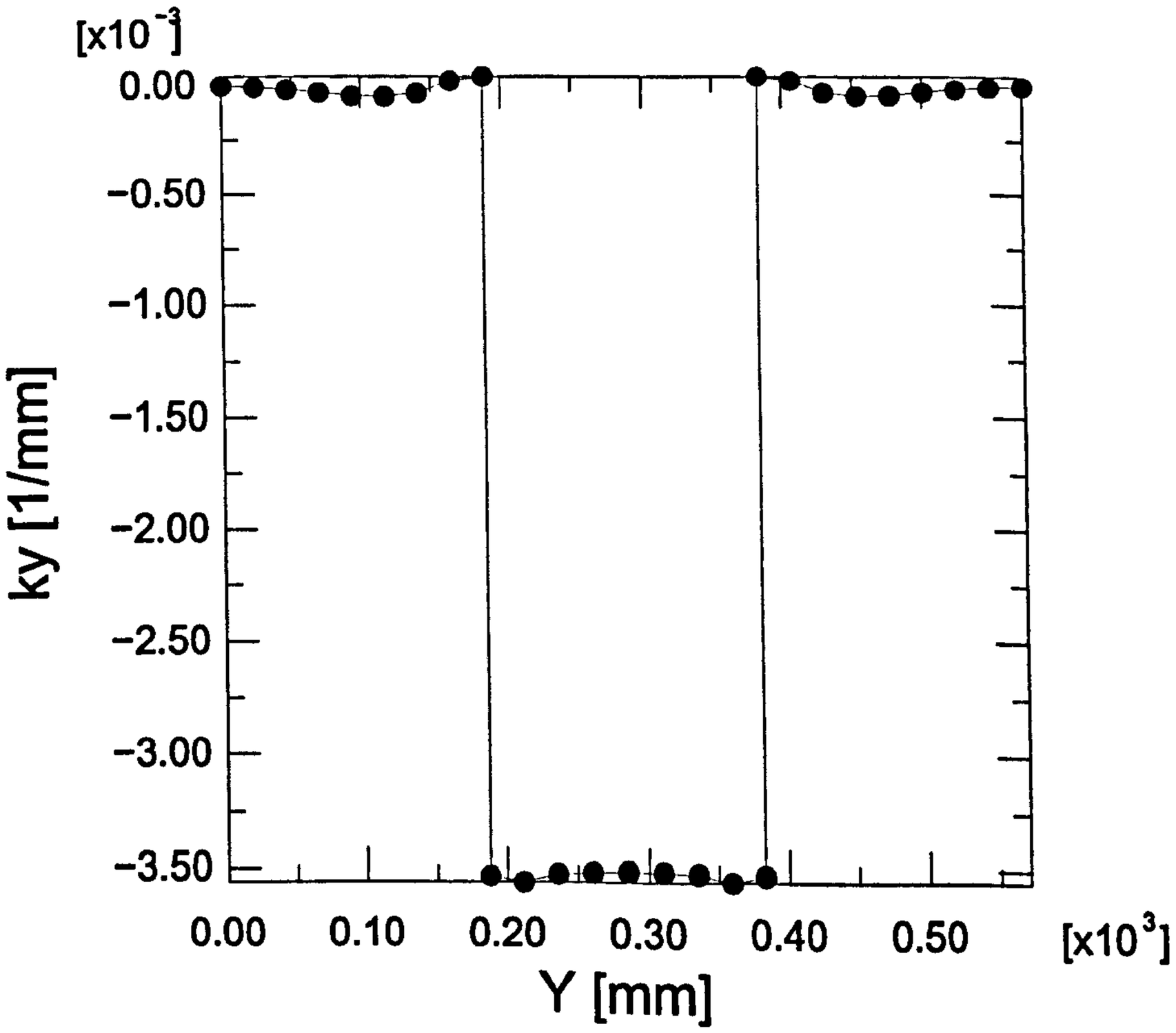

(b) k_y curvature

while the light areas are symmetric. The laminate schedule is the same as the basic bi-stable structures with $[0_2/90_2]_{SYM}$ and $[0_4/90_4]_{TOT}$ for the symmetric and the unsymmetric parts respectively. It is important to note that the continuity of the laminate around the right edge creates a load path for the transmission of the stresses between the upper and the lower surface. Each unsymmetric patch is bi-stable and therefore their combination makes the resulting structure truly multi-stable, with four possible equilibrium configurations. Fig. 4.37 shows the achievable configurations obtained through the numerical simulation of the cool-down. The cool-down analysis always provides the shape shown in Fig. 4.37b. To obtain the other shapes, a concentrated load is applied to induce the snap-through and the load is then removed to ensure the solution is stable. The first two configurations (Fig. 4.37a and Fig. 4.37b) show good potential for the realisation of morphing aerodynamic devices, as they can be attached to the trailing edge part of an airfoil providing the ability to change the profile's camber. The latter two configurations, (Fig. 4.37c and Fig. 4.37d) still show a good potential given the large deformations achieved, however their possible application is less obvious. For the sake of simplicity, only the first two shapes will be considered in the remainder of the chapter.

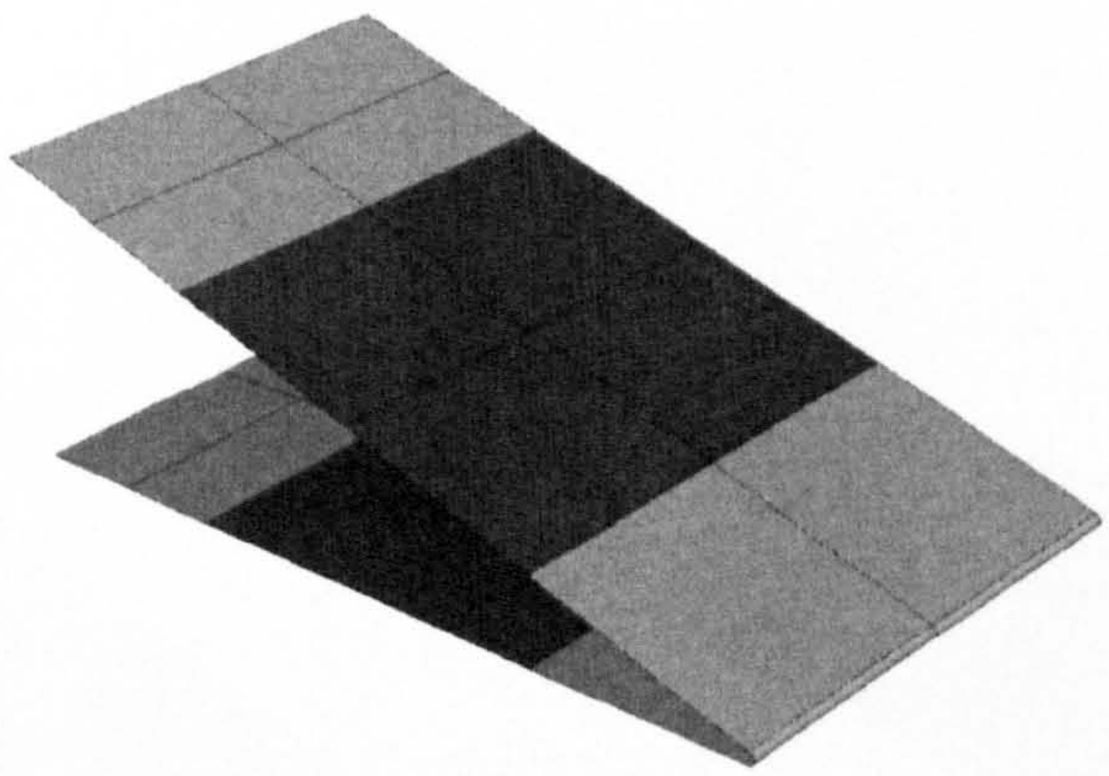

Figure 4.36: FEA model for the variable camber trailing edge

The connection between the upper and the lower surfaces of the trailing edge device (i.e. the right edge), represents a sensitive area from the aerodynamic point of view and a sharp edge would normally be preferred. From a practical point of view, this presents some difficulties and there are a number of ways it can be realised. A sharp edge, in addition, would not present any particular difficulty for the numerical model. However, this would incorrectly represent the real part where a small but finite radius is needed

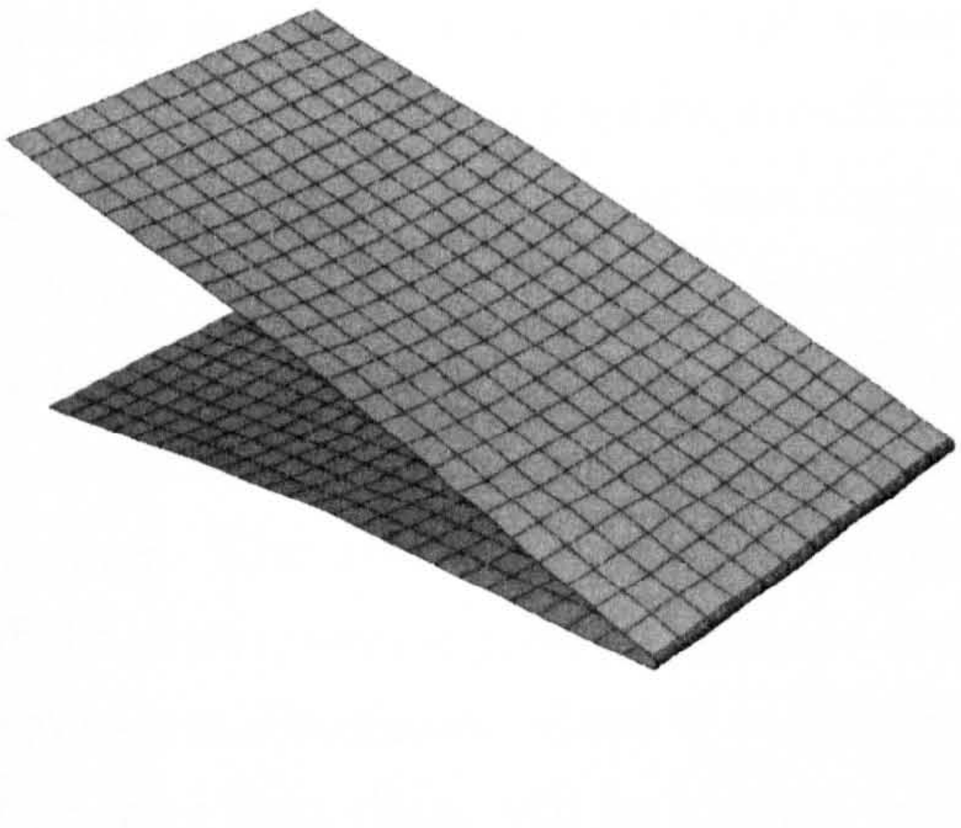

(a) De-cambered configuration

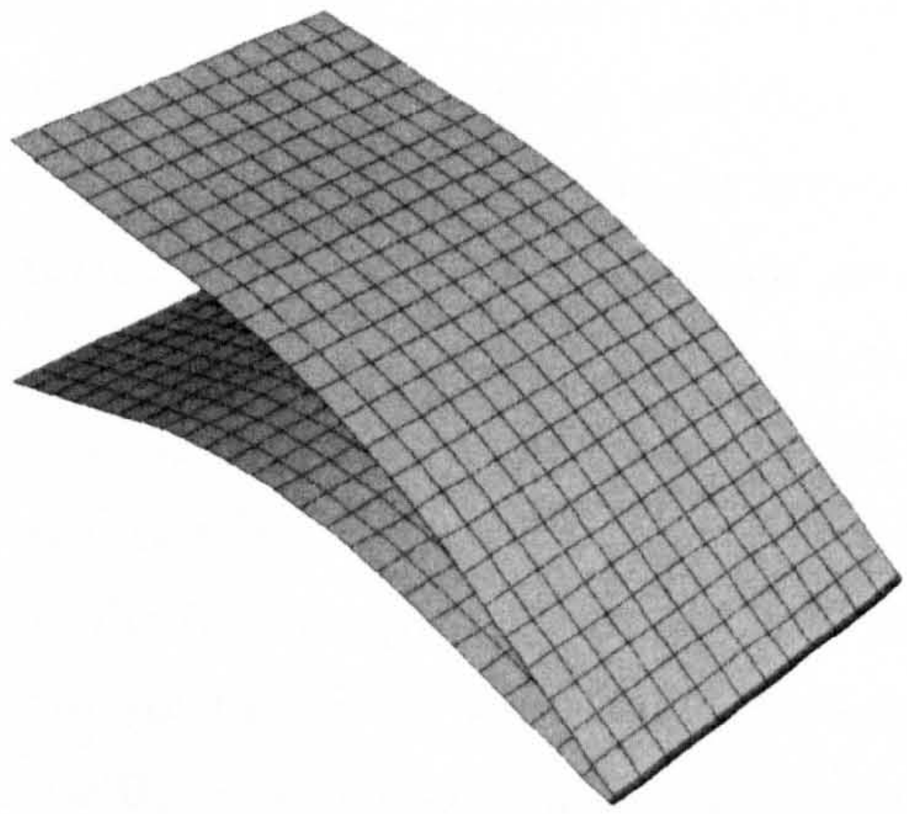

(b) Cambered configuration

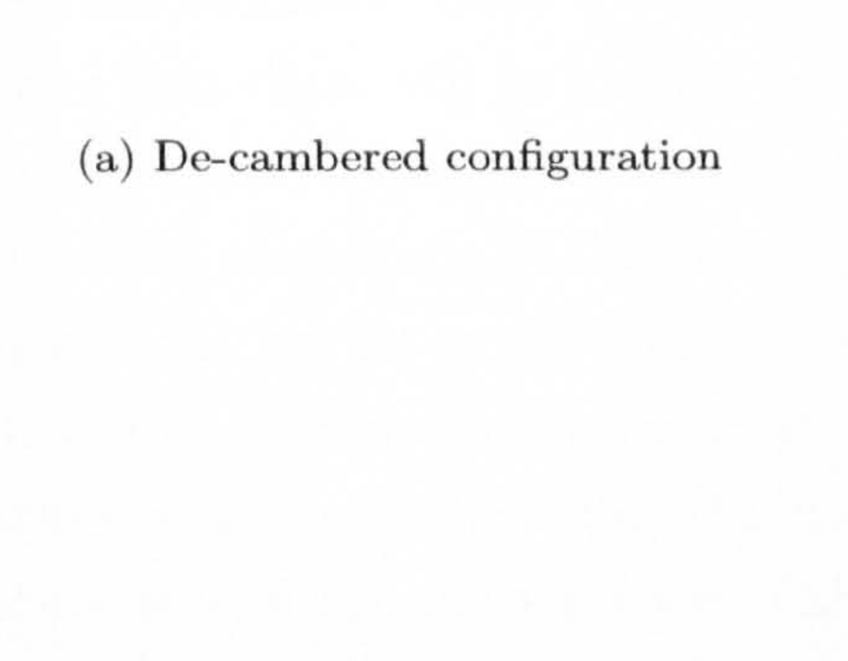

(c) Alternative configuration 1

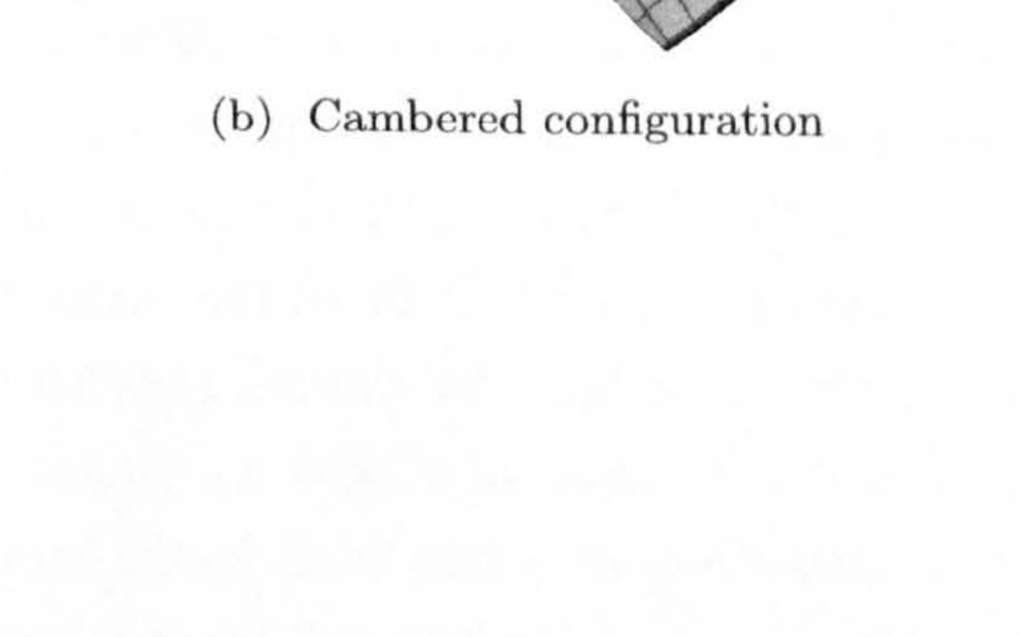

(d) Alternative configuration 2

Figure 4.37: Stable configurations for the variable camber trailing edge

to allow the material fibres to lap past the edge. For these reasons, it has been chosen to fillet the edge with a radius of 3mm.

By taking a closer look at the De-cambered and the Cambered configurations, it is possible to note a few important aspects. Longitudinally, the De-cambered configuration, does not seem to present significant deformations from the original tool shape and the angle between the upper and the lower surfaces is unchanged. This is an important feature, as it mean that it is possible to start from a given airfoil, with known aerodynamic properties, as a basis. By examining the cross-section however, the transverse curvature of the unsymmetric panel, deforms the outer edges creating slightly concave surfaces. The overall deformation is quite small and reaches its maximum at the centre of the unsymmetric panel where the out-of-plane deflection is approximately 7.5% of the transverse dimension. Even if small variations of the profile of the wing can be tolerated, it is clear that there will be a flight regime (or possibly several) for which the transverse deformation can be quite detrimental from an aerodynamic point of view. It is possible to reduce the magnitude of the deflection by increasing the stiffness of the supports (i.e. the symmetric parts) or by adding local transverse strips of laminate onto the external surfaces. Unfortunately however, these methods cannot eliminate completely the curvature because, if they did, the bi-stable behaviour would be lost. The transverse curvature is a direct consequence of the residual stress field and it is generated on the 0^0 and the 90^0 directions simultaneously; suppressing the curvature in one direction would significantly alter the stress distribution and hence the possibility of having two equilibrium states. Furthermore, to assess in detail the drawbacks associated with this geometry, wind tunnel tests and in-depth aerodynamic analysis would be required. A simple flexible aerodynamic fairing mounted on top of the worst affected areas could provide a simple solution.

Fig. 4.38 shows the longitudinal cross-section of the two configurations considered. The amount of deflection obtainable in the Cambered configuration, is approximately 20^0, similar to that currently achievable with standard flaps. The value can be increased or decreased by modifying the stacking sequence and the geometric dimension of the unsymmetric area. In addition to these modifications, it is possible to considered further adjustment of the Cambered configuration by mean of an actuation system. With such a system, the profile can be altered quite considerably by simply pulling or pushing the lower edge horizontally. The curved shape of the panels and its associated low bending stiffness in this configuration, would also have the additional advantage of requiring minimal power input to modify the shape. A few possible configurations are shown in Fig. 4.39

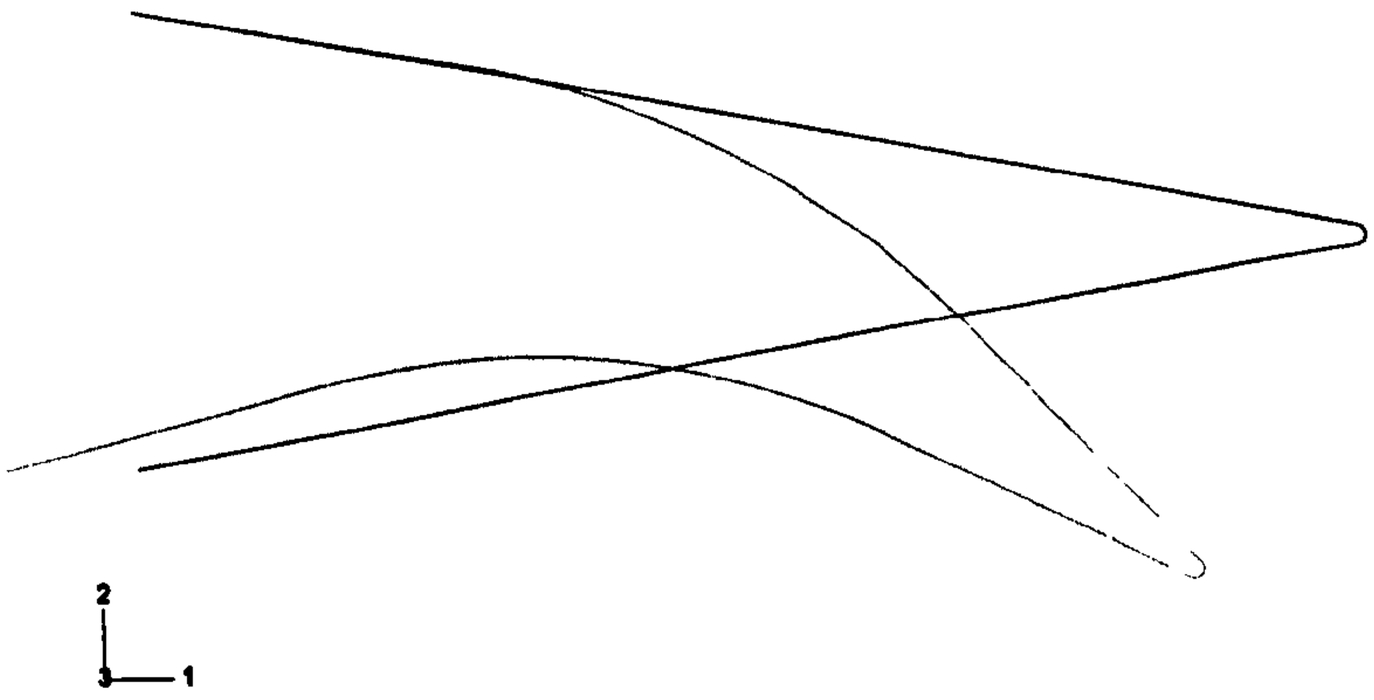

Figure 4.38: Deflection between the two configurations of the trailing edge

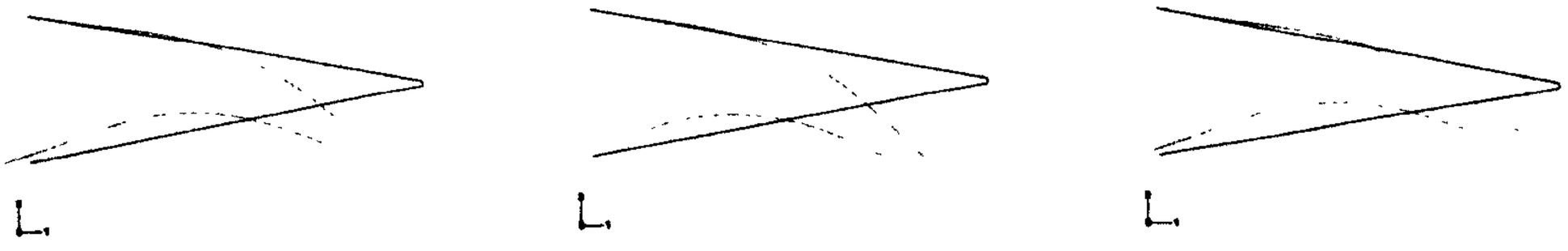

Figure 4.39: Different angles obtained actuating the lower edge

Configuration	ΔZ $[mm]$	$EI = \frac{PL^3}{3 \cdot \Delta Z}$ $[Nm^2]$
De-cambered	0.24	3639.5
Cambered - upward deflection	32	27.3
Cambered - downward deflection	70	12.5

Table 4.3: Vertical deflection and beam equivalent stiffness

During the operational mode, once the device is in either of the two configurations and the left edges are restrained from movements, the structure becomes quite stiff and it is no longer possible to snap between the two states. The Cambered configuration, because of the curvature of the surfaces, still shows some flexibility. This is more evident if the trailing edge is pushed downward, as this loading condition tends to increase the curvature of the panels. The load - displacement diagram for the two configurations is shown in Fig. 4.40. The diagrams are obtained by constraining the left edges and applying a concentrated load of 50N at the centre of the right edge, acting upward and successively downward. The differences in the bending stiffness for the different cases are evident by comparing the values shown in Table 4.3, where the deflections and the stiffness equivalent to that of a built-in beam are shown. For the De-cambered configuration the upward or downward direction of the load produces the same diagram, while for the Cambered configuration two different diagrams are obtained. This might suggest that, with a suitable actuation system, it is possible to "fine" tune the camber of the airfoil to suit different flight conditions. In addition, the energy required for the actuation is small because to increase the camber of the airfoil, the panels undergo bending deformation and therefore their flexibility is quite pronounced. Conversely, if the trailing edge is pushed upward, the load tends to flatten and stretch the component panels and therefore the associated stiffness is higher, which is useful to withstand aerodynamic loads.

The integration of the trailing edge device into a wing system to realise variable camber airfoils, presents some difficulties. This is clear by examining Fig. 4.38 where the upper edge of the trailing edge is bonded to the top of the airfoil and the lower edge is actuated. During the transition between the stable states, the lower edge undergoes a considerable translation, which is required to achieve the shape change. Leaving the lower edge free to move would be unacceptable for the aerodynamic performance, as such a big gap would certainly induce flow separation. It is required, therefore, that the lower surface of the trailing edge is always in contact with the lower part of the airfoil. A possible solution to obtain such a contact is to create a rail bonded to the base frame, which forces the lower surface to slide along a prescribed path. The rail should be made

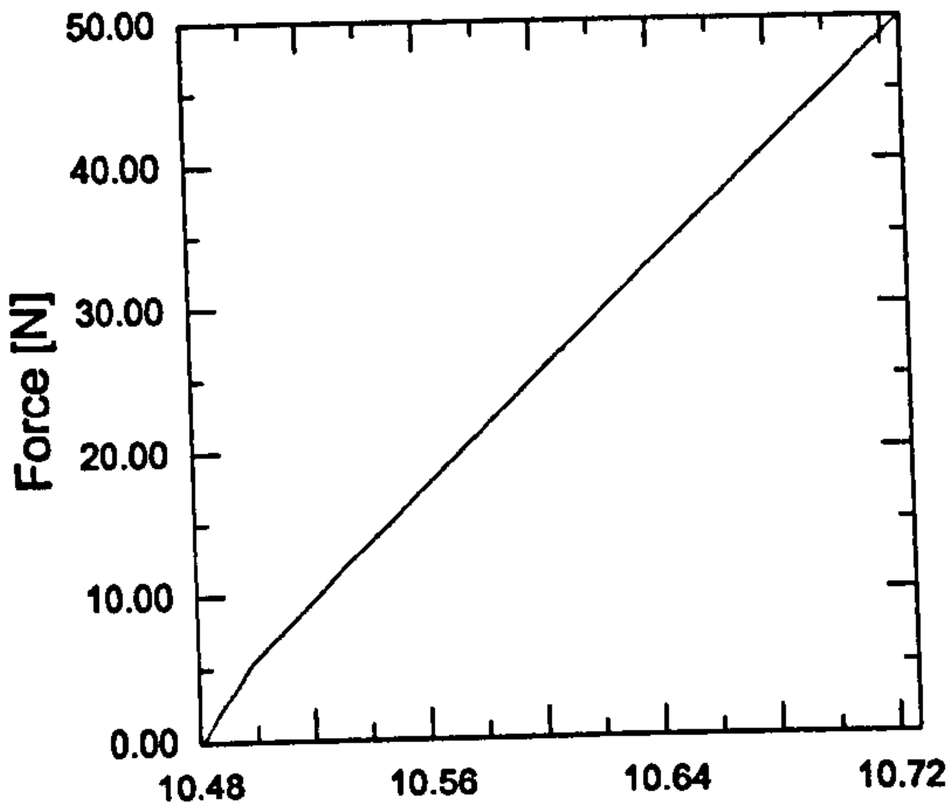

(a) Upward and downward force

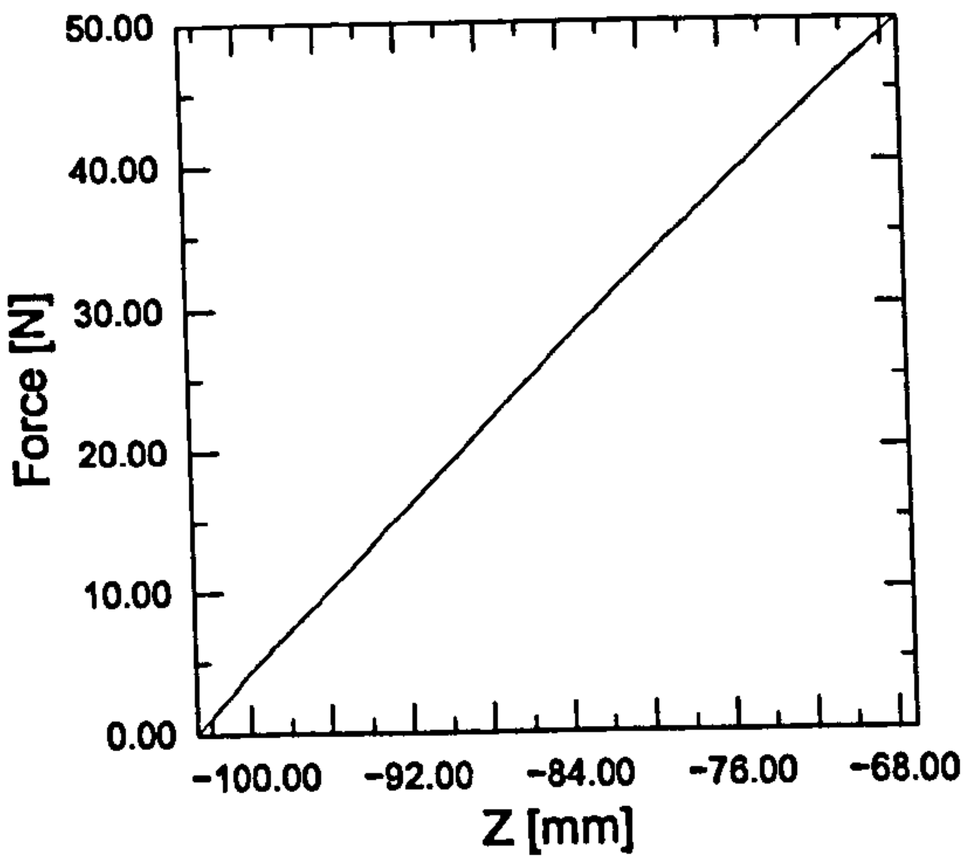

(b) Upward forced

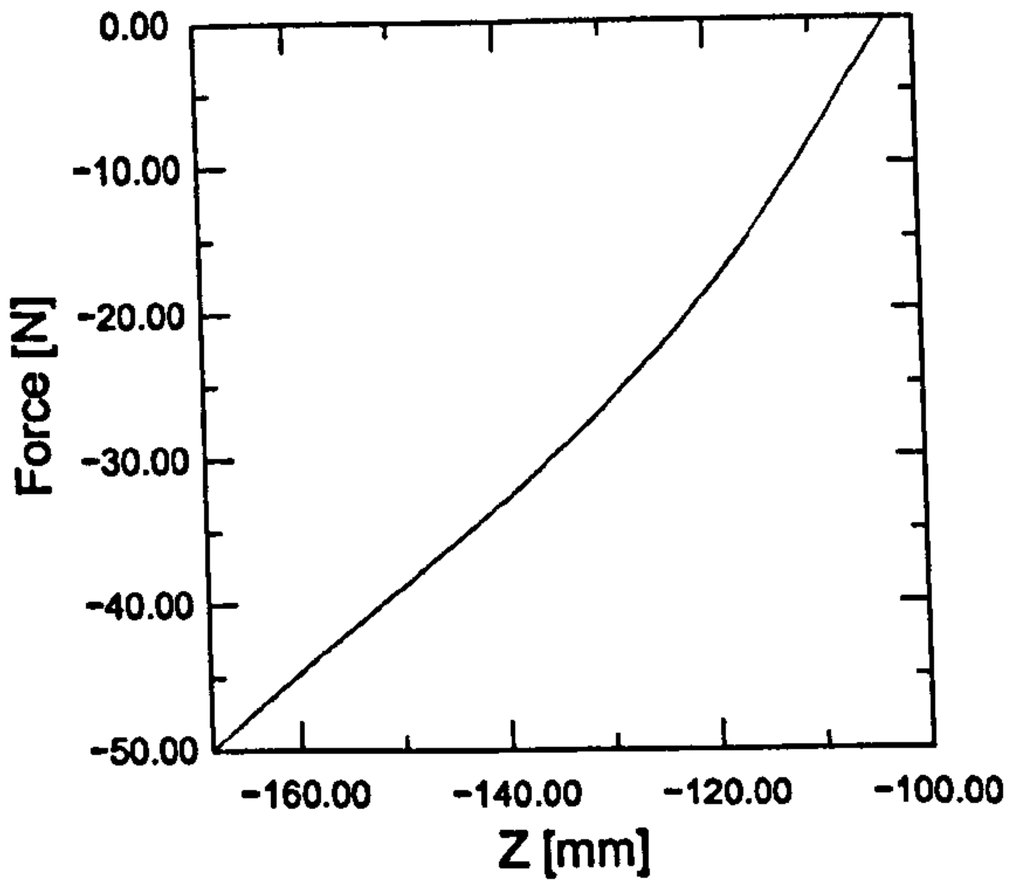

(c) Downward force

Figure 4.40: Load-displacement diagram for stiffness estimate

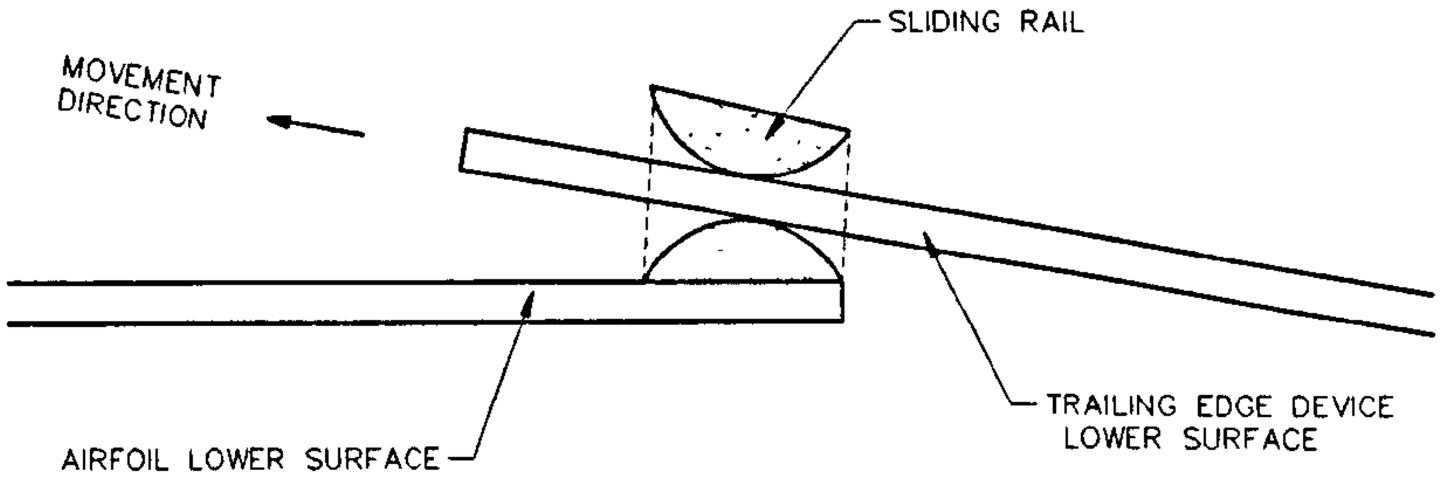

Figure 4.41: Lower edge rail

of low friction material such as *Nylon* or *Delrin* for smooth operation and should not present any particular strength requirement since the main load path would be along the composite surfaces. This concept is better shown schematically in Fig. 4.41. A linear actuator is connected to the rear spar on the left and on the lower part of the trailing edge device through a composite lug. By changing its length, the actuator drags the lower edge forward and backward. The machined rail, bonded to the fixed part of the lower surface, ensures that there is always contact between the two sliding parts. An elastic seal would eventually be required to obtain a smooth surface. The actuator should have enough power to overcome the critical forces to snap the device and also the possibility to provide a suitable locking system once the desired configuration has been obtained. Further adjustment of the actuator could be used to increase or decrease the camber of the section for control purposes or to keep a reduced drag configuration for different flight regimes (ref. Fig. 4.39). Depending on the characteristics of the original airfoil, it might be more convenient to bond the lower edge and leave the upper one free to slide, however this is entirely dependent on the aerodynamic considerations for each application since, as far the variable camber device is concerned, there is no preference for actuating the lower or the upper edge.

The actuation is simulated numerically with non-linear FEA in order to cope with the magnitude of the displacements and the multiple steps required to obtain the different shapes. During the analysis, the upper edge is clamped to simulate the bonding to the fixed part of the wing while the lower edge is subjected to the actuation load "*L*" and it is constrained to move horizontally (refer to Fig. 4.42). The boundary conditions do not aim at a realistic simulation of the actuation procedure but nevertheless provide a good engineering approximation of the system's elastic response. The load-displacement diagram thus obtained is shown in Fig. 4.43, assuming the Cambered configuration as the initial state. The actuation load is ramped linearly from 0 to 40N and the vertical displacement is measured at the right edge. The initial application of the load provokes

an increase in the curvature of the lower panel, which results in a backward displacement of approximately 10mm. From this point, the diagram is almost linear until the top surface snaps into the flat configuration (load $\cong$ 20N), then a new linear region is encountered until the lower surface snaps as well (load $\cong$ 33N). At this point the transition from the Cambered to the De-cambered configuration is completed and the "new" structure behaves linearly until the maximum applied load of 40N is reached. When the concentrated force is removed, the vertical deflection is reduced until the equilibrium position is reached (position $(0,0)$ on the diagram). The total vertical deflection between the two states can be measured by comparing the two positions on the horizontal axis, which are $(-75,0)$ for the Cambered and $(0,0)$ for the De-cambered. In this way a vertical deflection of 75mm is measured, corresponding to 20.5°. The actuation cycle is completed by reversing the applied load inducing the backward transition. During this process, the upper surface snaps when the load reaches a magnitude of $\cong -10$N (the negative sign being referred to the downward direction). The lower surface snaps when the load is increased to $\cong -12$N. After this point the load is increased to the maximum value of -20N and thereafter reduced to 0N. The load-displacement diagram, besides from giving useful information regarding the maximum loads needed to actuate the structure and the energy required for a complete actuation cycle (i.e. the area enclosed within the diagram), highlights some of the features of the device: the non-linear behaviour and the asymmetry in terms of actuation loads between the two states. Before take-off, the device will be in its De-cambered configuration. A force of $\cong$ 12N is then needed to obtain a highly cambered airfoil section. After take-off, to stow the trailing edge in the cruise configuration, a force of $\cong$ 33N will be required. In fact, due to the aerodynamic loads caused by the higher speed of the aircraft, the load might be considerably reduced, however the fact that a much higher load is needed to "extend" the trailing edge reflects the increased load bearing capability which is obtained in the Cambered configuration. This can considered a useful characteristic since it is in this configuration that the highest strength is needed (take-off in fact requires more lift and therefore higher wing loading to be generated, when compared to the cruise part of the flight).

An experimental model was built to validate the obtainable deformation and verify the feasibility. For this purpose a tool was manufactured from of aluminium plates each with a thickness of 3mm. These have been bent to match the triangular shape modelled numerically and thus a male mould was obtained for the lamination procedure. The choice of the material and the geometry for the tool was due to the availability of aluminium sheets and also to the ease of manufacturing. The fabric plies had an areal

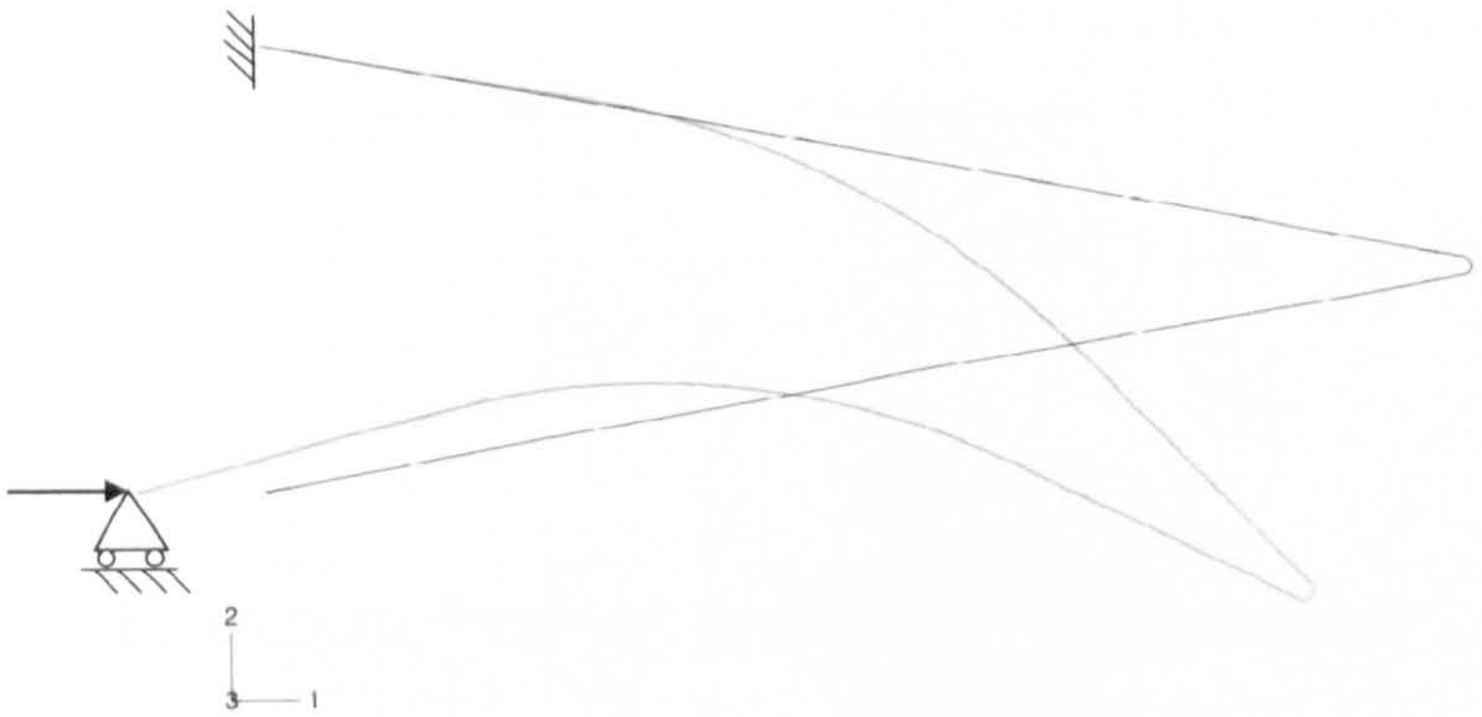

Figure 4.42: Boundary conditions for the actuation simulation

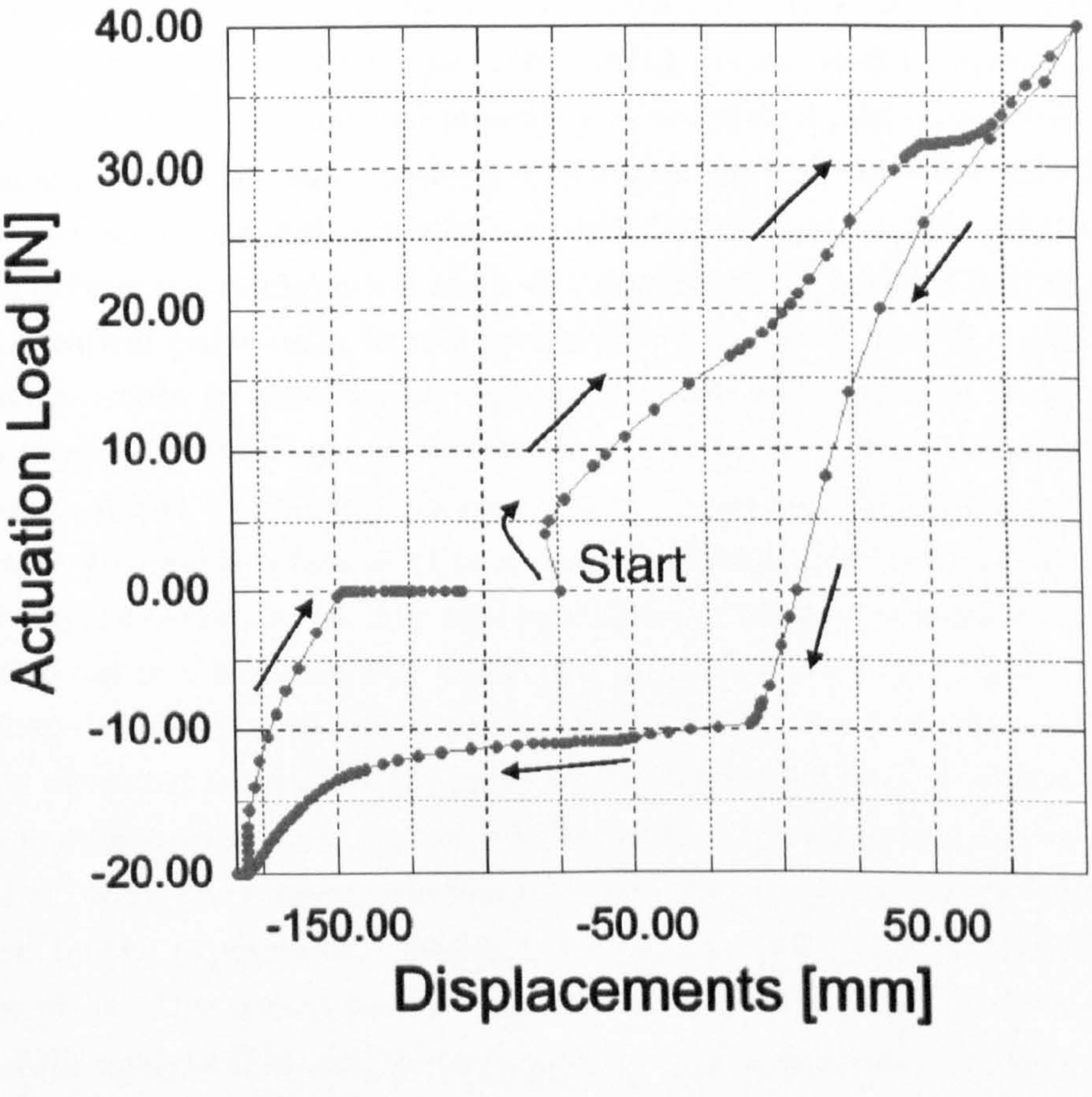

Figure 4.43: Load - displacement diagram for the variable camber trailing edge

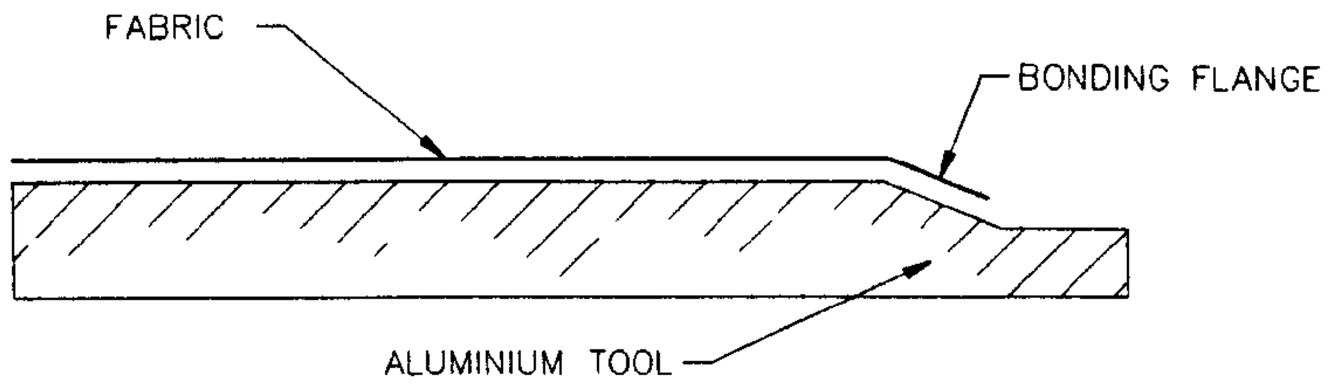

Figure 4.44: Proposed tool and assembly procedure

weight (i.e. mass per unit area) of 250gr/m^2 and a nominal thickness 0.25mm (ref. to table 2.1 for typical material properties). The lay-up was continuous from the upper to the lower surface. It must be mentioned that this does not make a particularly practical solution since it is quite difficult to lap fabrics past the small trailing edge radius, especially if considering the low drape-ability of high areal weights fabrics. In addition, during the cure process, the external pressure and the vacuum are quite likely to produce wrinkles in this region, a clearly undesired feature in such an aerodynamically sensitive area. The manufacturing defect would eventually result in a considerable wastage and therefore a different manufacturing method is envisaged. A possible solution is to laminate two identical parts on a female mould like that shown in Fig. 4.44. The tool should have a rebate to allow for an additional flange which will be used to bond the two parts together. The angle of the chamfer next to the rebate, should be equal to half of that required by the trailing edge. Once cured, the two parts can be bonded together with structural adhesive or co-cured if required. Such a construction method would not require particular tooling, and in addition it allows the manufacturing process to be carried out in a modular way ensuring a good structural continuity .

The shape obtained with the experimental model is shown in Fig. 4.46. The displacements measured experimentally show a good agreement with those computed using the aforementioned technique. In fact, the experimental model achieves an angular deflection of 21^0 while the numerical estimate is 20^0. An important aspect, which has been highlighted by the experimental model, is the join between the unsymmetric and the symmetric areas. This aspect has already been discussed in Section 3.1 where the inaccuracies of the analytical model, in the boundary region, have been pointed out. Besides from the theoretical assumptions, it is immediatly apparent that the structural continuity is compromised at the interface between the symmetric and unsymmetric areas.

(a) Symmetric and unsymmetric areas join interface

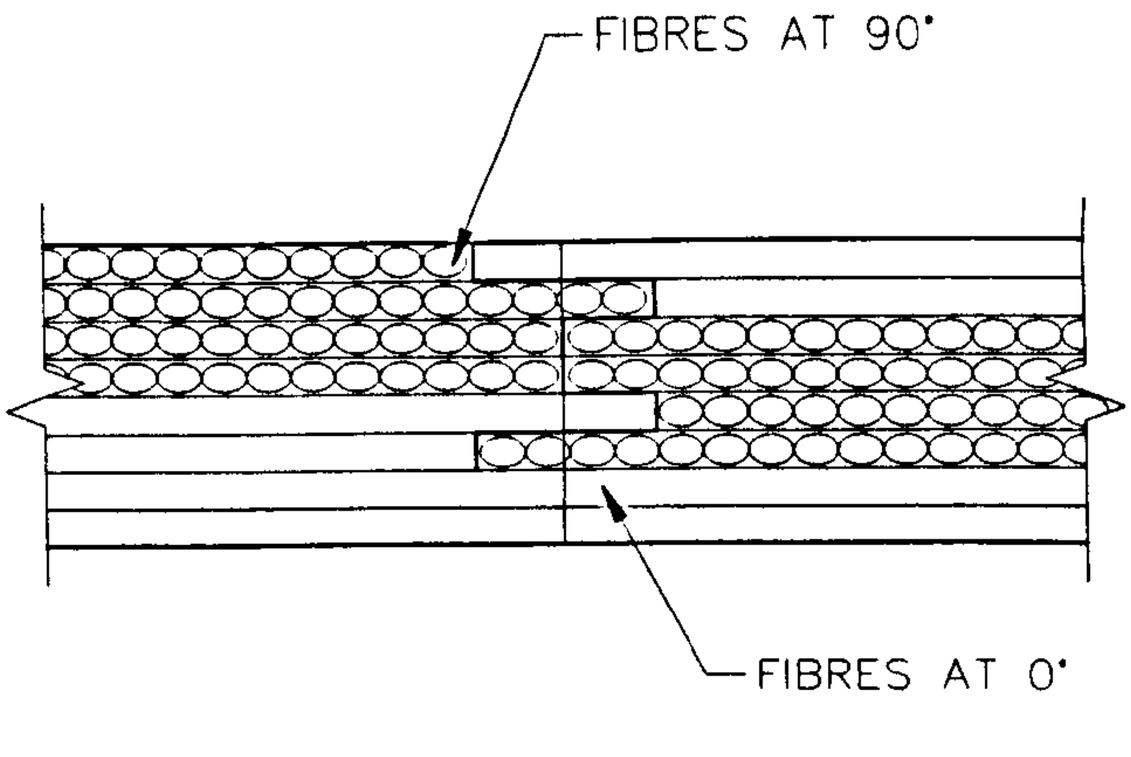

(b) Proposed alternate join between lamination areas

Figure 4.45: Interface between lamination areas

Examining the cross section of the laminate in this area (ref. Fig. 4.45a), it is noted that only the layers with fibres at 0^0 are continuous and this reduces the strength and the damage tolerance of the laminate in the cord-wise direction. Modifying the interface as shown in Fig. 4.45b will improve the characteristics, however it is clear that the problem needs to be addressed carefully and the possible interference with the bi-stability should be considered.

4.3.2 Variable Camber Airfoil

The main issue with the concept just presented, is related to the integration of the system into the wing structure. The join between the moveable part and the rest of

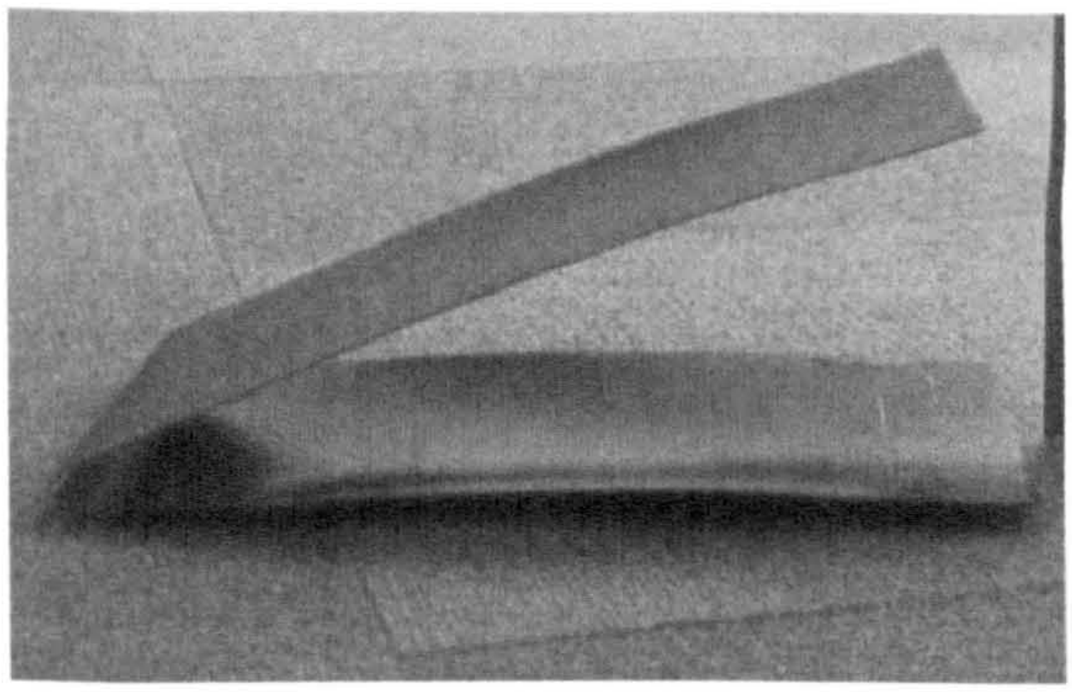

(a) De-cambered configuration

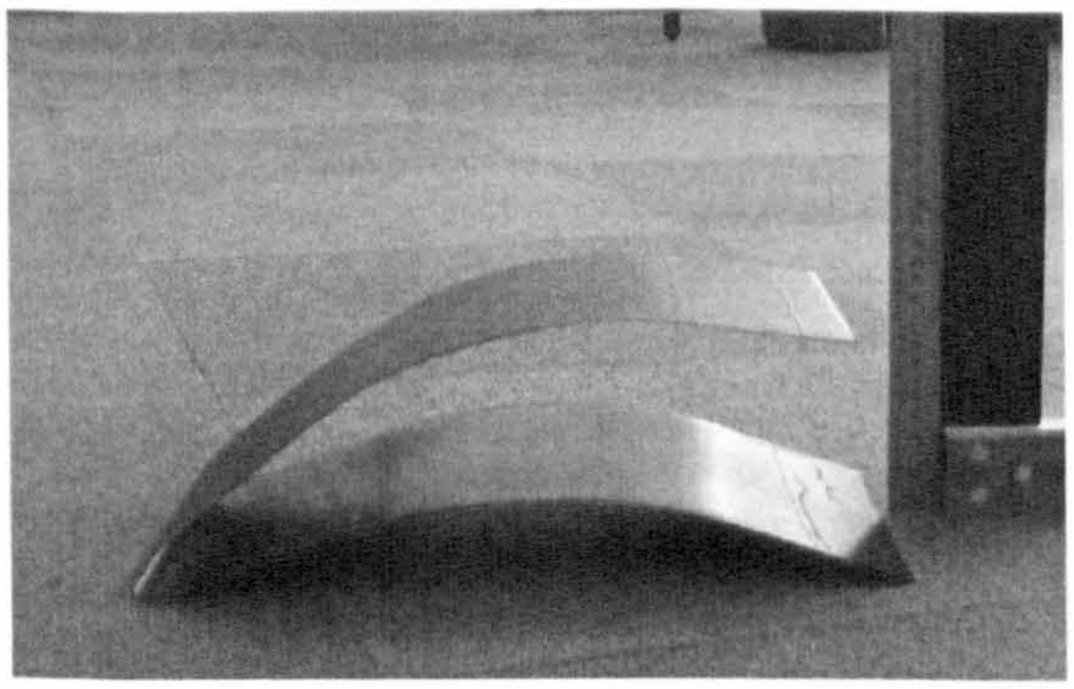

(b) Cambered configuration

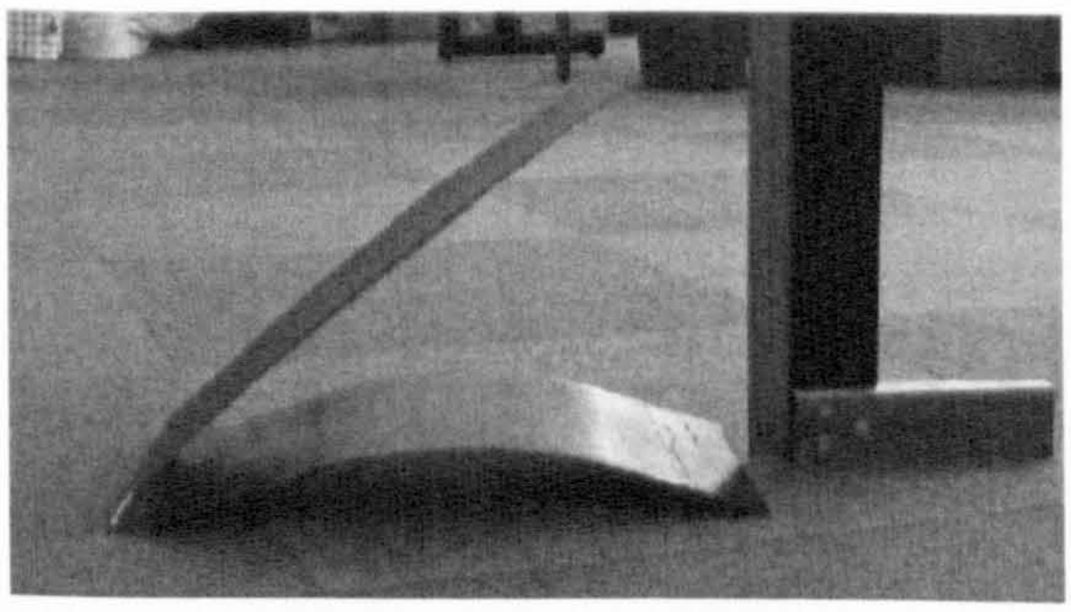

(c) Alternative configuration 1

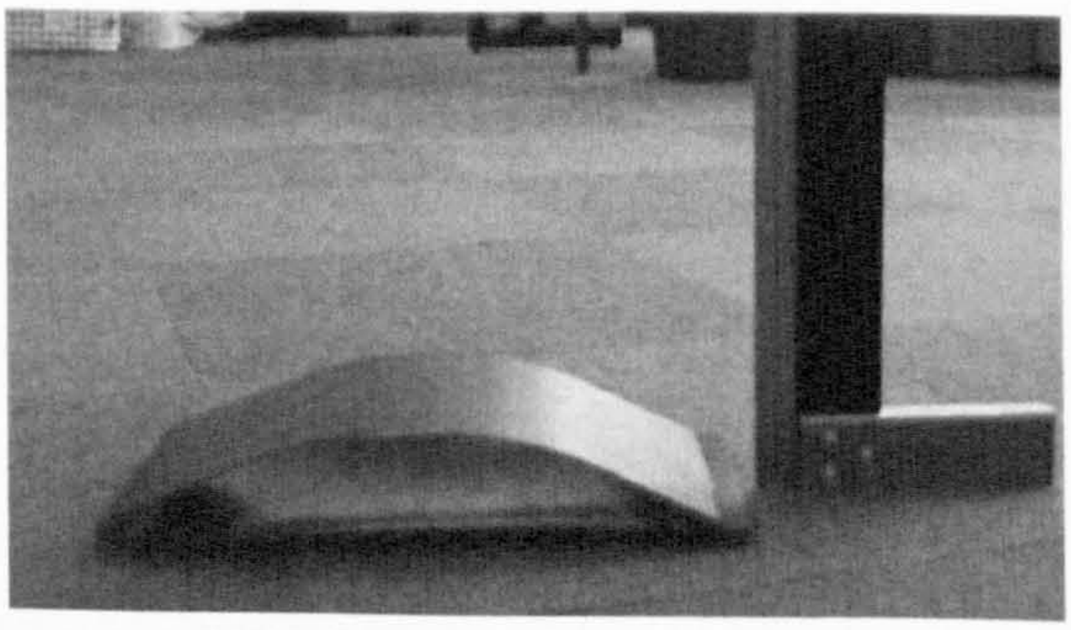

(d) Alternative configuration 2

Figure 4.46: Experimental model for the variable camber trailing edge

the wing presents some non trivial issues. To overcome this problem, another possible solution still using bi-stable patches, can be obtained by taking advantage of different materials to make the airfoil section. The two main characteristics of the variable camber trailing edge are, in fact, the multi-stability and consequently, the flexibility in certain configurations. These two properties can be enhanced by making use of different materials in different zones of the airfoil. Carbon-epoxy laminates have a very good stiffness/strength to weight ratio but, moreover, it is their great difference between the coefficients of thermal expansion α_1 and α_2 which makes them particularly suitable to create bi-stable components. Conversely, the high stiffness limits to a great extent the amount of deformation obtainable and poses more problems in the interaction with the surrounding structure. For this reason, using a more flexible fibre such as glass fibre, can be advantageous in some applications, especially if lower actuation loads and load bearing capabilities are sought. Glass-epoxy based laminates can help the transition between the bi-stable and the conventional areas of the structure and therefore can provide a viable solution to avoid some of the issues discussed above. Exactly how this translates into practice is shown with the examples shown in the following paragraphs.

A wing section obtained from a *NACA 23015* airfoil measuring 500mm ×150mm has been chosen as the basis for the experiment. The wing has been manufactured out of $100\,\mathrm{gr/m^2}$ unidirectional plies of E-glass epoxy laminated with a quasi-isotropic stacking sequence ($[0/90/+45/-45]_{SYM}$) as shown in Fig. 4.47. The wing section is made almost entirely of E-glass but for a square section on the belly measuring 150mm ×150 mm, which is made with unidirectional plies of $250\,\mathrm{gr/m^2}$ carbon-epoxy stacked with the usual laminate of $[0_4/90_4]_{TOT}$.

The material properties for the e-glass epoxy laminae are shown in Table 4.4 where it is also possible to note the much reduced difference between the coefficients of thermal expansion α_1 and α_2 and stiffnesses E_1 and E_2, when compared to Table 2.1.

The basic principle is that the local bi-stability of the carbon panel (due to the high values of α_1 and α_2 of carbon) will determine the global equilibrium shape of the whole wing section, despite being restrained at both ends (thanks to the low values of E_1 and E_2 of E-glass). The cool-down is simulated with FEA using the mesh shown in Fig. 4.48. The model contains 862 nodes and 260 elements (258 S8R 8-noded quadrilateral elements and 2 STRI65 6-noded triangular elements). Because the resin systems of the two types of laminate are the same, it has been possible to use the same curing process described for the previous panels and therefore the cool-down simulation has been carried out with exactly the same procedure. The two possible equilibrium shapes, obtained after the cool-down, are shown in Fig. 4.49. The "De-cambered" shape retains

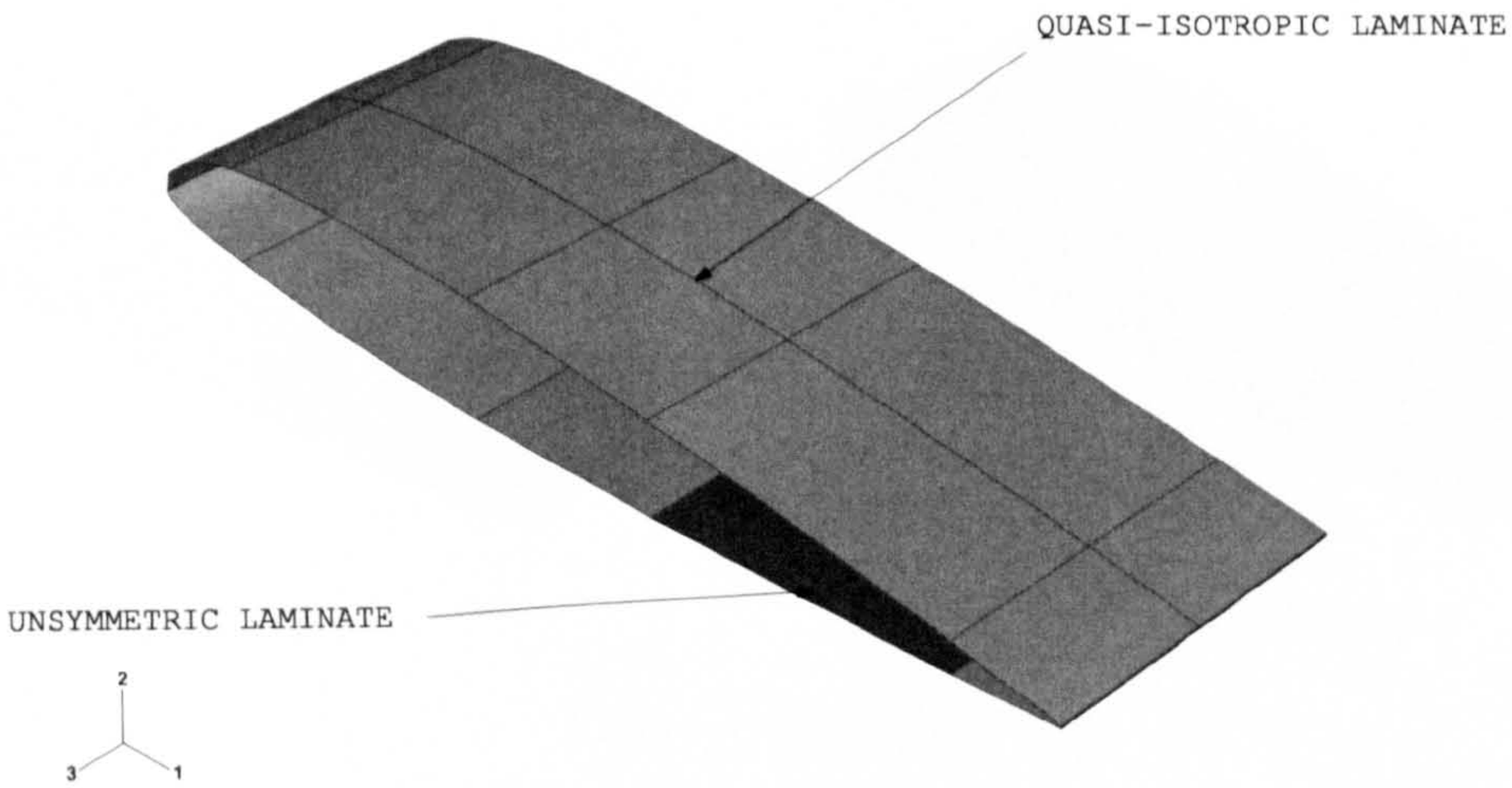

Figure 4.47: Stacking sequence of the *NACA 23015*

most of the original characteristics of the base *NACA23015* airfoil, with the exception of the transverse curvature in the bi-stable panel. The "Cambered" configuration is quite different from the base shape, particularly in the belly of the airfoil where a reversed curvature is achieved.

The analysis of the actuation is carried out in the same way as the previous example. However, due to the intrinsic differences between the two models (i.e. geometry and materials), a more appropriate set of loading and boundary conditions have been chosen. For this experiment, the whole airfoil section has been modelled, therefore the nodes representing the connection between the airfoil and the two spars have been constrained in all six degrees of freedom (ref. Fig. 4.48). Given the flexibility of the glass fibre skin, this assumption has been considered satisfactory to model the interaction with the spars. To obtain the load-displacement diagram, it would have been useful to use an "actuation load" similar to that used in the previous example, for a more direct comparison. Due to the different geometry, however, this has not been possible and the simulation was obtained through a concentrated force applied to the centre of the unsymmetric area. This type of loading condition is, in fact, very similar to that applied to model the elastic response of the compound plate. The main difference lies in having the forward and aft edges of the panel bonded to the symmetric laminate, rather than pinned. The load-displacement diagram, obtained by applying a maximum force of 20N and measuring the displacement at the centre of trailing edge, is shown in Fig. 4.50. The starting point A is representative of the cambered configuration. Immediately, the high flexibility of the

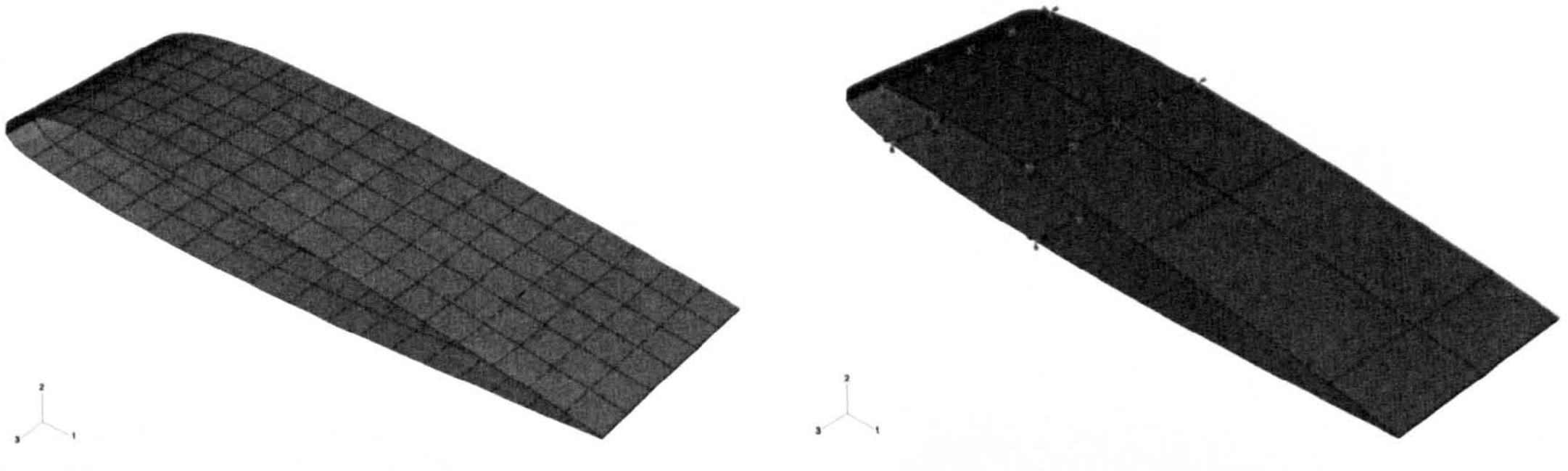

(a) Mesh (b) Boundary conditions

Figure 4.48: FEM

glass skins produces a non-linear increase in the displacement, which makes it difficult to identify the critical load. At point B, the transition between the cambered and the De-cambered configuration is completed and the structure deforms linearly until the load reached the maximum value of 20N in the downward direction (point C). Between points C and D, the load is removed and the device rests in its "De-cambered" configuration (ref. Fig.4.49). At point D, a load opposite in direction is applied to the same point. During this phase (segment DE of the curve), the overall profile remains almost unchanged, while it is the transverse curvature of the unsymmetric part that diminishes gradually. At point E, the carbon laminate is nearly flat and therefore the profile "jumps" into the highly cambered configuration F. Between points F and G, the load is increased until the maximum value of $20\,N$ in the upward direction is reached. At point G the curvature of the lower surface is highly pronounced causing the top of the airfoil to bend downward. This is undesireable but, because it is due to an excessive applied load, it can be easily avoided by limiting the actuation load. Between point G and A, the load is removed and the structure goes back to the initial configuration. The diagrams shown in Fig. 4.50 and Fig. 4.43 summarise the characteristics of the two models. Both present different actuation loads for the two configurations and while the glass based model show a more flexible/non-linear behaviour, the carbon based trailing edge presents several linear segments in the actuation cycle despite the much greater range of deformation.

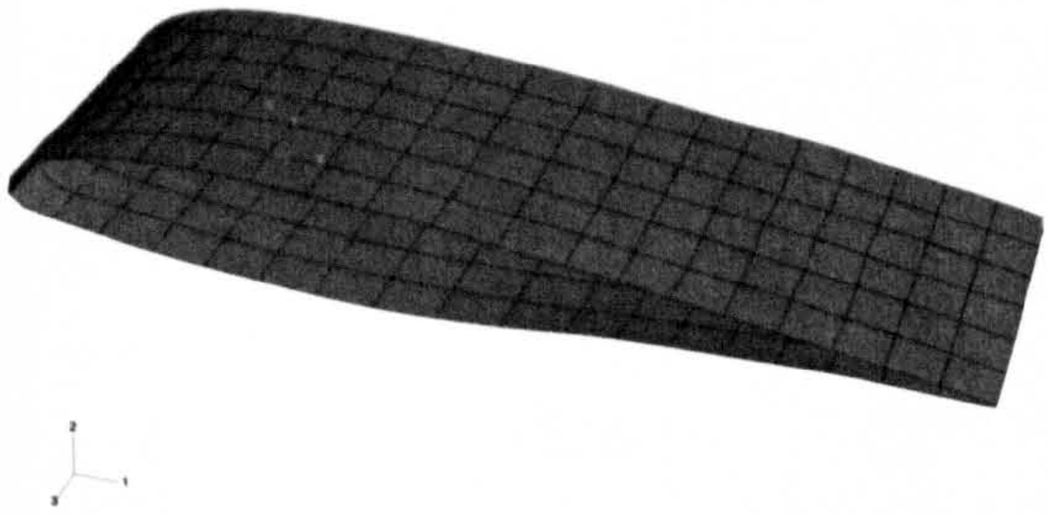

(a) De-cambered

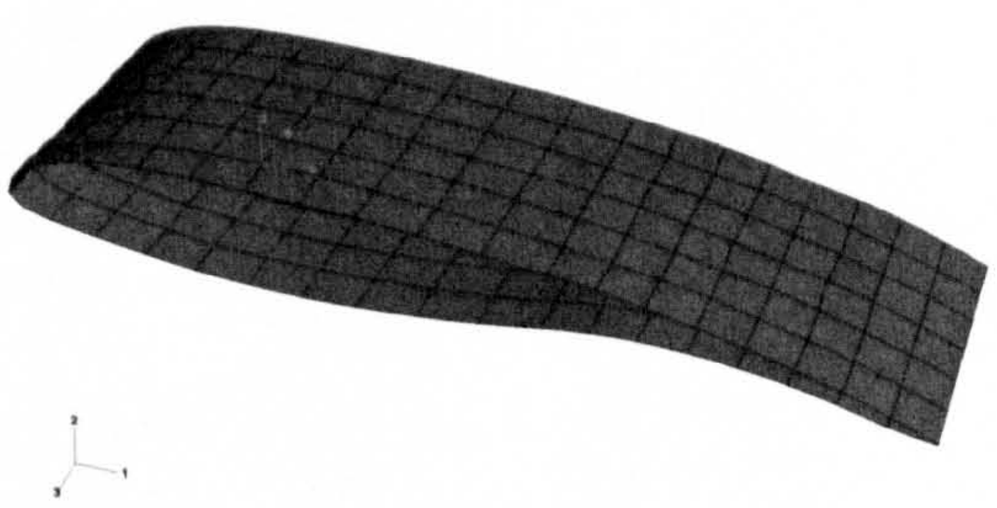

(b) Cambered

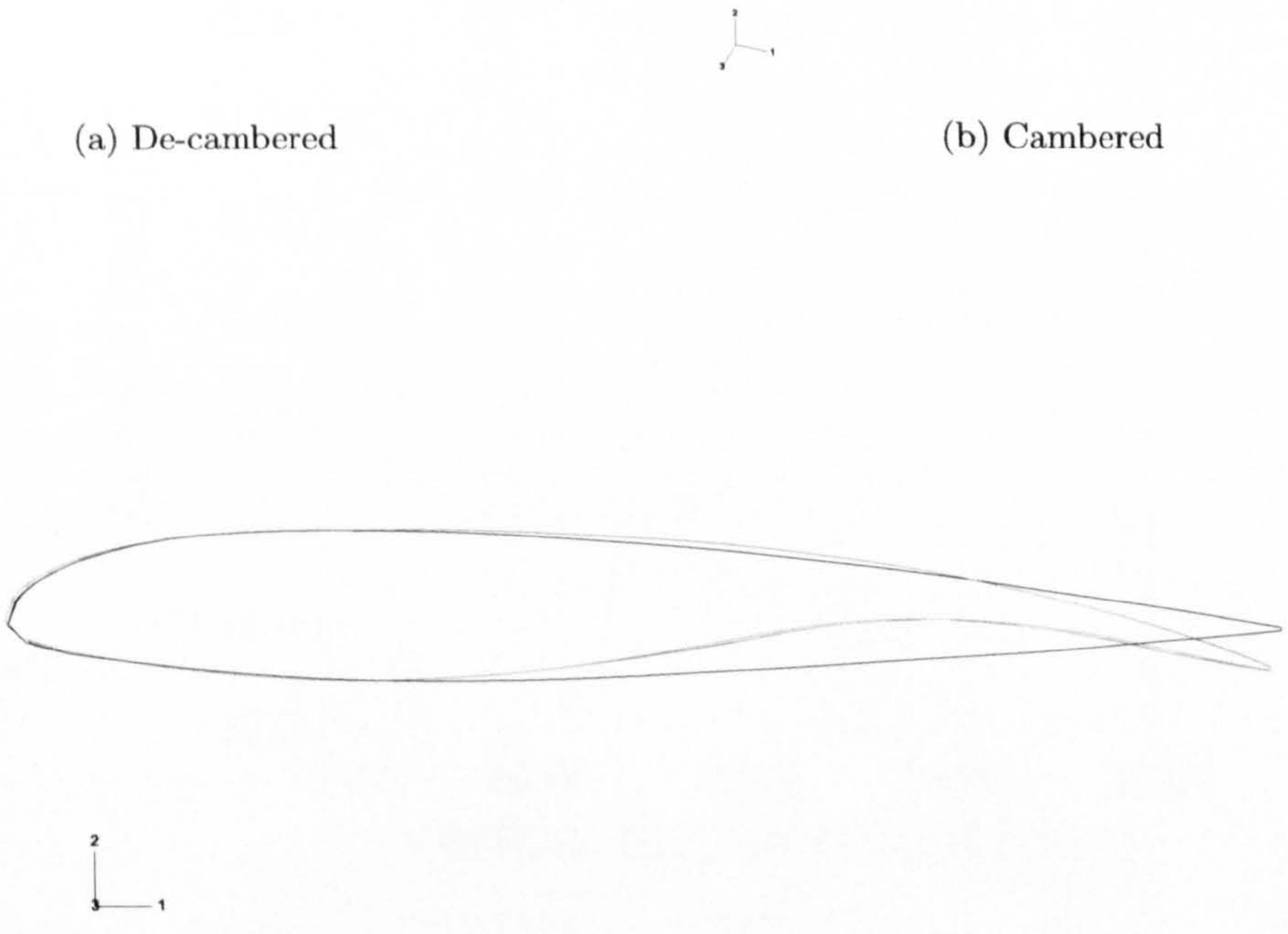

(c) Cross-section comparison

Figure 4.49: Equilibrium configurations

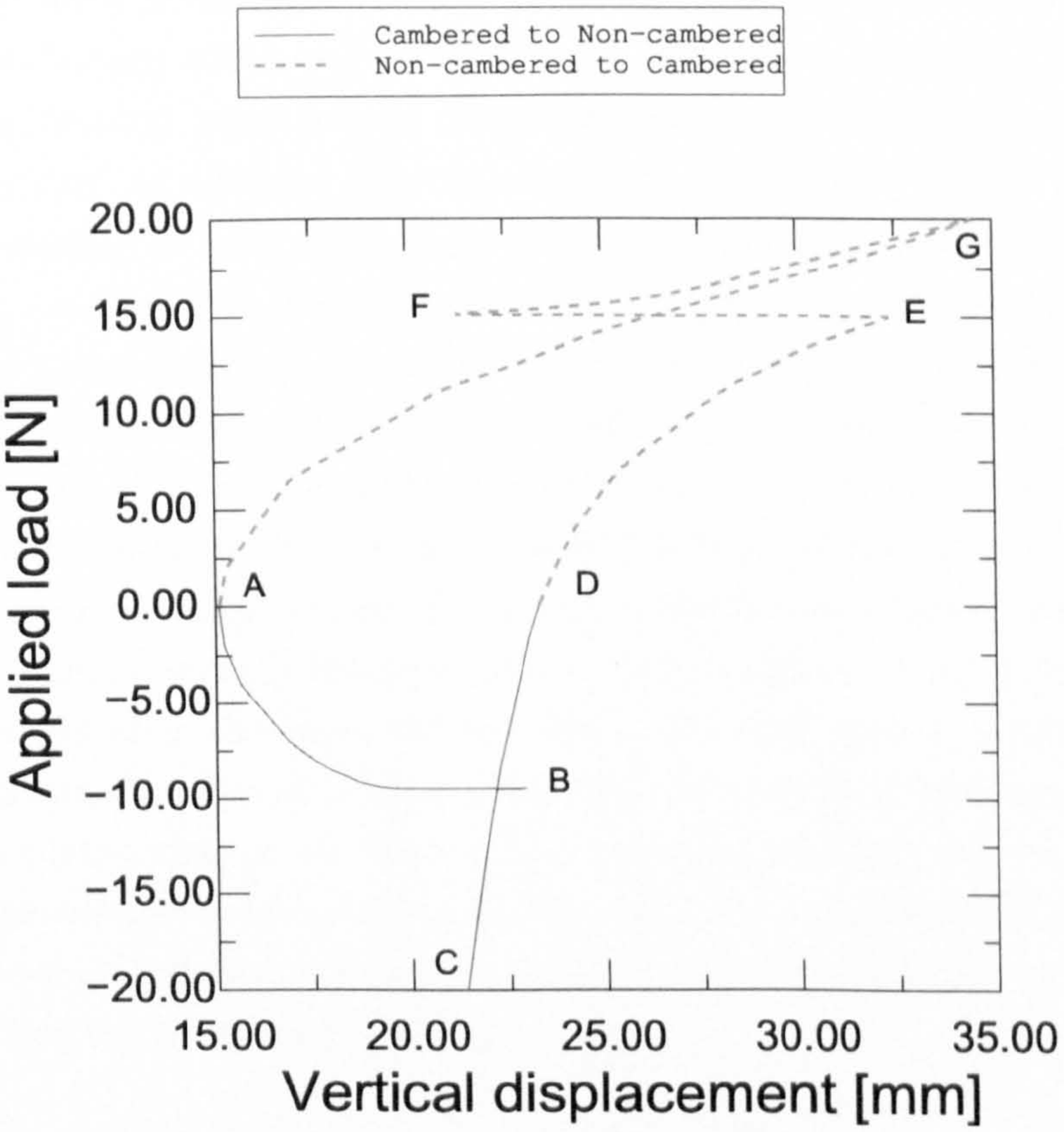

Figure 4.50: Equilibrium configuration

Table 4.4: Typical material properties for a pre-preg glass fibre lamina

Material	E_{11} [GPa]	E_{22} [GPa]	G_{12} [GPa]	v	α_1 [1/°C]	α_2 [1/°C]	t [mm]
E-glass/914	28.9	6.9	3.4	0.3	7e-6	24e-6	0.1

4.3.3 Remarks on the variable camber trailing edge

Both solutions present advantages and disadvantages. The first concept needs an additional sliding mechanism which can prove difficult to operate and could be more prone to mechanical failure, but benefits from more equilibrium states which may find a useful range of applications. In addition it is easier to lock the system in either configuration since it is not possible to induce the "snap-through" if both edges are restrained. The second concept, on the other hand, is particularly simple and therefore more robust since it does not have structural discontinuities. However it has a more limited number of equilibrium states and since it relies on flexible fibres, it could have lower structural properties. The fact that it is possible to snap it back from the cambered to the De-cambered configuration, is an interesting feature, but it could also prove to be a source of problems since involuntary changes in the airfoil shape are certainly undesireable. A locking system could potentially be implemented to limit this eventuality. Both concepts show a great potential in the range of the "shape tailoring" that is achievable by embedding unsymmetric patches of laminate. In addition, they show that one of the limits of the bi-stable plates, that is the limited load bearing capability, can be overcome by using different geometries to compensate for the stiffness. Combining stiff laminates (i.e. carbon) with flexible laminates (i.e. glass), appears to be a promising way to obtain the most benefits from the bi-stable behaviour.

Chapter 5

Conclusions and future work

The aim of the current work was to investigate the behaviour of bi-stable composite panels and understand the implication of their possible application for the realisation of morphing structures. This was done through the development of analytical models, numerical procedures and experimental tests.

The main achievements and results of the work are now summarised and areas needing further work identified.

Summary of the work presented

In the first part, the current scenario of morphing structures for the aeronautical sector is presented. A key requirement for successful applications, was identified which is to achieve a balanced compromise between flexibility and stiffness. In this respect bi-stable structures, realised with unsymmetric laminates are considered as one possible solution.

In order to help in the design phase of these components, a simple analytical model and a numerical procedure have been developed and presented as the second part of the work. The analytical model is an extension of previous models which express the strain state, at any point of the laminated plate, in terms of constant curvatures along the principal material axes. A new formulation for the displacement field is used to predict the out-of-plane displacements and to successfully add the capability of modelling non-constant curvatures. This facilitates the prediction of the equilibrium shapes of panels with areas of symmetric and unsymmetric laminates. The results are compared with FEA and experimental tests, achieving a satisfactory agreement. The extended model is used to investigate the effects of the boundary conditions on the bi-stable behaviour of a compound plate, obtained by joining together two square plates with symmetric and unsymmetric stacking sequences. Parametric studies on the thickness

and the stacking sequence of the symmetric part confirm the robustness of the bi-stable behaviour. The numerical procedure confirms the findings of the analytical approach and gave further insight into the problem. The importance of the inertia effects during the cooling process has been shown by demonstrating that it can influence the convergence of the solution. In addition, the variation of the curvatures with the temperature has been discussed and finally a detailed modelling of the snap-through process has been presented. By monitoring the reaction forces during loading made it possible to obtain the full equilibrium path between two stable states. The analysis of the curvature-temperature diagram highlighted a recovery of the effectiveness of the linear theory, for temperatures significantly lower than the critical temperature. The results have been compared with different numerical schemes and experimental tests, showing satisfactory agreement.

In the last part of the thesis, the feasibility of morphing structures obtained with bi-stable composites, has been discussed through three concepts for applications: the Variable Sweep Wing-box, the Bi-stable Blended Winglet and the Variable Camber Trailing Edge. During the research, particular attention has been devoted to manufacturing aspects and efforts have been put into proposing viable solutions, which are easy to realise, and therefore economic. The Variable Sweep Wing-box presented a novel concept for the realisation of the wing-sweep mechanism, based on composite spars with curved cross section, interconnected with a Z-type truss rib structure. The wing-box is capable of achieving any sweep angle and to alter the shape of the wing by changing the "hinge-point" position. An experimentaall demonstrator has been built and tested to confirm the feasibility of the concept and investigate critical aspects. It emerged that the rib structure and the join between the ribs and the curved spars, are critical components for the performance of the wing-box. The Bi-stable Blended Winglet consists of a shape-adaptable device based on bi-stable panels, which can be used as a high-lift device during low speed operations. With increasing dynamic pressure, the device snaps into a configuration similar to a winglet for high-speed/cruise operations. A combination of fibre orientation and unsymmetric and symmetric laminates has been used to obtain a shape to suit the aerodynamic purposes. FEA have been used to predict the configuration and an experimental model was built for validation. The device was then tested in the wind tunnel to verify its aerodynamic performance and a promising variation in the aerodynamics forces was found in the two configurations. The tests also highlighted dynamic peaks in the generated forces during the snap through, suggesting a more in-depth dynamic analysis of bi-stable components may be required. The last application, the Variable Camber Trailing Edge, was aimed to realise a trailing-edge de-

vice that changes the camber of an airfoil by morphing its geometry. The principle idea is to use unsymmetrically laminated patches whose bi-stability drives the shape change. FEA was used to investigate the possible shapes and load bearing characteristics. An experimental demonstrator has been built to verify the shapes predicted numerically and to emphasise important aspects related to the manufacturing of the device. Finally, an alternative configuration was presented and compared with the previous model. This is based on the combination of different material fibres and made it possible to alter the geometry of the complete airfoil without introducing discontinuity in the aerodynamic surface.

Suggestion for further work

The field of investigation is broad and therefore there are many areas which would benefit from a deeper level of understanding.

From a modelling perspective, a removal of the symmetry condition in the analytical model will allow the equilibrium shapes of angle-ply laminates to be obtained. This would increase the range of shapes which are achievable with this technique and ultimately, by using optimisation routines, it will be possible to solve the more practical problem of finding the stacking sequence needed to obtain a desired shape. The experimental tests highlighted that the dynamic behaviour, during the transition between the stable shapes, is of paramount importance and therefore an accurate dynamic characterisation is needed to assess possible instabilities. This would be useful for the logical next step, that is the implementation of actuation/control systems and the aeroelastic analysis of the proposed applications. The snap-through behaviour is very similar to the buckling behaviour and therefore post-buckling techniques could be used to improve some of the characteristics of bi-stable laminates.

From an application point of view, the effects of temperature (both below and above room temperature) and moisture should be investigated to define the envelope of usability of these devices. Solutions to improve the damage tolerance at the interface between the various lamination areas are also needed. The effects of the aeroelastic deformations and interactions for the presented concepts need to be investigated as well. This is particularly important for the Bistable Blended Winglet where the aeroelastic deformation plays a major role in the initiation of the snap-through deformation. Finally a morphing wing containing some, if not all of the bi-stable structures, would point out the problems related to the system integration, weight penalty and provide a test bed for the comparison with traditional structures.

Appendix A

Riks analysis of snap-through

The analysis of the snap-through of unsymmetric laminates is similar to unstable collapse of structures, involving large deformations (i.e. displacements) and abrupt variations in the reaction forces. These make the numerical analysis particularly challenging and consequently the traditional iterative techniques, such as Newton-Raphson, fail to find the solution of the system of non-linear equations associated with an unstable equilibrium. Modifications of the Newton-Raphson technique, such as "arc-length" methods, are commonly used to overcome this problem. A version of this method is implemented in ABAQUS and invoked through the keyword `*Riks`. The routine is based on the method that was first introduced by Wempner [1971] and Riks [1979] and later modified by Ramm [1980], Crisfield [1981] and Powell and Simons [1981]. The `*Riks` method is generally applicable to those cases in which the load varies very slowly and involves slow changes of configuration, typical of quasi-static conditions and therefore under these circumstances the contribution of the inertia forces can be neglected. During a Riks' analysis the solution is searched in a space defined by the nodal variables and the loading parameter, which is an additional unknown of the problem. During the analysis, the loading is always proportional and the current load magnitude is defined by $P = \lambda \cdot P_{ref}$, where P_{ref} is the intended applied load vector. The continuous sequence of equilibrium states corresponding to a continuous variation of load traces out an equilibrium path in the displacement-load space. The progress of the solution is measured through the "arc length," l, along the static equilibrium path. Starting from a known equilibrium configuration, an estimate for the next equilibrium point on the load-displacement curve, is determined as the tangential solution (i.e. Newton-Raphson method) at a prescribed distance Δl from the current position. Further iterations are performed to match a desired tolerance. The key point to obtain a successful analysis lies in the way the increment is

determined and generally good results are obtained with path-constraint equations. In *ABAQUS/Standard,* the initial step Δl, is suggested by the user and for the subsequent iterations it is adjusted automatically, based on the convergence rate. The arc length increments are bounded between values provided by the user. In this way the control over the load magnitude is quite limited. The approach provides solutions regardless of whether the response is stable or unstable. This is a clear advantage with respect to the stabilised analysis, since it allows the modelling of the unstable branch of the solution. It is possible, however, that in some cases where the response of the structure shows a very high curvature, the criteria adopted for the search of the arc-length increment, will choose an incorrect sign of the increment.

Unfortunately this is what has been noticed occasionally during the analysis of the snap-through of unsymmetric laminates performed with ABAQUS. To prove this, the same 8-layered compound plate analysed throughout the thesis, has been tested with the modified Riks method. The panel has been modelled with a rather fine mesh of 800 *S4R* elements and 861 nodes in order to rule out inaccuracies due to a coarse mesh. The cool-down simulation has been carried out with a basic non-linear analysis to limit the effects of any added viscosity and to focus the attention on the snap-through step. After the curled shape has been obtained, the same boundary and loading conditions discussed in Section 3.1 have been applied to the model. As a result, the Riks method did not successfully snap the panel from the curled to the flat configuration, as shown by the diagram in Fig. A.1 and A.2. The applied load was automatically increased until a load very close to the critical (ref. to Section3.1 and Fig. 3.35 for comparison) was reached. At this point the load proportionality factor was reduced to almost zero and eventually changed in sign, forcing the numerical solution to go back on itself. Figure A.3 shows a detail of Fig. A.1, in the region of the maximum load and the sign reversal. The physical effects of the incorrect loading are shown in Fig. A.4 where a few snapshots of the analysis are shown.

This does not mean that the Riks method is not able to find a physical solution in any conditions. The critical load is, in fact, very close to that obtained with the `*Stabilize` method and there are also many cases in which the Riks analysis reached convergence quickly. Furthermore, the Riks method does not need any a-priori information on the load required to snap the structure, whereas the `*Stabilize` method needs to have a load greater than the bifurcation load to achieve a complete snap-through. This is particularly useful during the initial phases of the design process, when little is know about the structure.

However, when a suitable combination of parameters and boundary conditions is

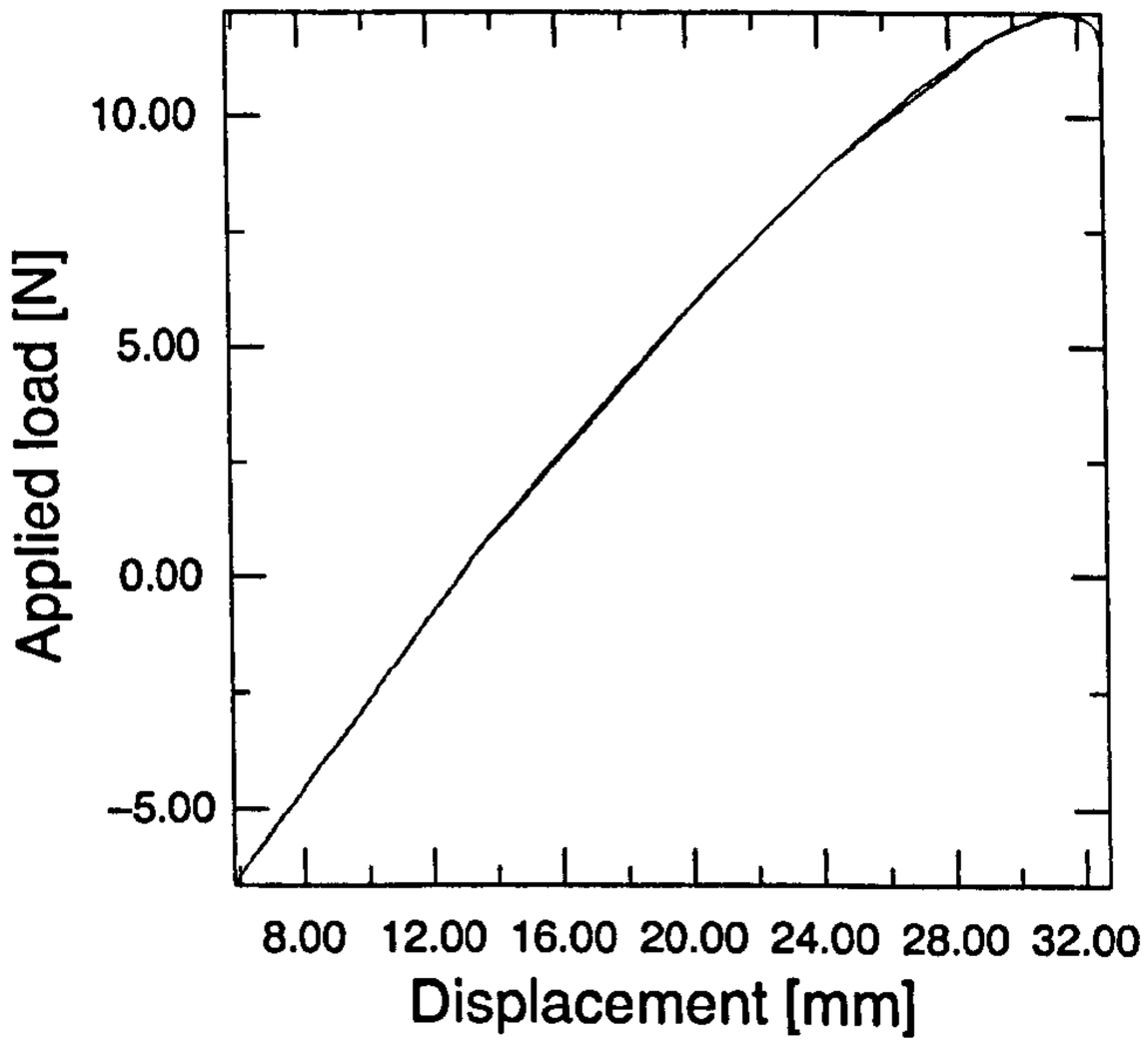

Figure A.1: Load-displacement diagram obtained with the Riks method

not found, the analysis is computationally expensive and requires continuous user input to achieve satisfactory results. It is for these reasons that this method was considered inappropriate for the purpose of the study presented in this thesis.

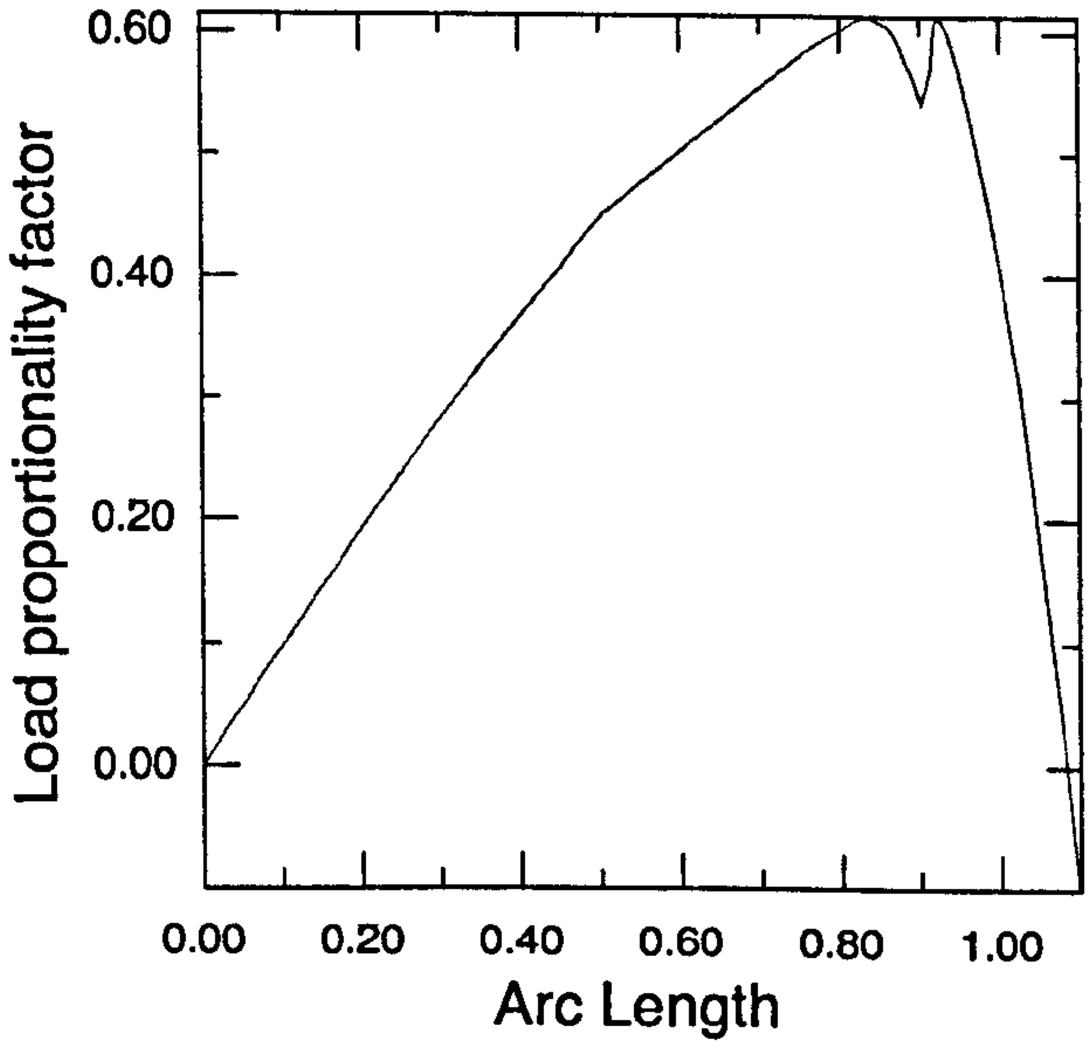

Figure A.2: Load proportionality factor for the snap-through analysis

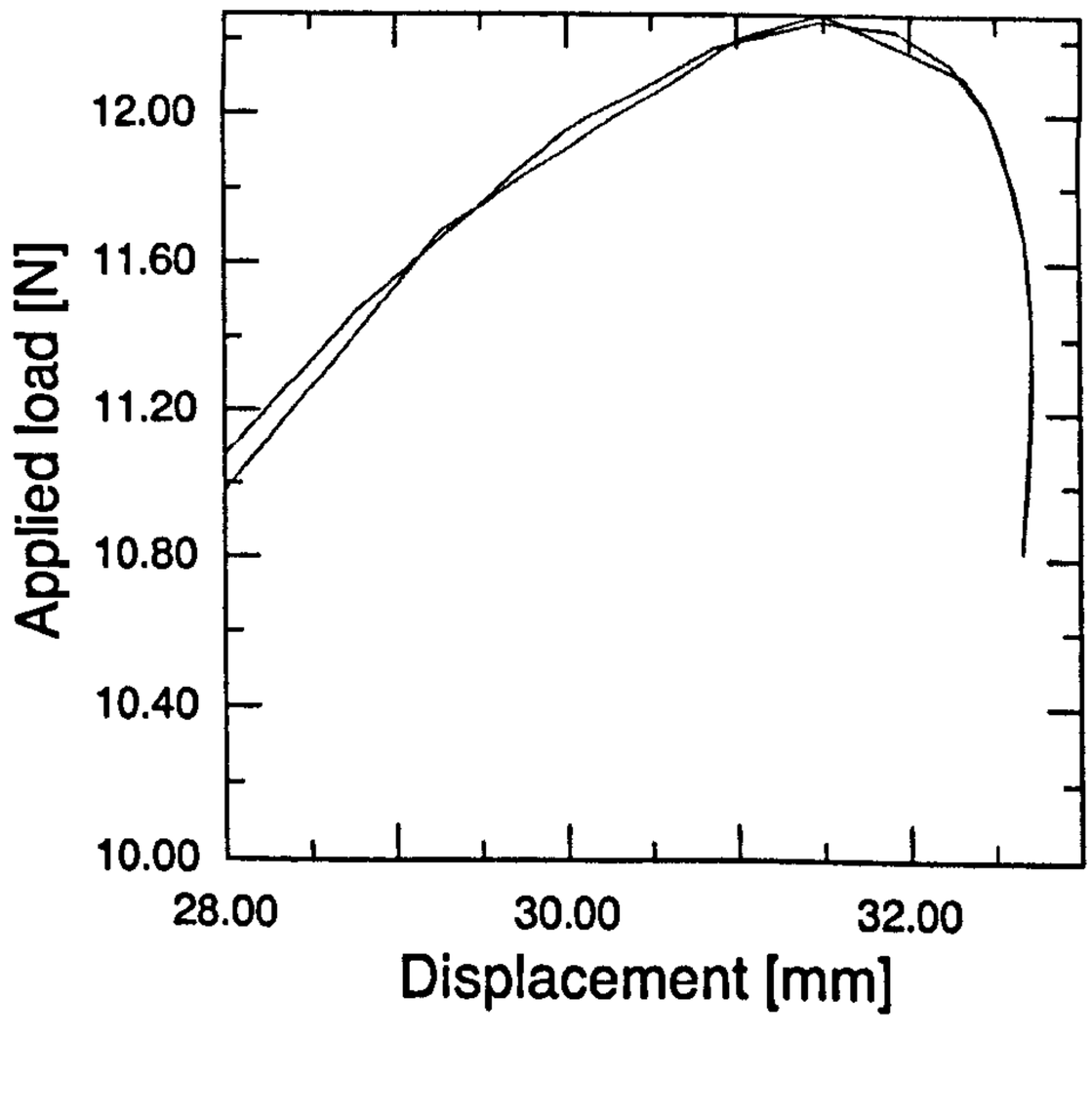

Figure A.3: Effect of the sign reversal

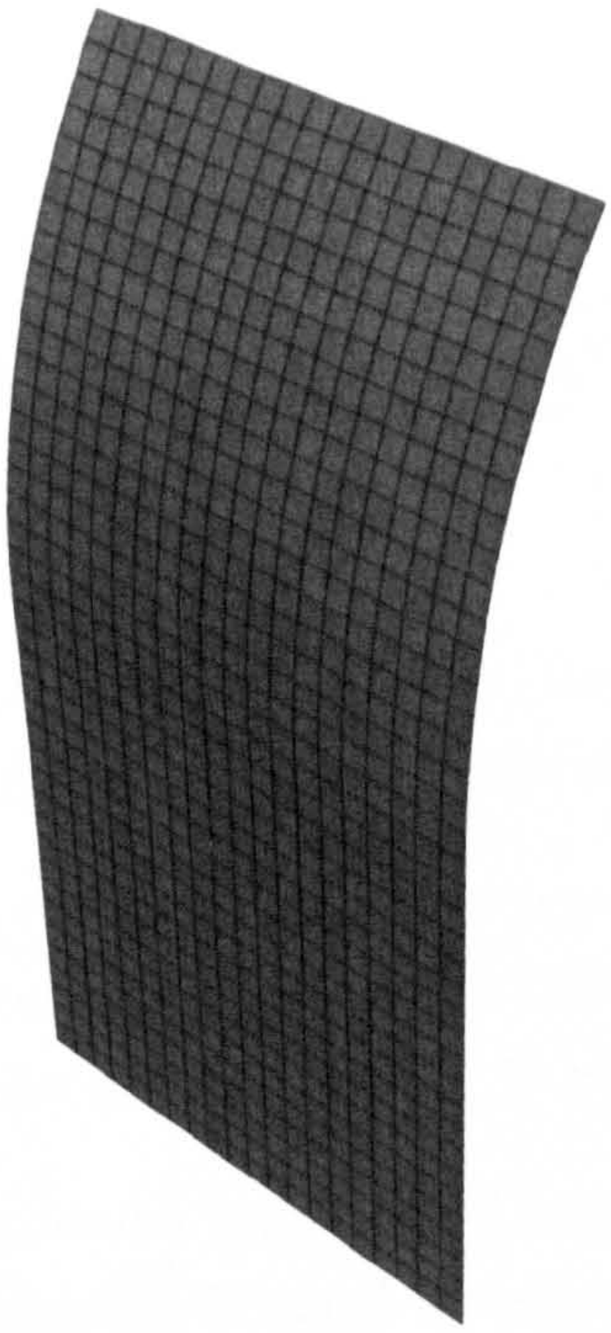

(a) Initial state

(b) At maximum load

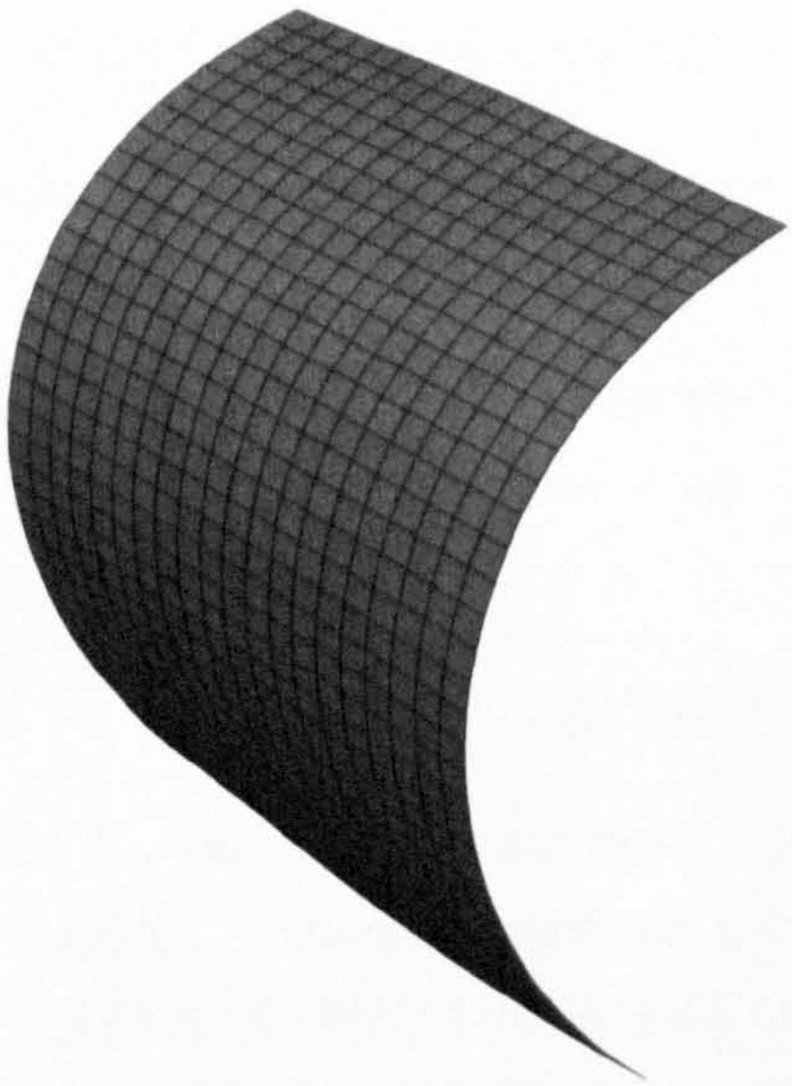

(c) Intermediate step after load reversal

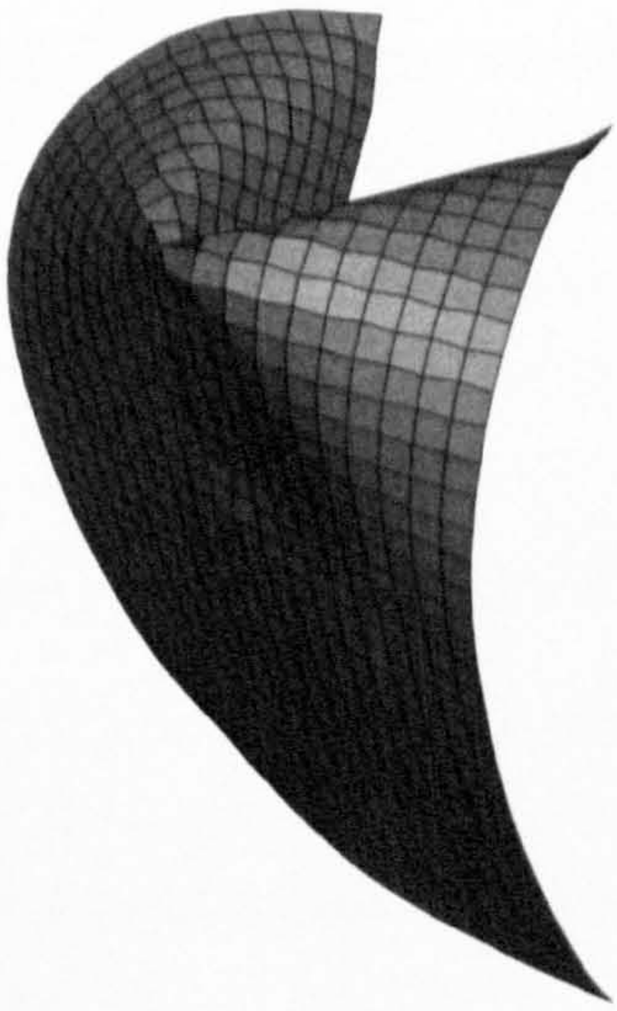

(d) Final state

Figure A.4: Intermediate snapshots during the analysis

Bibliography

I. H. Abbott and A. E. von Doenhoff. *Theory of Wing Sections: Including a summary of airfoil data.* Dover Publications Inc, New York, 1959.

M. Amprikidis and J. E. Cooper. Development of smart spars for active aeroelastic structures. In *44th AIAA/ASME/ASCE/AHS/ASC Structures, Structural Dynamics & Materials Conference*, Norfolk, Virginia, 7-10 April 2003.

M. Amprikidis and J. E. Cooper. Experimental validation of wing twist control using adaptive internal structures. In *45th AIAA/ASME/ASCE/AHS/ASC Structures, Structural Dynamics & Materials Conference*, 19-22 April, Palm Springs, California 2004a.

M. Amprikidis and J. E. Cooper. Development of an adaptive stiffness all-moving vertical tail. In *45th AIAA/ASME/ASCE/AHS/ASC Structures, Structural Dynamics & Materials Conference*, number AIAA-2004-1884, April 2004b.

John D. Anderson. *Modern compressible flows.* McGraw-Hill International Editions,, 1999.

J-S Bae, N-H Kyonh, M Seigler, and D. J. Inman. Aeroelastic considerations on shape control of an adaptive wing. *Journal of Intelligent Material Systems and Structures*, 16:1051–1056, 2005.

K. J. Bathe. *Finite elements procedure in engineering analysis.* Prentice Hall, 1982.

J. Bowman, B. Sanders, B. Cannon, J. Kudva, S. Joshi, and T. Weisshaar. Development of next generation morphing aircraft structures. In *48th AIAA/ASME/ASCE/AHS/ASC Structures, Structural dynamics and materials conference*, Honolulu, Hawaii., 23-26 April 2007.

D. R. Bye and P. D. McClure. Design of a morphing vehicle,. In *48th AIAA/ASME/ASCE/AHS/ASC Structures, Structural dynamics and materials conference*, Honolulu, Hawaii, USA, 23-26 April 2007.

L. F. Campanile and S. Anders. Aerodynamic and aeroelastic amplification in adaptive belt-rib airfoils. *Aerospace Science and Technology*, 9:55–63, 2008.

L. F. Campanile and D. Sachau. The belt-rib concept: a structronic approach to variable camber. *Journal of intelligent material systems and structures*, 11(3), 2000.

M. Cerini and B. G. Falzon. Use of arc-length method for capturing mode jumping in postbuckling aerostructures. *AIAA Journal*, 43(3), March 2005.

J. B. Cole. Variable camber airfoil. Technical report, US Patent and trademark office, 1976.

M. A. Crisfield. *Non-linear Finite Element Analysis of Solids and Structures*, volume 1. Wiley & Sons., 1997a.

M. A. Crisfield. *Non-linear Finite Element Analysis of Solids and Structures*, volume 2. Wiley & Sons., 1997b.

M. A. Crisfield. A fast incremental/iterative solution procedure that handles "snap-through". *Computers & Structures*, 13(1-3):55–62, 1981.

J. Dang and Y. Tang. Calculation of the room-temperature shapes of unsymmetric laminates. In *International symposium on composite materials and structures*, pages 201–6, Lancaster, PA, 1986. Technomic Publishing.

M. L. Dano and M. W Hyer. Thermally-induced deformation behavior of unsymmetric laminates. *Int. J. Solids Struct.*, 35(17):2101–2120, 1998.

M. L. Dano and M. W. Hyer. Snap-through of unsymmetric fiber-reinforced composite laminates. *International Journal of Solids and Structures*, 39(1):175–198, January 2002.

M. L. Dano and M. W. Hyer. Sma-induced snap-through of unsymmetric fiber-reinforced composite laminates. *International Journal of Solids and Structures*, 40(22):5949–5972, 2003.

M. L. Dano and M. W. Hyer. The response of unsymmetric laminates to simple applied forces,. *Mechanics of composite materials and structures*, 3:65– 80, 1996.

C. G. Diaconu, P. M. Weaver, and F. Mattioni. Concepts for morphing airfoil sections using bi-stable laminated composite structures,. *Thin-Walled Structures*, 46(6):689–701, 2008.

R. J. Englar, M. J. Smith, S. M. Kelley, and R. C. Rover. Application of circulation control to advanced subsonic transport aircraft, part ii: Transport application. *Journal of Aircraft*, 31(5):1169–1177, 1994.

ESDU. *Aerodynamic principles of winglets.* ESDU International, 98013, London, UK, 1998.

G. J. Frank, J. J. Joo, B. Sanders, D. M. Garner, and A. Murray. Mechanization of a high aspect ration wing for aerodynamic control. *Journal of Intelligent Material Systems and Structures*, 19:1101–1112, 2008.

M. Fujikake. A simple approach to bifurcation and limit point calculations. *Int. Journal for numerical methods in engineering*, 21:183–191, 1985.

F. Gandhi and A-I Phuriwat. Skin design studies for variable camber skin design studies for variable camber morphing airfoils. *Smart Materials and Structures*, 17, 2008.

M. Gigliotti, M. R. Wisnom, and K. D. Potter. Development of curvature during the cure of as4/8552 [0/90] unsymmetric composite plates. *Composites Science and Technology*, 63:187–197, 2003.

M. Gigliotti, M. R. Wisnom, and K. D. Potter. Loss of bifurcation and multiple shapes of thin [0/90] unsymmetric composite plates subject to thermal stress. *Composites Science and Technology*, 64(1):109–128, 2004.

W. Hufenbach and M. Gude. Analysis and optimisation of multistable composites under residual stress. *Composite structures*, 55:319–327, 2002.

W. Hufenbach, M. Gude, and L. Kroll. Design of multistable composites for application in adaptive structures. *Composites science and technology*, pages 2201–2207, 2002.

W. Hufenbach, M. Gude, and A. Czulak. Actor-initiated snap-through of unsymmetric composites with multiple deformation states. *Journal of Materials Processing Technology*, 175(1-3):225–230, 2006.

M. W. Hyer. Some observation on the cured shape of thin unsymmetric laminates. *J. Composite Materials*, 15:175–194, 1981a.

M. W. Hyer. Calculations of the room-temperature shapes of unsymmetric laminates. *Journal of composite materials*, 15:296–310, 1981b.

M. W. Hyer. The room-temperature shapes of four layer unsymmetric cross-ply laminates. *J. Composite Materials*, 16:318–340, 1985.

M. W. Hyer and P. C. Bhavani. Suppression of anticlastic curvature in isotropic and composite plate. *International Journal of Solids and Structures*, 20(6):553–570, 1984.

A. K. Jha and J. N. Kudva. Morphing aircraft concepts, classifications, and challenges. In E. H. Anderson, editor, *Proceedings of SPIE*, volume 5388, 2004.

R. M. Jones. *Mechanics of composite materials*. Taylor & Francis, 2nd edition edition, 1999.

W. J. Jun and C. S. Hong. Effects of residual shear strain on the cured shape of unsymmetricl cross-ply thin laminates. *Composites science and technology*, 38:55–67, 1990.

W. J. Jun and C. S. Hong. Cured shape of unsymmetric laminates with arbitrary lay-up angles. *Journal of Reinforce Plastics and composites*, 11:1352, 1992.

E. Kebadze, S. D. Guest, and S. Pellegrino. Bistable prestressed shell structures. *International Journal of Solids and Structures*, 41(11-12):2801–2820, 2004.

S. Kota, J. Hetrick, and R. Osborn. Design and application of compliant mechanisms for morphing aircraft structures. In *Proceedings of SPIE*, volume 5054, 2003.

S. Kuzmina, G. Amiryants, J. Schweiger, J. Cooper, M. Amprikidis, and O. Sensberg. Review and outlook on active and passive aeroelastic design concepts for future aircraft. In *Proceedings of the 23rd international congress of aerospace sciences, volume 4.3 of Structural dynamics II*, September 2002.

M. H. Love, P. S. Zinik, R. L. Stroud, D. R. Bye, S. Rizk, and D. White. Demonstration of morphing technology through ground and wind tunnel tests. In *48th AIAA/ASME/ASCE/AHS/ASC Structures, Structural Dynamics and Materials Conf.*, Honolulu, Hawaii, USA, April 2007.

M. E. McKinney. Variable camber trailing edge for airfoil. Technical report, US Patent and trademark office, 1982.

H. P. Monner. Realization of an optimized wing camber by using formvariable flap structures. *Aerospace Science and Technology*, 5(7):445–455, October 2001.

NextGen. Aeronautics, 2007. URL `http://www.nextgenaero.com/`.

M. C. Y. Niu. *Composite airframe structures: Practical design and information data.* Hong Kong Conmilit press ltd., 3rd edition edition, 2000.

M. C. Y. Niu. *Airframe structural design.* Hong Kong Conmilit press ltd., second edition, 1999a.

M. C. Y. Niu. *Airframe stress analysis and sizing.* Hong Kong Conmilit press ltd., second edition, 1999b.

K. Orlik-Ruckemann. Aerodynamic aspects of aircraft dynamics at high angles of attack. *Journal of Aircraft*, 20(9):737–752, 1983.

M. Papila, R. T. Haftka, W. H. Mason, and R. Alves. Tailoring wing structures for reduced drag penalty in off-design flight conditions. In *10th AIAA/ISSMO Multidisciplinary analysis and optimization conference*, Albany, NY, USA, August 30 - September 1 2004.

M. Pinto, A. D. Santos, P. Teixeira, and P.J. Bolt. Study on the usability and robustness of polymer and wood materials for tooling in sheet metal forming. *Journal of Materials Processing Technology*, 202(1-3):47–53, 20 June 2008.

P. Portela, P. Camanho, P. M. Weaver, and I. Bond. Analysis of morphing, multi stable structures actuated by piezoelectric patches. *Computers & Structures*, 86(3-5):347–356, 2008.

K. D. Potter and P. M. Weaver. A concept for the generation of out-of-plane distortion from tailored frp laminates. *Composite Part A: Applied Science and Manufacturing*, 35(12):1353–1361, December 2004.

G. Powell and J. Simons. Improved iterative strategy for nonlinear structures. *International Journal for Numerical Methods in Engineering*, 17:1455–1467, 1981.

E. Ramm. Strategies for tracing the nonlinear response near limit points. In W. Wunderlich, E. Stein, and K.J. Bathe, editors, *Nonlinear Finite Element Analysis in Structural Mechanics: Proceedings of the Europe-US Workshop*, 1980.

D. P. Raymer. *Aircraft Design: A conceptual approach.* AIAA, Inc., 370 L'enfant Promenade, S. W., Washington, D. C. 20024, 1992.

Libo Ren. Theoretical study on shape control of thin cross-ply laminates using piezoelectric actuators. *Composite structures*, 80(3):451–460, October 2007.

E. Riks. An incremental approach to the solution of snapping and buckling problems. *International Journal of Solids and Structures*, 15(7):529–551, 1979.

L. Saggere and S. Kota. Static shape control of smart structures using compliant mechanism. *AIAA Journal*, 37(5):572–578, May 1999.

T. Schioler and S. Pellegrino. Multi-configuration space frames. In *45th AIAA/ASME/ASCE/AHS/ASC Structures, Structural Dynamics & Materials Conference*, Palm Springs, California, 2004.

M. Schlecht and K Schulte. Advanced calculation of the room-temperature shapes of unsymmetric laminates. *Journal of Composite Materials*, 33(16):1472–1490, 1999.

M. Schlecht, K. Schulte, and M. W. Hyer. A comparative study for the calculation of the temperature dependent shapes of unsymmetric laminates based on finite element analysis and extended classical lamination theory. *Mechanics of Composite Materials*, 31(3):247–254, 1995.

M. Schultz and M. W. Hyer. Snap-through of unsymmetric cross-ply composites using piezoelectric actuators. *J. Intellig. Mater. Syst. Struct*, 14/12:795–814, 2003.

Marc R. Schultz. A concept for airfoil-like active bistable twisting structures. *Journal of Intelligent Material Systems and Structures*, 19:157–169, 2008.

K.A. Seffen, Z. You, and S. Pellegrino. Folding and deployment of curved tape springs. *nternational Journal of Mechanical Sciences*, 42(10):2055–2073, October 2000.

Martin Simonis. *Model aircraft aerodynamics.* Argus Books, 1989.

Omer Soykasap. Analysis of tape spring hinges. *International Journal of Mechanical Sciences*, 49(7):853–860, September 2007.

J.J. Spillmann. The use of variable camber to reduce drag, weight and costs of transport aircraft. *Aeronautical Journal*, 96(951):1–9, 1992.

Egon Stanewsky. Aerodynamic benefits of adaptive wing technology. *Aerospace Science and Technology*, 4(7):439–452, 2000.

F. F. Statkus. Continuous skin, variable camber airfoil edge actuating mechanism. Technical report, European patent application, 1984.

J. Szodruch. The influence of camber variation on the aerodynamics of civil transport aircraft. In *Aerospace Sciences meeting*, NV, January 14-17 1985. AIAA.

S. Tawfik, X. Tan, S. Ozbay, and E. Armanios. Anticlastic stability modeling for cross-ply composites. *Journal of Composite Materials*, 41(11), 2007.

C. Thill, J. Etches, I. Bond, K. D. Potter, and P. M. Weaver. Morphing skins. *The aeronautical Journal*, 112(1129), March 2008.

E. Torenbeek. *Synthesis of Subsonic Aeroplane Design.* Kluwer Academic Publishers, 1982.

G. A. Wempner. Discrete approximations related to nonlinear theories of solids. *International Journal of Solids and Structures*, 7:1581–1599, 1971.

R. Whitcomb. A design approach and selected wind-tunnel results at high subsonic speeds for wing-tip mounted winglets. Technical Report N76-26163, 1976.

J. C. H. Yee, O. Soykasap, and S. Pellegrino. Carbon fibre reinforced plastic tape springs. In *45th AIAA/ASME/ASCE/AHS/ASC Structures, Structural Dynamics, and Material Conference and Exhibit*, Palm Springs, California, April 2004.

W. C. Young. *Roark's Formulas for Stress and Strain.* McGraw-Hill, 6th edition, 2001.